Modelling and analysis of nonlinear thermoacoustic systems using frequency and time domain methods

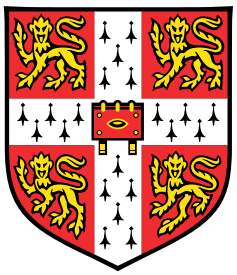

Alessandro Orchini

Department of Engineering
University of Cambridge

This dissertation is submitted for the degree of
Doctor of Philosophy

Robinson College September 2016

To my friends.

Mi fan patir costoro il grande stento,
Che vanno il sommo bene investigando,
E per ancor non v'hanno dato drento.
E mi vo col cervello immaginando,
Che questa cosa solamente avviene
Perché non è dove lo van cercando.
Questi dottor non l'han mai intesa bene,
Mai son entrati per la buona via,
Che gli possa condurre al sommo bene.
Perché, secondo l'opinion mia,
A chi vuol una cosa ritrovare,
Bisogna adoperar la fantasia,
E giocar d'invenzione, e 'ndovinare;
E se tu non puoi ire a dirittura,
Mill'altre vie ti posson aiutare.

– Galileo, 1590

Declaration

I hereby declare that, except where specific reference is made to the work of others, the contents of this dissertation are original and have not been submitted in whole or in part for consideration for any other degree or qualification in this, or any other University. This dissertation is my own work and contains nothing which is the outcome of work done in collaboration with others, except as specified in the text and Acknowledgements. This dissertation contains fewer than 65,000 words including appendices, bibliography, footnotes, tables and equations and has fewer than 150 figures.

Alessandro Orchini
September 2016

Acknowledgements

I would like to thank Professor Matthew Juniper, who offered me the opportunity to study in Cambridge. I have (hopefully) learnt from him the art of writing a scientific paper, being less impulsive and more critic with my research/myself. As a general rule, PhD students tend to treat their supervisor as a scapegoat in difficult situations. I likely have been no exception. Sorry for that.

Thanks to Dr. Simon Illingworth and Dr. Iain Waugh for their support during the first year of my PhD, and for having helped me in understanding LOTAN, LSGEN, and many other British acronyms. Thanks to Peter Benie for his invaluable help with (any sort of) programming problems. Thanks to Professors Jonas Moeck and Nicolas Noiray, who showed interest in my research and have advised me multiple times.

I have been lucky enough to meet and work with many great people in the last four years. Thanks to Giulio for everything, ranging from endless discussions on thermoacoustics to the nights spent in a caravan on the Dolomites. And thanks to George(ios) for another set of everlasting discussions on fluid mechanics, and for summer barbecues.

Thanks to all the other friends/colleagues – Vik, Karthik, José, Francesca, Caro, Chris, Outi, Ewa, Jack, Nick, Juan, Bernhard, Luca, Pau, Ubaid and Chiara – for the formals, hiking trips, work discussions, robot's brain programming, tango and salsa classes, drinks, chess games, punting and kayaking afternoons, picnics and language exchange we had together.

Thanks to my climbing mates, particularly Alex and Lisa, for all the fun we had at and around the wall.

Thanks to my family – Susy, Fede, Fra – and friends – Nuccia e Fede, Ema, Simone, Momo e Dado, Ari, Silvina, Bute, and the "physicists' gang" – who constantly checked that I am doing fine here, even if it always rains.

And thanks to Carolina for having shared with me part of this adventure. Unfortunately it had some collateral effects.

A PhD is a long and perilous path, which I would not have been able to walk on alone. Thank you all :)

Ale

Abstract

Thermoacoustic oscillations may arise in combustion chambers when unsteady heat release and acoustic fluctuations constructively interfere. These oscillations generally lead to undesired consequences, and need to be avoided. Linear stability analysis can be used to investigate the linear stability of a thermoacoustic system, by calculating the frequencies and growth rates of thermoacoustic modes. Adjoint methods can then be used to understand what parameters in the configuration under investigation have to be changed to make it less susceptible to thermoacoustic oscillations. Linear stability is, however, not sufficient in general to ensure safe operability conditions. This is because nonlinear and non-normal effects may trigger finite amplitude oscillations when the system is subject to finite amplitude perturbations. A thorough fully nonlinear investigation of thermoacoustic systems is prohibitively expensive both experimentally and numerically, and one needs to approximate the nonlinear response of the system.

In this thesis, low-order nonlinear models for the prediction of the nonlinear behaviour of thermoacoustic systems are developed. These models are based on thermoacoustic networks, in which linear acoustics is combined with a nonlinear heat release model. The acoustic networks considered in this thesis can take into account mean flow and non-trivial acoustic reflection coefficients, and are cast in state-space form to enable analysis both in the frequency and time domains.

Starting from linear analysis, the stability of thermoacoustic networks is investigated, and the use of adjoint methods for understanding the role of the system's parameters on its stability is demonstrated. Then, a fully nonlinear analysis using various state-of-the-art methods is performed, to highlight the strengths and weaknesses of each method. Two novel frameworks that fill some gaps in the available methods are developed: the first, called Flame Double Input Describing Function (FDIDF), is an extension of the Flame Describing Function (FDF). The FDIDF approximates the flame nonlinear response when it is forced simultaneously with two frequencies, whereas the FDF is limited to one frequency. Although more expensive to obtain, the FDIDF contains more nonlinear information than the FDF, and can predict periodic and quasiperiodic oscillations. It is shown how, in some cases, it corrects the prediction of the FDF about the stability of thermoacoustic oscillations. The

second framework developed is a general weakly nonlinear formulation of the thermoacoustic equations in the Rijke tube, in which the acoustic response is not limited to a single-Galerkin mode, and is embedded in a state-space model. The weakly nonlinear analysis is strictly valid only close to the expansion point, but is much cheaper than any other available method.

The above methods are applied to relatively simple thermoacoustic configurations, in which the nonlinear heat release model is that of a laminar conical flame or an electrical heater. However, in real gas turbines more complex flame shapes are found, for which no reliable low-order models exist. Two models are developed in this thesis for turbulent bluff-body stabilised flames: one for a perfectly premixed flame, in which the modelling is focused on the flame-flow interaction, accounting for the presence of recirculation zones and temperature gradients; the second for imperfectly premixed flames, in which equivalence ratio fluctuations, modelled as a passive scalar field, dominate the heat release response. The second model was shown to agree reasonably well with experimental data, and was applied in an industrial modelling project. When embedded in a thermoacoustic network, it is capable of predicting the value of the frequency at which thermoacoustic oscillations are prone to grow.

Table of contents

Chapter 1

Introduction

Thermoacoustic oscillations may arise in systems in which a heat source is enclosed in a confined environment, which acts as an acoustic resonator (Culick, 2006; Lieuwen, 2012). Although the phenomenon was first reported two centuries ago by Higgins (1802), and qualitative understood in terms of coupling between unsteady heat release and acoustic waves by Rayleigh (1878), it became a problem of academic and industrial relevance only in the last few decades, with the advent of rocket engine and gas turbine technologies.

Gas turbines play a major role in the conversion of energy from burning fuel. They are used to create thrust for aircraft, and provide more than 20% of the world's electrical energy production. Over the past decades more and more stringent regulations on pollution emissions have been imposed on gas turbine manufacturers. In particular, the demand of reducing NO_x emissions – which are responsible for acid rain, and react to produce ozone, which in turn causes breathing problems and is a strong greenhouse gas – led to the development of combustors working in lean, premixed regimes. These configurations, however, often exhibit thermoacoustic oscillations. In almost all situations, thermoacoustic oscillations are undesirable: they produce noise, structural vibrations, and impose limits to the gas turbines operating conditions, which may reduce the system's efficiency and power output (Culick, 2006; Lieuwen *et al.*, 2010; Lieuwen, 2012).

Thus, one of the manufacturer's goals is to design an engine that is not susceptible to thermoacoustic oscillations over the entire operating range. This is currently achieved by extensive experimental testing, repeated re-design, and sometimes by the retro-fitting of damping devices such as Helmholtz resonators. Experiments and high-fidelity numerical simulations, such as compressible Large Eddy Simulations (LES) of reacting flows (Pitsch, 2002; Moin & Apte, 2006; Moureau *et al.*, 2009), are the most accurate ways to investigate thermoacoustic oscillations, as they include all physical phenomena involved. They, however, face some major shortcomings (Poinsot, 2013). First, because the stability of a thermoacoustic

system depends on a large number of parameters (for example air/fuel composition, flow rate, and acoustic reflection coefficients), a very large number of experiments or simulations has to be performed to identify safe operating conditions. It is prohibitively expensive to use them to perform a thorough investigation on the system stability. Secondly, although these approaches provide a detailed description of the flow/flame dynamics, they typically provide little insight on the causes of thermoacoustic instabilities. As well as being of fundamental interest, this insight is crucial for the designing of strategies for passive control of thermoacoustic instabilities.

There is therefore considerable industrial motivation in developing low-order analytical and numerical tools that can predict whether thermoacoustic oscillations will occur in a system and, if so, understand how to change the system in order to damp them, or predict their amplitude. This thesis deals with developing and improving such tools.

1.1 Nonlinear phenomena in thermoacoustics

Linear stability analysis is the primary analytical tool that is applied to thermoacoustic systems to investigate their stability. Under the assumption that the heat source is compact – i.e., that the extension of the heat source is much smaller than the acoustic wavelengths of interest – the acoustic and heat release linear responses can be decoupled and measured separately. The linear dynamic response of a flame to perturbations in the acoustic field or equivalence ratio mixture is known as Flame Transfer Function (FTF) (Candel, 1992). The FTF and the combustor acoustic response form a positive feedback loop (see Figure 1.2). The closed-loop system is referred to as a thermoacoustic network. Its stability can be determined by looking at the location of the closed-loop system's poles in the complex plane. This, together with the aid of adjoint-based sensitivity analysis (Magri & Juniper, 2013*a*,*b*), gives information on the linear behaviour of the system and is helpful in understanding to what parameters the system's stability is most susceptible.

There exist situations, however, in which linear stability may fail to predict the real behaviour of the system, as illustrated in Figure 1.1. This is because noise or non-normal effects may trigger finite amplitude oscillations, even when the thermoacoustic system is linearly stable, and lead to a variety of complex behaviour (Balasubramanian & Sujith, 2008; Juniper, 2011; Waugh & Juniper, 2011). Nonlinear effects determine the nature of the final state of a thermoacoustic oscillation, which can be a fixed point, a limit cycle or a more complex (non-periodic) solution. All these type of oscillations have been observed experimentally in thermoacoustic systems (Noiray *et al.*, 2008; Gotoda *et al.*, 2011; Kabiraj & Sujith, 2012; Jegadeesan & Sujith, 2013; Kashinath *et al.*, 2014).

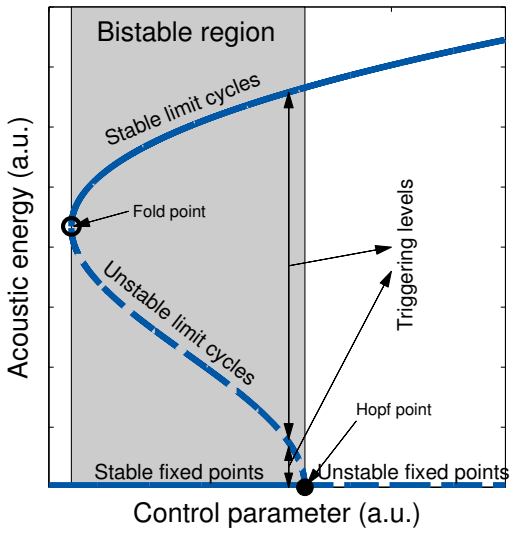

Fig. 1.1 Stable (solid) and unstable (dashed) states that a thermoacoustic system may exhibit close to a subcritical Hopf bifurcation. Linear stability analysis calculates the stability of fixed point solutions only with respect to small perturbations. In the bistable region, however, finite amplitude perturbations can trigger the state from the linearly stable fixed points to stable limit cycles, or vice versa.

1.1.1 Flame Describing Function

It is therefore important to gather information about and model the nonlinear behaviour of a thermoacoustic system, in order to predict the non-trivial effects of nonlinearities. An existing method able to predict part of the nonlinear thermoacoustic features is known as Flame Describing Function (FDF) analysis (Noiray *et al.*, 2008). The FDF generalises the concept of the FTF to perturbations with finite amplitude, but is a more expensive object to obtain from experiments or simulations than an FTF. It can be used to study the amplitude and stability of limit cycle oscillations, approximated as harmonic solutions (Noiray *et al.*, 2008; Boudy *et al.*, 2011; Illingworth *et al.*, 2013). However, the FDF analysis assumes that the dynamics of a given thermoacoustic mode is decoupled from the dynamics of the others. Situations exist in which this is not true (Moeck & Paschereit, 2012). The nonlinear coupling between the modes can lead to significant changes in the behaviour of a thermoacoustic system with respect to the one predicted by the FDF. For example, one can observe mode-switching – i.e., although the FDF approximation predicts thermoacoustic oscillations at a certain frequency, the system actually converges to oscillations with a different frequency – or non-periodic thermoacoustic vibrations (Noiray *et al.*, 2008; Kabiraj *et al.*, 2012*a*), which the FDF cannot predict.

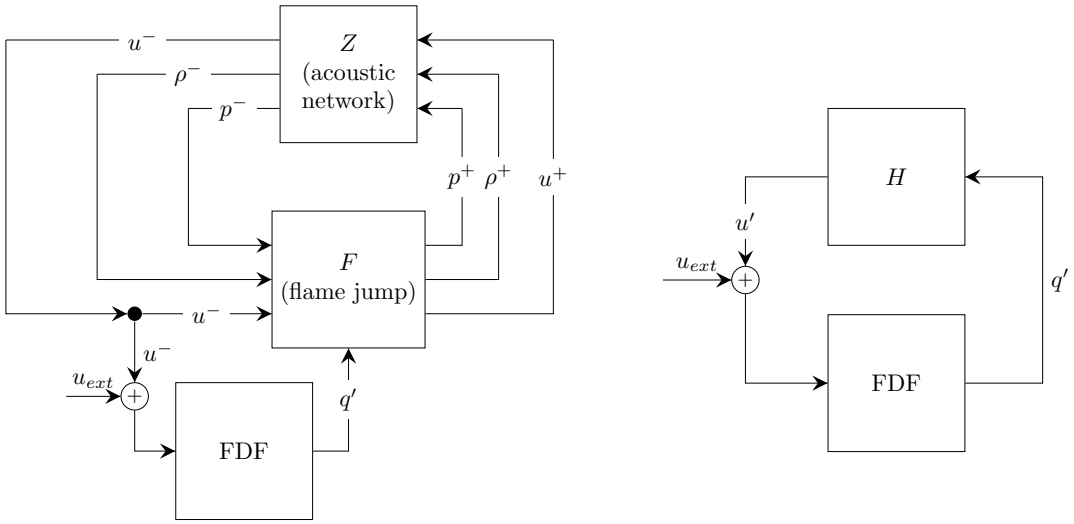

Fig. 1.2 Overview of a closed-loop thermoacoustic network. ρ, p and u denote the flow density, acoustic pressure and velocity variables. (a) The jump across the flame element is highlighted, using superscripts $-$ and $+$ for the acoustic properties upstream and downstream the flame, respectively. All the remaining acoustic information is embedded into the acoustic block Z. (b) The same closed-loop thermoacoustic network simplified across the FDF element; H contains all the linear acoustic response with respect to heat release perturbations.

Lastly, in a situation such as the one depicted in Figure 1.1, multiple stable states may exist. Because the system is subject to finite amplitude perturbations – such as the noise generated by the intrinsic combustion process or external causes – its behaviour may switch between these states in a non-deterministic way. If the effect of noise is modelled as a stochastic component in the governing equations, a statistical description of the system's behaviour in terms of a Probability Density Function (PDF) can be obtained. By extracting the stochastic modelling parameters from experimental data, this has been shown to accurately describe the transitions observed between different states in azimuthal thermoacoustic oscillations (Noiray & Schuermans, 2013*b*).

1.1.2 Harmonic balance

The calculation of an FDF can be expensive, but if the flame model is not changed, the same FDF can be used to test many acoustic configurations with a low-cost procedure, known as harmonic balance (Khalil, 2002).

Under the assumption that the flame is acoustically compact, a generic thermoacoustic network can be drawn as a block diagram as in Figure 1.2a. The acoustic jump conditions

across the flame (see Dowling (1995) and Chapter 2) have been highlighted. Their inputs are the acoustic variables upstream of the flame and the instantaneous heat release fluctuations, q'. The remaining acoustic response is contained in the acoustic block Z. For the simple configuration composed of two straight ducts interconnected by a flame, it contains information about the mean flow, end reflection coefficients, and wave time delays (Dowling, 1995). Lastly, the FDF converts velocity disturbances upstream of the flame into heat release fluctuations.

The feedback loop in Figure 1.2a can be simplified by choosing an external input signal u_{ext} just upstream of the FDF and the heat release as an output, so that the open-loop heat release response with respect to velocity fluctuations is given by:

$$q' = \mathrm{FDF}\left(u' + u_{ext}\right). \tag{1.1}$$

Furthermore, the entire open-loop acoustic response with respect to heat release fluctuations can be embedded into a single transfer function H so that, for velocity fluctuations upstream of the flame, we can write (see Figure 1.2b):

$$u' = Hq'. \tag{1.2}$$

For simple acoustic networks, the expression for the transfer function H can be found analytically (Heckl, 1988; Dowling, 1995, 1997). It becomes rather complicated for complex networks, and numerical methods are used in these cases to evaluate H over a certain range of frequencies.

Closing the feedback loop between the velocity at the reference point and the heat release fluctuations yields:

$$q' = \frac{\mathrm{FDF}(A,s)}{1-\mathrm{FDF}(A,s)\,H(s)}u_{ext}. \tag{1.3}$$

Equation (1.3) represents a Single Input Single Output system: if no input velocity is prescribed, the system will be linearly unstable if and only if it has poles in the r.h.s. of the complex plane in the zero amplitude limit. The harmonic balance extends this concept to perturbations with a finite amplitude. The system dynamics when the oscillations have an amplitude A is determined by the growth rates σ of the Laplace variable $s \equiv \sigma + \mathrm{i}\omega$ that satisfy the harmonic balance dispersion relation:

$$\mathrm{FDF}(A,s)H(s) = 1. \tag{1.4}$$

The dispersion relation (1.4) is also able to identify poles that have a negative growth rate at small amplitudes, but become unstable at finite amplitudes. This is a characteristic of subcritical Hopf bifurcations, and phenomena such as bistability and triggering may be observed (see Figure 1.1).

Solving the dispersion relation (1.4) at various amplitudes leads to harmonic limit cycle solutions of the closed-loop system, for which the growth rate σ is equal to zero. Their stability may be analysed by investigating the change in growth rate across the saturated amplitude (Noiray *et al.*, 2008; Boudy *et al.*, 2011).

1.2 Acoustic modelling

The compressible Navier–Stokes equations, together with mass and energy conservation laws, govern the air and fuel dynamics in a combustor. Assuming that viscous effects are negligible, and ignoring thermal diffusivity (Chu & Kovásznay, 1958; Dowling & Stow, 2003; Schuermans, 2003; Culick, 2006), they read:

$$\frac{\mathrm{D}\rho}{\mathrm{D}t} + \rho\nabla\cdot\boldsymbol{u} = 0 \tag{1.5a}$$

$$\frac{\mathrm{D}\boldsymbol{u}}{\mathrm{D}t} = -\frac{1}{\rho}\nabla p \tag{1.5b}$$

$$\rho T\frac{\mathrm{D}s}{\mathrm{D}t} = Q, \tag{1.5c}$$

where $\mathrm{D}/\mathrm{D}t \equiv \partial/\partial t + \boldsymbol{u}\cdot\nabla$ is the material derivative, $\boldsymbol{u}$ the flow velocity, p the pressure, ρ the density, T the temperature and Q the heat release rate per unit of volume. The energy equation is expressed in terms of the entropy, $s = c_v \log(p/\rho^\gamma)$.

Because we are interested in investigating the stability of thermoacoustic modes, the flow equations will be analysed using perturbation theory. In this context, the flow is decomposed into a mean, stationary component (denoted with overlines) on top of which small unsteady perturbations (denoted with primes) can grow. Because combustor geometries are typically axisymmetric, and the flow develops mostly in the axial direction, the conservation laws can be expanded in cylindrical coordinates $(\hat{r}, \hat{\theta}, \hat{x})$ on top of a uniform axial mean flow $\overline{u}$, yielding:

$$\frac{\partial\rho'}{\partial t} + \overline{u}\frac{\partial\rho'}{\partial x} + \overline{\rho}\frac{\partial u'}{\partial x} = 0 \tag{1.6a}$$

$$\frac{\partial u'}{\partial t} + \overline{u}\frac{\partial u'}{\partial x} = -\frac{1}{\overline{\rho}}\frac{\partial p}{\partial x} \tag{1.6b}$$

$$\frac{\partial p'}{\partial t}+\overline{u}\frac{\partial p'}{\partial x}+\gamma\overline{p}\frac{\partial u'}{\partial x}=0, \tag{1.6c}$$

where the entropy equation has been replaced with an equivalent expression for the pressure field, making use of the state equation $p=\rho RT$.

By assuming that solutions have the form $e^{\mathrm{i}\omega t+\mathrm{i}kx}$, where ω and k are the angular frequency and axial wavenumber, the linearised equations can be rewritten in matrix form as:

$$\begin{bmatrix} -\overline{u}k & -\overline{\rho}k & 0 \\ 0 & -\overline{u}k & -\frac{k}{\overline{\rho}} \\ 0 & -k\overline{\rho}c^2 & -\overline{u}k \end{bmatrix} \begin{bmatrix} \hat{\rho}' \\ \hat{u}' \\ \hat{p}' \end{bmatrix} = \omega \begin{bmatrix} \hat{\rho}' \\ \hat{u}' \\ \hat{p}' \end{bmatrix}, \tag{1.7}$$

where the speed of sound $c\equiv\sqrt{\gamma RT}$ has been defined. (1.7) is an eigenvalue problem with eigenmodes:

Eigenvalue	Eigenvector			
(ω)	$(\hat{\rho}',$	$\hat{u}',$	$\hat{p}')$	
$-k\overline{u}$	$(+\frac{1}{c^2},$	$0,$	$0)$	entropy wave $\hat{\alpha}$
$-k(\overline{u}+c)$	$(+\frac{1}{c^2},$	$+\frac{1}{\overline{\rho}c},$	$1)$	acoustic wave $\hat{f}$
$-k(\overline{u}-c)$	$(+\frac{1}{c^2},$	$-\frac{1}{\overline{\rho}c},$	$1)$	acoustic wave $\hat{g}$

The eigenvalue $\omega=-k\overline{u}$ reflects the convective property of the mean flow. It vanishes in the case of zero mean flow. The relative eigenmode affects only density and entropy fluctuations, and it is therefore labelled as an entropy mode. The other two eigenmodes are acoustic modes, and exist even in the case of zero mean flow. Their eigenvectors have pressure, velocity and density components, but they do not affect the entropy. Azimuthal modes can be straightforwardly included in the analysis by accounting for fluctuations in the azimuthal velocity, u_θ, decomposed into Fourier modes (Stow & Dowling, 2001; Noiray *et al.*, 2011).

By taking linear combinations of the eigenvectors, the fluctuating flow variables can be decomposed in terms of travelling waves:

$$p'(x,t)=\hat{f}e^{-\frac{xs}{\overline{u}+c}}+\hat{g}e^{-\frac{xs}{\overline{u}-c}} \tag{1.8a}$$

$$u'(x,t)=\frac{1}{\overline{\rho}c}\left(\hat{f}e^{-\frac{xs}{\overline{u}+c}}-\hat{g}e^{-\frac{xs}{\overline{u}-c}}\right) \tag{1.8b}$$

$$\rho'(x,t)=\frac{1}{c^2}\left(\hat{\alpha}e^{-\frac{xs}{\overline{u}}}+\hat{f}e^{-\frac{xs}{\overline{u}+c}}+\hat{g}e^{-\frac{xs}{\overline{u}-c}}\right). \tag{1.8c}$$

The decomposition of the acoustic variables into waves as described above constitutes the basic idea underlying acoustic network models. An acoustic network is formed by a series of axisymmetric, straight modules in which acoustic and entropy waves travel

upstream and downstream. Modules with different properties (for example cross-sectional area or temperature) are matched together by imposing mass, momentum and energy fluxes conservation through the Rankine-Hugoniot jump conditions (Dowling, 1995; Dowling & Stow, 2003). When an unsteady heat release model is embedded in the acoustic model, a low-order framework for a thermoacoustic system is obtained, referred to as a thermoacoustic network.

Thermoacoustic networks have been developed and are used for research purposes both by academia and industry: LOTAN was developed first in Cambridge University then by Rolls-Royce (Stow & Dowling, 2001), taX in TU Munich (Emmert *et al.*, 2013), OSCILOS in Imperial College London (Li *et al.*, 2014), Ta3 by (former) ALSTOM (Schuermans, 2003; Bellucci *et al.*, 2005), and LOMTI by Ansaldo Energia (Campa *et al.*, 2011). In this thesis, some of the acoustic functionalities of LOTAN have been exploited, as described in Chapter 2. Also, a simple acoustic network coded in MATLAB/Python and a way to cast the frequency response of an acoustic network into state-space form have been developed with Dr. Simon Illingworth, as described in (Orchini *et al.*, 2015).

1.3 Flame modelling

An FTF measured from experiments can be fed into a thermoacoustic network to investigate the linear stability of a combustor. However, when one is interested in investigating nonlinear effects, an FDF has to be measured, which can be expensive. Often, low-order models containing the most relevant features of the flame dynamics are used in place of an accurate FDF to obtain a cheaper tool to assess the thermoacoustic system's behaviour. As an example, simple static relations between the heat release rate and the acoustic pressure and velocity have been exploited for the analysis of azimuthal thermoacoustic oscillations (Noiray *et al.*, 2011; Ghirardo & Juniper, 2013). These models, however, tend to be oversimplistic, as they are static and therefore cannot capture the dependence of the heat release response on the frequency, which may contain relevant damping or source mechanisms.

For premixed flames, the kinematic G-equation is a common dynamic model used to determine the position and evolution of a thin flame front, as well as the amount of heat released by the flame, as functions of the oscillation frequency and amplitude. The G-equation is based on the assumption that chemical reactions between fuel and oxidisers are fast, and occur in a very thin region that defines the flame surface, which is found to be much smaller than laminar flow length scales. Under these conditions, the flame front can be treated as a surface discontinuity between the unburned and the burned region (Emmons, 1958; Markstein, 1964; Williams, 1985).

To identify the flame surface, it is convenient to define a scalar field G which takes negative values inside the flame (reactants zone), positive values outside (products zone), and is zero on the flame surface. The values of the G-field away from the interface have no physical meaning. Indeed, the identification of flame's surface with the $G = 0$ contour is just a convention, and any other isoline could have been chosen to locate the discontinuity. The field is assumed to be continuous and smooth, such that its first two derivatives in all spatial dimensions can be uniquely defined. The flame surface is thus defined in an implicit way, and pinch-offs, pockets of fuel that detaches from the main flame body, can be easily described. Also, geometrical quantities can be defined as functions of G. For example, the unit vector $\hat{\boldsymbol{n}}$ normal to the interface can be expressed as:

$$\hat{\boldsymbol{n}} \equiv -\frac{\nabla G}{|\nabla G|}. \tag{1.9}$$

The direction of the normal is chosen such that it points in the direction of the unburned gas. This is the direction along which the flame burns, at a speed s_L, which can be non-uniform along the interface.

Assume that an underlying unsteady, non-uniform flow-field $\boldsymbol{u}$ is prescribed. In a Lagrangian sense, we can follow a particle that at time $t = 0$ lies on the flame surface $G(\boldsymbol{x},t) = 0$ by means of the material derivative:

$$\frac{\mathrm{D}G}{\mathrm{D}t} = \frac{\partial G}{\partial t} + \frac{\partial \boldsymbol{x}}{\partial t} \cdot \nabla G = 0. \tag{1.10}$$

The term $\frac{\partial \boldsymbol{x}}{\partial t}$ in Eq. (1.10) represents the velocity experienced by a particle at position $\boldsymbol{x}$, which is the superposition of the flow and flame combustion velocities:

$$\frac{\partial \boldsymbol{x}}{\partial t} = \boldsymbol{u} + s_L \hat{\boldsymbol{n}} = \boldsymbol{u} - s_L \frac{\nabla G}{|\nabla G|}. \tag{1.11}$$

Substituting in Eq. (1.10), the kinematic G-equation governing the evolution of the flame surface is obtained:

$$\frac{\partial G}{\partial t} + \boldsymbol{u} \cdot \nabla G = s_L |\nabla G|. \tag{1.12}$$

The right hand side of equation (1.12) is highly nonlinear. Because the flame burns towards the reactants, when non-uniform perturbations in the velocity field or flame speed are considered, the unsteady flame shape becomes very structured, and pinch-offs may separate

from the flame. These pockets of fuel cannot be easily treated with an explicit formulation[1], and it is more convenient to use an implicit one. The latter allows for a fully nonlinear description of the flame surface dynamics, and naturally takes into account complex shapes and topological changes.

Calculations on the G-field in the entire computational domain require $\mathcal{O}(N^2)$ operations in 2-dimensions, where N is the number of grid points per dimension. If a high resolution is required, e.g., to capture the formation of small structures or short wavelength perturbations on the interface, the computational cost can become high, in contrast with the G-equation low-order model characteristics. Because we, however, are interested in tracking the evolution of the flame interface only, there is no need to solve for the G-field in the entire computational domain. Instead, one can solve for the evolution of the G-field only in a small tube surrounding the flame interface, as shown in Figure 1.3. If k is the number of grid points in a section of the tube, the number of operations required reduces to $\mathcal{O}(kN)$ in 2-dimensions: practically, it is about an order of magnitude faster than a full-matrix method. This formulation is known as Narrow Band Level Set method, and is accurately described in Sethian (1999); Peng *et al.* (1999). Without going into the formulation's details, the main steps performed by the algorithm used to integrate the G-equation are:

1. Two concentric tubes, of radii $0 < \beta < \gamma$ respectively, are constructed around the $G = 0$ interface.

2. A G-field is constructed in the largest tube as a signed distance function (negative inside the flame and positive outside) from the flame front. This is not a strict requirement, but is a convenient way to keep the G-field smooth. In practice, this goal is achieved by solving the Eikonal equation
$$|\nabla G| = 1 \tag{1.13}$$
with a High-order Constrained Reinitialisation (HCR) scheme, as described in Hartmann *et al.* (2010). This is done every time step, since G-dependent quantities, such as the local surface's normal vector and curvature, enter in the evolution equation and need to be accurately described.

3. A time step integration is performed. The integrated equation is:
$$\frac{\partial G}{\partial t} + c(G)\left(\boldsymbol{u} - s_L \frac{\nabla G}{|\nabla G|}\right) \cdot \nabla G = 0, \tag{1.14}$$

[1] An explicit formulation assumes that the flame front is a single-valued function in a certain reference system. This hypothesis may break down for simple flame configurations when a pinch-off is formed, and is certainly not true for complex flame shapes.

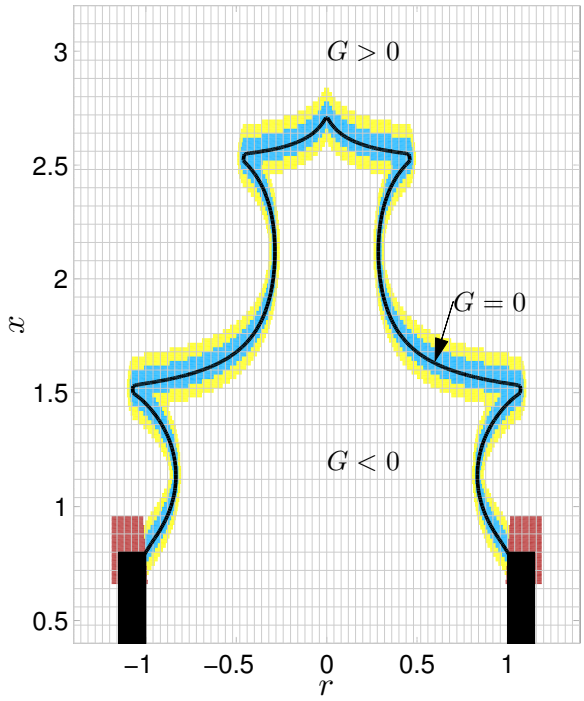

Fig. 1.3 Narrow Band Level Set method: the G-equation is solved only for points that lie in the red (boundary conditions), yellow (outer annulus), or light blue (inner tube) regions, which are close to the flame surface (black line). For illustration purposes, the grid resolution is reduced by a factor of 2 in both directions.

which is a modified version of Eq. (1.12), where

$$c(G) \equiv \begin{cases} 1 & \text{if} \quad |G| \leq \beta \\ (|G|-\gamma)^2(2|G|+\gamma-3\beta)/(\gamma-\beta)^3 & \text{if} \quad \beta < |G| \leq \gamma \\ 0 & \text{if} \quad |G| > \gamma \end{cases} . \tag{1.15}$$

This means, equation (1.12) is solved in the smaller tube of radius β, no equation is solved outside the largest tube of radius γ, and in the annular region in between them an equation that smoothly connects the two regimes is integrated (see Fig. 1.3). After this step, an iteration is completed, quantities such as the total flame surface area and heat release are calculated and the process restarts from point 1.

The numerical code used to integrate the G-equation in this thesis is LSGEN. It was originally developed by Hemchandra (2009) to investigate the nonlinear heat release response of 2D flames subject to forced acoustic and equivalence ratio perturbations with a finite amplitude. Kashinath *et al.* (2014) coupled the flame code with Fourier modes describing the acoustics, enabling for the analysis of self-excited thermoacoustic oscillations in a straight

pipe. Waugh (2013) extensively modified LSGEN to account for axisymmetric surfaces and more general boundary conditions, so that effects like flashback and side-bulging could be described. For the work presented in this thesis, LSGEN has been modify to account for: (i) the effect of local curvature corrections on the flame speed and heat release; (ii) the coupling between the flame dynamics and a generic acoustic state-space model – rather than a simplistic Fourier series – to allow for the investigation of more complex acoustic networks; (iii) non-uniform mean flows, allowing for the investigation of more complex flame shapes; (iv) a travelling wave perturbation model in a non-uniform mean flow; (v) the advection of a non-uniform equivalence ratio distribution in the flame domain and its interaction with the flame speed and heat release.

Using G-equation based formulations, transfer functions of conical and V shaped flames to harmonic velocity and heat release fluctuations have been evaluated analytically for a variety of underlying flow fields in the linear limit (Schuller *et al.*, 2003; Preetham *et al.*, 2008). In particular, a travelling wave model for flow perturbations has been shown to accurately reproduce the flow-flame interaction. Also, transfer functions of heat release fluctuations to harmonic velocity disturbances for these flame shapes have been proven to compare favourably against experimental results (Durox *et al.*, 2009; Karimi *et al.*, 2009). In the fully nonlinear case, G-equation models were shown to capture some of the complex dynamical features of thermoacoustic systems, such as period-doubling, secondary Hopf bifurcations, and routes to chaos (Kashinath *et al.*, 2014; Waugh *et al.*, 2014). The G-equation model will be considered throughout this thesis as a low-order model for the heat release response, with the exception of Chapter 5, in which an electrical heater is consider as a source of unsteady heat release instead of a flame.

1.4 Thesis scope

The general aim of this thesis is to introduce novel methods for the analysis of thermoacoustic networks in order to either reduce the cost currently required to investigate their linear and nonlinear regimes, or to improve the current state-of-the-art of modelling and analysis of thermoacoustic oscillations. This has been accomplished by achieving the following goals.

First, a framework in which the G-equation model for the flame dynamics is coupled with an arbitrarily complex acoustic network has been developed. The method chosen, state-space realisations, allows for naturally including the effects of mean flow, temperature rise across a flame, and frequency dependent reflection coefficients in the acoustic model.

Second, the above framework was used to investigate the linear stability of thermoacoustic systems with premixed flames. Adjoint sensitivity methods in thermoacoustic systems with

premixed flames were introduced as a tool to quickly understand with respect to what parameters the system's stability is most susceptible, and how to change them in order to make the system more stable[2]. Nonlinear calculations using state-of-the-art methods such as time marching, FDF analysis, and numerical continuation have been performed. The nonlinear calculations aim to (i) compare the numerical costs of the different nonlinear methods, (ii) understand the strengths and weaknesses of the various available methods and (ii) highlight the differences in the thermoacoustic system behaviour that arise when a detailed description of the acoustic network is included, in comparison to the case in which a straight duct with no mean flow or temperature variations is chosen as the acoustic configuration.

Third, novel frameworks for the investigation of nonlinear effects in thermoacoustics have been developed to go beyond the FDF paradigm, which can only predict harmonic oscillations. Two methods have been developed, and their capabilities outlined by using them to predict the amplitude and type of oscillations in thermoacoustic systems: (i) the Flame Double Input Describing Function (FDIDF), which naturally extends the FDF concept to oscillations containing more than one frequency, and highlights some weaknesses of the FDF method that may arise when assessing the stability of limit cycle oscillations; (ii) weakly nonlinear expansion of the thermoacoustic equations, which provides a very efficient way to calculate the evolution of the amplitude of periodic but non-harmonic oscillations close to Hopf bifurcations, via a so-called Stuart–Landau equation. Both methods give more information about the nonlinear behaviour of a thermoacoustic system than the FDF analysis, and represent a significant advance in the state-of-the-art.

Lastly, low-order models for thermoacoustic oscillations in complex combustors with non-conical premixed flames using the *G*-equation have been developed, which may be of interest in industrial applications as a quick tool to estimate the dangerous frequencies and amplitudes of thermoacoustic instabilities. Focus has been put on generalising the perturbation flow field models that have been originally developed for conical flames to more elaborate flame shapes, and including in the flame model a non-uniform distribution of the fuel/air mixture in the flame domain.

1.5 Thesis structure

All chapters of the thesis have been published in journal or conference proceeding articles[3], which are referred to at the beginning of each chapter, together with the relevant contributions

[2] An overview on adjoint methods is provided in Chapter 2, where they are introduced for the first time.
[3] Chapter 5 is currently under consideration for publication in the Journal of Fluid Mechanics.

	Linear	**Nonlinear**
Conical Flame	Chapter 2	Chapters 3 (FDF) and 4 (FDIDF)
Electric heater		Chapter 5 (Weakly nonlinear)
Bluff-body stabilised flame		Chapters 6 (perfectly premixed) and 7 (imperfectly premixed)

Table 1.1 Schematic overview of the thesis structure.

from co-authors. This justifies the use of the subject "we", which refers to all co-authors of the publication associated with the various chapters. In the Introduction of each chapter, a detailed literature review on the subject covered is outlined. The thesis is summarised in Table 1.1, and outlined in details in the following.

In Chapter 2, the state-space representation of the acoustic response to heat release fluctuations is presented in detail. It is then used to investigate the linear stability of a classic thermoacoustic configuration, a flame driven Rijke tube, taking particular care in the acoustic modelling. Using the G-equation, an analytical expression is derived for the conical FTF, which corrects a previous expression found in the literature. A fully-coupled method for the investigation of the thermoacoustic system stability is adopted rather than evaluating separately the FTF. This is more versatile and allows for the use of adjoint sensitivity analysis which, with one calculation, provides information about the system stability's sensitivity with respect to all (flame, flow and acoustic) parameters.

In Chapter 3, the same thermoacoustic system is investigated from a nonlinear point of view. An FDF is evaluated and the harmonic balance is used to predict the amplitude and stability of harmonic limit cycle oscillations. These results are compared against those obtained with time-marching simulations and a numerical continuation algorithm. All together, these methods represent the current state-of-the-art for predictions about the nonlinear behaviour of thermoacoustic systems. The strength and weaknesses of each method, together with their practical cost, are highlighted. Super- and subcritical Hopf and Neimark–Sacker bifurcations are identified, together with the Ruelle–Takens–Newhouse route to chaos. Results are compared with experimental data and previous numerical analyses, which used a simpler acoustic model.

In Chapter 4, the FDIDF analysis for a dynamic nonlinear flame model is presented. This method generalises the idea of the FDF to non-harmonic perturbations. The theory is developed, and criteria for the prediction of frequencies, amplitudes, and stability of periodic and non-periodic thermoacoustic oscillations are derived. It is shown how the information provided by the FDF in some cases is not sufficient to determine the stability of a limit cycle

solution. This is because the FDF neglects the interaction between thermoacoustic modes, which can destabilise some solutions. The FDIDF, instead, contains this information, and can also predict the amplitude of non-periodic oscillations, but is a more expensive object to obtain from experiments or simulations than the FDF. To overcome this issue, a methodology that improves the FDF predictions exploiting only some of the FDIDF features is outlined, which can be obtained roughly at the cost of two FDFs.

In Chapter 5, a high order weakly nonlinear analysis of a thermoacoustic system is presented. For consistency with previous analysis in the literature, an electrical heater model, consistent with fully nonlinear simulations of the heat released by an electrical wire, is used as a heat source rather than a flame. The weakly nonlinear expansion presented here greatly improves analogous analysis which can be found in the literature, because it considers the acoustics expressed in state-space form (thus, an entirely different acoustic system can be investigated using the very same equations), and takes into account the contribution of multiple acoustic modes on the thermoacoustic system dynamics. Because of the latter feature, adjoint methods are required to obtain the Stuart–Landau equation that governs the evolution of the oscillations amplitude. The method is shown to accurately predict the amplitude of thermoacoustic oscillations, and the frequency shift of the saturated oscillations with respect to the frequency predicted by linear stability analysis. It also accounts for the contribution of the harmonic components in the oscillations, which the FDF method ignores.

In Chapter 6, a more elaborate thermoacoustic configuration, consisting of a bluff-body stabilised flame, is considered. A G-equation based model is developed accounting for a realistic description of the flow field, obtained from URANS simulations. The travelling wave perturbation model, originally developed for conical and V flames, is extended to this configuration. Results show that the flow/flame model captures well the flame shape dynamics as compared to experimental and URANS results. The heat release rate, however, tends to overestimate the experimentally determined one. This is probably because neither turbulent model nor shear layer effects on combustion have been included in the G-equation model. Including these effects may improve the model, but would greatly increase the cost of the simulations, probably making it not interesting as a low-order tool.

In Chapter 7, the same thermoacoustic configuration as in the previous chapter is considered, but focus is put on the interaction between the flame and equivalence ratio fluctuations rather than flame and flow field interaction. Because equivalence ratio disturbances have a much stronger impact on the heat release dynamics than velocity perturbations, a detailed modelling of the flow field is superfluous. The G-equation based low-order model is shown to qualitatively compare well with experimental results, and improves previous modelling performed on the same system. FDFs are calculated and discussed, and are approximated

with sum of time delays models. It is shown how the latter provide an interesting alternative point of view to the FDF information, which can be used to understand what are the relevant physical time and length scales at which the flame responds. An acoustic network for the experimental geometry is constructed and coupled with the FDF, showing that the frequencies observed in self-excited oscillations are captured by the low-order model.

In the Conclusions, the results achieved are summarised and discussed, and suggestions for extensions of the methods developed and future work are presented.

Chapter 2

Linear stability and adjoint sensitivity analysis of thermoacoustic networks with premixed flames

This chapter contains a review of the linear stability theory and adjoint sensitivity analysis of thermoacoustic systems with premixed flames. A detailed derivation of the acoustic equations in an acoustic networks is presented, which is then used throughout the thesis. Furthermore, a methodology that enables to cast the network frequency response into state-space form is outlined, which was developed in collaboration with Dr. Simon Illingworth and published in Orchini *et al.* (2015). The state-space model is coupled with a linearised, discretized *G*-equation model, resulting in a versatile linear framework on which adjoint sensitivity methods are applied.

The content of this chapter was published in Orchini & Juniper (2016*b*).

2.1 Introduction

The stability of a thermoacoustic system is usually analysed by first calculating the Flame Transfer Function (FTF). This is the flame's heat release response to velocity, pressure, or equivalence ratio perturbations. The FTF is then combined with an acoustic network model.

There are several ways to formulate a linear acoustic model for a thermoacoustic analysis. Three common methods are i) a Fourier-Galerkin discretization (Culick, 1976*a*,*b*; Zinn & Lores, 1971); ii) a Green's function approach (Heckl & Howe, 2007), which may subsequently be used in a modal expansion (Schuermans, 2003); and iii) a wave-based approach (Lang *et al.*, 1987; Heckl, 1988). In any acoustic modelling method, it is useful to write the resulting

model in state-space form (to be defined in §2.2.2) because this allows powerful techniques from dynamics and control to be used. These include, for example, stability analysis of the coupled thermoacoustic system, analysis of its transient growth characteristics, and the design of feedback control to eliminate oscillations. For the Fourier-Galerkin discretization and the Green's function approach, methods to describe the resulting systems in state-space form have been developed. For the first case, a state-space description follows quite naturally from the Fourier modes, and for a Green's function approach, a state-space description can be generated by performing a modal expansion (Schuermans, 2003). For the wave-based approach, however, it is less straightforward to describe the resulting system in state-space form. This is largely due to time delay terms, which make the system infinite-dimensional, and which are not amenable to a state-space description in a straightforward way. A possibility is to approximate time delays with, e.g., Padé approximations, as in Bothien *et al.* (2007), or to make use of a state vector with memory, i.e., a state vector that includes the acoustic states at previous times, as in Mangesius & Polifke (2011). Here, we develop an alternative approach that allows us to cast the frequency response of the system in state-space form.

From the combustion point of view, we will focus on the response of laminar, conical flames, modelled with the linearised G-equation. Previous studies have shown that a kinematic description of the flame front, using a front-tracking version of the G-equation with a suitable velocity model, can capture the main features of the heat release response of conical premixed flames to inlet velocity fluctuations. Birbaud *et al.* (2006) have shown experimentally that acoustic perturbations are responsible for the formation of velocity perturbations that are advected along the flame at a characteristic speed, the convection speed, which in general is a function of the amplitude and frequency of the forcing oscillation. By measuring the velocity field inside the flame, they were able to identify two regions in which the velocity field behaved differently: close to the burner the velocity field oscillates with the acoustic field, whereas further downstream a travelling-wave behaviour of the flow field was observed. A pure travelling wave model of axial velocity perturbations, which uses the acoustic field as a boundary condition at the burner, qualitatively reproduces the flow and flame dynamics (Baillot *et al.*, 1992), and radial velocity fluctuations are found by choosing a divergence free flow field. In some studies in the literature, the radial component was neglected, because it was shown to be less important than the axial travelling wave on the flame response (Preetham *et al.*, 2008). The G-equation moving into a travelling wave velocity field has been shown to capture the most relevant features of conical flames dynamics - such as the formation of wrinkles on the flame surface - and the consequent heat release response.

This model has been developed and compared with experiments in several studies: Schuller *et al.* (2002) considered an axial dependence of the mean flow field; Schuller *et al.* (2003) compared the responses of conical and V-shaped flames; Karimi *et al.* (2009) compared FTFs from experiment with analytical results from Schuller *et al.* (2003); Preetham *et al.* (2008); Cuquel *et al.* (2011, 2013*b*) investigated the effect of confinement on conical flames FTFs and compared with G-equation based analytical models; Kashinath *et al.* (2013*b*) extracted a frequency-dependent convection speed from DNS and used it into a G-equation low-order model. For a complete review of premixed combustion and acoustic waves coupling see Lieuwen (2003). In this analysis we will assume that perturbations travel with a constant speed, which in general is different from the mean flow velocity. We also allow the flame speed to vary linearly with the local flame curvature, which avoids the formation of unphysical cusps on the flame surface. This has already been considered for V-shaped flames modelled with the G-equation (Wang *et al.*, 2009; Preetham *et al.*, 2010), but not for conical flames, which is a typical experimental configuration (Noiray *et al.*, 2008; Kabiraj & Sujith, 2012). The flame model we derive only captures the most relevant characteristics of conical flames dynamics. We do not model other effects which may be important in some cases, such as gas expansion (Creta & Matalon, 2011) and flame base motion (Cuquel *et al.*, 2013*a*) to keep the low-order flame model simple.

The analysis of FTFs helps to explain the linear dynamics of flames, such as a conical flame's low-pass characteristics. Analytical results are usually not available, however, meaning that simulations or experiments over a large range of frequencies are required, which can be expensive. This becomes even more demanding when one wants to investigate the effect of several parameters on the stability of a thermoacoustic system, because a new FTF has to be evaluated for every set of parameters. On the other hand, if a relation between the flame's heat release response and acoustic velocity or pressure fluctuations is known, one can apply classic linear stability techniques to the fully-coupled system, avoiding the explicit evaluation of flame and acoustic transfer functions (Bloxsidge *et al.*, 1988).

The aim of this chapter is to apply linear stability and adjoint sensitivity techniques to thermoacoustic networks with premixed flames, in which the flame and heat release dynamics are modelled by the kinematic G-equation. With this approach, the problem of identifying thermoacoustic instabilities is reduced to a classic eigenvalue problem of the coupled system. The resulting eigenvalue problem is small and all the eigenvalues can be calculated as the parameters of the model are changed. If the model were larger, a similar approach could be used, but only the eigenvalues with the largest growth rates would be calculated, using iterative methods.

Having obtained a description of the linear coupled thermoacoustic system, adjoint sensitivity analysis can be applied (Sipp *et al.*, 2010; Luchini & Bottaro, 2014; Magri & Juniper, 2013*b*). The premixed flame response is modelled with the linearised front-track G-equation model[1]. Sensitivity results can be used, for example, to calculate how to change the system in order to reduce the growth rate of each unstable eigenvalue. This change could be in the shape of the combustion chamber, the shape of the flame, or the acoustic boundary conditions. In this chapter, we demonstrate the usefulness of adjoint methods by calculating how the convection speed affects the most unstable eigenvalues.

The chapter is structured as follows: in §2.2 the acoustic network modelling that is used throughout the thesis is outlined, and we describe the state-space formulation used to couple it with the heat release dynamics. In §2.3 the linear flame model is derived. In §2.4 we solve the equations for the case where the flame speed is uniform and we present analytical results that correct the FTF expression contained in Preetham *et al.* (2008). In §2.5 we extend the model to the more general case of curvature-dependent flame speeds. In §2.6 we express the fully-coupled self-excited thermoacoustic equations as an eigenvalue problem. In §2.7 we present the parameters and geometrical details of the thermoacoustic network considered. In §2.7.2 we calculate its eigenvalues while varying two parameters, build a stability map and discuss the results. Finally, in §2.7.3, we perform a sensitivity analysis on the convection speed on the entire stability map calculated with stability analysis, and provide physical insights based on these results. In §2.8 we summarise our study and discuss the potential applications of these methods to larger problems.

2.2 Linear acoustics: wave-based approach and state-space representation

In this section the wave-based acoustic model is described, and the methodology used to generate a state-space acoustic model from it outlined. We start with a simple case: a flame in a one-dimensional duct open at both ends. This shows the important features of the wave-based method and highlights the difficulties in formulating its state-space description.

[1]Note that it would be troublesome to use this approach on the entire G-field, because the G-field itself has no physical meaning away from the G=0 level set, and care must be taken in calculating the sensitivities. This problem does not appear with a linearised formulation, because only the flame front position is tracked, which is a physical quantity.

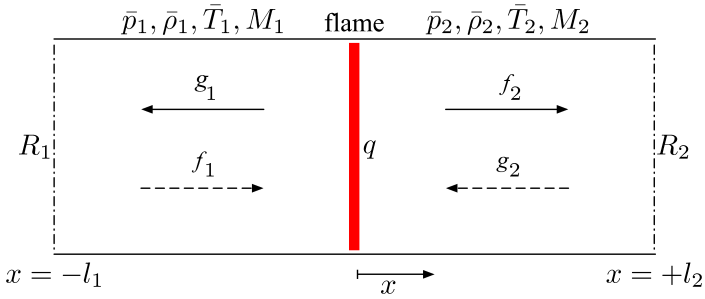

Fig. 2.1 Wave approach in a simple duct geometry. g_1 and f_2 are the waves radiated from the heat source towards the boundaries in the upstream and downstream regions respectively. f_1 and g_2 are the waves reflected by the boundaries.

2.2.1 Wave-based modelling approach

Figure 2.1 shows a prototype thermoacoustic network: an acoustically compact flame inside an open-ended duct. The mean flow, if non-zero, is from left to right. There is a temperature jump across the flame, which causes the sound speed to increase from c_1 to c_2. A perturbation in the heat release, $q'(t)$, generates outward-travelling waves that propagate both upstream (g_1) and downstream (f_2). These waves partially reflect at the upstream/downstream ends of the duct. The reflection coefficients are R_1 and R_2, and the reflected waves are f_1 and g_2. The flame is at $x = 0$, so $x \in [-l_1, 0)$ is upstream of the flame and $x \in (0, l_2]$ is downstream of the flame.

We solve the wave equations (1.8) in each of the two regions shown in Figure 2.1. Upstream of the flame, the acoustic pressure and velocity perturbations can be written in terms of the upstream- and downstream-travelling waves, g_1 and f_1:

$$p_1'(x,t) = g_1\left(t + \tfrac{x}{c_1 - \bar{u}_1}\right) + f_1\left(t - \tfrac{x}{c_1 + \bar{u}_1}\right) \tag{2.1a}$$

$$u_1'(x,t) = \frac{1}{\bar{\rho}_1 c_1}\left[-g_1\left(t + \tfrac{x}{c_1 - \bar{u}_1}\right) + f_1\left(t - \tfrac{x}{c_1 + \bar{u}_1}\right)\right]. \tag{2.1b}$$

We can write similar expressions for the downstream region (Evesque *et al.*, 2003). Note that, to simplify the notation, we have suppressed the subscript $_x$ for the axial velocity. These equations are supplemented by boundary conditions at each end of the duct, which provide a relationship between the outward-travelling waves, $g_1(t)$ and $f_2(t)$, and the inward-travelling waves, $f_1(t)$ and $g_2(t)$:

$$f_1\left(t + \tfrac{l_1}{c_1 + \bar{u}_1}\right) = R_1 g_1\left(t - \tfrac{l_1}{c_1 - \bar{u}_1}\right) \tag{2.2a}$$

$$g_2\left(t + \tfrac{l_2}{c_2 - \bar{u}_2}\right) = R_2 f_2\left(t - \tfrac{l_2}{c_2 + \bar{u}_2}\right). \tag{2.2b}$$

We need to relate the upstream and downstream flow to the heat release rate. This is achieved by considering the mass, momentum, and energy balances across the flame, through the Rankine-Hugoniot jump conditions (Dowling, 1995):

$$A_-\rho_-u_- = A_+\rho_+u_+ \tag{2.3a}$$

$$A_+p_- + A_-\rho_-u_-^2 = A_+p_+ + A_+\rho_+u_+^2 \tag{2.3b}$$

$$A_-\rho_-u_-\left(\frac{\gamma}{\gamma-1}\frac{p_-}{\rho_-}+\frac{1}{2}u_-^2\right) = A_+\rho_+u_+\left(\frac{\gamma}{\gamma-1}\frac{p_+}{\rho_+}+\frac{1}{2}u_+^2\right), \tag{2.3c}$$

where the subscripts $_-$ and $_+$ denote the flow variables just upstream and downstream the flame, respectively.

No entropy waves are found in the upstream duct (cold flow), but they are generated at the flame location. These waves travel downstream along the duct, and could be converted into acoustic waves if the flow accelerates, for example at a chocked outlet (Marble & Candel, 1977; Duran & Moreau, 2013). The amplitude of waves so generated, referred to as indirect noise, is typically small compared to that of direct noise, and is not modelled here. Thus, although entropy waves are present in our model, we are not interested in calculating them, as they are simply convected out of the domain.

We therefore solve only for the acoustic waves, given by the momentum and energy equations into which the expression for the downstream density – calculated from the mass flux equation – has been substituted. By considering the linearised disturbances of equations (2.3), and substituting in the travelling-wave solutions (2.1) with boundary conditions (2.2), we obtain the equations governing the time evolution of the outward-travelling waves:

$$X\begin{bmatrix}g_1(t)\\f_2(t)\end{bmatrix} = Y\begin{bmatrix}R_1g_1(t-\tau_1)\\R_2f_2(t-\tau_2)\end{bmatrix} + \begin{bmatrix}0\\1\end{bmatrix}\frac{q'(t)}{c_1}, \tag{2.4}$$

where $\tau_1 \equiv 2l_1c_1/(c_1^2-\bar{u}_1^2)$, $\tau_2 \equiv 2l_2c_2/(c_2^2-\bar{u}_2^2)$, and

$$X \equiv \begin{bmatrix} -1+M_1(2-\frac{\bar{u}_2}{\bar{u}_1})-M_1^2(1-\frac{\bar{u}_2}{\bar{u}_1}) & 1+M_2 \\ \frac{1-\gamma M_1}{\gamma-1}+M_1^2-\frac{1}{2}M_1^2(1-M_1)((\frac{\bar{u}_2}{\bar{u}_1})^2-1) & \frac{c_2}{c_1}\left(\frac{1+\gamma M_2}{\gamma-1}+M_2^2\right)\end{bmatrix} \tag{2.5a}$$

$$Y \equiv \begin{bmatrix} 1+M_1(2-\frac{\bar{u}_2}{\bar{u}_1})+M_1^2(1-\frac{\bar{u}_2}{\bar{u}_1}) & -1+M_2 \\ \frac{1+\gamma M_1}{\gamma-1}+M_1^2-\frac{1}{2}M_1^2(1+M_1)((\frac{\bar{u}_2}{\bar{u}_1})^2-1) & \frac{c_2}{c_1}\left(\frac{1-\gamma M_2}{\gamma-1}+M_2^2\right)\end{bmatrix} \tag{2.5b}$$

are 2×2 matrices and are functions of the mean flow properties only. These matrices are a more general form of the matrices contained in Dowling (1997), as they are valid for any (even frequency dependent) reflection coefficient.

In order to demonstrate the wave-based approach, we consider the zero mean flow case. This simplifies the analysis significantly, whilst still retaining the most important features. Taking the Laplace transform of equation (2.4) for no mean flow, and assuming that the reflection coefficients are frequency-independent, we find

$$\begin{bmatrix} 1+R_1e^{-s\tau_1} & -1-R_2e^{-s\tau_2} \\ 1-R_1e^{-s\tau_1} & \frac{c_2}{c_1}(1-R_2e^{-s\tau_2}) \end{bmatrix} \begin{bmatrix} g_1(s) \\ f_2(s) \end{bmatrix} = \begin{bmatrix} 0 \\ \frac{\gamma-1}{c_1} \end{bmatrix} q'(s), \tag{2.6}$$

where $s \equiv \sigma + \mathrm{i}\omega$ is the Laplace variable and σ the growth rate. The modes are now given by those values of s for which the determinant $\Omega(s)$ of the matrix in (2.6) vanishes. This gives us the relation:

$$\Omega(s) \equiv \left(1+\frac{c_2}{c_1}\right)\left(1-R_1R_2e^{-s(\tau_1+\tau_2)}\right) + \left(1-\frac{c_2}{c_1}\right)\left(R_2e^{-s\tau_2}-R_1e^{-s\tau_1}\right) = 0, \tag{2.7}$$

which makes clear the influence of the ratio of the speeds of sound, c_2/c_1. When $c_2/c_1 = 1$ (i.e., no temperature change across the flame) the modes are equispaced and given simply by:

$$R_1R_2e^{-s(\tau_1+\tau_2)} = 1. \tag{2.8}$$

When $c_2/c_1 \neq 1$ there is an extra term in equation (2.7) and the modes are no longer equispaced.

Solving equations (2.6) for the waves $g_1(s)$ and $f_2(s)$, and substituting these into the expressions (2.1) for the pressure and velocity, we find for the upstream region that

$$\frac{p_1'(x_1,s)}{q'(s)} = \frac{\gamma-1}{c_1}\frac{[1+R_2e^{-s\tau_2}]\left[1+R_1e^{-s\left(\tau_1-\frac{2x_1}{c_1}\right)}\right]}{\Omega(s)}e^{-s\frac{x_1}{c_1}} \tag{2.9a}$$

$$\frac{u_1'(x_1,s)}{q'(s)} = \frac{\gamma-1}{2\bar{\rho}_1c_1^2}\frac{[1+R_2e^{-s\tau_2}]\left[-1+R_1e^{-s\left(\tau_1-\frac{2x_1}{c_1}\right)}\right]}{\Omega(s)}e^{-s\frac{x_1}{c_1}}. \tag{2.9b}$$

Similar relations can be derived for the pressure and velocity in the downstream region. Note that the transfer functions defined in equations (2.9) differ from those in the rest of the thesis, which will include mean flow and area variations. The important point here is

that the relations for the pressure and velocity include time delay terms of the form $e^{-s\tau}$, and it is therefore not possible to cast them directly in state-space form. Time delays can be approximated by Padé approximations in order to make them amenable to state-space descriptions (Bothien *et al.*, 2007). Alternatively, state vectors that includes the acoustic states at previous times can be used (Mangesius & Polifke, 2011). However, we have opted for a different approach to the state-space formulation, which is presented in the next section.

2.2.2 Finding a state-space model

Having outlined the most important features of the wave-based model, we now obtain its state-space description using knowledge of its acoustic modes and frequency response. Rather than discretize the system using an expansion such as Fourier modes, we discretize the system by finding its eigenvalues directly. This involves finding the roots, $\lambda_k \equiv \sigma_k + \mathrm{i}\omega_k$, of $\Omega(s)$ introduced in equation (2.7). This is achieved using Newton–Raphson iteration in the complex plane. We also require the frequency response function, which is found by setting $s = \mathrm{i}\omega$ in equations (2.9). We then approximate the frequency response with a state-space model, as described in the next section.

Calculating the state-space matrices

We want to write the acoustic model described in §2.2 in state-space form:

$$\dot{\boldsymbol{x}}(t) = A\boldsymbol{x}(t) + \boldsymbol{B}q'(t) \tag{2.10a}$$

$$y'(t) = \boldsymbol{C}\boldsymbol{x}(t), \tag{2.10b}$$

where $\boldsymbol{x}$ is the state vector, q' is an input, and y' is some output of interest. A is the state-space matrix, and its eigenvalues determine the acoustic system stability. $\boldsymbol{B}$ and $\boldsymbol{C}$ are a column and row vector respectively; they are matrices for Multi-Input Multi-Output systems. In our case the system has a Single-Input – the fluctuating heat release – and a single output – either velocity or pressure fluctuations. Taking Laplace transforms of (2.10) and rearranging, we arrive at the transfer function

$$H(s) \equiv \frac{y'(s)}{q'(s)} = \boldsymbol{C}(sI - A)^{-1}\boldsymbol{B}, \tag{2.11}$$

where I is the identity matrix.

A state-space realisation is not unique. There are many state-space realisations that give the same transfer function. The realisation that is convenient for our purposes is a modal

form, where the A matrix is written as a diagonal matrix with its eigenvalues on its diagonal. For this realisation, the term $(sI - A)^{-1}$ can be written simply as

$$(sI - A)^{-1} = \begin{bmatrix} s-\lambda_1 & \cdots & 0 \\ \vdots & \ddots & \vdots \\ 0 & \cdots & s-\lambda_n \end{bmatrix}^{-1} = \begin{bmatrix} \frac{1}{s-\lambda_1} & \cdots & 0 \\ \vdots & \ddots & \vdots \\ 0 & \cdots & \frac{1}{s-\lambda_n} \end{bmatrix}, \tag{2.12}$$

and the transfer function, $H(s)$, becomes:

$$H(s) = \sum_{k=1}^{n} \frac{c_k b_k}{s-\lambda_k} = \sum_{k=1}^{n} \frac{\theta_k}{s-\lambda_k}. \tag{2.13}$$

Here we have defined $\theta_k \equiv c_k b_k$. This is for the single-input-single-output case, for which $\boldsymbol{B}$ is a column vector and $\boldsymbol{C}$ is a row vector, but is easily extended to the multi-input-multi-output case. If we evaluate the frequency response of $H(s)|_{s=\mathrm{i}\omega}$ at the frequencies $\omega_1, \omega_2, \ldots, \omega_p$, then

$$\begin{bmatrix} H(\mathrm{i}\omega_1) \\ \vdots \\ H(\mathrm{i}\omega_p) \end{bmatrix} = \begin{bmatrix} (\mathrm{i}\omega_1 - \lambda_1)^{-1} & \cdots & (\mathrm{i}\omega_1 - \lambda_n)^{-1} \\ \vdots & \ddots & \vdots \\ (\mathrm{i}\omega_p - \lambda_1)^{-1} & \cdots & (\mathrm{i}\omega_p - \lambda_n)^{-1} \end{bmatrix} \begin{bmatrix} \theta_1 \\ \vdots \\ \theta_n \end{bmatrix}, \tag{2.14}$$

which we can solve for $\begin{bmatrix} \theta_1 \ldots \theta_n \end{bmatrix}^T$. We need the frequency response at $p = n$ frequencies to make the matrix in (2.14) invertible. In practice, however, it is better to evaluate the frequency response at many more than n frequencies, $p \gg n$, and then solve equations (2.14) in the least squares sense. Note that we are free to choose any c_k, b_k, provided they satisfy $c_k b_k = \theta_k$.

A validation of the agreement between the original frequency response and the approximated state-space form has been given by Illingworth & Juniper (2014): for an approximation order $n = 23$, the agreement is excellent at low-frequencies, and slightly deteriorates at high frequencies. This is expected because the state-space model cuts off the contribution of modes with high frequencies.

2.3 Linear flame dynamics

We describe the premixed flame's dynamics with the kinematic G-equation model, assuming that there is no density jump across the flame. This assumption precludes the Darrieus-Landau instability in the flame. This instability can cause the formation of small-scale wrinkles leading to turbulence (Darrieus, 1938; Landau, 1944*a*; Creta & Matalon, 2011). This, and

other physical phenomenon such as reaction mechanisms and turbulence effects, can be taken into account in an LES simulation with a G-equation formulation, see for example Moureau *et al.* (2009). However, for our purposes we want to keep the model low-order, and we consider a laminar flame, assuming that the flame is an infinitely thin interface separating reactant and products and neglecting temperature variations across the flame. Under this assumption the G-equation model reads:

$$\frac{\partial \tilde{G}}{\partial \tilde{t}} + \tilde{\boldsymbol{u}} \cdot \tilde{\nabla} \tilde{G} = \tilde{s}_L^0 (1 - \mathcal{L}\tilde{\kappa}) |\tilde{\nabla} \tilde{G}|, \tag{2.15}$$

where $\tilde{\boldsymbol{u}}$ is a prescribed flow field, $\tilde{s}_L^0$ is the propagation speed of a laminar flat flame, $\mathcal{L}$ is the Markstein length, and $\tilde{k}$ is the local flame curvature. The flame front is identified by the $\tilde{G} = 0$ level set. We describe axisymmetric flames in the laboratory framework, indicating with $\tilde{r}$ and $\tilde{x}$ the radial and axial directions respectively. We denote mean quantities with overlines and perturbations with primes. Dimensional quantities are indicated with a tilde. We also assume that the mean flow is uniform in the axial direction, and that the axial flow perturbations do not depend on the radial component. Radial velocity fluctuations are found by solving the continuity equation, assuming that the flow is incompressible. This is a well-established model that has been shown to accurately reproduce experimentally determined conical FTFs when coupled with the G-equation dynamics. Comparisons between FTFs determined from experiments and G-equation models that use this type of flow field can be found in Schuller *et al.* (2002); Cuquel *et al.* (2011); Kashinath *et al.* (2013*b*). Therefore, we can write the two components of $\tilde{\boldsymbol{u}}$ as:

$$\tilde{u}_x = \overline{u}(1 + \varepsilon u_x'(x,t)), \qquad \tilde{u}_r = -\frac{1}{2}\varepsilon \overline{u}\tilde{r}\frac{\partial u_x'}{\partial \tilde{x}}, \tag{2.16}$$

where $\varepsilon \ll 1$ is the perturbation parameter, and $u_x' \sim \mathcal{O}(1)$ is the axial velocity fluctuation, which can be forced or self-excited. We will consider forced fluctuations in order to examine how FTFs are affected by changes in flame speed due to curvature. However, we will not use these FTF results in the self-excited configuration. Instead, we will rewrite the equations in the frequency domain so that linear stability and adjoint methods can be applied without an explicit knowledge of the FTF.

Because we study small perturbations and are interested in the linear limit, it is correct to assume that the flame front is single-valued in a well-chosen reference system. The linearised conical flame front is always single valued in the laboratory framework with respect to the

radial coordinate, with $\tilde{r}$ spanning the range $[0,R]$ at any instant[2]. Thus the $\tilde{G}=0$ level set is expressed as:

$$\tilde{G}(\tilde{x},\tilde{r},\tilde{t}) = \tilde{x} - \bar{\tilde{F}}(\tilde{r}) - \varepsilon\tilde{f}(\tilde{r},\tilde{t}) = 0, \tag{2.17}$$

where $\bar{\tilde{F}}$ and $\tilde{f}$ are the explicit functions that define the shape of the mean flame and its perturbation, respectively.

For an axisymmetric surface $\tilde{x}=S(\tilde{r})$, the mean curvature is expressed by:

$$\tilde{\kappa}(S) = \frac{\frac{\mathrm{d}^2 S}{\mathrm{d}\tilde{r}^2}}{\left(1+\left(\frac{\mathrm{d}S}{\mathrm{d}\tilde{r}}\right)^2\right)^{3/2}} + \frac{\mathrm{d}S}{\mathrm{d}r}\frac{1}{r\sqrt{1+\left(\frac{\mathrm{d}S}{\mathrm{d}r}\right)^2}}. \tag{2.18}$$

By substituting equations (2.16), (2.17) into (2.15) we obtain:

$$\begin{aligned} &-\varepsilon\frac{\partial\tilde{f}}{\partial\tilde{t}} + \bar{u}(1+\varepsilon u_x') + \frac{1}{2}\bar{u}\tilde{r}\varepsilon\frac{\partial u_x'}{\partial\tilde{x}}\left(\frac{\mathrm{d}\bar{\tilde{F}}}{\mathrm{d}\tilde{r}} + \varepsilon\frac{\partial\tilde{f}}{\partial\tilde{r}}\right) = \\ &= \tilde{s}_L^0\sqrt{1+\left(\frac{\mathrm{d}\bar{\tilde{F}}}{\mathrm{d}\tilde{r}} + \varepsilon\frac{\partial\tilde{f}}{\partial\tilde{r}}\right)^2}\left(1-\mathcal{L}\tilde{\kappa}\left(\bar{\tilde{F}}+\varepsilon\tilde{f}\right)\right), \end{aligned} \tag{2.19}$$

where the velocity field has to be evaluated at the flame position $\tilde{x}=\bar{\tilde{F}}+\varepsilon\tilde{f}$.

Geometrical inspection shows that $\sqrt{1+(\mathrm{d}\bar{\tilde{F}}/\mathrm{d}\tilde{r})^2} = 1/\sin\alpha(\tilde{r})$, where $\alpha(\tilde{r})$ is the internal angle that the mean flame front forms locally with the vertical axis (see Figs. 2.2, 2.4). By expanding the r.h.s. of equation (2.19) in ε, we obtain the zero and first order equations for the flame dynamics:

$$1 = \frac{\tilde{s}_L^0}{\bar{u}}\left[\frac{1}{\sin\alpha} - \mathcal{L}\left(\sin^2\alpha\frac{\mathrm{d}^2\bar{\tilde{F}}}{\mathrm{d}\tilde{r}^2} + \frac{\frac{\mathrm{d}\bar{\tilde{F}}}{\mathrm{d}\tilde{r}}}{\tilde{r}}\right)\right] \tag{2.20a}$$

$$\begin{aligned} &\frac{1}{\bar{u}}\frac{\partial\tilde{f}}{\partial\tilde{t}} - u_x' - \frac{1}{2}\tilde{r}\frac{\mathrm{d}\bar{\tilde{F}}}{\mathrm{d}\tilde{r}}\frac{\partial u_x'}{\partial\tilde{x}} = -\frac{\tilde{s}_L^0}{\bar{u}}\left[\sin\alpha\frac{\mathrm{d}\bar{\tilde{F}}}{\mathrm{d}\tilde{r}}\frac{\partial\tilde{f}}{\partial\tilde{r}}\ldots\right. \\ &\left.-\mathcal{L}\left(\sin^2\alpha\frac{\partial^2\tilde{f}}{\partial\tilde{r}^2} - 2\sin^4\alpha\frac{\mathrm{d}\bar{\tilde{F}}}{\mathrm{d}\tilde{r}}\frac{\mathrm{d}^2\bar{\tilde{F}}}{\mathrm{d}\tilde{r}^2}\frac{\partial\tilde{f}}{\partial\tilde{r}} + \frac{\frac{\partial\tilde{f}}{\partial\tilde{r}}}{\tilde{r}}\right)\right]. \end{aligned} \tag{2.20b}$$

The flame is anchored at the burner at $(\tilde{r},\tilde{x})=(R,0)$ and is axisymmetric and smooth with respect to the centerline $\tilde{r}=0$. Therefore equations (2.20) are subject to the boundary

[2]The conical flame is single valued also in the axial direction. However, to work with a function which has $\tilde{x}$ as an independent variable is an unfortunate choice, because the flame tip moves along this direction and the domain of existence of the flame front becomes time dependent, $[0,\tilde{x}_{\mathrm{end}}(\tilde{t})]$, unnecessarily complicating the formulation (Humphrey *et al.*, 2014).

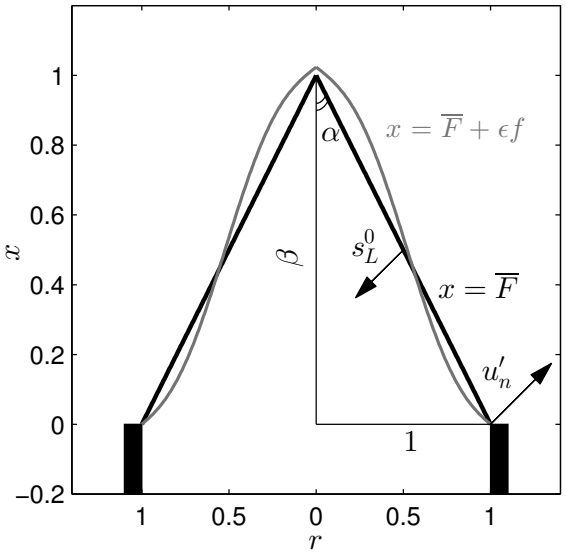

Fig. 2.2 Schematic of the front-tracking model for a flame with constant flame speed. The steady solution is a cone on top of which the perturbation oscillates. The transfer functions are normalised by the normal velocity at the flame base.

conditions:

$$\tilde{\overline{F}}(R) = 0, \quad \left.\frac{\mathrm{d}\tilde{\overline{F}}}{\mathrm{d}\tilde{r}}\right|_{\tilde{r}=0} = 0, \qquad \tilde{f}(R,\tilde{t}) = 0, \quad \left.\frac{\partial \tilde{f}}{\partial \tilde{r}}\right|_{\tilde{r}=0} = 0. \tag{2.21}$$

We also need to evaluate the total heat released by the flame (Lieuwen, 2012):

$$Q \equiv 2\pi\rho h_r \tilde{s}_L^0 \int_0^R (1-\mathcal{L}\tilde{k})\sqrt{1+\left(\frac{\mathrm{d}\tilde{\overline{F}}}{\mathrm{d}\tilde{r}}+\varepsilon\frac{\partial \tilde{f}}{\partial \tilde{r}}\right)^2}\,\tilde{r}\mathrm{d}\tilde{r}. \tag{2.22}$$

Expanding the integrand in ε we can evaluate the steady heat release $\overline{Q}$ and the fluctuations Q'. The ratio $q' = Q'/\overline{Q}$ is the non-dimensional quantity we are interested in:

$$q' = \frac{\displaystyle\int_0^R \left[\sin\alpha\frac{\mathrm{d}\tilde{\overline{F}}}{\mathrm{d}\tilde{r}}\frac{\partial \tilde{f}}{\partial \tilde{r}} - \mathcal{L}\left(\sin^2\alpha\frac{\partial^2 \tilde{f}}{\partial \tilde{r}^2} - 2\sin^4\alpha\frac{\mathrm{d}\tilde{\overline{F}}}{\mathrm{d}\tilde{r}}\frac{\mathrm{d}^2\tilde{\overline{F}}}{\mathrm{d}\tilde{r}^2}\frac{\partial \tilde{f}}{\partial \tilde{r}} + \frac{\frac{\partial \tilde{f}}{\partial \tilde{r}}}{\tilde{r}}\right)\right]\tilde{r}\mathrm{d}\tilde{r}}{\displaystyle\int_0^R \left[\frac{1}{\sin\alpha} - \mathcal{L}\left(\sin^2\alpha\frac{\mathrm{d}^2\tilde{\overline{F}}}{\mathrm{d}\tilde{r}^2} + \frac{\frac{\mathrm{d}\tilde{\overline{F}}}{\mathrm{d}r}}{\tilde{r}}\right)\right]\tilde{r}\mathrm{d}\tilde{r}} \tag{2.23}$$

2.4 Forced response to harmonic fluctuations

We first consider the following case: we impose forced, harmonic fluctuations of angular frequency ω at the flame's inlet, we assume that they are convected axially with a velocity

$\overline{u}_c \neq \overline{u}$ (Birbaud *et al.*, 2006), and we compute radial fluctuations assuming that the flow is incompressible (Preetham *et al.*, 2008; Kashinath *et al.*, 2013*b*). Therefore:

$$\tilde{u}_x = \overline{u}(1+\varepsilon\cos(\omega\tilde{t}-k\tilde{x})), \qquad \tilde{u}_r = \varepsilon\frac{\overline{u}k\tilde{r}}{2}\sin(\omega\tilde{t}-k\tilde{x}), \tag{2.24}$$

where k_c is the wavenumber of the harmonic waves. For now, we neglect the contribution of the curvature on the flame speed, by setting $\mathcal{L}=0$. This problem has already been investigated by Preetham *et al.* (2008). The results we derive, however, differ slightly from the ones they obtained.

To simplify a comparison between our results and those of Preetham *et al.* (2008), we apply the same non-dimensional scheme to both. In particular, we scale axial lengths by the mean flame height L_f, radial lengths by the burner width R, speeds by the mean velocity $\overline{u}$, and time by the characteristic time $L_f/\overline{u}$. The complete set of non-dimensional variables, which do not have a tilde, is presented in Appendix A. The parameters relevant for this section are the ratio between the mean velocity and the convection speed K, the Strouhal number $\mathrm{St}\equiv\omega L_f/\overline{u}$ and the flame aspect ratio $\beta\equiv L_f/R=[(\overline{u}^2-\tilde{s}_L^{0^2})/\tilde{s}_L^{0^2}]^{1/2}=\cot\alpha$ (see Figure 2.2).

Note that the explicit non-dimensional form of the radial velocity component is:

$$u_r=\frac{\tilde{u}_r}{\overline{u}}=\varepsilon\frac{k\tilde{r}}{2}\sin(\omega\tilde{t}-k\tilde{x})=\varepsilon\frac{\mathrm{St}Kr}{2\beta}\sin[\mathrm{St}(t-Kx)]. \tag{2.25}$$

This is different from equation (13) in Preetham *et al.* (2008), because they missed the β factor in the denominator. This missing factor affects only the results obtained by Preetham *et al.* (2008) using Model B. We will now show how the transfer functions of heat release to harmonic velocity fluctuations changes with this correction.

When $\mathcal{L}=0$, equation (2.20a) admits an analytical solution, which in non-dimensional units is $\overline{F}=1-r$. The first order perturbation equation, (2.20b), simplifies to:

$$\frac{\partial f}{\partial t}-\frac{\beta^2}{1+\beta^2}\frac{\partial f}{\partial r}=\cos[\mathrm{St}(t-K(1-r))]-\frac{1}{2}K\mathrm{St}\,r\sin[\mathrm{St}(t-K(1-r))]. \tag{2.26}$$

The solution of this linear PDE can be obtained, e.g., by performing a Laplace transform. The heat release fluctuations simplify to:

$$q'(t)=-\frac{2\beta^2}{1+\beta^2}\int_0^1\frac{\partial f}{\partial r}r\mathrm{d}r=\frac{2\beta^2}{1+\beta^2}\int_0^1 f(r,t)\mathrm{d}r. \tag{2.27}$$

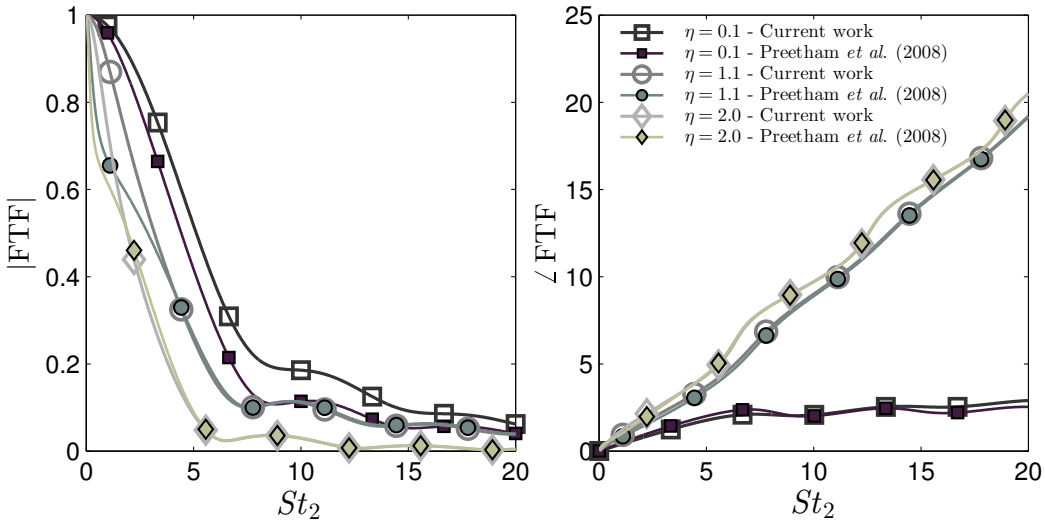

Fig. 2.3 Gain and phase of axisymmetric, conical, FTFs for different values of η. Lines with empty markers correspond to our results (equation (2.29)). Lines with filled markers are the results of Model B in Preetham *et al.* (2008). Differences can be observed mainly in the gain response in the low- or high-frequency limits, depending on the value of η.

We define the Flame Transfer Function (FTF) as in Preetham *et al.* (2008), by:

$$\mathrm{FTF}(\mathrm{St}) \equiv \frac{\hat{Q}'/\overline{Q}}{\hat{\tilde{u}}'_n(x=0,r=1)/\overline{u}\sqrt{1+\beta^2}}, \tag{2.28}$$

where $\hat{\tilde{u}}'_n(x=0,r=1)$ is the Fourier component with angular frequency St of the velocity normal to the flame at the flame base. Introducing the parameters $\eta \equiv K\beta^2/(1+\beta^2)$ and $\mathrm{St}_2 \equiv \mathrm{St}(1+\beta^2)/\beta^2$, the analytical expression we obtain for the transfer function is:

$$\mathrm{FTF}(\mathrm{St}_2) = \frac{2i\left(e^{i\eta \mathrm{St}_2} - (\eta-1)^2 + \eta\,(\eta-2)\,e^{i\,\mathrm{St}_2}\right) + 2\mathrm{St}_2\eta\,(\eta-1)\left(1+\eta\left(e^{i\,\mathrm{St}_2}-1\right)\right)}{\eta(\eta-1)^2\,(2i+\eta\,\mathrm{St}_2)\,\mathrm{St}_2^2}. \tag{2.29}$$

This result can be recovered from the result of Preetham *et al.* (2008) Model B by setting the explicit β terms to 1 in their equation (35), without changing the definitions of St_2 and η, which implicitly contain β. In Figure 2.3 we compare our FTF with that of Preetham *et al.* (2008). Differences can be observed mainly in the gain response, especially in the high-frequency region if $\eta < 1$, and in the low-frequency limit otherwise. No major differences are observed in the phase response. Also, in Cuquel *et al.* (2011) an analytical expression for the FTF was derived using the same flow field as in equation (2.24), but assuming that perturbations convect with the same speed as the mean flow, which is not necessarily the case (Birbaud *et al.*, 2006; Kashinath *et al.*, 2013*b*). They cannot be directly

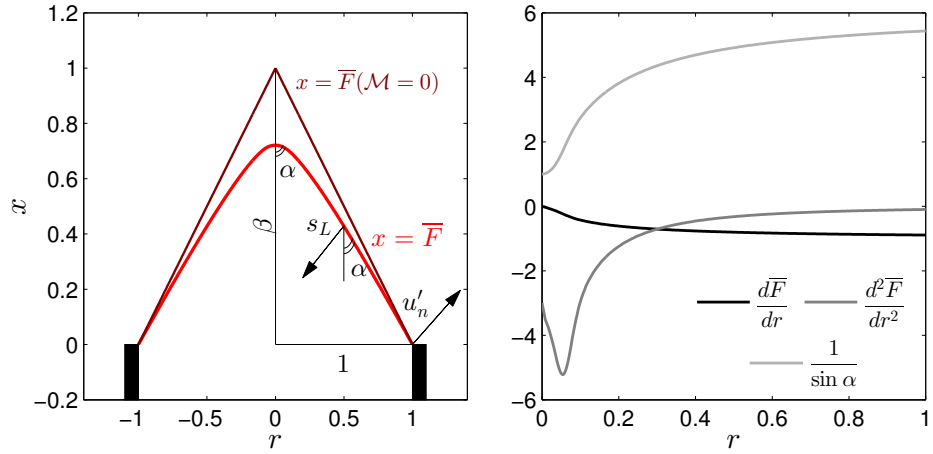

Fig. 2.4 The steady flame shape for $\beta = 6$ and $\mathcal{M} = 0.02$. Curvature corrections to the flame speed round off the cusp at the flame tip, and the angle α now varies with respect to the radial position of the mean flame front.

compared because different scalings for the FTFs were chosen. However, we have verified that normalising the FTF with respect to axial (rather than normal to the flame) velocity fluctuations, the result we obtain in the special case $K = 1$ collapses onto the one reported by Cuquel *et al.* (2011).

In the low-frequency limit the transfer function (2.29) can be expanded as:

$$\mathrm{FTF}(\mathrm{St}_2) = 1 + \frac{\mathrm{i}}{6}(2+3\eta)\mathrm{St}_2 + \mathcal{O}\left(\mathrm{St}_2^2\right), \tag{2.30}$$

and one can see that the particular case of uniformly perturbed flames, in which $\eta = 0$, yields $\mathrm{FTF}(\mathrm{St}_2) \approx 1 + \frac{\mathrm{i}}{3}\mathrm{St}_2$, in agreement with the results reported by Schuller *et al.* (2003) in the long flame limit, for which $\beta \to \infty$ and radial fluctuations are negligible according to equation (2.25). We conclude this section by highlighting that, although we have presented here the correct expression for the FTF, the discussion and main results of the study conducted by Preetham *et al.* (2008) are unaffected.

2.5 Curvature effects

In the previous section we derived analytical results for the special case $\mathcal{L} = 0$. We now allow the flame speed s_L to vary linearly with curvature, and use the same velocity model and non-dimensional scheme as in §2.4 to calculate FTFs. A linear curvature correction to the flame speed was originally proposed by Markstein (1964) to explain the existence of stable flame fronts, which were predicted to be unconditionally unstable due to gas expansion by

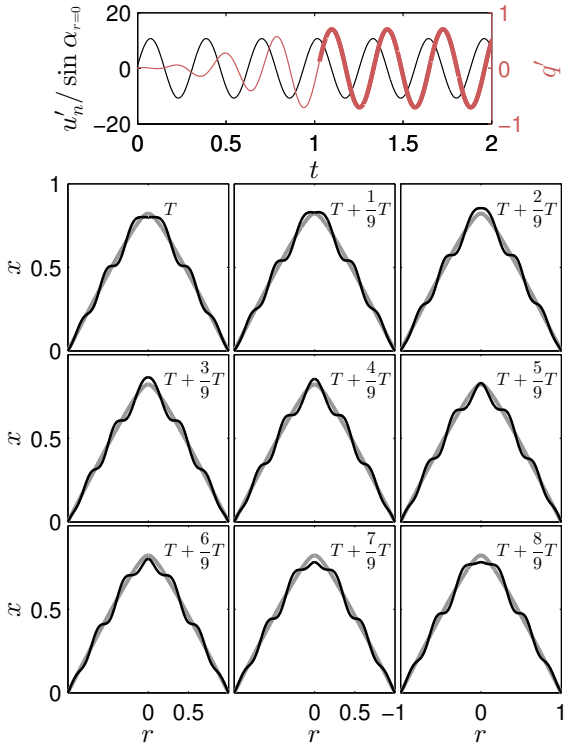

Fig. 2.5 Time integration for $\beta = 6$, $\mathcal{M} = 0.01$, $\eta = 1.1$, and $\mathrm{St} = 20$. Top: normal velocity at the flame base and heat release fluctuations during the transient (thin line) and steady-state solution (thick line). Bottom: evolution over a steady cycle of the perturbed flame front around the mean flame.

the constant flame speed analysis of Darrieus (1938); Landau (1944*a*). In Creta & Matalon (2011) it was shown that analogous results are obtained by accounting also for flame speed corrections due to hydrodynamic strain effects. Although we are not modelling gas expansion, a curvature dependence on the flame speed avoids the formation of unphysically sharp cusps, and it rounds the flame shape at the centerline guaranteeing continuity of the flame normals. We do not account for hydrodynamic strain effects because the flow field model we adopt is too simplistic, and only reproduces the travelling wave form of velocity disturbances.

We introduce the non-dimensional curvature $\kappa \equiv L_f \tilde{\kappa}$, and the Markstein number $\mathcal{M} \equiv \mathcal{L}/L_f$. Note that the characteristic length L_f here is not the actual flame height, but is the height that the flame would have without any curvature correction to the flame speed (see Figure 2.4). This is because we can find no analytical expression for the mean flame shape when $\mathcal{L} \neq 0$, and we cannot know the mean flame height *a priori*. The non-dimensional form

of equations (2.20) is:

$$1 = \frac{1}{\sqrt{1+\beta^2}}\left[\frac{1}{\sin\alpha} - \mathcal{M}\beta^2\left(\sin^2\alpha\frac{\mathrm{d}^2\overline{F}}{\mathrm{d}r^2} + \frac{\frac{\mathrm{d}\overline{F}}{\mathrm{d}r}}{r}\right)\right] \tag{2.31a}$$

$$\frac{\partial f}{\partial t} - \cos\left[\mathrm{St}(t-K\overline{F})\right] - \mathrm{St}K\frac{r}{2}\frac{\mathrm{d}\overline{F}}{\mathrm{d}r}\sin\left[\mathrm{St}(t-K\overline{F})\right] = \ldots$$

$$-\frac{\beta^2}{\sqrt{1+\beta^2}}\left[\sin\alpha\frac{\mathrm{d}\overline{F}}{\mathrm{d}r}\frac{\partial f}{\partial r} - \mathcal{M}\left(\sin^2\alpha\frac{\partial^2 f}{\partial r^2} - 2\beta^2\sin^4\alpha\frac{\mathrm{d}\overline{F}}{\mathrm{d}r}\frac{\mathrm{d}^2\overline{F}}{\mathrm{d}r^2}\frac{\partial f}{\partial r} + \frac{\frac{\partial f}{\partial r}}{r}\right)\right]. \tag{2.31b}$$

We require numerical integration techniques to evaluate FTFs when $\mathcal{L} \neq 0$. The steady equation (2.31a) can be efficiently solved numerically with a Newton–Raphson method. The mean quantities $\mathrm{d}\overline{F}/\mathrm{d}r$, $\mathrm{d}^2\overline{F}/\mathrm{d}r^2$, $\sin\alpha$ (Figure 2.4), and the perturbation f are discretized in space using a second-order finite difference scheme. The linear PDE (2.31b) is then marched forward in time using an explicit third-order Runge-Kutta method (Gottlieb & Shu, 1998). The final time is sufficiently large for the transient behaviour to disappear, and for a few forced cycles to fully travel along the mean flame (Figure 2.5). The steady-state heat release fluctuations q' are evaluated according to equation (2.23) at every time step. The FTF definition generalises equation (2.28):

$$\mathrm{FTF}^{\mathcal{M}}(\mathrm{St}) = \frac{\hat{q}'}{\hat{u}'_n(x=0,r=1)\sqrt{1+\beta^2\left(\frac{\mathrm{d}\overline{F}}{\mathrm{d}r}\right)^2_{r=1}}}, \tag{2.32}$$

where

$$\hat{u}'_n(x=0,r=1) = \left.\frac{\hat{u}'_x - \beta\frac{\mathrm{d}\overline{F}}{\mathrm{d}r}\hat{u}'_r}{\sqrt{1+\beta^2\left(\frac{\mathrm{d}\overline{F}}{\mathrm{d}r}\right)^2}}\right|_{x=0,r=1} \tag{2.33}$$

is the velocity component normal to the mean flame at the flame base.

The numerical code has been benchmarked against theoretically known perturbed flame evolutions such as equation (2.26), and transfer functions such as (2.29), showing that the numerical results for gain and phase converge to the correct values in proportion to Δr^2, where Δr is the grid spacing used in the discretization scheme. Figure 2.5 shows the integrated heat release and normal velocity time-traces during the transient and steady-state solutions of the forced system. The gain and phase can be calculated by taking the ratio between the steady-state amplitudes and the (normalised) distance between the peaks of the time series respectively. In the bottom panels the evolution of the perturbed flame front around the mean one is shown over a forced cycle.

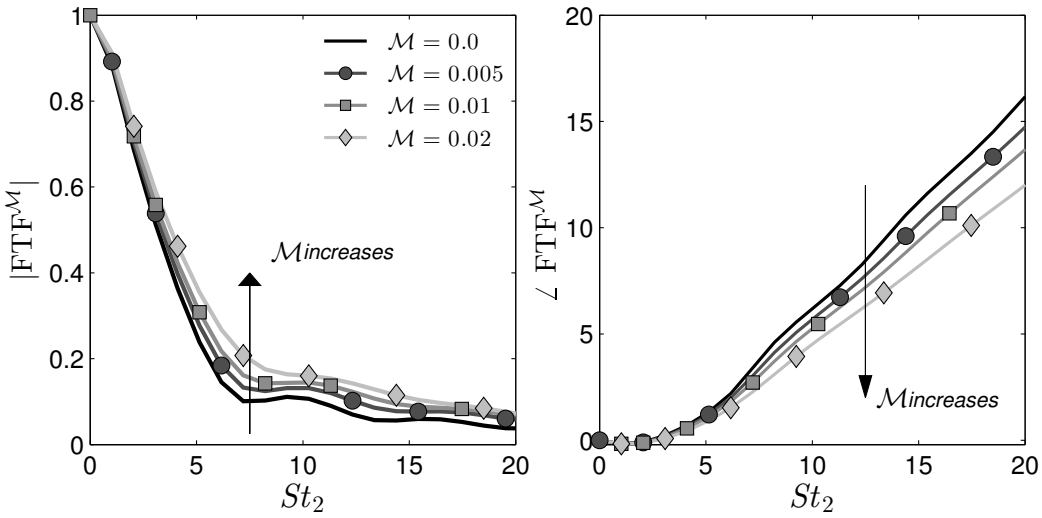

Fig. 2.6 Transfer functions of conical flames with curvature-dependent flame speed. Gain and phase for $\beta = 6$, $\eta = 1.1$, and different $\mathcal{M}$. Increasing the Markstein number decreases the flame's mean height. As a consequence the time delay of perturbations lowers (shifts in phase), and in the low-frequency limit increases the effect of small perturbation on the heat release.

The higher the frequency of the forcing fluctuations, the smaller the wavelengths of the perturbations that are generated on the flame. This has a consequence for the numerical cost required to evaluate the transfer functions: at high-frequencies, the perturbation wavelengths are shorter and the grid spacing Δr has to be smaller. The time step decreases accordingly and the time-marching integration can become expensive. This phenomenon partly justifies the technique developed in §2.6.

Figure 2.6 shows the heat release transfer function for $\beta = 6$ and $\eta = 1.1$ while increasing the Markstein length. At small frequencies the perturbed flame is not highly wrinkled and first order curvature effects are small. At the same time, when the Markstein length is larger, the flame slope $\mathrm{d}\overline{F}/\mathrm{d}r$ at the base is smaller (see Figure 2.4). Therefore, the projection of the radial velocity onto the flame's normal reduces, the denominator in equation (2.32) reduces, and the FTF gain increases. At higher frequencies the flame is highly wrinkled and curvature corrections play a crucial role in reducing the size of these wrinkles, which lowers the gain. These arguments are consistent with the gain's dependence on $\mathcal{M}$ shown in Figure 2.6. Furthermore, the fact that the FTF phase shifts towards zero with $\mathcal{M}$ has a clear physical cause: when the Markstein number is larger, the flame is shorter and the perturbations take less time to travel along the flame.

As shown in Figure 2.6, curvature corrections to the FTF are small, and comparisons between the G-equation model without curvature effects and experiments can be found in

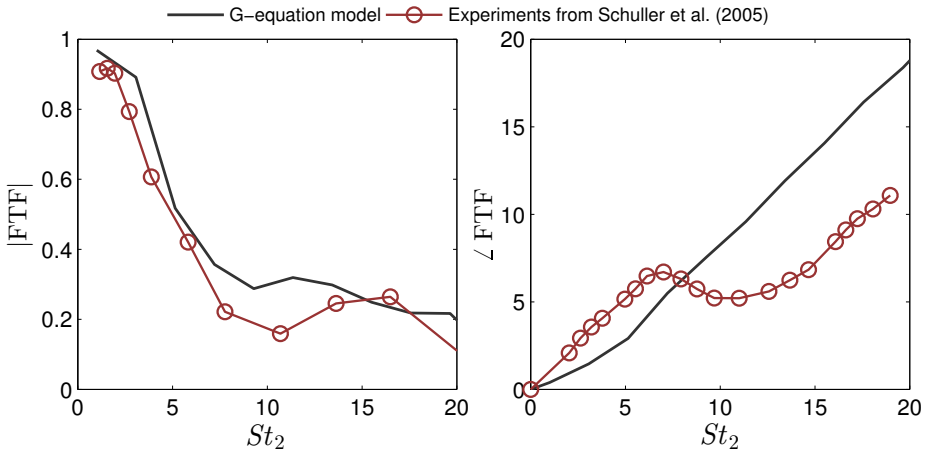

Fig. 2.7 Comparison between our low-order model and an experimentally determined (Schuller *et al.*, 2002) FTF. The FTFs here are scaled with respect to axial velocity fluctuations. Parameters for the simulation were chosen to match experimental values; the gain responses compare reasonably well, especially at low frequencies, whereas we cannot capture the phase inflection because we fix the convection speed value.

the literature (Schuller *et al.*, 2002; Karimi *et al.*, 2009; Cuquel *et al.*, 2011; Kashinath *et al.*, 2013*b*). Nonetheless, in Figure 2.7 we compare the FTF derived from our model (with curvature correction) with that determined from experiments, extracted from Schuller *et al.* (2002). The flame aspect ratio was set to $\beta = 2.64$, and was derived by imposing a mean velocity $\overline{u} = 1.1$ m/s and a flame speed $s_L^0 = 0.39$ m/s, as suggested in Schuller *et al.* (2002). Because we have no information on the other parameters, we set the convection speed ratio and the Markstein length to the reasonable values $K = 1.2$ and $\mathcal{M} = 0.01$ respectively (Kashinath *et al.*, 2013*b*). Note that, in order to compare the results, in Figure 2.7 we have scaled the FTF with respect to axial velocity fluctuations, and not to normal velocity at the flame base as in the rest of this study. The gains compare reasonably well, especially at low frequencies, which is a known result (Schuller *et al.*, 2003; Cuquel *et al.*, 2011). The phase response difference may be adjusted at low frequencies by choosing a suitable value for K. However, our current model cannot capture the inflection that occurs at $St_2 \approx 7.5$, because we are fixing the value of K. To capture this phenomenon, a possibility would be to use a frequency dependent convection speed extracted from experiments or DNS as in Kashinath *et al.* (2013*b*). However, we also note that the inflection of the phase response is not always observed in experiments. For example in Karimi *et al.* (2009); Cuquel *et al.* (2011) the phase is shown to increase linearly and to saturate at high frequencies. In this study we do not aim to accurately reproduce a specific experiment, and in the following we will retain K constant.

As a final remark, we note that Shin & Lieuwen (2013) showed that turbulence effects on the flame dynamics – modelled with a low-intense stochastic component in the velocity field – are analogous to curvatures effects on the flame speed (and consequent dynamics) of the ensemble-averaged flame front. Using their result, we can thus expect an analogy between the curvature corrections to FTFs discussed above and variations in the FTFs of flames with small turbulent fluctuations.

2.6 Self-excited problem: eigenvalue problem formulation

So far, we have investigated the forced response of conical premixed flames to harmonic fluctuations. Although the knowledge of FTFs has some importance, usually one is interested in the analysis of a closed flame-flow-acoustics feedback loop. In this context the flame dynamics is not forced, but is coupled with the acoustic equations and the flow field dynamics. Perturbations will grow unboundedly in time if and only if at least one thermoacoustic mode has a positive growth rate.

If a model that couples fluid and combustion fluctuations is prescribed, then explicit knowledge of the FTF is not needed in order to assess the system's stability. Indeed, one can simply construct a larger eigenvalue problem, whose state vector contains all the variables of the fully-coupled thermoacoustic system, and use Arnoldi methods to calculate the eigenvalues with the largest growth rate. As we will show in §2.7.3, this formulation also allows for straightforward use of adjoint methods to calculate eigenvalues' sensitivities with respect to any system's parameter. The latter is precluded when a numerically (or experimentally) measured FTF is used, because the explicit dependence of the linear operator on the base state and system's parameters is unknown. In the following, we will describe the method using the same G-equation model as presented in §2.3, but it could as well be used in a network with a higher order model for the premixed flame, as the ones developed by Hemchandra (2012); Blanchard *et al.* (2015).

To keep the model low-order, we divide the thermoacoustic problem conceptually into three components, which are connected in a feedback loop: (i) the flame front f and heat release fluctuations q' dynamics are governed by the kinematic, linear G-equation (equations (2.20b) and (2.23)); (ii) the heat release acts as a point source in the (linear) acoustic equations. Unsteady heat dilates the surrounding air and is a monopole source of acoustic waves, which in turn provoke velocity fluctuations at the flame base (Dowling, 1999; Kashinath *et al.*, 2013*a*); (iii) axial velocity fluctuations are convected downstream in the flame domain, and radial fluctuations are calculated to guarantee mass conservation (Birbaud *et al.*, 2006; Preetham *et al.*, 2008).

The acoustic equations can conveniently be written in state-space form:

$$\frac{\mathrm{d}\boldsymbol{x}}{\mathrm{d}t} = A\boldsymbol{x} + \boldsymbol{B}q'(t) \tag{2.34a}$$

$$u'_x = \boldsymbol{C}_u\boldsymbol{x}, \qquad p' = \boldsymbol{C}_p\boldsymbol{x}, \tag{2.34b}$$

as described in §2.2.2. Equations (2.34) are scaled in non-dimensional units consistently with (A.1). Note that, so far, no particular acoustic configuration has been chosen, and the matrix A and vectors $\boldsymbol{B}$, $\boldsymbol{C}_{u/p}$ refer to any possible acoustic configuration. Typical non-dimensional numbers that appear in the matrices are the mean flow Mach number $M \equiv \overline{u}/c$, where c is the speed of sound, and the ratio between the flame and acoustic characteristic lengths. In the Laplace space, the acoustic transfer function can be expressed as:

$$H_u(s) = \frac{u'_x(s)}{q'(s)} = \boldsymbol{C}_u\,(sI - A)^{-1}\,\boldsymbol{B}, \tag{2.35}$$

where s is the Laplace variable. Note that it is unimportant how the state-space model has been derived from the acoustic equations. One can use a Galerkin decomposition in Fourier modes as in Culick (2006); Kashinath *et al.* (2013*a*), a state vector with memory as in Mangesius & Polifke (2011) or Padé approximations as in Bothien *et al.* (2007); Orchini *et al.* (2015).

Finally, the convective model for the velocity field reads:

$$\frac{\partial u'_x}{\partial t} + \frac{1}{K}\frac{\partial u'_x}{\partial x} = 0, \qquad u'_x(x=0,t) = \boldsymbol{C}_u\boldsymbol{x}(t), \tag{2.36}$$

where the second equation corresponds to the boundary condition that the axial velocity at the flame base is given by the acoustic state-space model.

Because we are interested in finding the global modes of the coupled system, we look for solutions of the type $f(r,t) = \hat{f}(r)e^{\lambda t}$, $\boldsymbol{x}(t) = \hat{\boldsymbol{x}}e^{\lambda t}$, $u'_x(x,t) = \hat{u}'_x(x)e^{\lambda t}$. We then discretize $\overline{F}$, $\hat{f}$, and $\hat{u}'_x$ in space, as well as the derivative and integral operators, and combine the discrete versions of equations (2.20b), (2.23), (2.34), (2.36) to obtain the eigenvalue problem:

$$M\boldsymbol{z} = \lambda\boldsymbol{z}, \tag{2.37}$$

where $\lambda \equiv \sigma + \mathrm{i}\,\mathrm{St}$ are the complex eigenvalues sought, $\boldsymbol{z}$ defines the thermoacoustic state as $\boldsymbol{z} \equiv \left[\hat{f}^1, \ldots, \hat{f}^{N_r}, \hat{x}^1, \ldots, \hat{x}^{N_s}, \hat{u}_x'^1, \ldots, \hat{u}_x'^{N_x}\right]^T$, and the matrix M can be written as

$$M = \begin{bmatrix} M_{ff} & M_{fs} & M_{fu} \\ M_{sf} & M_{ss} & M_{su} \\ M_{uf} & M_{us} & M_{uu} \end{bmatrix}, \tag{2.38}$$

where the submatrix M_{ff} represents the coupling between the flame evolution and the flame state, M_{fs} the coupling between the flame evolution and the acoustic state, and so on. Their explicit expressions are given in Appendix B.

We observe that equation (2.36) could be analytically solved, yielding:

$$\hat{u}_x'(x) = \boldsymbol{C}_u \hat{\boldsymbol{x}} e^{-\lambda K x} = \boldsymbol{C}_u \left(\lambda I - A\right)^{-1} \boldsymbol{B} e^{-\lambda K x} \hat{q}, \tag{2.39}$$

where we have used equation (2.35) in the second equality. Note that the eigenvalue λ appears both in the exponential and in the matrix inversion operation. Because of this, if we were to substitute the velocity field expression into the flame dynamics we would obtain a smaller eigenvalue problem – the state would be fully determined by the flame shape $\hat{f}$ – but the problem would be nonlinear. Because of the small size of the eigenvalue problems we are solving, we have decided to solve the larger but linear eigenvalue problem (2.37).

By solving the eigenvalue problem, we can determine whether, for a given acoustic configuration and set of flame/flow parameters, there exist modes with a positive growth rate. We can determine their frequencies without having explicit knowledge of the FTF. This is useful because we do not need to evaluate a new FTF if we change a flame parameter, and we can investigate a large set of parameters at a lower computational cost. Numerical cost for the evaluation of FTFs becomes large at high-frequencies, where the wavelengths are short and the CFL condition for the time step gives:

$$\Delta t < \mathrm{CFL}\frac{\Delta r}{U_{max}} \approx \mathrm{CFL}\frac{1+\beta^2}{\beta^2}\frac{\Delta r^2}{\Delta r + \mathcal{M}\frac{2+\beta^2}{\sqrt{1+\beta^2}}}, \tag{2.40}$$

where the advection velocity U_{max} can be estimated from equation (B.1a). For non-small curvature effects, the time step scales as Δr^2, and evaluating transfer functions at high frequencies becomes numerically expensive. Also, the dimension of the eigenvalue matrix M increases at high-frequencies because the spatial discretization has to be very dense in order to capture small wavelengths fluctuations. We are not interested in determining all the eigenvalues of the matrix, however, but only those with the most positive real parts. Thus

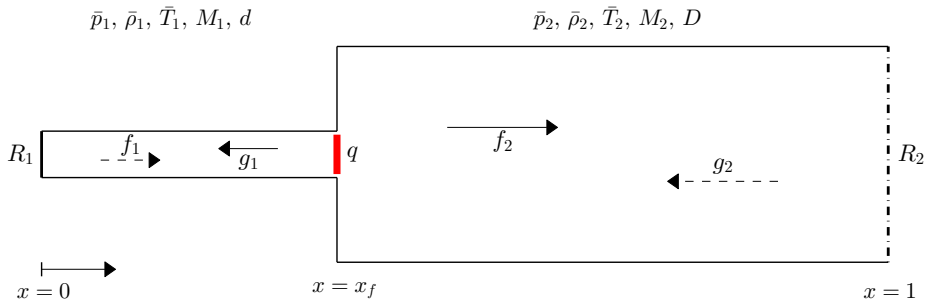

Fig. 2.8 Acoustic network considered in this study. It is based on the experimental setup described by Kabiraj & Sujith (2012). The flame position x_f is the bifurcation parameter we will investigate. The flame, assumed to be acoustically compact, induces a mean temperature change and consequent mean flow properties variations. An area change models the blockage introduced by the burner holding the flame.

one can use numerical algorithms such as Arnoldi methods to compute the few eigenvalues of interest, greatly reducing the cost of the problem.

2.7 Linear analysis of a thermoacoustic network

We now apply the theory outlined so far to the case of a laminar conical flame confined in a duct.

The acoustic geometry we consider, sketched in Figure 2.8, consists of a straight pipe with a non-zero mean flow. The pipe radius abruptly increases at the flame location, to emulate the blockage of the burner holding the flame. The acoustic mean properties suddenly vary across the flame and across area variations to satisfy mass, momentum and energy balances. We impose a closed, perfectly reflecting acoustic boundary condition at the inlet, and an open frequency dependent reflection coefficient at the outlet.

2.7.1 Model parameters

The thermoacoustic network parameters were inspired by the experimental setup of Kabiraj & Sujith (2012): a laminar conical flame is attached to a burner (diameter $D = 11$ mm), and confined in an acoustically open-closed pipe of length $L = 860$ mm and diameter $D_L = 25.6$ mm. The area increase is treated as a discontinuity, and we use jump conditions dictated by mass, momentum and energy conservation to solve for the flow after the area change (Stow & Dowling, 2001). The temperature ratio is $T_2/T_1 = 2$. The value for T_2 has to represent the mean temperature in the downstream part of the duct. This number should be a function of the flame position in the duct: the more downstream is the flame, the

higher is the mean temperature in the last section, because less heat is dissipated through the walls. Nonetheless, we decide to keep this parameter independent from the flame location for simplicity. The mean flow speed is $\overline{u} = 1.55$ m/s. A lean equivalence ratio regime is analysed, with $\phi = 0.51$. The Markstein length is fixed to $\mathcal{L} = 0.6$ mm, and the laminar flame speed is varied to change the flame aspect ratio. When $s_L^0 = 0.25$ m/s, the steady flame has an aspect ratio $\beta \equiv L_f/R \approx 6$. Damping effects are included by means of losses at boundaries; the closed inlet reflection coefficient is set to $R_1 = 1.0$, whereas for the outlet reflection coefficient we use the expression derived analytically, using the Wiener-Hopf technique, of an unflanged cylindrical open end in the low Mach number limit (Munt, 1977; Cargill, 1982; Eldredge & Dowling, 2003; Peters *et al.*, 1993):

$$R_2 = -(1+0.9M)\left(1-\frac{1}{2}\frac{\omega^2 R^2}{c^2}\right). \tag{2.41}$$

(2.41) has been validated against experiments in Peters *et al.* (1993). Lastly, we fix the convection speed to $K = 1.2$. Fixing K has a strong influence on the flame time lag response. Experiments and DNS have shown that the convection speed ratio K is in general a function of the perturbation amplitude and frequency (Birbaud *et al.*, 2006; Kashinath *et al.*, 2013*b*). For simplicity we decided to fix K to a reasonable value that fits their findings. Similar values have been used in other numerical analysis (Kashinath *et al.*, 2013*a*; Waugh *et al.*, 2014; Orchini *et al.*, 2015). The non-dimensional flame position is $x_f \equiv l_1/L$, where $L \equiv l_1 + l_2$ is the length of the pipe. The acoustic time scale is defined by the acoustic Strouhal number $St_2 \equiv \omega L/c_1$.

Although the acoustic configuration is simple, the presence of multiple jump conditions (flame and area increase) makes it harder to find analytically an expression for the acoustic transfer function to heat release fluctuations. Therefore, we rely on numerical methods. We use LOTAN, which is a low-order thermoacoustic network model developed by Dowling & Stow (2003) for the simulation of longitudinal and annular combustion systems. The low-order modelling approach is based on the fact that the main nonlinearity is in the combustion response to flow perturbations rather than in the acoustics (Chu, 1963; Culick, 1971). LOTAN has been verified experimentally against both a sector rig (Stow & Dowling, 2001) and an atmospheric test rig (Stow & Dowling, 2004). The combustion system is modelled as a series of interconnected modules. Longitudinal ducts, annular ducts, combustion zones and area changes are amongst the module types that can be modelled. The model decomposes the flow into a steady mean axial component and small perturbations. The perturbations throughout the combustor are related via wave propagation, in which acoustic, entropy, and vorticity waves are all included. The flow conservation equations are used to track the evolution of

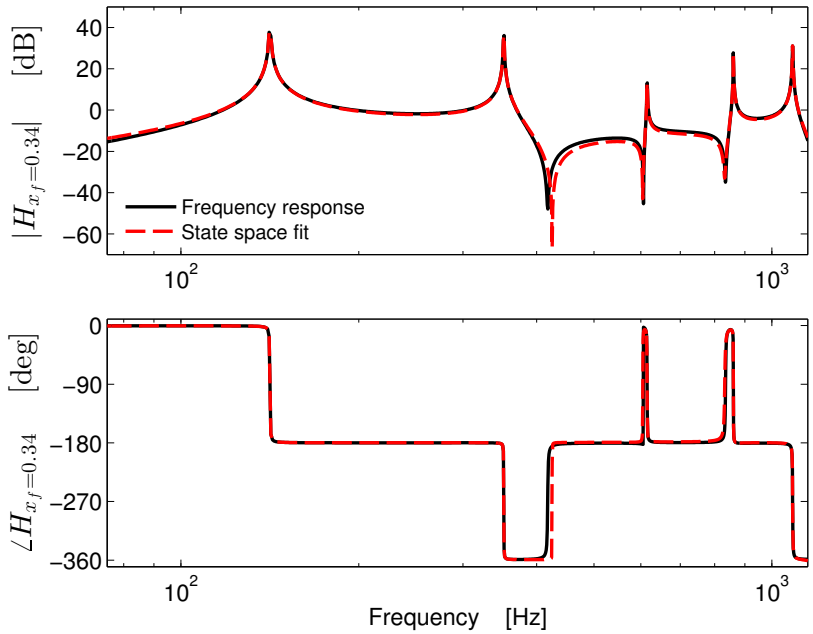

Fig. 2.9 Comparison between the frequency response calculated with LOTAN (solid black) and the state-space approximation (dashed red) at $x_f = 0.34$. The approximation works well over a wide range of frequencies.

these waves. The connecting modules are modelled as acoustically compact, meaning that their axial length is short in comparison to the acoustic wavelengths of interest. The acoustic boundary conditions at the inlet and outlet of the combustor are assumed to be known, and these can be prescribed as frequency-dependent functions. The flame is assumed to combust at one axial location, i.e., to be acoustically compact.

Although LOTAN is able to model quite complex acoustic geometries, the range of flame models currently available in LOTAN is relatively limited. We therefore use LOTAN in an unconventional way. We take full advantage of LOTAN's advanced acoustic modelling capabilities by extracting the acoustic eigenfrequencies and the network frequency response. Then we cast it in state-space form as in §2.2.2. This is necessary to extend the frequency response – calculated at $s = \mathrm{i}\omega$ – in the full Laplace space, in which the growth rate σ can be non-zero. Figure 2.9 shows that the state-space approximation fits the frequency response evaluated with LOTAN well over a wide range of frequencies. We find that an approximation order $n = 20$ is always sufficient to properly describe the frequency response with a state-space model. Finally, rather than coupling this with a flame model directly in LOTAN, we couple the extracted acoustic model with the *G*-equation model described in §3.2. By doing so, we are able to model the coupled dynamics of complex acoustics with a

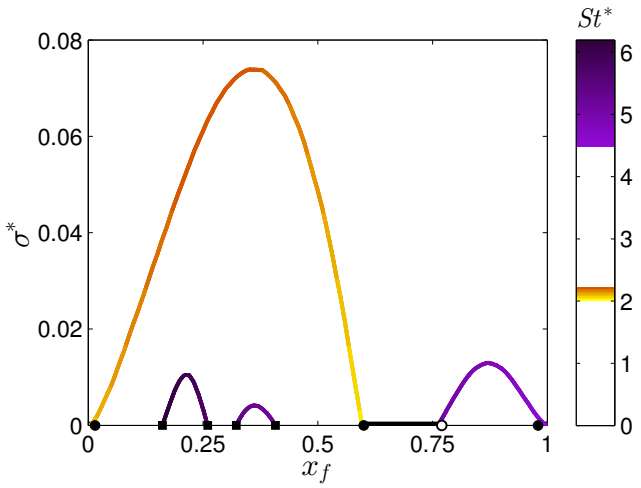

Fig. 2.10 Growth rates of the eigenvalues λ with a non-negative real part. Line colours indicates the frequency of the mode. Thick lines and circles at $\sigma^* = 0$ correspond to brute-force time marching results, as described in 3. Full and empty circles correspond to super- and subcritical Hopf bifurcations respectively.

flame model which is also complex. This can be used to study the thermoacoustic system both in the frequency and the time domain.

2.7.2 Linear stability of a ducted flame

The first bifurcation parameter we investigate is the position of the flame in the duct $x_f \in [0,1]$, fixing the flame aspect ratio to $\beta = 6$. The corresponding FTF is analogous to the one shown in Figure 2.6 for $\mathcal{M} = 0.02$. We can take advantage of the fact that (i) its gain never exceeds unity, and (ii) it acts as a low-pass filter, to deduce that if a thermoacoustic mode has a positive growth rate, then (i) it is associated with one of the acoustic resonant frequencies, for which the gain is much larger than one and (ii) it is a low-frequency mode. This will be shown to be true in Chapter 3 also in the nonlinear limit, by means of the harmonic balance technique. Only modes associated with the first two acoustic resonant frequencies were found to be unstable. Therefore, we can reduce the size of the eigenvalue problem by using a small state-space model that characterizes only the first few acoustic modes ($N_s = 4$), and by using a relatively large grid spacing Δr, because we do not need to describe short wavelengths ($N_r = N_x = 399$). Limiting the analysis to 4 acoustic modes is a good approximation for the case considered here, because only low-frequency modes can be unstable, and their projection on high-frequency modes is negligible. A higher order approximation needs to be considered if modes with higher frequencies can be unstable.

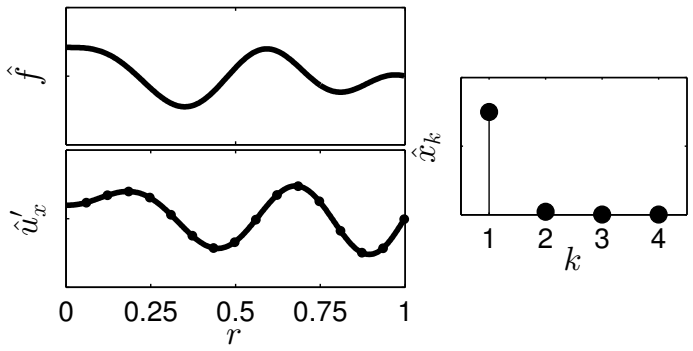

Fig. 2.11 Real parts of the eigenstate of the unstable mode for $x_f = 0.27$. Top left: perturbed flame shape state. Bottom left: axial velocity fluctuations. Right: components of the acoustic state-space vector.

Figure 2.10 shows the results of the eigenvalue problem. Only the growth rates $\sigma^* \equiv \sigma/(2\pi)$ and frequencies $\mathrm{St}^* \equiv \mathrm{St}/(2\pi)$ of the eigenvalues with a non-negative real part are shown. We clearly identify two modes, whose frequencies can be shown to be very close to the first and second acoustic resonant frequencies. We have verified with convergence tests that these modes are physical modes, and not spurious modes that arise because of the discretization of the equations. We observe that for some flame positions, x_f, both modes may have a positive growth rate. We have indicated with squares the Hopf bifurcations of the high-frequency mode, which lie inside the region of instability of the low-frequency mode. When both modes have a positive real part, the growth rate of the of the low-frequency mode dominates over the growth rate of the high-frequency one, which is consistent with the system's low-pass characteristics. All these results agree with the fully nonlinear analysis carried out by Orchini *et al.* (2015). We have plotted in Figure 2.10 with thick black lines and circles the linearly stable regions identified by brute-force time marching of the fully nonlinear equations. According to these results, filled and empty circles locate super- and subcritical Hopf bifurcations respectively.

Figure 2.11 shows the eigenvector of the unstable mode at $x_f = 0.27$. Moving from the flame anchoring point $r = 1$ to the centreline $r = 0$, the top-left frame shows that the flame perturbation grows in amplitude spatially. On the other hand, velocity fluctuations, shown in the bottom panel, decrease in amplitude while moving in the same direction. This is physically correct because we are using a convective model with speed $1/K$, so the velocity amplitude at $r = 0$ at time t is the amplitude that the velocity perturbation had at $r = 1$ at time $t - 1/K$ and, because λ has a positive growth rate, the earlier perturbation had a smaller amplitude than the current one. We showed in equation (2.39) the analytical solution for the convective model along the flame. The analytical result is plotted with circles in Figure 2.11,

and is in perfect agreement with the numerically evaluated eigenstate. This comparison can be used as a test to assess the convergence of the eigenvalue problem. For example, high-frequency modes will not converge with the current grid-space size but we know that they will be stable because the flame acts as a low-pass filter. Finally, the right panel shows the intensity of the acoustic eigenstate. The fact that only the first mode has a large intensity is an indicator of the fact that this thermoacoustic mode is closely linked to the first acoustic resonant mode.

Given the relatively small size of the eigenvalue problem, we can quickly calculate the stability of the thermoacoustic system for a wide range of parameters. We start by focusing on two parameters: the position of the flame in the duct and the flame aspect ratio β, which can also be interpreted as the ratio between the flame speed and the mean flow velocity (see equations (A.1)). We vary x_f along the full length of the duct in steps of $\Delta x_f = 0.01$, and β in the range $[0.5, 10]$ in steps of $\Delta\beta = 0.1$. For each couple of parameters, we solve the eigenvalue problem (2.37), and we investigate the two eigenmodes with the largest growth rate. We will refer to the low- and high-frequency modes as mode 1 and mode 2 respectively because they are closely linked to the acoustic fundamental and second hamonic resonant modes. Note that we are not tracking the eigenvalues, but we are just looking at the two eigenvalues with the largest growth rate. We find that, in our system, some of the eigenvalues may cross each other in the complex plane while varying the bifurcation parameters. Because they cross, the growth rate map we evaluate is continuous, but its derivative is not, as is discussed in §2.7.3. We have verified that the eigenvalue crossing always occurs when the growth rates of the crossing modes are negative (dashed lines in Figure 2.12), and we are not missing any region of instability in the following analysis.

The growth rate maps of the two modes are shown in Figure 2.12. We have highlighted with black lines the zero growth rate contours, which are the neutral curves along which Hopf bifurcations are located. The thin straight lines (and circles) at $\beta = 6$ on the two maps correspond to the growth rates (and Hopf bifurcations) shown in Figure 2.10. Note that we have used two different colour maps for the stability diagrams of the two modes to highlight that the growth rate of mode 1 is higher than the growth rate of mode 2, which agrees with the fact that the flame acts as a low-pass filter.

Looking at the size of the regions with positive (or negative) growth rates, we observe that mode 1 shows very large zones in which the sign of the growth rate does not change, and they approximately extend over the whole length of the duct. On the other hand, mode 2 shows several smaller regions with a positive growth rate, and they extend approximately over 1/3 of the duct.

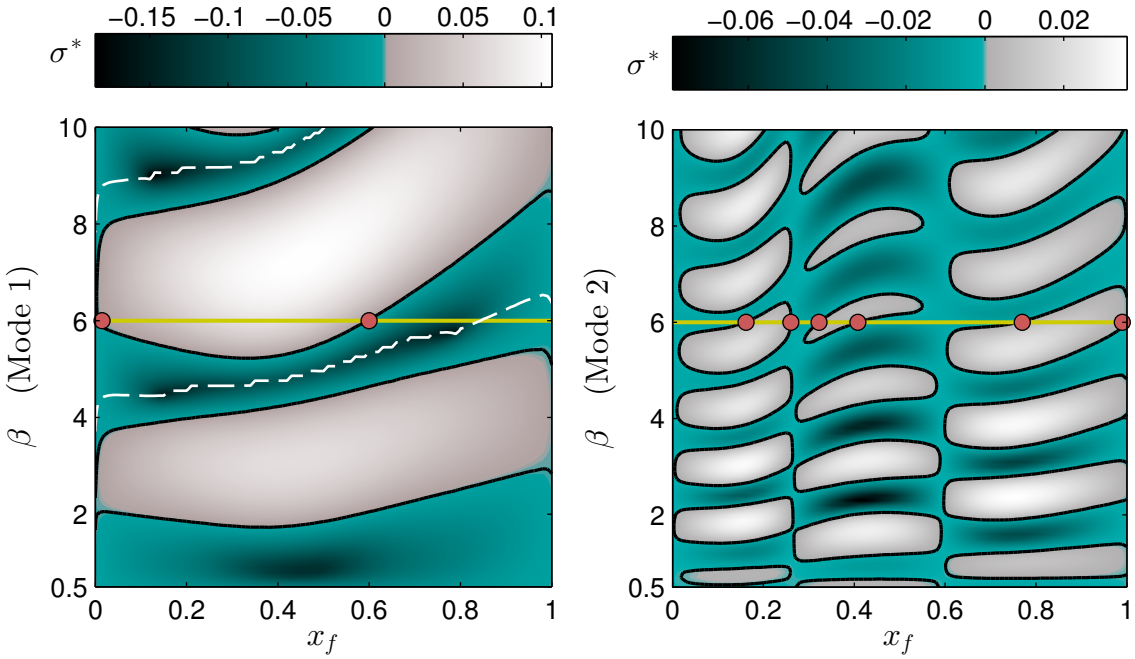

Fig. 2.12 Growth rate maps of two thermoacoustic modes. Dark regions are associated with a negative growth rate (the mode is stable), and light regions with positive growth rates (the mode is unstable). Two different colour map scales are used to highlight the growth rate gradients. Neutral lines (zero growth rate) are highlighted in black. The straight thin line and the circles correspond to the results and the Hopf bifurcations shown in Figure 2.10. In mode 1 we observe an eigenvalue crossing phenomenon: the curves along which the eigenvalues cross are highlighted with dashed white lines.

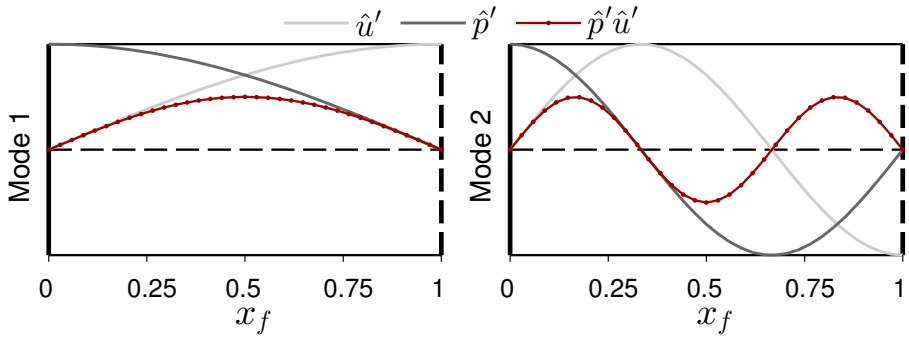

Fig. 2.13 Fundamental (mode 1) and second hamonic (mode 2) modes in a closed-open pipe, which roughly approximates the acoustic network under consideration. The location of nodes and maxima/minima closely resembles those observed in Figure 2.10. Thus, we find that the system is more prone to thermoacoustic instabilities where the Rayleigh index (2.42) is largest, as expected.

This can be explained through the Rayleigh criterion, which states that a necessary condition for thermoacoustic oscillations to occur is that pressure and heat release fluctuations need to be sufficiently in phase (Rayleigh, 1878). More quantitatively, the Rayleigh index, which quantifies the rate of energy produced over a thermoacoustic cycle and is defined by

$$\mathrm{Ry} \equiv \frac{\gamma-1}{\gamma\overline{p}} \int_0^T p'(x_f,t)q'(x_f,t)\,\mathrm{d}t, \tag{2.42}$$

has to be larger than the sum of the acoustic energy losses (Ferreira & Carvalho Jr., 1997; Nicoud & Poinsot, 2005). Assuming that the heat release fluctuations are proportional to (delayed) velocity fluctuations, the Ry index becomes

$$\mathrm{Ry} \propto \hat{p}'(x_f)\hat{u}(x_f) \int_0^T \cos(\omega t)\cos(\omega(t-\tau))\,\mathrm{d}t, \tag{2.43}$$

where $\hat{p}'(x_f)$ and $\hat{u}'(x_f)$ are the values that the acoustic modeshapes of eigenfrequency ω assume at the flame location. τ is the time delay between acoustic velocity and heat release fluctuations, which is connected to the convection speed and flame length, as discussed later. Because the acoustic network we are considering has a temperature jump across the flame and a cross sectional area variation, the shape of the modes is different for every value of x_f. However, our network can be roughly approximated by a closed-open pipe with no area or temperature variations, as shown in Figure 2.13. In mode 1, the interaction between pressure and velocity acoustic waves has nodes ($\hat{p}'(x_f)=0$ or $\hat{u}'(x_f)=0$) at the boundaries and a maxima (or minima) is found at the centre of the duct. For the second mode, the acoustics waves have nodes at $x_f = 1/3$ and $2/3$, and maxima or minima are found at $x_f = 1/4$, $2/4$, $3/4$. These same patterns can be observed (with some modifications due to temperature and area variations of the acoustic network we are considering) in the growth rate maps of the two thermoacoustic modes. Varying the delay τ causes a time shift between velocity and pressure fluctuations, which may alter the sign of the Rayleigh index, as discussed later.

2.7.3 Adjoint-based sensitivity

Having evaluated steady solutions and the stability of small perturbations around them over a fairly large parameter space, a natural question that arises is: how does the stability map change by making a tiny change to one of the parameters in the governing equations? This information is contained in the so-called base state sensitivity map, which measures the drift of the eigenvalues $\delta\lambda$ with respect to a given perturbation in a parameter δK (Giannetti & Luchini, 2007; Sipp *et al.*, 2010; Luchini & Bottaro, 2014). Adjoint methods for eigenvalue sensitivity were introduced in thermoacoustics by Magri & Juniper (2013*b*) on a Rijke tube

system, and extended to the analysis of enclosed diffusion flames with a Fourier-Galerkin based acoustics by Magri & Juniper (2014). Here we extend the use of adjoint-based sensitivity methods to wave-based acoustic networks with premixed flame models. This is indispensable information for gradient-based optimization algorithms, in which one changes the flame or cavity shape to minimize the growth rate of a particular mode.

To perform a sensitivity analysis, we need to define the adjoint operator of the direct equations (2.37). We can either derive the continuous adjoint equations from the continuous governing equations, or we can obtain a discrete version of the adjoint equations directly from the discretized version of the direct equations (Chandler *et al.*, 2012; Magri & Juniper, 2013*b*). Here we will use the second approach, i.e., we will define the adjoint matrix $M^\dagger$ to be $M^\dagger = M^H$, where the superscript ^{H} stands for Hermitian conjugation. Under this assumption, the drift in the eigenvalue is given by the known relation (Sipp *et al.*, 2010; Luchini & Bottaro, 2014):

$$\delta\lambda_i = \frac{\left\langle \boldsymbol{z}_i^\dagger, \delta M \boldsymbol{z}_i \right\rangle}{\left\langle \boldsymbol{z}_i^\dagger, \boldsymbol{z}_i \right\rangle}, \tag{2.44}$$

where $\boldsymbol{z}_i$ is a right eigenvector of the direct matrix, $M\boldsymbol{z}_i = \lambda_i \boldsymbol{z}_i$, and $\boldsymbol{z}_i^\dagger$ is the corresponding right eigenvector of the adjoint matrix, $M^H \boldsymbol{z}_i^\dagger = \lambda_i^* \boldsymbol{z}_i^\dagger$, where the superscript * stands for complex conjugation. The symbol $\langle \cdot, \cdot \rangle$ denotes an inner product. To define the adjoint discrete operator as the transpose conjugate of the direct discrete operator, is equivalent to choosing the scalar product as an inner product, i.e.:

$$\langle \boldsymbol{z}_1, \boldsymbol{z}_2 \rangle = \boldsymbol{z}_1^H \cdot \boldsymbol{z}_2 = \sum_{i=1}^{N_r+N_s+N_x} z_1^{i^*} z_2^i. \tag{2.45}$$

Note that here we are only interested in evaluating sensitivities of the eigenvalues. The drift in the eigenvalue is a well-defined physical quantity, and can be proven to be independent of the choice of the inner product (Luchini & Bottaro, 2014). This choice allows a very simple connection between the adjoint right eigenvectors $\boldsymbol{z}^\dagger$ and the left eigenvectors $\boldsymbol{z}_L$ of the direct matrix M. In particular we have that $\boldsymbol{z}^\dagger = \boldsymbol{z}_L^H$, meaning that, by computing both the right and left eigenvectors of M, we have all the information required to evaluate sensitivities. Finally, recall that M is the discrete operator of the governing equations linearised around a steady solution. Indicating the base state with $\bar{\boldsymbol{z}}$, the eigenvalue drift with respect to parameter p is:

$$\delta\lambda = \frac{\boldsymbol{z}_L \cdot \delta M(\bar{\boldsymbol{z}}, p)\boldsymbol{z}}{\boldsymbol{z}_L \cdot \boldsymbol{z}} = \left(\frac{\boldsymbol{z}_L \cdot \frac{\partial M}{\partial p}\boldsymbol{z}}{\boldsymbol{z}_L \cdot \boldsymbol{z}} + \frac{\boldsymbol{z}_L \cdot \frac{\partial M}{\partial \bar{\boldsymbol{z}}}\frac{\partial \bar{\boldsymbol{z}}}{\partial p}\boldsymbol{z}}{\boldsymbol{z}_L \cdot \boldsymbol{z}} \right) \delta p, \tag{2.46}$$

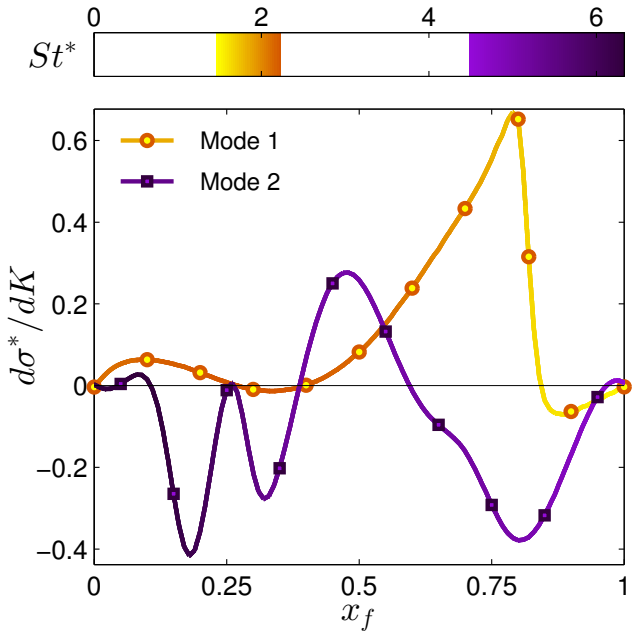

Fig. 2.14 Growth rate sensitivity at $\beta = 6$ of the two modes with the largest growth rate to convection speed perturbations. Lines correspond to sensitivity calculations with adjoint methods; the line's colour refers to the frequency of the unperturbed modes. Markers refer to sensitivity calculations with a finite difference approach, and validate the adjoint calculations.

where we have used the chain rule to account for the fact that the steady-state solution is in general a function of the parameter p as well. The quantity $\frac{\partial \bar{\mathbf{z}}}{\partial p}$ cannot be easily evaluated in general, and another adjoint problem can be set up to calculate it. The left and right eigenvectors of M have already been evaluated when solving the eigenproblem (2.37). Therefore, with simple matrix multiplication operations, we can compute the sensitivity of the system with respect to *any* parameter.

Here, we will focus on the role of the convection speed, K, on the stability of the system. This parameter does not affect the steady solution so the sensitivity is simply given by the first term in the r.h.s. of equation (2.46). The convection speed is of crucial importance in modelling premixed flames and it has been investigated by Preetham *et al.* (2008); Kashinath *et al.* (2013*b*). In Orchini & Juniper (2015) it is shown that it severely affects the gain response of non-conical Flame Describing Functions. The matrix $\frac{\partial M}{\partial K}$ can be evaluated explicitly from equations (B.5), and only the derivatives of the blocks (B.5h) and (B.5i) are non-zero.

It is known that the adjoint eigenvectors of the finite-difference discretized equations can be noisy close to non-Dirichlet boundary conditions (Hartmann, 2007; Chandler *et al.*, 2012). This is because the discrete forms of the boundary conditions have been chosen to

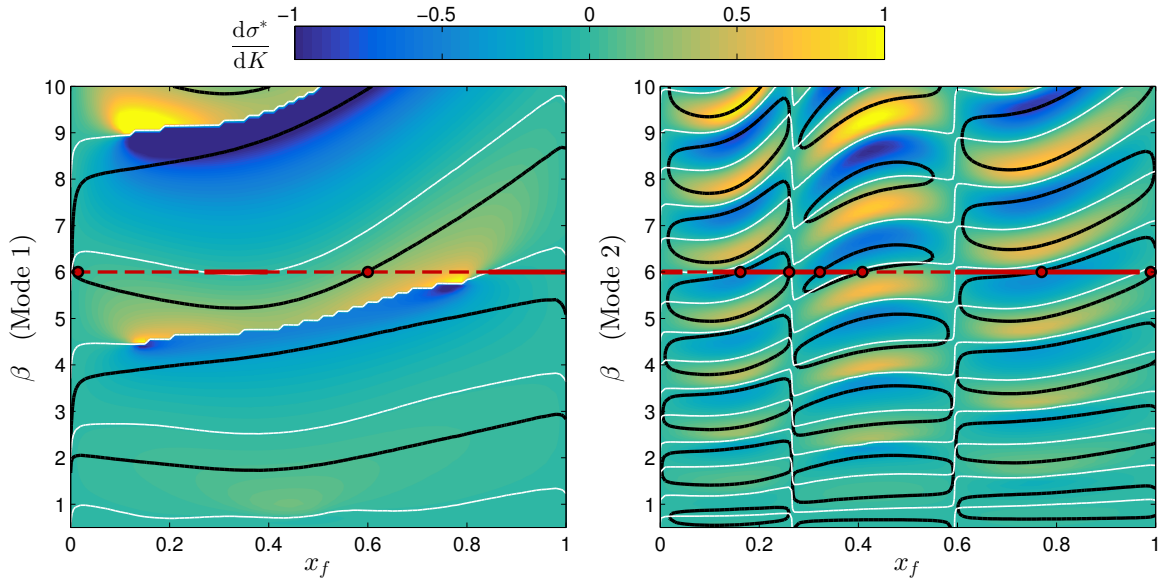

Fig. 2.15 Growth rate sensitivity to convection speed variations in the parameter space $x_f \times \beta$. Thick black lines are the neutral lines of the growth rate map. Thin light lines are the zero contours of the sensitivity maps, i.e., where the system is insensitive to small changes in the parameter K. The red lines highlight results shown in Figure 2.14: solid and dashed red lines have a negative and positive sensitivity, respectively.

work well with the right eigenvectors, but there is no guarantee that they will work with the same accuracy on the left ones. Indeed, we observe some noise in the left eigenvectors of M close to the Neumann boundary condition relative to the flame tip, so we first validate the adjoint-based sensitivity results with a brute-force finite difference method.

Using the same parameters as in §2.7.2, and fixing $\beta = 6$, we show in Figure 2.14 the growth rate sensitivity to variations in the convection speed evaluated with adjoint-based (solid lines) and finite-difference (markers) methods for thermoacoustic modes 1 and 2. Although we observe some noise in the adjoint eigenvectors close to the flame Neumann boundary condition (not shown), the results obtained with the two methods agree perfectly. From now on we will always refer to the adjoint-based sensitivity results. At a given x_f location in Figure 2.14, if the sensitivity of a mode is positive, then a small decrease of the parameter K will make the growth rate smaller and vice versa. Note that a change in K could make one mode grow and another mode decay. This is typically a disadvantageous result, because a change that tends to stabilise one mode may destabilise another one. Also, at this stage, no clear pattern can be observed for the behaviour of the two modes.

To gain more insight into the physical mechanisms that trigger the instabilities, we extend the growth rate sensitivity analysis to the parameter space $x_f \times \beta$ as in §2.7.2. Figure 2.15 shows the sensitivity of the growth rate for mode 1 (top panel) and mode 2 (bottom panel).

Thick black lines correspond to the zero growth rate level sets of Figure 2.12, and thin light lines to the zero contour lines of the sensitivity maps, i.e., the lines along which the system is insensitive to small changes in the convection speed. Every horizontal slice of Figure 2.15 produces a graph analogous to Figure 2.14, which corresponds to the horizontal lines highlighted in red at $\beta = 6$. Note that the sensitivity of mode 1 is actually discontinuous across the lines where one eigenvalue takes over from another, the dashed lines of Figure 2.12. This is because, as discussed in §2.7.2, the dominant eigenvalue switches along these lines.

Note how in mode 2's sensitivity map, the zero growth-rate isolines cross the zero sensitivity isolines at the acoustic nodes $x_f \approx 1/3$ and $2/3$. This is because the location of the nodes is a purely acoustic property, and it is unaffected by a change in the convection speed, which only alters the flow and flame dynamics. Also, note how all the zero sensitivity isolines cross the zero growth rate isolines always in the same fashion in both mode's maps: the lower parts of the neutral curves always lie in regions with a positive sensitivity (light colours), and the upper parts in regions with a negative sensitivity (dark colours). As a consequence, increasing the convection parameter K, shifts the edges of the instability towards a smaller β value, i.e., towards shorter flames. This has a very simple physical explanation: according to the Rayleigh criterion (2.42), a thermoacoustic oscillation can occur only when unsteady heat release and acoustic pressure fluctuations are sufficiently in phase. Changing the parameter K does not affect the acoustics, but it does change the phase of heat release fluctuations. In particular, we can relate the time delay of heat release fluctuations with the time that a perturbation needs to travel from the base to the tip, given by:

$$\tau \propto L_f \frac{1}{\overline{u}_c} = \beta R \frac{K}{\overline{u}}. \tag{2.47}$$

The onset of thermoacoustic instabilities is found at specific values of time delays τ. Thus, if we increase the convection parameter K and we wish to find where the new zero growth rate contours lies by keeping the time delay constant, then we need to reduce β, in agreement with the sensitivity analysis. This also means that the sensitivities with respect to K and β must have the same sign, because increasing K or β causes an increase in the time delay. This can be verified by qualitatively evaluating $\mathrm{d}\sigma^*/\mathrm{d}\beta$ along vertical lines in the growth rate maps of Figure 2.12.

All the results obtained with adjoint sensitivity are in line with an intuitive physical argument based on the time delay induced by the convection speed model, and can be used to understand changes in the stability of thermoacoustic system's with premixed flames. This example shows how sensitivity analysis has great potential for the design and passive

control of thermoacoustic systems, one of its main advantages being that the process can be embedded within a gradient-based optimization algorithm.

2.8 Conclusions

In this chapter we have outlined the wave-based acoustic network modelling adopted in this thesis. A methodology to cast the acoustic response in state-space has been presented. We have evaluated Flame Transfer Functions (FTF) for laminar, conical flames excited by an incompressible, travelling wave flow model. We obtain analytical results for the case of uniform flame speeds (which contains a correction to a previously published result), and numerical results when we account for curvature's corrections on the flame speed. We show how in the latter case the numerical evaluation can become unnecessarily expensive even for low-order models. Therefore we tackle the thermoacoustic problem from a different perspective, by avoiding the explicit evaluation of FTFs and directly evaluating the stability of the fully-coupled thermoacoustic system. In this way the stability problem is cast in a classic eigenvalue problem and one can efficiently solve only for the eigenvalues of interest, typically the ones with the largest growth rates. With minimal computational resources we can calculate the stability of the system over a wide range of parameters, and we identify and discuss the location of stability lines (Hopf bifurcations) in the parameter space. Finally, we show how adjoint sensitivity methods can be applied to this model without any further expensive calculation. Sensitivity results help to extract even more information out of the eigenvalue problem. We explicitly evaluate the sensitivity with respect to the convection speed parameter, but any other parameter of the system could be chosen. We observe that the system's stability is strongly connected to the time delay $L_f/\overline{u}_c$ induced by the convective model, as expected. Future analysis can extend them to systems with premixed flames using more elaborated models for the flame and heat release dynamics and to the more sophisticated question of optimizing a burner shape.

Chapter 3

Frequency domain and time domain nonlinear analysis of thermoacoustic oscillations with wave-based acoustics

In this chapter a thorough nonlinear analysis of the thermoacoustic system described in §2.7 is performed. Current state-of-the art methods in the frequency and time domain are used to predict the nonlinear behaviour of this system. The aim is to compare the strengths and weaknesses of the various methods, together with their cost. This information will be used in the next chapters of the thesis as a guidance to develop novel techniques that fill the deficiencies of the current methods, or reduce their cost.

The content of this chapter was published in Orchini *et al.* (2015).

3.1 Introduction

The calculation of thermoacoustic oscillations' amplitude in systems with confined premixed flames involves the interaction of linear acoustics and nonlinear combustion. In order to model these oscillations in a numerically tractable way, it is usually necessary to use a low-order model for the flame. This reduced order model allows the system's stability to be investigated either in the frequency or time domains, and gives insight into the underlying mechanisms without resorting to full CFD (Dowling, 1997, 1999; Culick, 2006; Noiray *et al.*, 2008; Lieuwen, 2012).

A widely-used frequency domain approach is to measure or calculate the Flame Describing Function (FDF), which approximates the nonlinear unsteady heat release response to finite amplitude harmonic velocity or equivalence ratio fluctuations. In the linear limit,

the FDF reduces to the Flame Transfer Function (FTF), for which analytical expressions can be derived for some flames (Schuller *et al.*, 2003; Preetham *et al.*, 2008; Shreekrishna *et al.*, 2010). In a nonlinear framework, the FDF can be coupled with a model for the acoustics, and can predict the stability of a thermoacoustic system, as well as the frequency and amplitude of steady-state harmonic oscillations (Dowling, 1997; Noiray *et al.*, 2008). However, it is restrictive to assume that the velocity fluctuations are harmonic. This precludes non-harmonic periodic oscillations, as well as more complex dynamical behaviour such as period-2, quasiperiodic, and chaotic oscillations, which are common in thermoacoustics (Subramanian *et al.*, 2010; Gotoda *et al.*, 2011; Kabiraj & Sujith, 2012; Kabiraj *et al.*, 2012*a*; Gotoda *et al.*, 2014).

On the other hand, time domain simulations do not make any *a priori* assumptions about the form of the acoustic fluctuations. These have been used successfully by Kashinath *et al.* (2014) and Waugh *et al.* (2014) to simulate the nonlinear behaviour of thermoacoustic systems by time integration and numerical continuation of limit cycles. These simulations qualitatively reproduce the elaborate dynamical behaviour found experimentally. However, so far only a simplistic acoustic configuration has been considered in such studies: a duct with uniform cross-sectional area and no temperature variation across the flame. In this analysis we present a general method to evaluate the acoustic response of an axisymmetric resonator containing, for example, area changes and temperature variations, and how to couple it with a kinematic flame model based on the G-equation both in the frequency and time domains. This allows the methods of Kashinath *et al.* (2014) and Waugh *et al.* (2014) to be generalised to practical thermoacoustic systems.

The chapter is structured as follows: in §3.2 we present the fully nonlinear combustion and flow models. Details on the methods used to numerically integrate it and on the acoustic model have already been presented in the thesis. In §3.3 the acoustic model improvements with respect to previous analogous analyses are outlined. In §3.4 a numerically evaluated FDF is shown, and we perform a nonlinear stability analysis of our thermoacoustic system by means of the harmonic balance technique. The same thermoacoustic configuration is investigated in §3.5.1 in the time domain with two different techniques. In §3.6 bifurcation diagrams are shown, and we discuss the analogies and differences between the results predicted by the various methods. Finally, in §3.7 we discuss the nonlinear dynamical behaviour that we have observed, and we compare it with other analogous studies.

3.2 Nonlinear flame modelling

In this section we describe the nonlinear model for the flame dynamics and unsteady heat release fluctuations. It is based on the well-known G-equation model (Markstein, 1964; Williams, 1985), accounting for curvature effects on the flame speed. We also introduce the flow field model, which is based on previous studies (Birbaud *et al.*, 2006; Kashinath *et al.*, 2013*b*).

The G-equation model provides a low-cost method that enables premixed flame dynamics and heat release to be described qualitatively. In contrast to Chapter 2, here we consider the fully nonlinear dynamics of the flame front (the $G = 0$ level set), which is governed by the transport equation:

$$\frac{\partial G}{\partial t} + \boldsymbol{u} \cdot \nabla G = s_L |\nabla G| \,. \tag{3.1}$$

The local flame speed s_L is in general a function of the equivalence ratio ϕ, the type of fuel, the flame curvature, and, for turbulent flames, the turbulent intensity. In this analysis, we consider conical, laminar, fully premixed flames. Therefore, the equivalence ratio is constant and uniform, and the flame speed depends only on local curvature effects (Markstein, 1964; Creta & Matalon, 2011):

$$s_L = s_L^0 (1 - \mathcal{L}\kappa) \,. \tag{3.2}$$

Here s_L^0 is the speed of a laminar, flat flame sheet, $\kappa \equiv \nabla \cdot \hat{\boldsymbol{n}}$ is the local flame curvature, and $\mathcal{L}$ is the Markstein length.

We consider the same axisymmetric thermoacoustic configuration as described in §2.7, using a cylindrical coordinate system $(\hat{r}, \hat{\theta}, \hat{x})$. The velocity field $\boldsymbol{u} = (u_r, u_\theta = 0, u_x)$ is decomposed into mean ($\overline{\boldsymbol{u}}$) and fluctuating ($\boldsymbol{u}'$) components. The mean flow is assumed to be uniform and flow in the axial direction $\hat{x}$. For the perturbation (Birbaud *et al.*, 2006), the axial velocity (forced or self-excited) is imposed at the burner (x_b) every instant and advected downstream, and the radial velocity is found by continuity:

$$\begin{aligned} &\frac{\partial u'}{\partial t} + U_c \frac{\partial u'}{\partial x} = 0 \qquad u'(x = x_b) = u'_{ac}(t), \\ &\frac{1}{r}\frac{\partial (r u'_r)}{\partial r} + \frac{\partial u'}{\partial x} = 0 \qquad u'_r(r = 0) = 0. \end{aligned} \tag{3.3}$$

DNS calculations show that these perturbations advect axially at a frequency-dependent speed that is slower than the mean flow (Kashinath *et al.*, 2013*b*). We do not know the acoustic frequencies *a priori*, so we fix this speed at $U_c = 0.833\overline{u}_x$, which is the largest value observed by Kashinath *et al.* (2013*b*).

Substituting the flow field and flame speed expression (3.2) into (3.1), and introducing the non-dimensional parameters

$$\frac{x}{L_f} \to x \qquad \frac{r}{R} \to r \qquad \frac{u_x}{\overline{u}_x} \to u_x \qquad \frac{u_r}{\overline{u}_x} \to u_r \qquad \frac{t\,\overline{u}_x}{L_f} \to t, \tag{3.4}$$

we obtain

$$\frac{\partial G}{\partial t} + \beta u_r' \frac{\partial G}{\partial r} + \left(1 + u_x'\right) \frac{\partial G}{\partial x} = \frac{s_L^0}{\overline{u}_x} \left(1 - \mathcal{M}\kappa\right) \sqrt{\left(\beta \frac{\partial G}{\partial r}\right)^2 + \left(\frac{\partial G}{\partial x}\right)^2}, \tag{3.5}$$

where L_f is the flame height, R is the burner radius, $\beta \equiv L_f/R$ is the flame aspect ratio, and $\mathcal{M}$ is the ratio between the Markstein length and the flame height.

The nonlinear PDE (3.5) summarises the nonlinear combustion model adopted. It is integrated numerically using LSGEN, as discussed in §1.3.

3.3 Effect of the temperature jump on the acoustic response

The acoustic network and the corresponding state-space model chosen for the analysis in this chapter are the same as those described in §2.7. Because our wave-based acoustic approach includes a mean flow, a temperature jump, and frequency dependent reflection coefficients, it significantly improves previous low-order time domain modelling of analogous thermoacoustic networks, as discussed below. Furthermore, the state-space formulation allows us to perform calculations both in the frequency and time domain, with no approximations between the two domains from an acoustic point of view. Therefore, differences in the nonlinear results obtained with the various methods that will be applied can only be due to approximations introduced in the nonlinear flame response.

Previous studies in the time domain (Kashinath *et al.*, 2014; Waugh *et al.*, 2014) have examined straight pipes with uniform acoustic mean properties and zero mean flow. The low-order thermoacoustic framework proposed here, however, includes a mean flow, temperature and cross-sectional area variations, and can therefore analyse more general configurations.

Varying the flame position in the acoustic network, we evaluate transfer functions $H_{x_f}(s)$ and fit them to state-space models as described in §2.2.2. When the reflection coefficients are equal to ± 1, the acoustic response (evaluated at, say, the flame position) can be thought of as a Galerkin discretization onto a basis set formed by the orthogonal acoustic eigenmodes ψ_k^{ac}:

$$u'(x_f,t) \approx \sum_{k=1}^{N} \hat{u}_k'(t)\, \psi_k^{ac}(x_f). \tag{3.6}$$

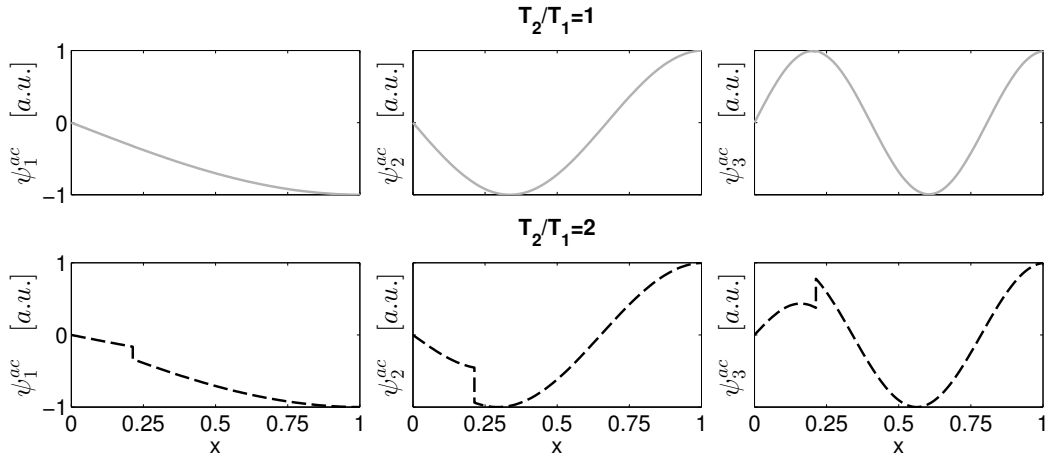

Fig. 3.1 Acoustic velocity modeshapes evaluated with a Fourier-Galerkin basis (top panels), analogous to the limit $T_2/T_1 \to 1$, and wave-based acoustics (bottom panels), with $T_2/T_1 = 2$. In the former case the modes are continuous and correspond to the natural acoustic eigenmodes of the open-closed pipe, in the latter a discontinuity is located at the flame position because of a sudden change in the mean flow temperature.

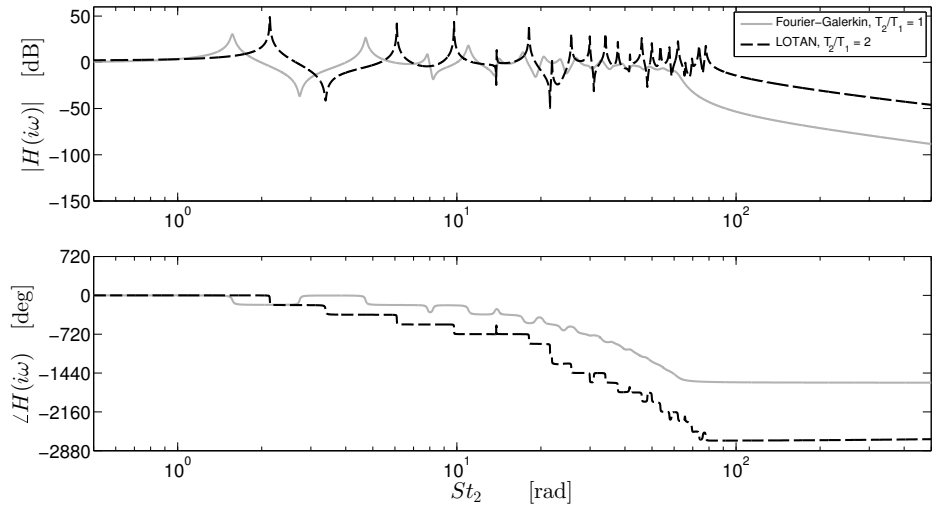

Fig. 3.2 Transfer functions of velocity fluctuations with respect to heat release fluctuations for a straight open-closed duct with a flame positioned at $x_f = 0.213$. Fourier-Galerkin (solid line) state-space, as in Kashinath *et al.* (2013*b*): pole's locations are equispaced and remain at the natural frequencies of the open-closed pipe. LOTAN (dot-dashed line) state-space, with $T_2/T_1 = 2$: the position of the poles is shifted because the mean acoustic properties vary with T_2/T_1, and they are no longer equispaced.

Indeed, one can choose the state-space vector $\boldsymbol{C} = \left[\psi_1^{ac}(x_f), \ldots, \psi_N^{ac}(x_f)\right]$ in equation (2.10b). Note that this analogy is not true in general, because the acoustic eigenvectors are non-orthogonal for non-trivial reflection coefficients (Nicoud *et al.*, 2007). Figure 3.1 shows a comparison between the first three eigenmodes of an open-closed pipe with $R_1 = 1.0$ and $R_2 = -1$ with and without a temperature jump. In the latter case, the Galerkin basis functions correspond to a Fourier expansion, i.e., $\psi_k^{ac} = e^{\mathrm{i}kx}$, which we find in the limit $T_2/T_1 \to 1$. In both cases, the thermoacoustic modes contain a discontinuity at the flame location, which is typically modelled with a Dirac delta in systems with no mean temperature effects, as was seen for example in Magri & Juniper (2013*b*); Waugh *et al.* (2014). In networks with a temperature jump across the flame, a discontinuity is naturally present in all the acoustic basis functions when a wave-based approach is adopted, which relaxes the Gibbs phenomenon.

Furthermore, thermoacoustic oscillation frequencies are often found to be close to the acoustic natural frequencies (Dowling & Stow, 2003; Noiray *et al.*, 2008). This will be the case in our configuration, as we discuss in the next section. These acoustic eigenfrequencies change significantly when the mean temperature is non-uniform, as is shown in Figure 3.2, and are no longer multiples of the fundamental frequency (see equation (2.7)). This reduces coupling between the modes, which will be discussed later.

3.4 Nonlinear analysis in the frequency domain

In this section we analyse thermoacoustic oscillations in the frequency domain. This is accomplished by numerically evaluating a Flame Describing Function (FDF) to inlet harmonic velocity fluctuations. The FDF is coupled in a feedback loop with acoustic transfer functions.

3.4.1 Flame Describing Function

In most thermoacoustic systems, the flame is the main source of nonlinearity (Chu, 1963; Culick, 1971). The FDF method exploits this characteristic; it approximates the flame's nonlinear response to an imposed input signal. We denote with $\mathrm{FDF}(\mathrm{St}, A)$ the FDF of a sinusoidal-input with angular frequency $2\pi\mathrm{St}$ and amplitude A. When we close the FDF in a feedback loop with an acoustic transfer function $H(\mathrm{St})$, we can predict the frequency, amplitude, and stability of limit cycles via the harmonic balance (or Describing Function method) (Khalil, 2001).

We numerically construct an FDF by harmonically forcing the axial flow at the flame inlet at various frequencies $f = \omega/(2\pi)$ and amplitudes. Solving continuity and advection

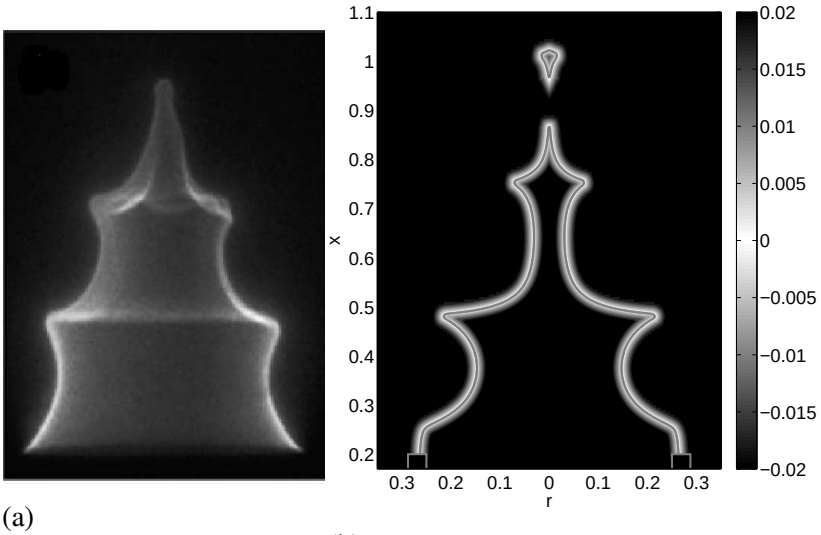

(a) (b)

Fig. 3.3 Flame wrinkling due to vortex formation and roll up. (a) Experimental forced conical flame image, reprinted from Karimi *et al.* (2009), with permission from Elsevier. (b) G-field obtained from a numerical simulation of a forced conical flame. In both cases, the forcing is harmonic, with a frequency $\mathrm{St} = 20/(2\pi)$ and an amplitude $A = 0.3$. The flame contour $G = 0$ is highlighted and it qualitatively reproduces experimental results.

equations, the perturbation flow reads

$$u' = A\cos\left[2\pi\mathrm{St}\left(Kx - t\right)\right] \qquad u'_r = A\frac{K}{\beta}\frac{r}{2}2\pi\mathrm{St}\sin\left[2\pi\mathrm{St}\left(Kx - t\right)\right], \tag{3.7}$$

where $\mathrm{St} \equiv fL_f/\overline{u}$ is the flame Strouhal number, and $K = 1.2$ is the ratio between the axial mean flow speed and the convection speed, as in Kashinath *et al.* (2013*b*). This perturbation model has been proven to reproduce the characteristic vortex formation at the burner lip and roll up along the flame. It causes flame wrinkling, which strongly influences flame surface area and consequent heat release fluctuations (Preetham *et al.*, 2008). A qualitative comparison with experimental results is shown in Figure 3.3.

The heat released by the flame is evaluated through:

$$Q(A,t) \equiv 2\pi\rho s_L^0 h_R \int\!\!\int_{\mathcal{D}} \left(1 - \mathcal{L}\kappa\right)|\nabla G|\,\delta(G)\,r\,\mathrm{d}r\,\mathrm{d}x. \tag{3.8}$$

Heat release fluctuations $q'(A,t) = Q(A,t) - \overline{Q}$ are decomposed into Fourier modes

$$q'(A,t) = \sum_{k=1}^{\infty} q'_k(A)\cos(2\pi k\mathrm{St}t + \varphi_k(A)). \tag{3.9}$$

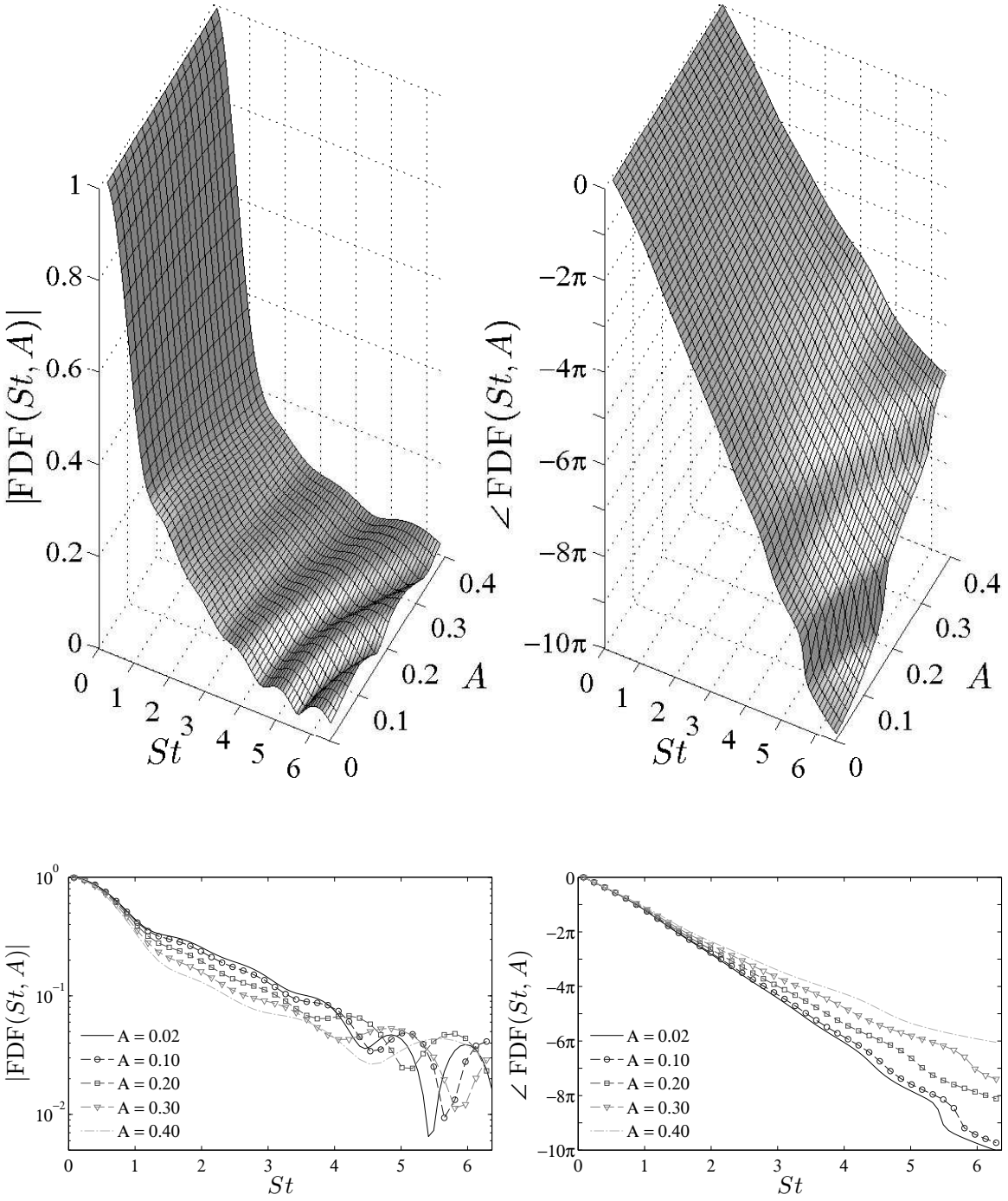

Fig. 3.4 FDF gain (left) and phase (right) of the heat release rate of a laminar, conical flame to velocity fluctuations. The flame aspect ratio is $\beta = 6$ and curvature effects on the flame speed are accounted for, with a non-dimensional Markstein length $\mathcal{M} = 0.02$. The top and bottom panels show the same data.

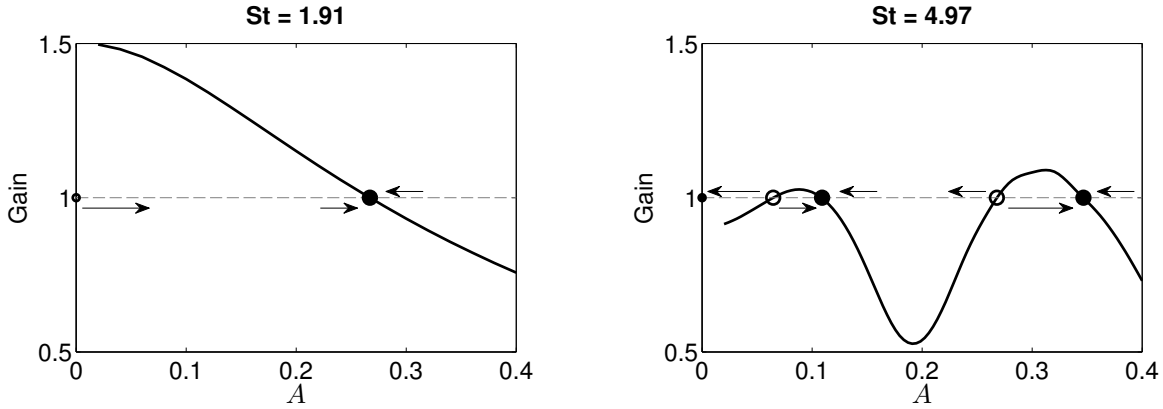

Fig. 3.5 Amplitude dependence of the closed-loop Describing Function gain $|N_{0.5}(\mathrm{St},A)|$ for two St values. Left panel: at small frequencies, a monotonical decay of the gain suggests that the system can be either linearly stable (if the gain at $A=0$ is less than one) or supercritically unstable and saturate to a limit cycle. Right panel: at higher frequencies, the gain does not monotonically decay and subcritical instabilities may exist, as well as multistability. Filled and empty circles indicate hypothetical stable and unstable limit cycles (fixed points at zero amplitude) respectively. For these limit cycles to be solutions, a phase condition has to be met, which is not considered here.

Since we are looking for harmonic cycles, we consider only the first harmonic contribution in the Fourier transform of heat release fluctuations:

$$\hat{q}'(\mathrm{St},A) \approx q_1'(A)e^{\mathrm{i}\varphi_1(St,A)}. \tag{3.10}$$

The FDF is defined by

$$\mathrm{FDF}(\mathrm{St},A) \equiv \frac{\hat{q}'(\mathrm{St},A)/\overline{Q}}{\hat{u}'(A)/\overline{u}}, \tag{3.11}$$

and is shown in Figure 3.4. It contains the features that are characteristic of describing functions of conical flames: unitary gain and a linear behaviour at small frequencies, the presence of amplitude-dependent zeros due to destructive wave interference, and a general monotonic decrease of the phase, typical of time delayed systems. They are described in detail in experimental and numerical studies (Schuller *et al.*, 2003; Karimi *et al.*, 2009).

3.4.2 Harmonic balance

We can now study the stability of the thermoacoustic system. The FDF is closed in a positive feedback loop with the acoustics, as shown in Figure 1.2. Figure 3.5 shows the amplitude dependence of the gain of the closed-loop system $N_{x_f}(\mathrm{St},A) \equiv \mathrm{FDF}(\mathrm{St},A)H_{x_f}(\mathrm{St})$ at two frequencies. It gives insight into the possible types of bifurcations of the thermoacoustic

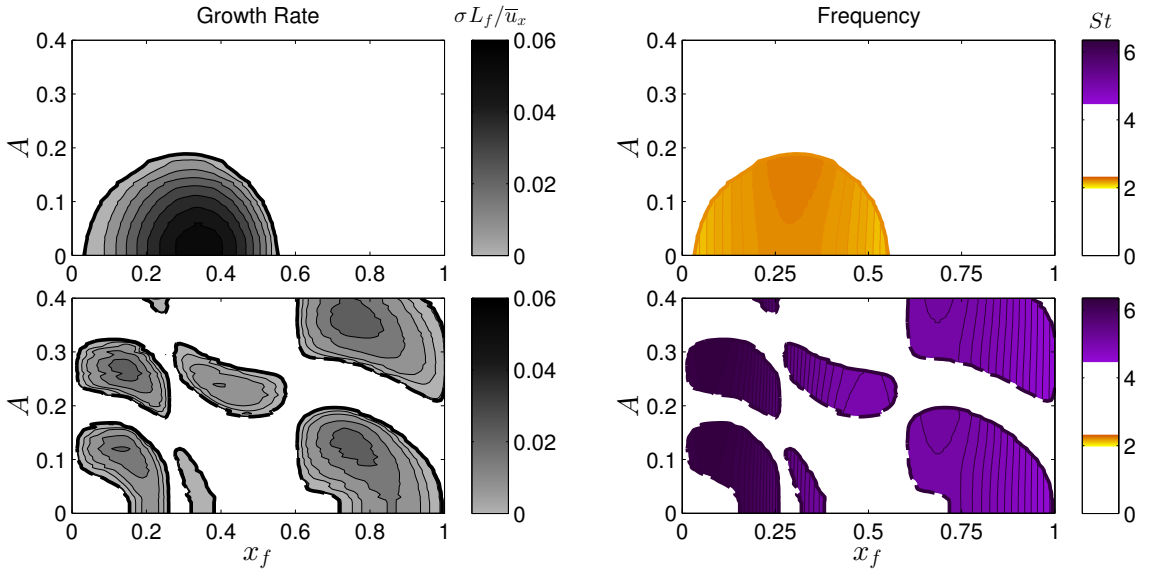

(a) (b)

Fig. 3.6 Harmonic balance stability analysis of the first (top) and second (bottom) thermoacoustic modes. (a) Positive growth rates of the modes as a function of the velocity fluctuations amplitudes. Moving from low to high amplitudes, if the growth rate passes from positive (negative) to negative (positive), a stable (unstable) limit cycle is found. (b) Frequency maps of regions with positive growth rates.

system. In particular, we can predict that supercritical bifurcations are expected at low oscillation frequencies, whereas a subcritical response can be found at higher frequencies.

However, the condition described in Figure 3.5 is only a necessary condition for the existence of limit cycles. In order to correctly predict limit cycles amplitudes and frequencies, we have to consider the closed-loop plant phase dependence as well. On saturated limit cycles the growth rate σ of thermoacoustic modes is zero, and harmonic oscillations are found for the pairs (A, St) that satisfy the dispersion relation (harmonic balance):

$$N_{x_f}(\mathrm{St}, A) \equiv \mathrm{FDF}(\mathrm{St}, A) H_{x_f}(\mathrm{St}) = 1. \tag{3.12}$$

We determine the stability of limit cycles by looking at the change in sign of the growth rate around the saturated amplitudes (Schmid *et al.*, 2013). Growth rate and frequency maps away from limit cycles are determined by fitting the FDF to a state-space model for each amplitude section, and replacing St with the Laplace variable s in the dispersion relation (3.12) (Schmid *et al.*, 2013).

We investigate the stability of modes with a maximum frequency $St_{max} = 40/(2\pi) \approx 6.37$, which is the maximum frequency at which we forced the system when evaluating the FDF.

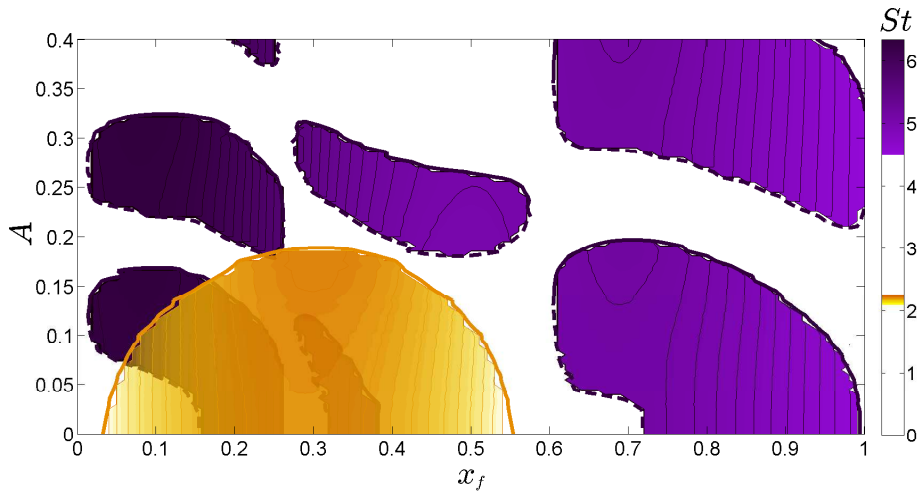

Fig. 3.7 Harmonic balance bifurcation diagram. The amplitudes and frequencies of the thermoacoustic modes with non-negative growth rate are shown while varying the position of the flame in the duct. Super- and subcritical bifurcations of two thermoacoustic modes are observed. Stable and unstable limit cycles are indicated with solid and dashed lines, respectively. In some regions, both modes have a positive growth rates.

Note that, according to the harmonic balance condition (3.12), an oscillation can arise only if the product between the FDF and the acoustic transfer function's gain exceeds unity. The gain of the laminar, conical FDF shown in Figure 3.4 does not exceed unity, so oscillation frequencies for this flame are always expected to be close to an acoustic eigenfrequency; this is verified in §3.6, Figure 3.10. Therefore, we label thermoacoustic modes by the acoustic mode with the closest frequency.

Two thermoacoustic modes can have a positive growth rate in the range of parameters considered. The first mode (Figure 3.6, top panels) has a positive growth rate in the region $0.04 \leq x_f \leq 0.56$. Within this region, fixed point solutions are unstable and small perturbations cause oscillations with a frequency $St \in (2.1, 2.3)$ to grow in amplitude, until they saturate on stable limit cycles indicated with solid lines. Two supercritical Hopf bifurcations are located at the edges of this region. The second mode (Figure 3.6, bottom panels) exhibits several super- and subcritical Hopf bifurcations, fold points, and multistable regions. Stable and unstable limit cycles are identified, and oscillate at a frequency in the range $St \in (4.5, 6.3)$. In some cases, the saturation amplitude of the oscillations exceeds the maximum forcing amplitude we have considered when obtaining the FDF, and cannot be predicted from our data.

Figure 3.7 superposes the frequency maps of the positive growth rate regions of the two modes. In some regions, both thermoacoustic modes have positive growth rates. This raises questions about the physical interpretation of results obtained with the harmonic balance

analysis. The main assumption, that the limit cycles are harmonic, becomes particularly weak if more than one mode is linearly unstable. If both modes grow, how does the flame behave? If the two modes have incommensurate frequencies, is the final attractor of the thermoacoustic system a limit cycle? If the oscillations are non-harmonic, how different is their amplitude compared with those predicted with the FDF? These questions cannot be tackled in a single-mode frequency domain framework, and different approaches need to be used.

3.5 Nonlinear dynamics in the time domain

The general behaviour of thermoacoustic oscillations is not limited to harmonic limit cycles. Several experimental and numerical studies report that small variations in a single parameter in the thermoacoustic state – equivalence ratio, position of the flame in a duct, intensity of the mean flow – lead to profound changes in the oscillations dynamics, which can exhibit for example quasiperiodic and chaotic behaviour (Gotoda *et al.*, 2011; Kabiraj & Sujith, 2012; Kashinath *et al.*, 2014). In this section we use two different time domain techniques to analyse the thermoacoustic system that was investigated with the harmonic balance technique in the previous section. We interpret the results with nonlinear time series analysis and Floquet theory.

3.5.1 Time-marching

Analysis in the time domain does not require the restrictive assumptions required for analysis in the frequency domain, particularly that the acoustic oscillations are harmonic. We couple the acoustic state-space models with the G-equation dynamics (3.5) and we time integrate the thermoacoustic system. The acoustics induce axial velocity perturbations at the base of the flame. Continuity and advection equations are integrated numerically in the flame domain. The G-field is updated. The unsteady heat release is evaluated through equation (3.8). This acts as a source in the acoustic equations, closing the loop. The analysis is performed by integrating the thermoacoustic dynamics from fixed points for 350 non-dimensional time units in the range $0 \leq x_f \leq 1$, with steps of $\Delta x_f = 0.01$, and a higher resolution in regions of interest. For $0.65 \leq x_f \leq 0.78$ we have also integrated the thermoacoustic response starting from a highly perturbed initial condition, in order to analyse the subcritical response of the system. The time series of acoustic velocity fluctuations at the flame position are stored and used for post-processing analysis. The resulting bifurcation diagram (Figure 3.11) is shown in §3.6.

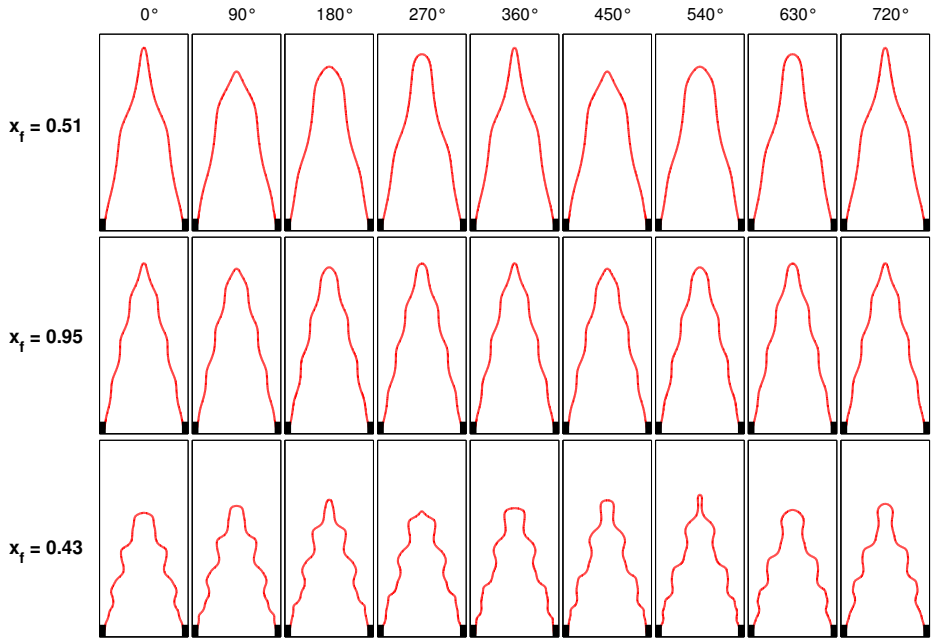

Fig. 3.8 Instantaneous self-excited flame images at different flame locations over two cycles of the PSD dominant frequency. At $x_f = 0.51$ the system exhibits periodic, non-harmonic oscillations, with a dominant frequency associated with the first thermoacoustic mode. At $x_f = 0.95$ the oscillations are still periodic, but they are associated with the second thermoacoustic mode, with a higher frequency; the characteristic flame perturbation wavelength varies accordingly. At $x_f = 0.43$ the system has undergone a Neimark–Sacker bifurcation: two incommensurable frequencies describe the motion, which is aperiodic and the flame shape is never exactly the same.

Figure 3.8 shows instantaneous flame shapes at different flame locations over two cycles of the dominant oscillation frequency. We observe that for some flame locations, $x_f = 0.51, 0.95$, the flame shape evolution repeats itself after one cycle; i.e., the system exhibits non-harmonic limit cycle oscillations. On the other hand, at $x_f = 0.43$ the flame shape does not repeat itself, meaning that the motion is aperiodic; at least two incommensurable frequencies are governing the dynamics, which cannot be described by a limit cycle.

Nonlinear time series analysis

To further characterise the system, we use methods from nonlinear time series analysis (Gotoda *et al.*, 2011; Kabiraj & Sujith, 2012). Figure 3.9 left panels show the time series of velocity fluctuations at the flame position for different flame locations. Moving from top to bottom, they identify limit cycle, frequency-locked, quasiperiodic, and chaotic oscillations respectively; the region $260 < t < 265$ has been enlarged to highlight the shape of the oscillations. In limit cycles the time trace exactly repeats itself after a period T. Frequency-

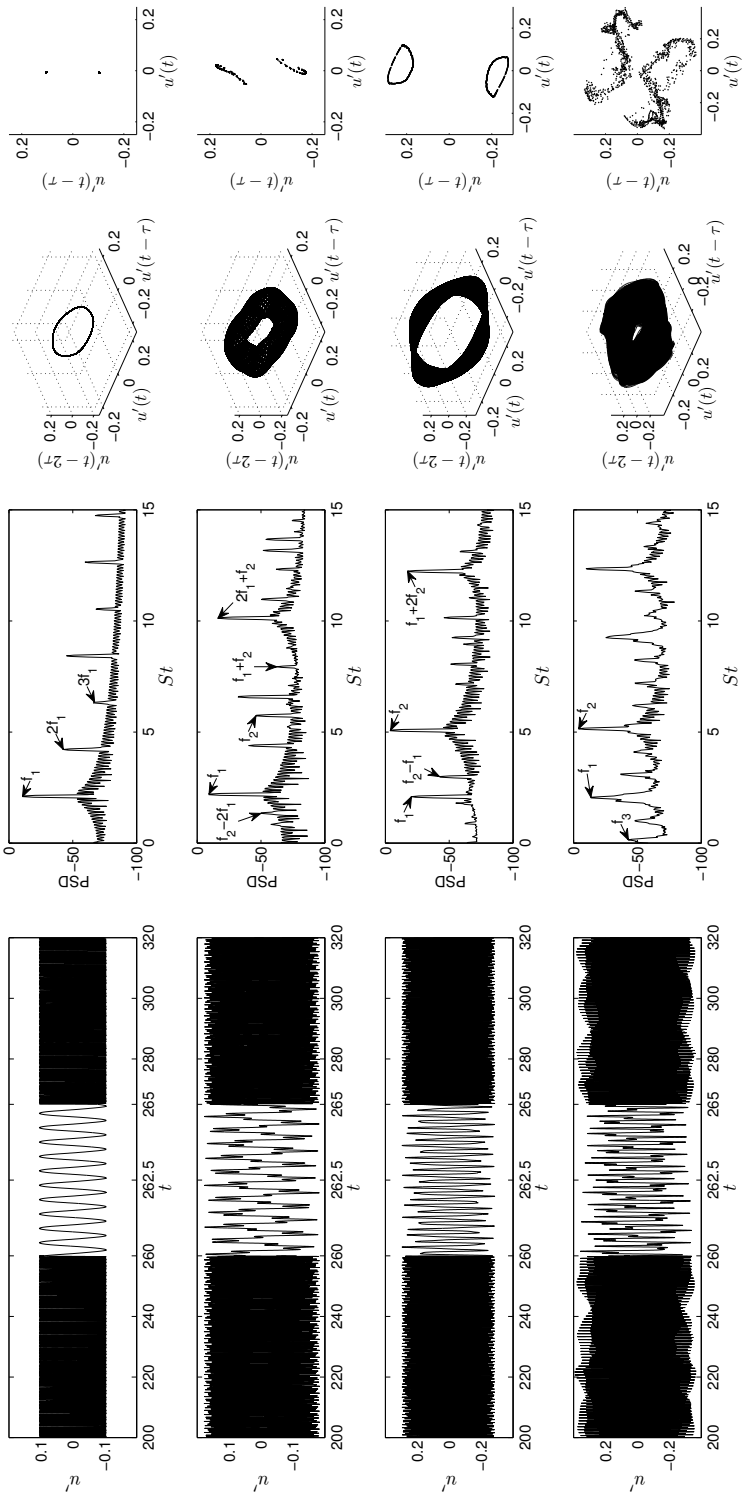

Fig. 3.9 Characterisation of the dynamical behaviour observed in our thermoacoustic model. From top to bottom: limit cycle, frequency-locked, quasiperiodic, and chaotic oscillations. From left to right, saturated time series, Power Spectral Density, phase space portraits, and Poincaré sections. For illustration purposes, the time series have been stretched between $260 \leq t \leq 265$.

locked oscillations exhibits several peaks and troughs, and the time series exactly repeats itself after a certain number of oscillations, which are characterised by two well-defined time scales. Also in the quasiperiodic time trace we can identify two time scales, but on close inspection these oscillations never repeat themselves. Finally, in chaotic solutions it becomes harder to distinguish precise time scales and the time series is certainly aperiodic.

It is difficult to distinguish between the various types of oscillations just by looking at the temporal evolution of the velocity fluctuations. We use Power Spectral Density (PSD), phase portraits, and Poincaré sections to characterise the dynamical behaviour of each thermoacoustic oscillation (Guckenheimer & Holmes, 1983; Thompson & Stewart, 2001; Kantz & Schreiber, 2004). Figure 3.9 shows the results of nonlinear time series analysis for each type of dynamics we observe. All these methods play a role in a detailed discussion of the bifurcations and the nonlinear thermoacoustic regime, which is postponed until §3.6 and §3.7.

3.5.2 Numerical continuation of limit cycles

Time-marching is the most accurate technique to study a nonlinear system. The main shortcoming of time-marching is its computational cost. The transient between an unstable thermoacoustic state and the final stable attractor can pass through several intermediate states and can take a long time (Kashinath *et al.*, 2014). Therefore, there is the need for a tool that gives more information than the FDF technique, but that has lower computational cost than time integration. Numerical continuation of limit cycles achieves this. Assuming that a periodic (but not necessarily harmonic) solution is known for a set of thermoacoustic parameters, we can vary one parameter slightly and iteratively solve a linear problem to find a thermoacoustic cycle with the new set of parameters. The use of this technique on low-order models is particularly efficient because the number of relevant degrees of freedom of a thermoacoustic state $\boldsymbol{x}$ is fairly small, $\mathcal{O}(10^3)$. Matrix-free methods can be used to decrease even further the memory and time required to solve the set of linear equations. Matrix-free method for limit cycles have been introduced to thermoacoustics by Waugh *et al.* (2013) and have been successfully used in analysing a ducted premixed flame with Fourier-Galerkin acoustics (Waugh *et al.*, 2014).

Let us indicate with $\left[\boldsymbol{x}^0(0,x_f), T^0\right]$ an initial guess for a starting state and period of a thermoacoustic cycle. We integrate the system forward in time over a cycle and compute the residual $\boldsymbol{r}^0 \equiv \boldsymbol{x}^0(0,x_f) - \boldsymbol{x}^0(T^0,x_f)$. Then we iteratively solve the linear problem $J^0\Delta\boldsymbol{x}^0 =$

$-\boldsymbol{r}^0$, with the Jacobian matrix J^0 defined by a shooting iteration

$$J^0_{ij} \equiv \frac{\partial\left(\boldsymbol{x}^0_i(0,x_f) - \boldsymbol{x}^0_i(T^0,x_f)\right)}{\partial \boldsymbol{x}^0_j(0,x_f)}, \tag{3.13}$$

to find a correction $\left[\Delta\boldsymbol{x}^0, \Delta T^0\right]$ to be added to the initial guess and obtain a new starting state

$$\left[\boldsymbol{x}^1(0,x_f), T^1\right] = \left[\boldsymbol{x}^0(0,x_f), T^0\right] + \left[\Delta\boldsymbol{x}^0(0,x_f), \Delta T^0\right], \tag{3.14}$$

which is closer to a limit cycle solution. The process is iterated until the residual falls below a threshold value, set to 5×10^{-4}.

Matrix-free methods are used to solve the linear problems $J^n\Delta\boldsymbol{x}^n = -\boldsymbol{r}^n$ (n indicates the $n+1$ shooting iteration) by means of an implementation of the Generalised Minimal Residual (GMRES) algorithm (Saad & Schultz, 1986). Solution approximations $\Delta\boldsymbol{x}^n \approx \Delta\boldsymbol{x}^n_k$ are evaluated on a k-dimensional Krylov subspace by minimising the GMRES residual

$$\beta^n_k \equiv ||-\boldsymbol{r}^n - J^n\Delta\boldsymbol{x}^n_k||. \tag{3.15}$$

The algorithm is stopped when the residual (3.15) falls below a predefined threshold, $\beta^n_k \leq 5\times10^{-2}$. One period of time-marching integration is required whenever we add a new dimension to the Krylov subspace. For our system, convergence is achieved within $k = 30$ iterations. Considering that the thermoacoustic state is formed from around 600 variables, the matrix-free method is 20 times faster than the computation of the entire Jacobian. Further information on the method can be found in Waugh *et al.* (2013).

Once two (or more) limit cycles have been found for different values of the bifurcation parameter, we can improve the initial guess of the next cycle by extrapolating the values of the variables in the thermoacoustic state, allowing for a further speed-up in the calculations. The bifurcation diagram obtained with numerical continuation is shown in Figure 3.12. In some regions no solution is shown because limit cycles do not exist, or because the continuation algorithm does not converge. This happens when the flame shape becomes very complicated, i.e., when the flame is oscillating at high frequencies. This is a technical problem with our implementation, not the technique in general. Nevertheless, we have been able to track limit cycles in most of the parameter regions we have considered.

Floquet analysis of limit-cycles

We can straightforwardly analyse the stability of cycles found with continuation by means of Floquet theory (Guckenheimer & Holmes, 1983). Floquet multipliers are complex numbers

associated with the linear response of limit cycle oscillations to infinitesimal perturbations. If one of them has a magnitude larger than one, the cycle is unstable. Thus, bifurcation locations and types are found by studying when and where Floquet multipliers cross the unit circle. We evaluate numerically the four Floquet multipliers with the largest magnitude. If a multiplier crosses the circle at $+1$, a Limit Point of Cycle (LPC) is found, meaning that the limit cycle branch changes its stability; this corresponds to cyclic fold or saddle-node bifurcations. Period-doubling (flip) bifurcations happen when a Floquet multiplier crosses the circle at -1. Finally, Neimark–Sacker (secondary Hopf) bifurcations are found when a pair of complex conjugate multipliers crosses the unit circle. The next section contains a discussion on the location of the bifurcations predicted by Floquet theory.

3.6 Comparison between frequency and time domain results

In this section we compare the results obtained with the three types of nonlinear analysis. We start by comparing the oscillation frequencies on stable attractors. Then we compare the results obtained with the harmonic balance against those obtained with time-marching. In particular we examine the location of bifurcation points, the nature of the oscillatory states and the amplitudes of oscillations.

3.6.1 Quasi-linear regime: frequency of oscillations

Figure 3.10 top panel shows the frequencies of stable limit cycles found with the harmonic balance method. It shows that the predicted limit cycle frequencies are always very close to the acoustic natural frequencies, as we had anticipated when discussing the FDF. In this analysis, the oscillation frequencies are well-defined because the cycles are harmonic. On the other hand, oscillations in the time domain are not necessarily harmonic. For time-marching simulations, we compute the PSDs of steady-state oscillations and normalise them with respect to the intensity of the highest peak. We assign to the PSD's intensity at each frequency a colour: the higher the intensity, the darker the colour. For each vertical slice of Figure 3.10 central panel, the black region indicates the frequency at which we have the highest peak, and grey regions are secondary peaks. For numerically continued cycles, which are plotted in the bottom panel, we plot only the fundamental oscillation frequency. Solid lines indicate stable cycles and dashed lines indicate unstable cycles, which have a complex pair of Floquet multipliers with magnitude larger than one, i.e. cycles that have undergone a Neimark–Sacker bifurcation. For these cycles, Floquet theory also predicts

the frequency of the mode that is linearly unstable around the cycle. These frequencies are plotted in Figure 3.10 bottom panel with dot-dashed lines. They are close to the frequencies in Figure 3.10 central panel. They are not exactly the same because the frequency shifts as these unstable cycles evolve towards the stable attractor.

The frequencies predicted by the three methods compare favourably. Referring to the time domain simulations, note that the first mode dominates in the region $x_f < 0.6$, shown by the fact that its PSD intensity is dominant and the second mode never oscillates alone. This is in agreement with the harmonic balance predictions (see Figure 3.7): the fixed point of the first mode is mainly unstable in this region, whereas the fixed point of the second mode is mainly stable. Finite amplitude oscillations are therefore needed to trigger limit cycles with high-frequencies. For $x_f > 0.6$, the second mode is dominant. However, a major difference between the methods is observed here: the harmonic balance does not predict oscillations of the first mode in this region, but its frequency appears in the time-marching time series. This is probably due to nonlinear effects, which couple the response of the modes and may induce oscillations that cannot be observed when examining the modes one by one. This suggests that, if the thermoacoustic feedback enhances higher harmonics of the nonlinearity, a frequency domain analysis based on a single mode does not accurately predict the system's nonlinear behaviour.

3.6.2 Fully nonlinear regime: limits of the FDF method

Figure 3.11 superposes the bifurcation diagram obtained with the harmonic balance (lines, as in Figure 3.7) and that obtained with the time domain (dots). Dots correspond to peaks and troughs of the acoustic velocity time series. Solid lines at $u' = 0$ indicate linearly stable fixed points.

Let us compare results for the region $x_f > 0.6$ in detail. The harmonic balance predicts a supercritical Hopf bifurcation at $x_f = 0.98$, which ends in a fold at $x_f = 0.61$. The subcritical Hopf associated with the fold point is located at $x_f = 0.72$. A second set of stable limit cycles with higher amplitudes is also found within the same range of parameters, and it has a triggering amplitude $u' \geq 0.2$.

Time-marching simulations qualitatively reproduce this behaviour: the system has a supercritical Hopf bifurcation at $x_f = 0.96$ and the resulting oscillations persist as the flame moves upstream. Figures 3.11 and 3.12 show that there are two stable solutions in the region $0.65 \leq x_f \leq 0.78$: a stable fixed point and an oscillating solution. Time-marching finds a subcritical Hopf bifurcation at $x_f = 0.78$. Thus, time-marching simulations confirm the bistability predicted by the harmonic balance in this region.

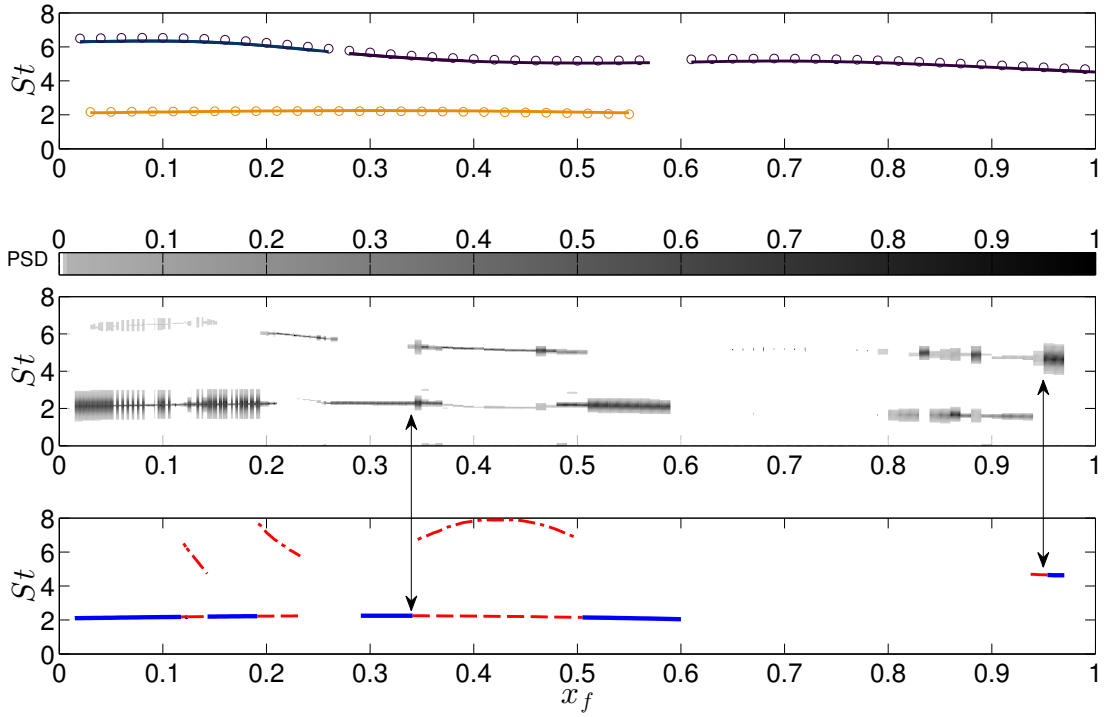

Fig. 3.10 Comparison between predicted frequencies. Top panel: circles indicate the first two natural acoustic frequencies of the geometry considered. Lines refer to Strouhal numbers of stable limit cycles found with the harmonic balance technique. Central panel: intensity of the normalised PSDs of converged time series. Bottom panel: dominant frequency of cycles obtained with numerical continuation (lines). Dot-dashed lines correspond to the frequency of the incipient unstable mode predicted by Floquet analysis when a Neimark–Sacker bifurcation occurs, as indicated by the arrows.

However, we observe quantitative differences between the two analyses: one of the main problems is that the positions of Hopf and fold bifurcations obtained with the two methods do not exactly match. One reason for this is that the heat release response to forced harmonic oscillations can be very non-harmonic, and it is a large approximation to consider only the contribution of the first harmonic. This is particularly true for high-amplitude oscillations, because the heat release response is highly nonlinear and can affect the position of fold points. However, it cannot explain a shift of the Hopf bifurcations. The latter is probably due to the fact that the frequency domain analysis relies on interpolation and extrapolation in the Laplace variable and amplitude of the FDF data when solving the dispersion relation (3.12). If the FDF is not well-resolved around the most important frequency regions (the frequencies of the thermoacoustic modes), it causes inaccuracies in the harmonic balance predictions. If the interpolation underestimates the FDF gain, then we underestimate also the overall gain of H_{x_f} in (3.12), and the Hopf bifurcations are shifted. Increasing the FDF frequency

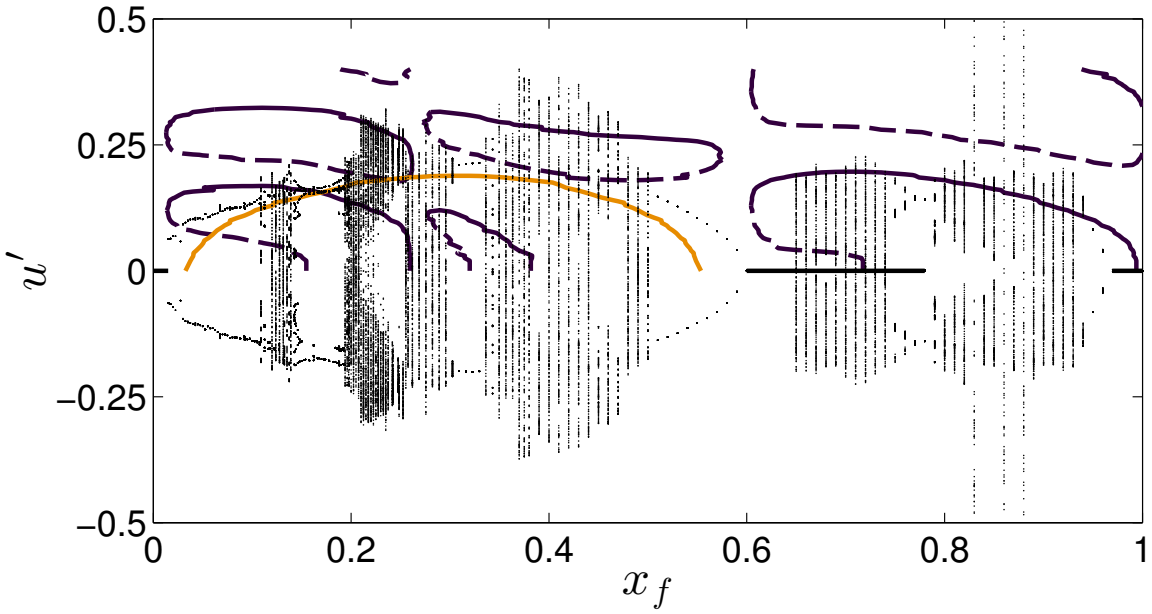

Fig. 3.11 Time integration bifurcation diagram (dots) and FDF predicted stable and unstable limit cycles (lines). Light and dark lines refer to the first and second thermoacoustic modes, respectively. Time series peaks and troughs of the final stable thermoacoustic state are shown as a function of the flame position in the duct. Solid lines at $u' = 0$ indicate linearly stable fixed points.

resolution improves the agreement between the location of the bifurcations, as demonstrated in Chapter 4, but cannot address the second major difference between the two analysis, which is one of the main results of this chapter: steady-state solutions found from time-marching are usually not limit cycles. Looking at the corresponding PSDs while moving the flame from $x_f = 1$ to $x_f = 0$, we observe the appearance of a new frequency incommensurate with respect to the first one at $x_f = 0.94$, meaning that the oscillations are quasiperiodic. When this happens, the absolute maximum and minimum velocity often greatly exceed those predicted by the harmonic balance method (see Figure 3.11). For some cases ($x_f = 0.83, 0.86, 0.88$), we find that another quasiperiodic stable attractor exists with an even higher maximum amplitude of oscillation, $u' > 0.5$. It is thus possible that the thermoacoustic system exhibits a triggering mechanism between two quasiperiodic attractors, although this phenomenon is not investigated in this analysis.

Similar features are found in the region $x_f \leq 0.6$, where the harmonic balance predicts stable and unstable limit cycles of two modes. As mentioned in §3.4, there exist parameter regions where the fixed points of two thermoacoustic modes are simultaneously unstable: because of the nonlinearity in the governing equations, a superposition of the mode responses does not represent the correct evolution of the system. One cannot infer a criterion from the

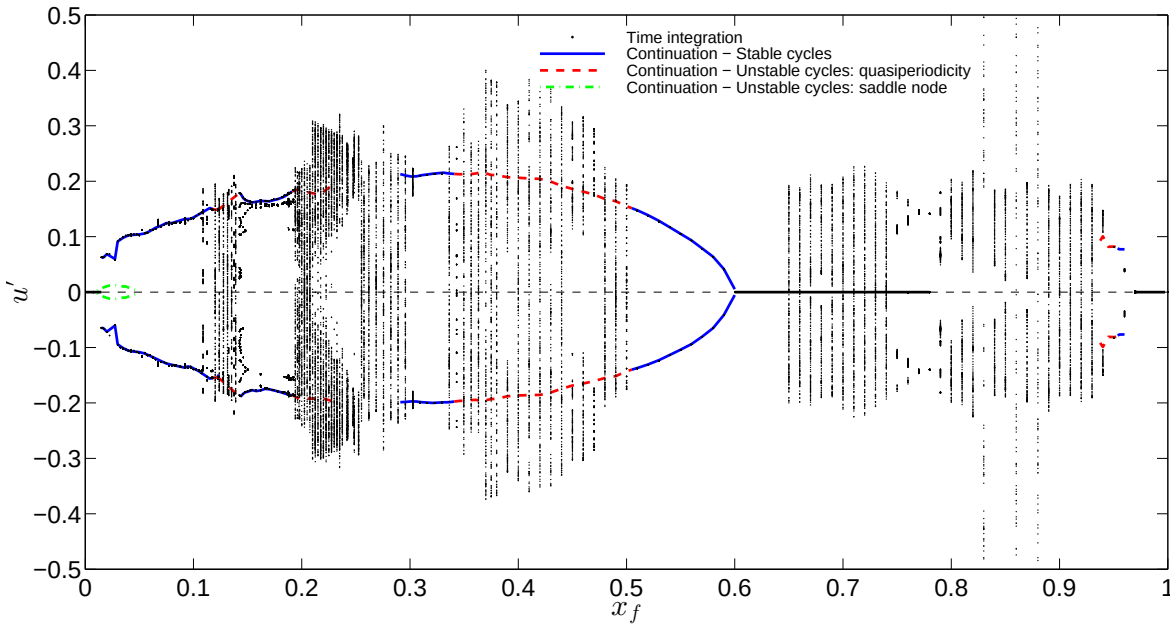

Fig. 3.12 Thermoacoustic bifurcation diagrams obtained with time integration (dots, see Figure 3.11) and numerical continuation (lines). The bifurcation parameter x_f is the dimensionless flame's position in the combustion chamber. The amplitude of self-excited acoustic velocity fluctuations is shown. Lines connect the absolute maximum and minimum amplitudes of cycles found with numerical continuation: solid lines indicate stable limit cycles, dashed lines two different types of limit cycle instability mechanisms: saddle-node (dot-dashed) and Neimark–Sacker (dashed).

FDF analysis to determine whether the system will oscillate with one of the two frequencies or if the oscillations will be aperiodic. Thus, we conclude that the FDF is not suitable for studying the correct nonlinear dynamics. In theory, it would be possible to obtain more accurate solutions by evaluating a multi-input FDF, $\mathrm{FDF}_N(\mathrm{i}\omega_1,\ldots,\mathrm{i}\omega_N,A_1,\ldots,A_N)$, and solving a set of dispersion relations as described by Moeck & Paschereit (2012) for a static nonlinear flame model.

3.6.3 Numerical continuation results

Cycles found with numerical continuation and the harmonic balance fundamentally differ. In numerical continuation, we impose no further constraints on the cycles dynamics other than those included in the governing equations. Therefore limit cycles evaluated with numerical continuation are solutions of the thermoacoustic model, not harmonic approximations. In addition, numerical continuation methods reveal the stability of cycles by means of Floquet

theory. This is particularly useful because we can predict the location of Neimark–Sacker bifurcations, which cause transitions from periodic to quasiperiodic dynamics.

Results from numerical continuation and time-marching are compared in Figure 3.12. The locations of Hopf and Neimark–Sacker bifurcations predicted by Floquet theory compare extremely well with those found from time-marching analysis. For stable limit cycles, the oscillation amplitudes of the two methods compare well. This is, of course, not the case for unstable limit cycles. Floquet analysis shows the parameter values at which a quasiperiodic solution exists but cannot predict its amplitude. It can be very different from that of the unstable limit cycle, as shown in Figure 3.12.

Although it would be theoretically possible to perform a Floquet analysis in the frequency domain (Basso *et al.*, 1997), this requires a multi-input FDF, which is expensive to evaluate. The results in this section show that numerical continuation combined with Floquet analysis is a useful tool for the analysis of thermoacoustic models. Its main weakness is that, if any parameter is changed, the entire analysis has to be performed again. This is impractical when one wants to study the effect of several parameters on the nonlinear behaviour of the system.

3.7 Nonlinear dynamical behaviour

We conclude by looking in detail at the nonlinear dynamical behaviour we observe, and by discussing analogies and differences between the nonlinear regimes of our system and those found in similar experimental and numerical studies.

Our bifurcation diagram (Figure 3.12) can be compared with the one determined in the experiments performed by Kabiraj & Sujith (2012); Kabiraj *et al.* (2012*b*), on which we have based our geometry. Major differences are found between the two diagrams: as an example, Kabiraj & Sujith (2012) find that the thermoacoustic system is linearly stable for $1 \leq x_f \leq 0.343$ (however, in the experiments the response of the system to finite perturbations was not investigated), whereas for the same flame position range we observe a wide region of oscillations.

We were, however, not expecting any quantitative agreement between the two results, because we have introduced several approximations in our thermoacoustic system. Our flame model is very simplistic and a more detailed model might be needed to accurately reproduce the correct flame dynamics and heat release response. Also, our lack of knowledge about the acoustic reflection coefficients of the experimental setup might be important: although we have chosen reasonable models for the geometry considered, the real reflection coefficients may differ. For example, if the damping of high-frequency modes were stronger than the one we considered, the instability of the second mode observed in our analysis at the end of the

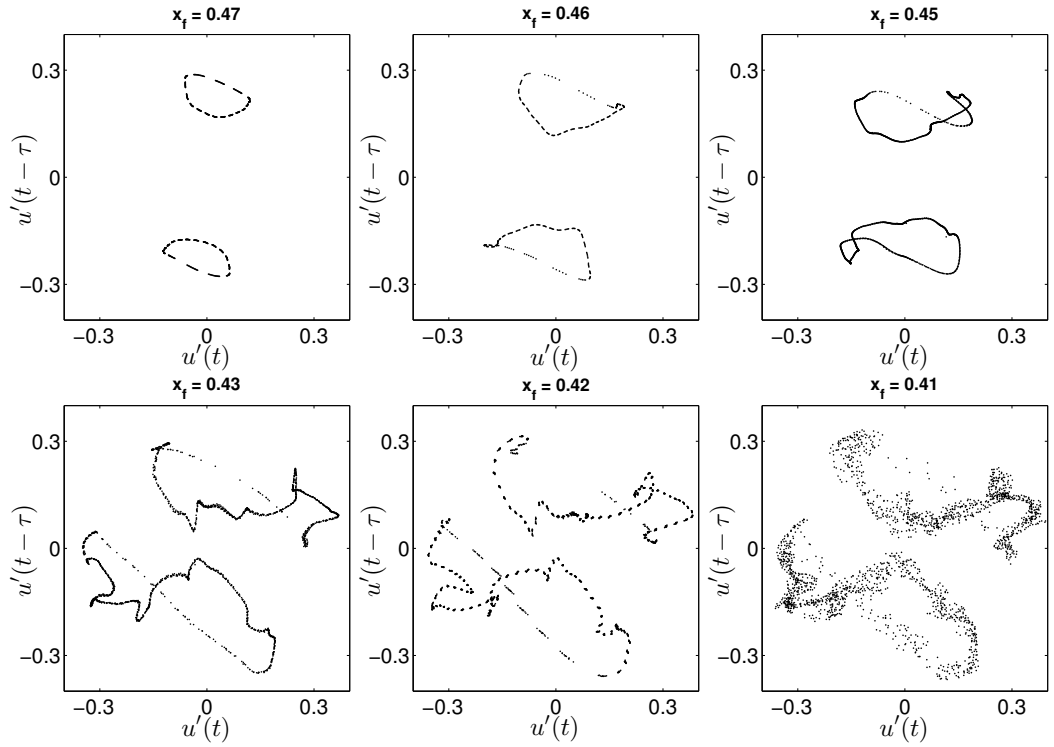

Fig. 3.13 Ruelle–Takens–Newhouse route to chaos. Poincaré sections show the creation of a strange attractor from a quasiperiodic solution. The torus of a quasiperiodic solution first folds, then develops corrugations on its surface and eventually disintegrates into a strange attractor.

duct would be suppressed. Including experimentally measured reflection coefficients may improve the agreement with experiments.

Nevertheless, we observe some qualitative common features between the two studies. For example, experimental oscillations after the first Hopf bifurcation have a period of about 5.4 ms, which correspond to a Strouhal number $St \equiv L_f f/\overline{u} \approx 2.4$ (assuming a flame height of 4 cm). This is consistent with the frequency of the low-frequency mode observed in our numerical analysis (Figure 3.10), which is 2.1. Also, the types of bifurcations found by Kabiraj & Sujith (2012) match the ones we observe: a Hopf bifurcation, followed by a Neimark–Sacker bifurcation, chaos, and flame blowout. In the experiments, before chaos an intermittent behaviour associated with the flame lifting off and returning to the burner was observed; we cannot describe this effect because our flame can slide on the burner, but cannot lift off. For the same reason, our low-order simulations cannot model flame blowout, but we reproduce the same route to chaos. By analysing the phase portraits and PSDs of the thermoacoustic time series in the whole range of parameters considered, we identify one type of route to chaos, which is summarised in Figure 3.13. It starts from a quasiperiodic solution,

whose Poincaré section (a torus) folds, develops corrugations and finally breaks down. The Poincaré sections of the first and last frames of Figure 3.13 correspond to the time series in the last two rows of Figure 3.9, respectively. By looking at the PSDs, we see that during the torus breakdown process a new frequency appears in the spectrum, a sign that a Hopf bifurcation has occurred. Thus, we can identify three subsequent Hopf bifurcations which lead to chaos: at $x_f = 0.59$ a first Hopf bifurcation creates limit cycle oscillations from fixed points; at $x_f = 0.5$, a secondary Hopf transforms the dynamics into quasiperiodic oscillations; finally at $x_f = 0.42$ a third Hopf occurs, and the torus starts to break down, leading to chaotic oscillations. This is the signature of the Ruelle–Takens–Newhouse route to chaos.

The same route to chaos, together with the period-doubling route to chaos, is observed by Kashinath *et al.* (2014). However, they considered as acoustic resonators straight pipes with no area changes, and assumed zero temperature jump across the flame. The same acoustic configuration is considered by Waugh *et al.* (2014), where fold, period-doubling, and Neimark–Sacker bifurcations are identified. As mentioned in §3.3, in those simple acoustic configurations the natural acoustic eigenfrequencies are all integer multiples of the fundamental duct frequency. This enhances the interaction between the modes: if the fundamental frequency (or a subharmonic) is excited, its harmonics respond as well due to nonlinear effects and, because these harmonics are the resonant frequencies of the higher modes, a coupling between the modes is induced. Thus, one may argue that the highly nonlinear dynamics observed is influenced by the too simplistic geometry considered. In this chapter we have shown that this is not the case. Accounting for temperature and area variations, the frequencies of the acoustic modes are no longer equispaced, and the interaction between the modes is reduced. Nevertheless, we still observe very rich nonlinear dynamics.

3.8 Conclusions

In this chapter we have developed a nonlinear low-order thermoacoustic model for premixed flames. Particular care has been taken to describe the acoustics by adapting an existing tool, LOTAN, and casting wave-based frequency response functions into suitable state-space models. This allows us to consider complex acoustic geometries accounting for area and temperature variations, and to easily analyse the stability of a thermoacoustic system both in the frequency and time domains.

An FDF has been evaluated numerically and the stability of this thermoacoustic network has been investigated via the harmonic balance technique. Stable and unstable limit cycles of the first two thermoacoustic modes have been calculated while varying the flame position in the duct. By comparing these results with time-marching simulations, we observe that

the harmonic balance technique predicts the onset of instability reasonably accurately and captures the oscillation frequencies well. However, the harmonic balance technique does not, in general, predict well the amplitudes observed in time-marching results. This is because the combustion model we use, which is based on the kinematic G-equation, is highly nonlinear at high amplitudes of oscillations. Consequently, accounting for only the first harmonic component of the heat release fluctuations induces large approximations in the Flame Describing Function, which is a crucial ingredient in the description of the system in the frequency domain. Secondly, we observe that neglecting the interaction between the modes can lead to very different results in the dynamical behaviour of the system. If the harmonic balance predicts simultaneous growth of two thermoacoustic modes with incommensurate frequencies, limit cycle oscillations cannot be always expected. We observe this in the time domain simulations, in which we find aperiodic solutions. We determine their dynamical nature by means of nonlinear time series analysis techniques. We identify the position of secondary Hopf bifurcations which lead to quasiperiodic oscillations through Neimark–Sacker bifurcations. We also identify the Ruelle–Takens–Newhouse route to chaos.

Finally, we apply a numerical continuation algorithm to the system. The method is able to track non-harmonic limit cycles in the parameter space, and does not contain the approximations required when analysing the system in the frequency domain. As a result, the frequencies and amplitudes of cycles obtained with this method approximate results from time-marching simulations very well. Importantly, we can straightforwardly apply Floquet theory on cycles found with numerical continuation and determine their stability. This is particularly important because we can predict the location of Neimark–Sacker bifurcations: when they occur, oscillations cease to be periodic and we need to rely on time-marching methods to have a full characterisation of the nonlinear dynamics.

This chapter shows that time domain techniques, such as numerical continuation analysis, can be applied to reduced order models containing a G-equation flame and complex acoustics. Furthermore, it shows that these provide more accurate information on the stability and nature of thermoacoustic oscillations than the harmonic FDF method. On the other hand, a new set of calculations based on numerical continuation has to be performed when a parameter of the system is changed, whereas the same FDF can be used in several acoustic configurations. This is a promising new development for the analysis and understanding of realistic thermoacoustic systems.

Chapter 4

Flame Double Input Describing Function analysis

In this chapter a novel method for the prediction of non-periodic thermoacoustic oscillations is developed. The method relies on an extension of the FDF, called the Flame Double Input Describing Function (FDIDF), which quantifies the nonlinear heat release response when a flame is subject to two, simultaneous harmonic forcings. Starting from the FDF assumptions, the theory that couples linear acoustics with a generic non-static nonlinear flame model approximated by the FDIDF is developed. The dispersion relations that identify the frequencies and amplitudes of non-periodic oscillations are derived, together with analytical criteria to assess their stability. It is shown how the FDIDF (i) improves the FDF assessment on the stability of periodic oscillations; (ii) can predict the onset of Neimark–Sacker bifurcations, together with the frequency of the oscillations that arise on top of unstable limit cycles; (iii) can calculate the amplitude and stability of quasiperiodic solutions.

The content of this chapter was published in Orchini & Juniper (2016*a*).

4.1 Introduction

In Chapter 3, we have seen how the Flame Describing function (FDF), together with the harmonic balance method, can be used to calculate the amplitude and stability of periodic thermoacoustic oscillations. Its solutions are, however, only harmonic approximations of the actual response of the system. Furthermore, if the growth rate of more than one thermoacoustic mode is positive, then the oscillations are non-periodic. Because the FDF is calculated by forcing the flame harmonically, it cannot be used to predict the amplitude of non-periodic oscillations. In particular, one cannot linearly superpose two periodic solutions

that are found from the harmonic balance at a given operating point. This is simply because the flame's behaviour when forced by two finite amplitude signals is not a linear superposition of its behaviour when forced by each finite amplitude signal independently. When using the FDF, therefore, one cannot rule out the possibility that the long time behaviour is non-periodic.

A detailed investigation of the interplay between two oscillating modes has been performed experimentally only for simple configurations (Kabiraj *et al.*, 2012*a*; Balachandran *et al.*, 2008), due to its high cost. Nonetheless, the presence of multiple, incommensurate frequencies in the spectrum of thermoacoustic oscillations has been reported in several experimental studies (Gutmark *et al.*, 1992; Dunstan *et al.*, 2001; Lamaroui *et al.*, 2011). The study of the nonlinear interaction between the modes may be relevant for the analysis of these systems. It has also been observed in experiments that, although a single eigenmode is found to be linearly unstable, nonlinear effects may actually stabilise the oscillations at this frequency and trigger oscillations at a different frequency (Noiray *et al.*, 2008). The FDF can predict the existence of oscillations of the two modes independently, but will fail in predicting their stability, as the latter is connected to the nonlinear coupling between the two modes. This phenomenon is usually called mode-switching, and was observed also by Moeck & Paschereit (2012), and in gas turbines experiments by Cazalens *et al.* (2008); Anisimov *et al.* (2015). In Moeck & Paschereit (2012) it was shown that mode-switching can be attributed to the existence of an unstable quasiperiodic attractor in the phase-space of thermoacoustic trajectories, which the FDF framework cannot calculate.

In order to predict the amplitude of at least some classes of non-periodic oscillations, a different approximation of the nonlinear flame model has to be calculated. This is known as the Double Input Describing Function (DIDF), and is created by forcing the flame with a signal composed of two harmonic components with independent amplitudes and incommensurate frequencies (Gelb & Velde, 1968). The calculated Flame DIDF (FDIDF) can then be fed into an acoustic network in a similar manner to that in Figure 1.2. The harmonic balance procedure yields two coupled dispersion relations which have to be solved simultaneously, as was first shown by Moeck & Paschereit (2012) for a thermoacoustic system.

The aim of this chapter is to present a numerical analysis that exploits frequency domain calculations of a non-static (or dynamic[1]) nonlinearity based on a low-order model for the flame dynamics. This is the major difference between our analysis and that of Moeck & Paschereit (2012), where a static model for the flame was considered. For static nonlinearities, a Wiener-Hammerstein model can be adopted, which decouples the nonlinear amplitude saturation process from the linear dynamic response. This is not possible for dynamic

[1] A nonlinearity is non-static if it depends on time derivatives of the input state.

nonlinearities, and the FDIDF we calculate is a nonlinear object that couples the input amplitudes and frequencies. We also obtain an analytical criterion for the stability of quasiperiodic oscillations, which is different from the one discussed in Moeck & Paschereit (2012). A different attempt to extend the concept of the FDF was proposed by Selimefendigil & Polifke (2011); Selimefendigil *et al.* (2012), where higher order transfer functions that account for modal coupling were derived using Volterra series expansions. However, the dependence of the higher order transfer functions upon the relative amplitude of the input modes was not considered in these studies. The non-static model we adopt for the flame is the kinematic nonlinear G-equation, which is known to lead to quasiperiodic oscillations when coupled with an acoustic network (Kashinath *et al.*, 2014; Waugh *et al.*, 2014; Orchini *et al.*, 2015). The FDIDF method is able to predict the location of Neimark–Sacker bifurcations, the frequency of unstable oscillations around limit cycles, and also the saturation amplitude and the stability of quasiperiodic oscillations.

The chapter is structured as follows: in §4.2 we present FDF results and calculate harmonic limit cycles amplitudes and frequencies, together with their stability, highlighting strong points and weaknesses of the method; in §4.3 and §4.4 the FDIDF is presented and tested against the FDF in the limit of a small forcing amplitude; the dispersion relations that couple it with the acoustic response are derived and solved; the frequencies and amplitudes of periodic and non-periodic solutions are calculated with the harmonic balance method based on the FDIDF; criteria for the stability of these solutions are outlined; results are compared with the FDF method analysis and with time domain simulations of the same nonlinear system. Finally in §4.5 the chapter is summarised and the benefits and problems of the methods are discussed.

4.2 Review of the FDF analysis approximations

The thermoacoustic model we will investigate in this chapter, sketched in Figure 4.1, is the same as that considered in Chapter 3, to allow a comparison between the FDF and the FDIDF methods. The acoustic network is described in §2.7, and the nonlinear flame model based on the G-equation, as discussed in §3.2.

By FDF, we refer to the frequency domain approximation of the nonlinear flame response to harmonic velocity perturbations (see Figure 4.2). We therefore set $u'_{ac} = A\sin(\omega t)$, time march equations (3.1)-(3.3), and calculate the heat release according to equation (3.8). Given that the velocity perturbation is harmonic with angular frequency ω, it is reasonable to

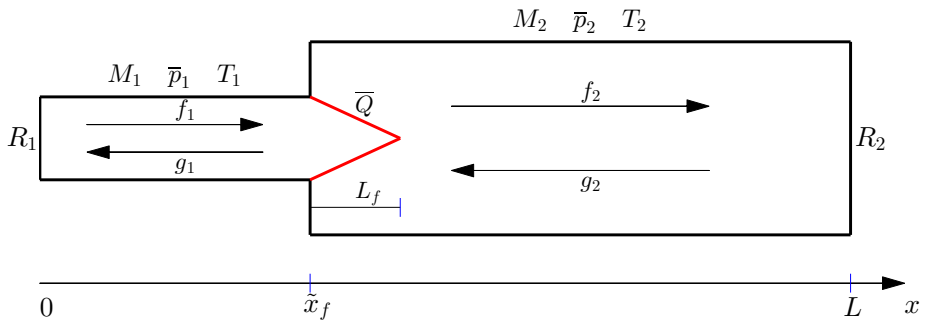

Fig. 4.1 Sketch of the thermoacoustic network. A compact flame connects two ducts with different diameters and mean temperatures. The linearised Euler equations are solved on top of a uniform mean flow solution. Jump conditions at the flame and prescribed reflection coefficients at the inlet/outlet provide closure for the model.

assume that the heat release response can be expanded in a Fourier series as:

$$Q = \sum_{k=1}^{\infty} \hat{q}_k \sin(k\omega t + \phi_k). \tag{4.1}$$

This assumes that the heat release is periodic, with the same period as the forcing. For laminar flames, this is supported by experimental evidence (Ducruix *et al.*, 2000; Schuller *et al.*, 2002; Durox *et al.*, 2009; Karimi *et al.*, 2009). This model cannot capture a possible response of the nonlinearity at subharmonics. Also, for laminar flames that oscillate in the absence of forcing at an intrinsic frequency (Juniper *et al.*, 2008), it cannot capture the response that may appear at non-integer multiples of the forcing frequency.

The FDF that is fed into the harmonic balance dispersion relation, defined by (1.4), is then defined as:

$$\mathrm{FDF}(A, \mathrm{i}\omega) \equiv \frac{\hat{q}_1 e^{\mathrm{i}\phi_1}}{\hat{u}} \frac{\overline{u}}{\overline{Q}}, \tag{4.2}$$

where $\hat{u}$ is the Fourier component of the input velocity signal at the burner.

Rather than performing the FDF calculations over all possible frequencies, in the following we provide an argument that allows us to limit the calculations only over certain sets of dangerous frequencies. We first recall that the dispersion relation (1.4) is derived from the harmonic balance method (Gelb & Velde, 1968). Its solutions, which for a fixed value of the amplitude can be interpreted as the poles of the closed-loop thermoacoustic system, are those for which the loop-gain, $|\mathrm{FDF}||H|$, is equal to 1 and the total (wrapped) phase is equal to 0. To find limit cycle oscillations, we impose the additional condition that the growth rate is equal to zero. From the loop-gain condition, one can infer that a necessary (but not sufficient) condition for a thermoacoustic oscillation to exist is that either the acoustic transfer function

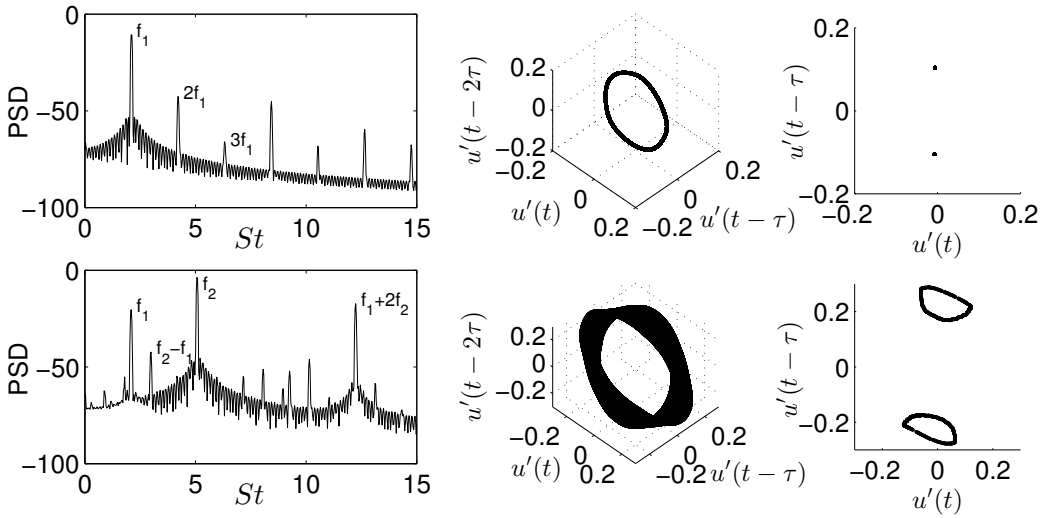

Fig. 4.2 Velocity Power Spectral Density (PSD), phase plane and Poincaré sections of self-excited thermoacoustic oscillations. Top row: periodic oscillations. The system responds also at the harmonics, which are neglected in the FDF framework. Bottom row: quasiperiodic oscillations. The system responds also at the harmonics and linear combination of the fundamental frequencies, which are neglected by the FDIDF.

H or the FDF must have a gain larger than 1. For the acoustic transfer function, this happens close to the acoustic eigenfrequencies, whereas the FDF may or may not have regions in which the gain is larger than 1. If the FDF gain is larger than 1 over some frequency range, the frequency of thermoacoustic oscillations may lie in this region, and can be far from the acoustic eigenfrequencies (Tay-Wo-Chong *et al.*, 2012). It has been shown that these oscillations may persist even in the extreme case in which anechoic boundary conditions for the acoustic network are imposed, and therefore no purely acoustic mode exists (Hoeijmakers *et al.*, 2014*b*; Emmert *et al.*, 2014; Hoeijmakers *et al.*, 2014*a*; Courtine *et al.*, 2015). For this reason, these thermoacoustic modes have been labelled as intrinsic thermoacoustic modes.

When the unconfined laminar conical flame model we are considering is forced harmonically, its gain |FDF| never exceeds 1. Within the G-equation framework, this can be proven analytically in the low forcing amplitude limit when curvature corrections on the flame speed are neglected (Preetham *et al.*, 2008; Cuquel *et al.*, 2011; Orchini & Juniper, 2015). Numerical and experimental studies have shown that this holds true even in the fully nonlinear case (Schuller *et al.*, 2003; Karimi *et al.*, 2009; Kashinath *et al.*, 2013*a*; Orchini *et al.*, 2015). For this reason, no intrinsic thermoacoustic instabilities can be observed in our system, and we can deduce that thermoacoustic oscillations are possible only in certain frequency bands, given by the regions in which the acoustic gain $|H|$ is larger than one. For

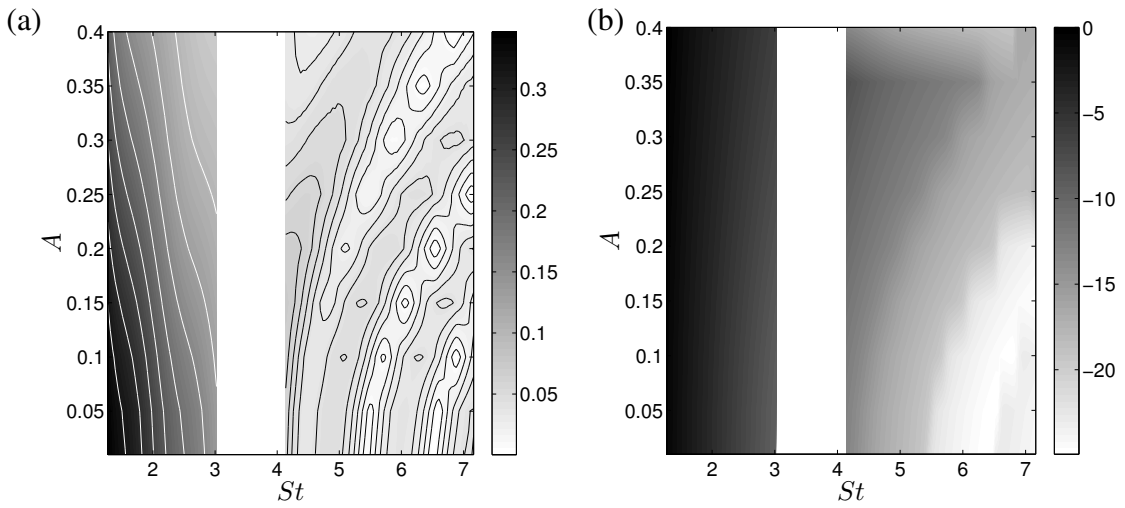

Fig. 4.3 Gain (a) and phase (b) of a laminar, conical flame's FDF. The FDF is evaluated numerically only around frequencies that may give rise to thermoacoustic oscillations.

example, at $x_f = 0.34$ one can see from Figure 2.9 that oscillations can be expected only in the [118, 197] Hz and [303, 371] Hz band regions.

This is useful information because we can reduce the cost of the FDF calculations by evaluating the FDF only over these frequency regions[2]. We identify these regions while varying the bifurcation parameter x_f over the entire range [0, 1]. Let us define the Strouhal number $\mathrm{St} \equiv L_f f/\overline{u}$, where L_f and $\overline{u}$ are the characteristic flame length and mean flow speed respectively. For the thermoacoustic system under consideration in this chapter, oscillations are possible only in the frequency ranges $\mathrm{St} \in [1.273,\ 3.024]$, associated with the fundamental acoustic eigenfrequency, and $\mathrm{St} \in [4.138,\ 7.162]$, associated with the second acoustic eigenfrequency. Note that this range is obtained by considering all possible values of x_f and is therefore different from the one discussed in the previous paragraph, because the latter was considering only a specific position of the flame. We carry out a detailed evaluation of the FDF in these frequency ranges, varying the amplitude of the oscillation between 0 and 0.4. The FDF gain is shown in Figure 4.3, and contains the usual features of conical, premixed flames: the gain is larger at low frequencies and overall it tends to decrease with the amplitude, a signature of the nonlinearity saturation effect. This holds true at low frequencies, whereas at high frequencies the gain can also increase with the amplitude, meaning that subcritical bifurcations and triggering may be observed.

[2] A broad knowledge of the FDF is needed to ensure that a flame's gain never exceeds unity. For our model, we already have this information from Chapter 3. Practically, one could first evaluate the FDF on a coarse set of frequencies, and them refine the measurements around those frequencies at which the gain is high.

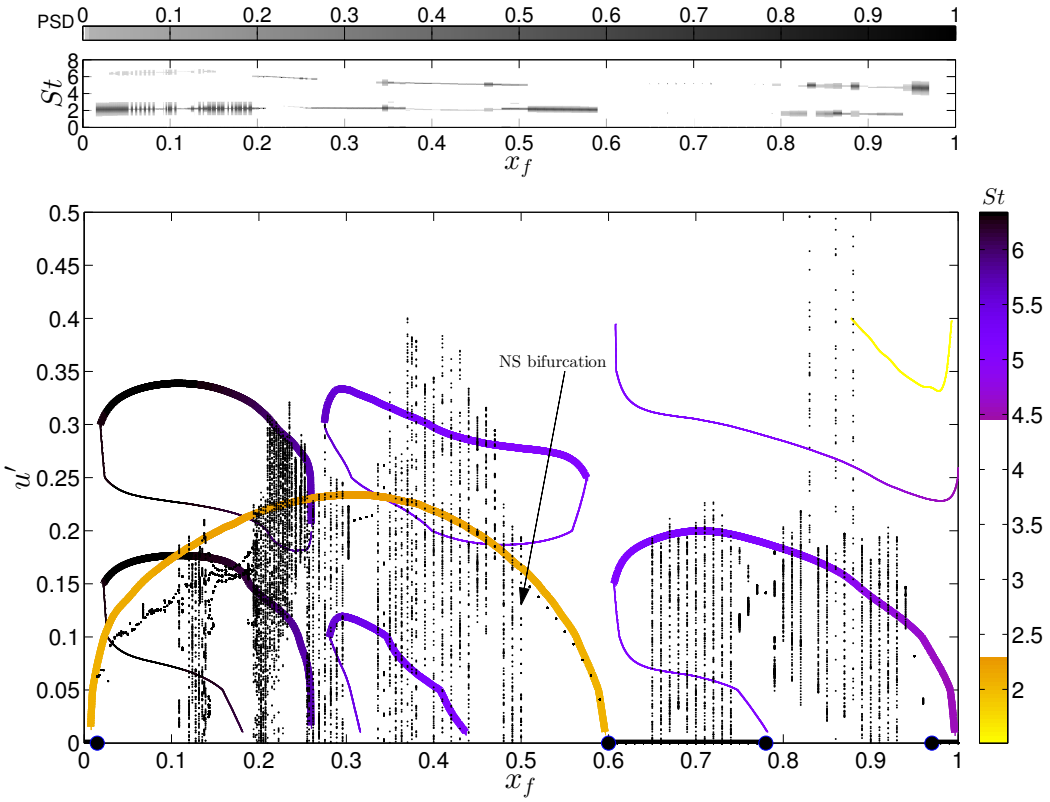

Fig. 4.4 Bottom frame: bifurcation diagrams calculated with time domain simulations (dots) and the FDF method (lines), using the flame position, x_f, as the bifurcation parameter. Thick and thin lines correspond to stable and unstable limit cycles, respectively, and their colour to the limit cycle oscillation frequency. Dots represent peaks of time domain simulations, as described in 3. The FDF method predicts Hopf bifurcations and periodic oscillations well (e.g. between $x_f = 0.50$ and 0.60) but cannot predict quasiperiodic oscillations (e.g. between $x_f = 0.34$ and 0.50). The top graph shows the PSD of time domain simulations at every flame location.

Having calculated both the acoustic transfer function H and the FDF, we can close the thermoacoustic feedback loop (as shown in Figure 1.2) and calculate the thermoacoustic eigenfrequencies according to the dispersion relation (1.4). We recall that (1.4), deriving from the harmonic balance method, works well when the so-called filtering hypothesis is satisfied, meaning that the closed-loop system does not respond greatly at the harmonics of the input frequency. Experimental and numerical studies have shown that laminar, conical flames act as low-pass filters (Schuller *et al.*, 2002, 2003; Preetham *et al.*, 2008), and Figure 4.3 shows that our model contains this feature. Also the acoustics tends to damp high frequencies more, although gain peaks are found at the resonance frequencies. For these reasons, we shall assume that the filtering hypothesis is satisfied.

Limit cycles are found when the dispersion relation (1.4) is satisfied, with the additional constraint that the growth rate of the oscillations is equal to zero. At this stage, no further approximation has been introduced, because we have knowledge of the FDF at harmonic oscillations. However, to assess the stability of the cycles we need to perturb the saturation amplitude and calculate the shift in frequency and growth rate that it causes, i.e., we want to find the $\Delta s = \Delta\sigma + \mathrm{i}\Delta\omega$ that satisfies:

$$\mathrm{FDF}\left(A_{LC} + \Delta A, s_{LC} + \Delta s\right) H\left(s_{LC} + \Delta s\right) - 1 = 0, \tag{4.3}$$

where A_{LC} and $s_{LC} = \mathrm{i}\omega_{LC}$ are a limit cycle solution of (1.4), and ΔA is an imposed infinitesimal perturbation. If $\Delta\sigma/\Delta A$ is positive, the limit cycle is unstable, and if it is negative then the cycle is stable. To solve (4.3) the FDF needs to be extended into the complex plane $\mathbb{C}$. Following Schmid *et al.* (2013), we have tried two different techniques: (i) extrusion, by assuming that the FDF does not vary with σ, and (ii) analytic continuation, by fitting every amplitude slice of the FDF onto a state-space. Both methods give the same results.

The bifurcation diagram we obtain by varying the flame position is shown in Figure 4.4. Thick and thin lines indicate stable and unstable limit cycles as predicted by the harmonic balance method. Results are compared with time domain simulations of the same system (Orchini *et al.*, 2015). Solid lines at $A = 0$ indicate regions in which the time domain simulations are linearly stable, and Hopf bifurcations are marked with circles. The dots represent peaks of velocity fluctuations in the time domain. At x_f locations where multiple dots are plotted, the oscillations therefore are non-periodic. For example, at $x_f = 0.5$ time domain oscillations cease to be periodic, and quasiperiodic solutions arise through a Neimark–Sacker bifurcation, marked with an arrow in Figure 4.4. The two methods give similar locations of Hopf bifurcations and amplitudes of periodic oscillations. However, the FDF method fails to predict the amplitude of non-periodic oscillations. Further, although many stable limit cycles are predicted by the FDF method, time domain simulations rarely converge to these solutions. This is because they are not, in fact, stable. The FDF criterion for stability misses this because it only considers growth or decay of the mode that is already oscillating. It cannot consider growth or decay of another mode on top of the oscillating limit cycle, which is considered with the FDIDF in the next section.

Note that, a similar comparison between the time and frequency domain methods was presented in Chapter 3. However, a mismatch between the locations of the Hopf bifurcations predicted by the FDF and those found by time integration was observed there. In this chapter we have resolved the FDF more accurately around the frequencies at which thermoacoustic oscillations are expected, which has led to a better match between the two methods.

4.3 FDIDF assumptions and calculation

By FDIDF, we refer to the frequency domain approximation of the nonlinear flame response to a quasiperiodic velocity perturbation of the form:

$$u'_{ac} = A_1 \sin(\omega_1 t) + A_2 \sin(\omega_2 t), \tag{4.4}$$

where ω_1 and ω_2 are incommensurate frequencies. This choice guarantees that the phase between the two signals does not affect the resulting dynamics. In the following subsections we discuss in details the approximations and assumptions we make concerning the nonlinearity.

4.3.1 FDIDF definition

First, as in the FDF case, we assume that the nonlinearity does not excite the subharmonics of the forcing frequencies, and that no intrinsic dynamical instabilities exist. Because the heat release is a nonlinear function of the forcing signal (4.4), we expect that its response will contain all the possible combinations of the input frequencies. By using a double Fourier series expansion (Gelb & Velde, 1968), we can write:

$$q' = \sum_m \sum_n \hat{q}_{mn} \sin\left[(m\omega_1 + n\omega_2)t + \phi_{mn}\right], \tag{4.5}$$

where the heat release amplitude coefficients $\hat{q}_{mn}$ and the phases ϕ_{mn} are functions of the input velocity frequencies and amplitudes. The integers m, $n \in \mathbb{Z}$ are varied over all the possible combinations giving a non-negative value of the angular frequency $m\omega_1 + n\omega_2$.

In order to proceed with the harmonic balance analysis, we need to assume that the heat release response is dominated by the frequency components at the two input frequencies (see Figure 4.2), so that it can be approximated by:

$$q' \approx \hat{q}_{10} \sin\left(\omega_1 t + \phi_{10}\right) + \hat{q}_{01} \sin\left(\omega_2 t + \phi_{01}\right). \tag{4.6}$$

This assumption is less well-justified than the filtering hypothesis of the previous section, because the latter only requires that high-frequency oscillations are damped by the system. For the FDIDF, the coupling between the frequencies can also lead to low-frequency oscillations (e.g., at an angular frequency of $|\omega_2 - \omega_1|$) for which the filtering hypothesis does not necessarily hold. Therefore, we are implicitly assuming that the nonlinearity's response at these frequencies is either filtered by the system or is weak. This holds true at small forcing amplitude, for which nonlinear effects are small, but it has to be tested at larger amplitudes.

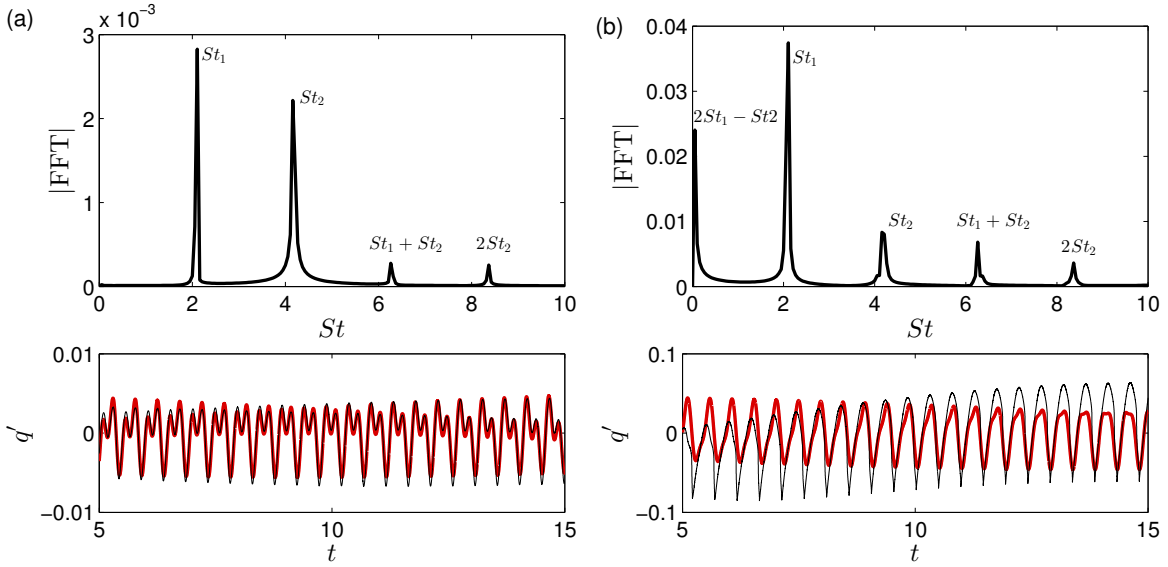

Fig. 4.5 FFT of the heat released by the flame when the forcing is quasiperiodic with the form (4.4). Top frames: (a) At low forcing amplitudes, $A_1 = 0.01$, $A_2 = 0.05$, the forcing frequencies dominate the heat release spectrum. (b) At large forcing amplitudes, $A_1 = 0.2$ and $A_2 = 0.25$, peaks at other frequencies become relevant. Bottom frames: nonlinear heat release fluctuations (thin black) and heat release reconstructed using only the peaks at the forcing frequencies (thick red).

Figure 4.5 shows examples on the quality of the FDIDF approximations: at low forcing amplitude nonlinear effects are weak and the heat release approximated by (4.6) compares well with the fully nonlinear output. At larger input amplitudes the quality of the approximation deteriorates. This is because the nonlinearity couples the modes, and high peaks can be observed in the heat release FFT at frequencies which are simple combinations of the input ones. For example, in Figure 4.5b one can see that the peak at the very low frequency $2\mathrm{St}_1 - \mathrm{St}_2$ has a large amplitude, meaning that the heat release exhibits large fluctuations over long time scales. The FDIDF approximation cannot see these long time scale fluctuations, as shown in the bottom frame. This is because it ignores all the FFT contributions which are not at St_1 and St_2. For this reason, we cannot expect the FDIDF method to work well at large amplitudes. Therefore, we limit the FDIDF calculations in amplitude so that both A_1 and A_2 are smaller than 0.4, and their sum is less than 0.5.

The FDIDF is defined as:

$$\mathrm{FDIDF} \equiv [\mathcal{F}_{10}, \mathcal{F}_{01}] \equiv \frac{\overline{u}}{\overline{Q}} \left[\frac{\hat{q}_{10} e^{\mathrm{i}\phi_{10}}}{\hat{u}_{10}}, \frac{\hat{q}_{01} e^{\mathrm{i}\phi_{01}}}{\hat{u}_{01}} \right], \tag{4.7}$$

where $\hat{u}'_{10}$ and $\hat{u}'_{01}$ are the Fourier components of the input velocity at ω_1 and ω_2 respectively. $\mathcal{F}_{10}$ ($\mathcal{F}_{01}$) contains information on how the amplitude and phase of heat release fluctuations at ω_1 (ω_2) vary when the flame is forced quasiperiodically. The total (non-dimensional) heat release fluctuations are then approximated by:

$$\hat{q}' \approx \text{FDIDF} \cdot [\hat{u}_{10}, \hat{u}_{01}]^T = \mathcal{F}_{10}\hat{u}_{10} + \mathcal{F}_{01}\hat{u}_{01}. \tag{4.8}$$

Note that the heat release in (4.8) is not a simple linear superposition of two FDFs. This is because the FDIDF's gains and phases are functions of all the four input variables $(A_1, \omega_1, A_2, \omega_2)$. Finally, notice that the FDIDF is a symmetric object with respect to the input pairs (A_1, ω_1) and (A_2, ω_2) so that:

$$\mathcal{F}_{10}(A_1, \omega_1, A_2, \omega_2) = \mathcal{F}_{01}(A_2, \omega_2, A_1, \omega_1). \tag{4.9}$$

4.3.2 FDIDF amplitude saturation

In §4.2, using knowledge of the flame's gain response from the literature, we performed calculations only for frequencies close to the first two acoustic modes. No information is available about the gain response of conical flames when they are forced with quasiperiodic signals. However, it is reasonable to assume that, when fixing the amplitude A_1 and increasing the amplitude A_2 (or viceversa), the gains of the FDIDF will decrease. This is because we expect the flame nonlinear responses $\mathcal{F}_{10}$ and $\mathcal{F}_{01}$ to saturate, at least on average, with respect to the amplitudes A_1 and A_2 of both forcing modes. This is proven to be correct for a simple cubic nonlinearity in Moeck & Paschereit (2012), where also some experimental evidence of this fact is provided.

We therefore assume that the FDIDF gains are less than 1. As a consequence, we expect that self-excited thermoacoustic oscillations can only be found at frequencies for which the acoustic gain is larger than one (see the FDIDF dispersion relations (4.11)). These frequency ranges are the same as in the FDF case, because we have not modified the acoustic system. Because we expect two modes to be unstable, it is reasonable to guess that one of the mode's frequencies will be close to the fundamental acoustic frequency, and the other one will be close to the acoustic second acoustic eigenfrequency. Note that, if two modes with similar frequencies were to oscillate simultaneously, beating phenomena could occur, and one should also investigate the coupling between these close frequencies. However, this does not happen for the system we are considering, as was also shown via the time domain analysis carried out in Orchini *et al.* (2015) on the same thermoacoustic system. Given this, and the symmetry condition (4.9), we will limit the calculations to the cases in which

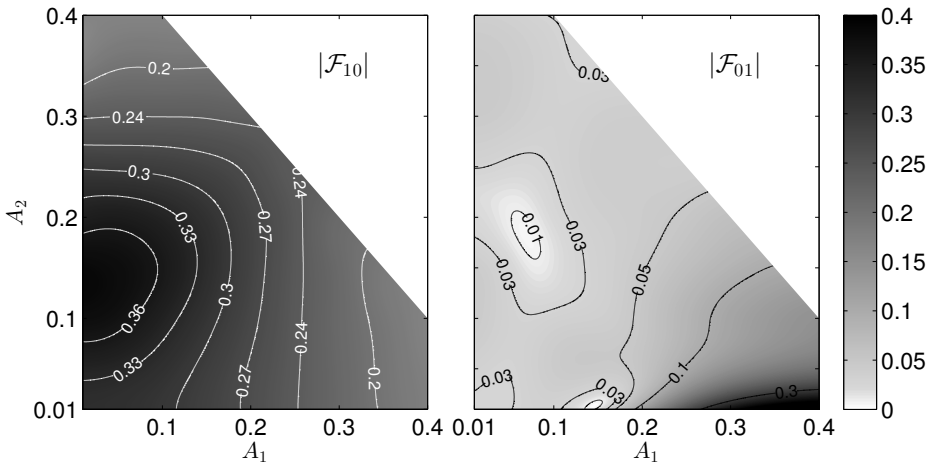

Fig. 4.6 Amplitudes dependence of the FDIDF gains. The forcing frequencies have been fixed at the arbitrary values $\mathrm{St}_1 = 1.513$ and $\mathrm{St}_2 = 5.153$. The region $A_1 + A_2 > 0.5$ has not been investigated.

the non-dimensional frequencies $\mathrm{St}_n \equiv L_f f_n / \overline{u}$ lie in the ranges $\mathrm{St}_1 \in [1.273,\ 3.024]$ and $\mathrm{St}_2 \in [4.138,\ 7.162]$ respectively. In the following, we will refer to mode 1 and mode 2 when referring to oscillations with a frequency in the range spanned by St_1 and St_2 respectively.

4.3.3 FDIDF calculation and validation

Figure 4.6 shows an example of the FDIDF gains as a function of the two forcing amplitudes. The forcing frequencies are fixed at arbitrary values. We observe that the gain of $\mathcal{F}_{10}$ (low frequencies) is generally larger than the gain of $\mathcal{F}_{01}$ (high frequencies); this is in line with the low-pass filter characteristics of the conical flame we are investigating. Also, for $\mathcal{F}_{10}$ we see that the gain tends to decrease with respect to both amplitudes, as was discussed in the previous section. This is not always true for the $\mathcal{F}_{01}$. It is not surprising because $\mathcal{F}_{01}$ contains the heat release response at frequencies spanned by St_2. Even in the FDF analysis we observed that, in this frequency range, the gain does not decrease monotonically with the amplitude, meaning that subcritical Hopf bifurcations and regions with multi-stable solutions may be observed.

In rare cases, we observe that the gain of $\mathcal{F}_{01}$ is larger than one. This always happens when the amplitude of A_1 is large (between 0.3 and 0.4), and the amplitude of A_2 is at its minimum, 0.01. This is due to the fact that, although we numerically ensure that the two forcing frequencies are incommensurate, their ratio can be close to a simple fraction. For example, in some cases the frequency St_2 is close to a harmonic of St_1. If the velocity amplitude at St_1 is large, the heat release responds significantly also at its harmonics. Because we perform FFTs

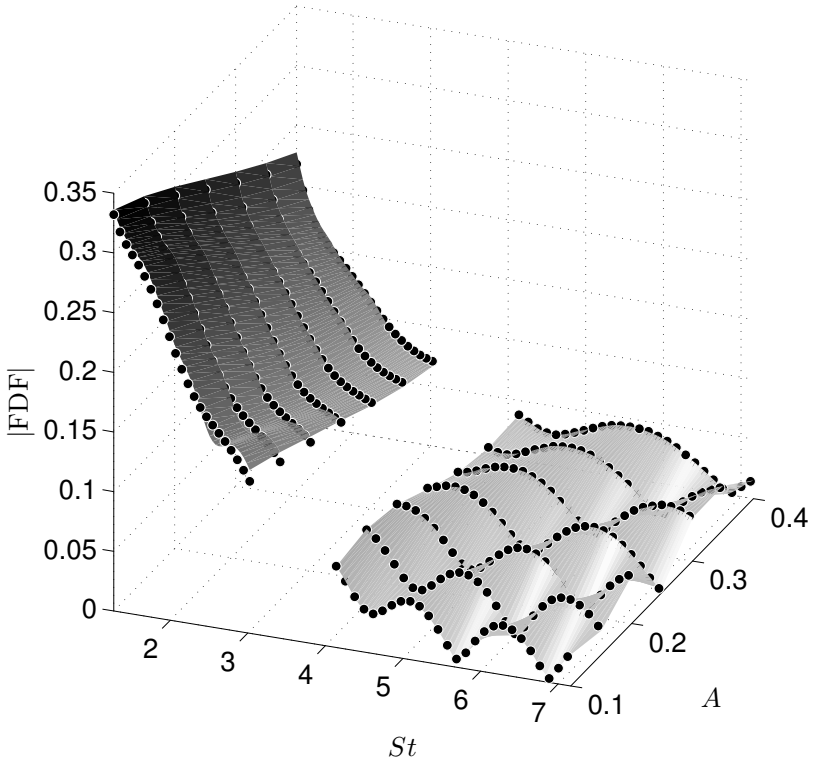

Fig. 4.7 In the limit in which one of the two amplitudes vanishes, the FDIDF tends to the FDF. FDIDF limits are plotted as surfaces and the FDF results as dots. In the region $\mathrm{St} \in [1.273,\ 3.024]$ the limit of $|\mathcal{F}_{10}|$ is plotted fixing $\mathrm{St}_2 = 5.153$ and $A_2 = 0.01$ in (4.10); in the region $\mathrm{St} \in [4.138,\ 7.162]$ the limit of $|\mathcal{F}_{01}|$ is plotted fixing $\mathrm{St}_1 = 1.513$ and $A_1 = 0.01$. The results compare well over the entire set of parameters investigated.

on signals of finite length, the FDIDF component at St_2 will contain part of the harmonic contribution of St_1, artificially increasing the gain of the second mode (see Figure 4.6). This is a source of error which increases when the thermoacoustic eigenfrequencies are close to multiples of each other. It could be reduced by integrating the governing equations over a longer time period, in order to have a better frequency resolution in Fourier space and distinguish the various peak contributions. However, this would lead to an extra numerical cost, which is undesirable.

A good test to assess the accuracy of the FDIDF calculations is to look at the limit in which the amplitude of one of the two modes goes to zero. From the definitions of the FDIDF and FDF one can verify that:

$$\begin{aligned} \lim_{A_2 \to 0} \mathcal{F}_{10}(A_1, \omega_1, A_2, \omega_2) &= \mathrm{FDF}(A_1, \omega_1) \qquad \forall\, \omega_2 \\ \lim_{A_1 \to 0} \mathcal{F}_{01}(A_1, \omega_1, A_2, \omega_2) &= \mathrm{FDF}(A_2, \omega_2) \qquad \forall\, \omega_1 \end{aligned}, \tag{4.10}$$

meaning that $\mathcal{F}_{10}$ tends to the FDF results in the region covered by St_1 when A_2 vanishes and, by exploiting the symmetry condition (4.9), $\mathcal{F}_{01}$ tends to the FDF results in the region covered by St_2 when A_1 vanishes.

By assuming that the FDIDF is a continuous function, we use the calculations at the smallest amplitudes we have investigated (0.01) as limits. Therefore, the horizontal slice of $|\mathcal{F}_{10}|$ at $A_2 = 0.01$ and the vertical slice of $|\mathcal{F}_{01}|$ at $A_1 = 0.01$ in Figure 4.6 need to match the FDF gain at $\mathrm{St} = 1.513$ and $\mathrm{St} = 5.153$ respectively (vertical slices of Figure 4.3). Figure 4.7 shows this comparison over the entire range of frequencies and amplitudes we have investigated. The limits agree well with the FDF results, with the largest difference between the FDF and the FDIDF limit being about 10^{-3}.

4.4 FDIDF analysis

We now couple the FDIDF with the acoustic response in a similar fashion as in Figure 1.2 and find the dispersion relations that need to be satisfied for quasiperiodic oscillations to exist. The coupling between the acoustic network and the FDIDF is sketched in Figure 4.8. Note that, although $\hat{q}_{10}$ is explicitly proportional only to $\hat{u}_{10}$ through $\mathcal{F}_{10}$, the latter is an implicit nonlinear function of both $\hat{u}_{10}$ and $\hat{u}_{01}$. Therefore, the dispersion relations we obtain when imposing the harmonic balance condition are coupled, and need to be simultaneously satisfied:

$$\begin{aligned} \mathcal{F}_{10}(A_1, s_1, A_2, s_2) H_{x_f}(s_1) - 1 = 0 \\ \mathcal{F}_{01}(A_1, s_1, A_2, s_2) H_{x_f}(s_2) - 1 = 0. \end{aligned} \tag{4.11}$$

Quasiperiodic oscillations of the form (4.4) exist when the growth rates of the Laplace variables $s_n = \sigma_n + \mathrm{i}\omega_n$ are both equal to zero, which is the condition under which the FDIDF was calculated. However, to investigate the stability of the FDIDF solutions, we want to calculate the rate of change of the growth rates when the calculated amplitudes are perturbed. This will yield solutions of (4.11) with non-zero growth rates. Because we are working with a non-static nonlinearity, the FDIDF is a function of two complex variables, and it is not straightforward to extend it to the complex $\mathbb{C}^2$ space. Thus, we decide to use the extrusion method of Schmid *et al.* (2013), by assuming that $\mathrm{FDIDF}(A_1, s_1, A_2, s_2) = \mathrm{FDIDF}(A_1, \mathrm{i}\omega_1, A_2, \mathrm{i}\omega_2)$, which is a zero-order approximation of the FDIDF around the steady-state solutions. This complication is not present in the study of Moeck & Paschereit (2012), because static nonlinearities were used. In that case, the FDIDF is a simpler object and depends only on the forcing amplitudes, not on the frequencies.

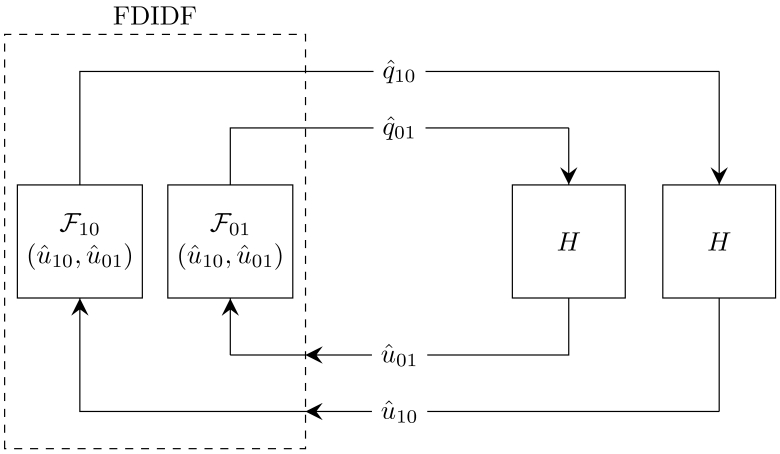

Fig. 4.8 Sketch of the FDIDF feedback loop with the acoustics. The FDIDF (dashed block) is a two-input, two-output nonlinear object. The output is formed with the superposition of two, coupled, nonlinear elements which respond at different frequencies. The two harmonic components of the quasiperiodic signal are indicated with subscripts $_{10}$ and $_{01}$ respectively. The implicit dependence of $\mathcal{F}_{10}, \mathcal{F}_{01}$ with respect to both $\hat{u}_{10}$ and $\hat{u}_{01}$ has been highlighted to emphasise that the dispersion relations (4.11) are coupled.

4.4.1 Linear stability of limit cycles: Neimark–Sacker bifurcations

A first set of solutions of the FDIDF are those for which the amplitude of one of the two modes is equal to zero. These are the FDF harmonic solutions. For example, if $A_2 = 0$ then we look for periodic solutions (with zero growth rate) of mode 1. From (4.11) we have:

$$\begin{aligned} \mathrm{FDF}(A_1, \mathrm{i}\omega_1) H_{x_f}(\mathrm{i}\omega_1) - 1 = 0 \\ \mathcal{F}_{01}(A_1, \mathrm{i}\omega_1, 0, s_2) H_{x_f}(s_2) - 1 = 0. \end{aligned} \tag{4.12}$$

The first equation derives from the limit (4.10) and converges to the FDF dispersion relation (1.4). It is now decoupled from the second equation. We have already calculated its solutions, shown as yellow lines in Figure 4.4. The second dispersion relation, however, contains information that the FDF cannot provide. It has to be solved for the frequency ω_2 and the growth rate σ_2 by fixing the frequency and amplitude of the other mode at the FDF solution. If the growth rate σ_2 is positive, then oscillations at frequency ω_2 are linearly unstable around the limit cycle with amplitude A_1 and frequency ω_1. The onset of these instabilities is known as a secondary Hopf or Neimark–Sacker bifurcation.

Figure 4.9 shows the bifurcation diagram of periodic solution when their stability is assessed with the FDIDF method. Most of the limit cycles that were found to be stable with the FDF method are now predicted to be unstable because, according to the solution

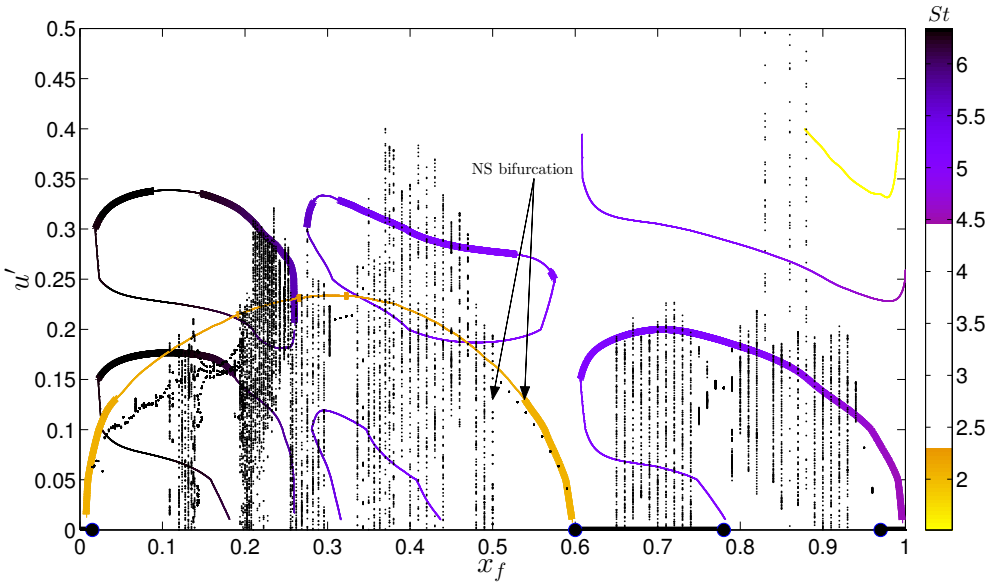

Fig. 4.9 Comparison between time domain (as in Figure 4.4) and FDIDF period bifurcation diagrams. The flame position x_f is used as a control parameter. Thin and thick lines are used to plot unstable and stable limit cycles respectively. Neimark–Sacker (NS) bifurcations are found at the edges of the stable solution with a non-zero amplitude.

of (4.12), oscillations at a different frequency will grow around them. This is consistent with the time integration results, in which we rarely observe periodic oscillations. Time domain and FDIDF results cannot compare perfectly throughout the entire bifurcation map, because the latter neglects contributions away from the input frequencies, which may be important at large amplitudes. However, the FDIDF correctly captures some of the system's bifurcations. For example, analysing Figure 4.9 from $x_f = 0.60$ backwards, time marching results show a supercritical Hopf bifurcation at $x_f = 0.59$, a Neimark–Sacker bifurcation at $x_f = 0.50$, and an inverse Neimark–Sacker at $x_f = 0.11$. The FDIDF method locates correctly the first Hopf bifurcation for mode 1, and predicts Neimark–Sacker bifurcations at $x_f = 0.53$ and $x_f = 0.045$.

With the FDIDF we can also calculate the frequency of oscillations that grow around limit cycles after Neimark–Sacker bifurcations. At $x_f = 0.53$ the FDIDF predicts that oscillations with a non-dimensional frequency $\mathrm{St}_2 = 5.0136$ are linearly unstable ($\sigma_2 = 2.86 \times 10^{-5}$) around the limit cycle with $A_1 = 0.1305$ and $\mathrm{St}_1 = 2.1132$. This prediction can be compared with self-excited time domain results. Figure 4.10 shows the FFT of the velocity signal just before and after the Neimark–Sacker bifurcation in the time domain (see Figure 4.9). In the former case, the oscillation is dominated by a component at frequency $\mathrm{St}_1 = 2.148$ with

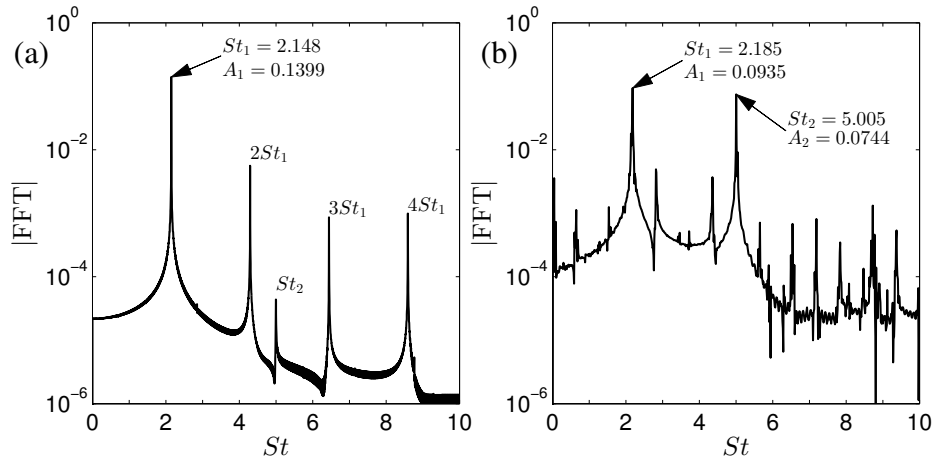

Fig. 4.10 FFT of velocity fluctuations of time domain simulations as described in 3. (a): $x_f = 0.51$, the solution is periodic, only a dominant peak at $\mathrm{St}_1 = 2.148$ is found; its harmonics are present but negligible. (b) $x_f = 0.49$, a second intense peak is found at $\mathrm{St}_2 = 5.005$; the system has undergone a subcritical Neimark–Sacker bifurcation.

intensity $A_1 = 0.1399$. Just after the bifurcation a second high peak appears at $\mathrm{St}_2 = 5.005$. All these results are consistent with the FDIDF predictions.

Discussion on cost and practical implementation

The FDIDF is a function of four independent input parameters. As a consequence, the numerical cost of building such an object increases quickly when wide ranges of parameters are investigated. By using the arguments in §§4.3.1-4.3.2, we limit as much as possible the width of these ranges. However, it is non-trivial to determine how to discretize these regions to appropriately estimate the FDIDF response. Because our model is low-order, we can afford to carry out a very detailed calculation of the FDIDF, and then investigate its dependence on the number of points used. We use about 60 discretization points for each frequency range. We vary the amplitudes in the range $[0.01, 0.4]$ in 9 steps, with the additional constraint that their sum does not exceed the threshold value of 0.5. With these limits, the total number of simulations we run to build the FDIDF is about 200 000. About 70 000 CPU hours were required to perform the analysis, which is approximately 5 times more expensive than the continuation method used by Waugh *et al.* (2014) to calculate limit cycle bifurcations on a similar thermoacoustic system with a continuation algorithm. We then use a four-dimensional cubic spline method to interpolate the real and imaginary parts of the FDIDF between calculated points onto a much finer grid, as functions of the input amplitudes

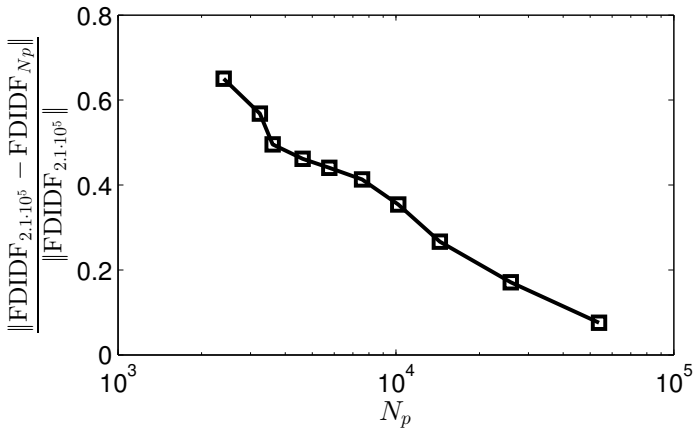

Fig. 4.11 Interpolated FDIDF relative error dependence with respect to the number of discretization points N_p used. Choosing fewer than 30 000 points leads to deviations from the actual response larger than 10%.

and frequencies. The interpolation is performed using either the full set of simulations or partial information only, to assess the effect of the discretization on the system dynamics.

Figure 4.11 shows the relative error of the interpolated FDIDF as a function of the number of points (always uniformly spaced) used for the interpolation. The results at the finest discretization, which are those used for the analysis in the rest of this chapter, are used as reference. By halving the number of discretization points used for St_1 and St_2, the cost of the FDIDF is reduced by a factor of 4 and the percentage error is about 5%. However, further reduction in the number of points used for the interpolation lead to larger errors, and significant deviation from the actual dynamic response should be expected. This shows that a large number of calculations is required to accurately estimate the FDIDF. This makes it currently non-affordable for, say, compressible LES studies, in which many CPU hours are already required to calculate the FDF only (Han *et al.*, 2015).

Part of the high cost of the current FDIDF analysis is due to the fact that all possible flame positions are investigated. Because a temperature jump follows the flame, the eigenfrequencies vary significantly when x_f spans from 0 to 1, and wide a range of frequencies needs to be investigated. In practical situations, this is probably not the case, and the frequency bands of interest may be narrower, thus reducing the number of calculations required for the FDIDF. Also, we emphasise that, to calculate the stability of limit cycles found with the FDF (as discussed in §4.4.1), we need only a part of the FDIDF calculation. This is because we examine cases in which one of the two amplitudes is small. The only parameter that has to be varied is the frequency of the small amplitude mode. In this framework, the FDIDF method is much cheaper (it approximately reduces to the cost of two FDFs), and is comparable in cost with the continuation method described by Waugh *et al.* (2014). The latter remains

more accurate, because it studies the stability of periodic solutions (i.e., the spectrum of the oscillations may contain peaks at the harmonics of the fundamental frequency), whereas the FDIDF is limited to harmonic solutions (i.e., the spectrum of the oscillations contains only one peak at the fundamental frequency). The advantage of the FDIDF is that it can be reused in different acoustic networks to calculate the stability of several thermoacoustic systems, whereas a new set of calculations has to be performed with numerical continuation for every acoustic network.

The use of the FDIDF to assess the stability of periodic solutions could also be exploited in experiments at approximately the cost of two FDFs by means of the following procedure: (i) measure an FDF; (ii) obtain harmonic solutions and their stability – with respect to a single mode – with the harmonic balance; (iii) for solutions that are predicted to be stable by the FDF method, perform another set of experiments to assess again their stability with respect to other forcing frequencies. This is accomplished by forcing the flame with a signal of the form (4.4), by fixing the amplitude and frequency of a mode at the FDF solution and the amplitude of the other mode at a small value. The only parameter left is the frequency of the second mode. It has to be varied over a range of dangerous frequencies, which can be obtained by the FDF results and the acoustic response. The stability of the FDF solutions with respect to other frequencies can then be calculated following the procedure described in §4.4.1.

4.4.2 Prediction and stability of quasiperiodic oscillations

Once limit cycles have become unstable, thermoacoustic oscillations converge towards another stable solution. This can be another periodic solution, with a different frequency and amplitude, a quasiperiodic attractor, or even a strange attractor. The FDIDF can approximate the location and stability of periodic and quasiperiodic solutions, but cannot predict the existence of other types of attractors, which were shown to exist in this type of thermoacoustic system by Kashinath *et al.* (2014); Orchini *et al.* (2015).

When looking for quasiperiodic attractors, the dispersion relations (4.11) need to be solved by fixing the growth rates σ_1 and σ_2 at zero, and looking for solutions with finite amplitudes for both modes. We rely on numerical techniques to find the roots of (4.11) that satisfy this conditions starting from a good initial guess. Because five parameters (two amplitudes, two frequencies and the bifurcation parameter) can be varied, a large number of initial guesses can be chosen, which is numerically inefficient. To reduce the numerical cost, we first locate isolated solutions by starting from a coarse grid of initial guesses that covers the parameter space. Then, we extend the solutions to continuous lines with an arclength continuation method by slowly varying the bifurcation parameter.

Stability criterion

We find several sets of quasiperiodic solutions and require a criterion to assess their stability. From a dynamical system viewpoint, the coupled evolution of the oscillations' amplitudes can be written in terms of a linear operator L and a nonlinear operator $N(\boldsymbol{A})$ as

$$\frac{\mathrm{d}A_j}{\mathrm{d}t} = L_{jj}A_j + N_j(\boldsymbol{A}) \equiv \sigma_j(\boldsymbol{A})A_j, \tag{4.13}$$

where $\boldsymbol{A}$ is the amplitudes vector. Although the explicit expressions for the linear and nonlinear operators are not known, σ_j represents a nonlinear growth rate, in the sense that its intensity varies with the amplitudes of the oscillations. A steady-state solution is found when (4.13) equals zero. A solution for which at least one $A_j \neq 0$ is a non-trivial solution of the dynamical system (i.e., not a fixed point). The amplitude of each mode varies with respect to the value of its growth rate only, which is implicitly a function of all the amplitudes. For our system, which contains only two modes, the dynamical system (4.13) reduces to:

$$\begin{aligned} \dot{A}_1 &= \sigma_1(A_1, A_2)A_1 \\ \dot{A}_2 &= \sigma_2(A_1, A_2)A_2. \end{aligned} \tag{4.14}$$

Equations (4.14) will slowly vary the oscillations' amplitudes, which in turn will change the growth rates and frequencies according to the solution of (4.11) at the current amplitudes. Equations (4.14) were also discussed in Moeck & Paschereit (2012), where their interpretation in terms of an averaging procedure was also provided.

Let us now indicate a solution of (4.14) with overlines. These solutions are fixed point if both amplitudes are equal to zero, limit cycles if only one amplitude is zero, or quasiperiodic if both amplitudes are non-zero. By linearising equation (4.14) around a solution, the evolution of small perturbations, indicated with Δ, is given by:

$$\frac{d}{dt}\begin{bmatrix} \Delta A_1 \\ \Delta A_2 \end{bmatrix} = \begin{bmatrix} \frac{\partial \sigma_1}{\partial A_1}\overline{A}_1 + \overline{\sigma}_1 & \frac{\partial \sigma_1}{\partial A_2}\overline{A}_1 \\ \frac{\partial \sigma_2}{\partial A_1}\overline{A}_2 & \frac{\partial \sigma_2}{\partial A_2}\overline{A}_2 + \overline{\sigma}_2 \end{bmatrix} \begin{bmatrix} \Delta A_1 \\ \Delta A_2 \end{bmatrix} \equiv \boldsymbol{J}\Delta\boldsymbol{A}, \tag{4.15}$$

where the partial derivatives are evaluated at the solution. If the eigenvalues of the Jacobian $\boldsymbol{J}$ have negative real parts, the solution under consideration is stable.

It is worth discussing the forms that the Jacobian assumes for the different types of solutions. For a fixed point, both amplitudes vanish and $\boldsymbol{J}$ simply contains the growth rates $\overline{\sigma}_1$ and $\overline{\sigma}_2$ on the main diagonal, retrieving the classic linear stability result. For a limit cycle

solution (say of mode 1), the Jacobian takes the form

$$\boldsymbol{J}_{LC} = \begin{bmatrix} \frac{\partial \sigma_1}{\partial A_1}\overline{A}_1 & \frac{\partial \sigma_1}{\partial A_2}\overline{A}_1 \\ 0 & \overline{\sigma}_2 \end{bmatrix} \tag{4.16}$$

and has eigenvalues $\partial\sigma_1/\partial A_1\overline{A}_1$ and $\overline{\sigma}_2$. Because $\overline{A}_1$ is positive, the stability is determined by the signs of $\partial\sigma_1/\partial A_1$ (the FDF condition) and $\overline{\sigma}_2$. This is a rigorous derivation of the stability condition that was intuitively discussed in the previous section. Furthermore, the eigenvector corresponding to the limit cycle eigenvalue $\partial\sigma_1/\partial A_1\overline{A}_1$ is orientated along the A_1 direction. The second eigenvector, however, has a non-trivial direction and can be calculated only having the FDIDF. We will shortly return to the significance of these eigenvectors in the FDIDF analysis.

Lastly, for quasiperiodic solutions we obtain that the stability is determined by the eigenvalues of the Jacobian

$$\boldsymbol{J}_{QP} = \begin{bmatrix} \frac{\partial \sigma_1}{\partial A_1}\overline{A}_1 & \frac{\partial \sigma_1}{\partial A_2}\overline{A}_1 \\ \frac{\partial \sigma_2}{\partial A_1}\overline{A}_2 & \frac{\partial \sigma_2}{\partial A_2}\overline{A}_2 \end{bmatrix} \tag{4.17}$$

This is not exactly the condition that was suggested by Moeck & Paschereit (2012), whose Jacobian does not depend on the solution amplitudes. Nonetheless, condition (4.17) derives from the linearisation of the amplitudes' evolution around a solution. Given that we retrieve correct physical conditions for the stability of fixed point and limit cycles, we shall expect it to hold even for quasiperiodic oscillations.

Two methods can be used to calculate the partial derivatives of the growth rates with respect to the amplitudes. By brute force, in analogy with equation (4.3), one can fix one amplitude at its solution's value, slightly perturb the other amplitude, and determine the variations in frequency and growth rate of both modes by solving (4.11) with an iterative method. Alternatively, the implicit function theorem may be used, as suggested by Moeck & Paschereit (2012). The latter is quicker and more reliable because no iterative methods need to be used. Details on the implicit function theorem method are given in C. Both methods have been tested and yield the same results.

FDIDF bifurcation analysis

Figure 4.12 contains the FDIDF solutions when the bifurcation parameter is varied between $0.40 \leq x_f \leq 0.60$. Limit cycle solutions lie on $A_1 = 0$ and $A_2 = 0$, whereas solutions for which both amplitudes are non-zero are quasiperiodic. We have plotted with black filled circles attractors (solutions for which both eigenvalues have a negative real part), with red

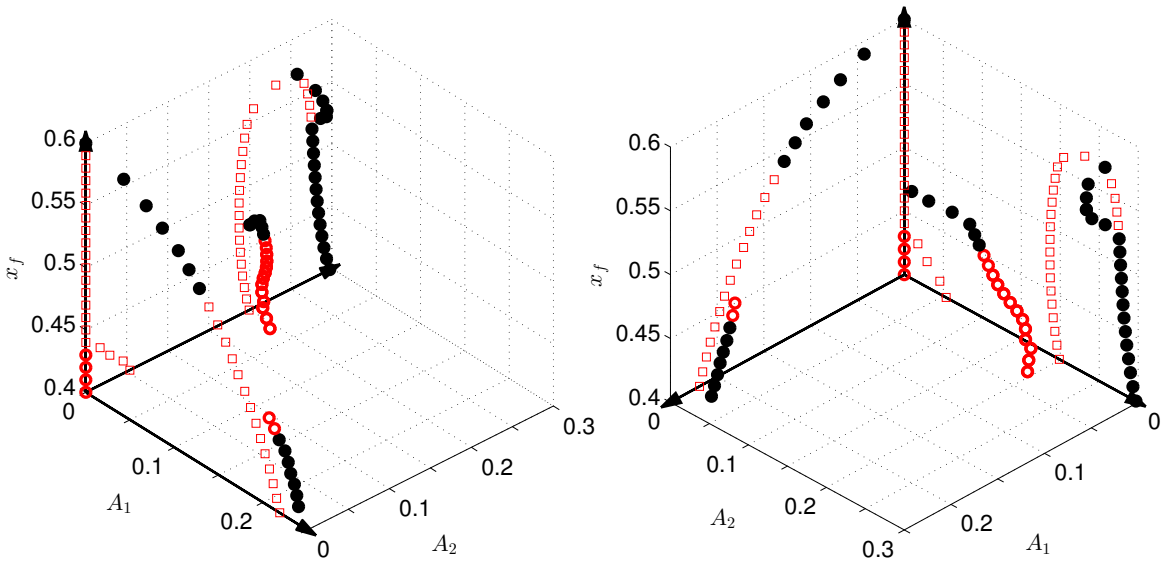

Fig. 4.12 FDIDF bifurcation diagram in the region $0.40 \leq x_f \leq 0.60$. The FDF solutions of mode 1 and 2 lie on the $A_2 = 0$ and $A_1 = 0$ planes, respectively. The fixed point solutions lie on the line $A_1 = A_2 = 0$. Super- and subcritical quasiperiodic oscillations are found. The stability of all solutions is assessed with the FDIDF conditions. Stable attractors are indicated with filled black circles, repellors with empty red circles and saddle-nodes with empty red squares. Two views of the same bifurcation diagram are shown.

empty circles repellors (both eigenvalues have a positive real part), and with red squares saddle-nodes (one eigenvalue has a positive real part, and the other a negative real part). The latter are particularly interesting because thermoacoustic oscillations can be first attracted towards them along their stable manifold, and only later diverge along the unstable manifold towards an attractor. If the growth rate of the unstable mode is small, the oscillations may persist for a long time around the saddle-node state. This can be problematic for time domain simulations or experiments, because the system has to be observed for a long time before being sure that the final attractor has been reached. Saddle-nodes in thermoacoustic systems were also discussed in Kashinath *et al.* (2014), where they were referred to as "unstable attractors".

A convenient way of representing the FDIDF results is through phase-planes. A phase-plane contains the trajectories that the amplitudes will follow before converging to an attractor. Starting from different initial conditions can lead thermoacoustic oscillations towards different attractors. The set of initial conditions that converge towards an attractor is known as the basin of attraction of the attractor. On a theoretical basis, it should be possible to identify the basins of attraction boundaries by investigating the growth rates of the thermoacoustic modes while varying the oscillations' amplitudes. However, we find

that when we are not close to steady-state solutions of our system, the growth rates that satisfy equations (4.11) quickly become large. The FDIDF was not evaluated under these conditions, therefore it cannot be used to build the phase-planes because the extrusion method we adopted is no longer valid. Note that, for a static nonlinearity as the one considered by Moeck & Paschereit (2012), this problem does not arise because the FDIDF is a function of the amplitudes only.

For the non-static nonlinearity we are considering in this chapter, the FDIDF can still be used to estimate the phase-planes. This is accomplished by calculating the eigenvectors of the Jacobian (4.15). By means of the Centre Manifold Theorem (Guckenheimer & Holmes, 1983), the eigenspaces spanned by the eigenvectors associated with the stable and unstable eigenvalues are locally tangent to the stable and unstable manifolds respectively. A sketch of the phase-planes of our system across the Neimark–Sacker bifurcation at $x_f = 0.53$ is shown in Figure 4.13. Stable and unstable solutions are plotted with the same shape and colour scheme of Figure 4.12, together with vectors pointing in the direction of their eigenvectors. For saddle-nodes, these vectors are locally tangent to the stable and unstable manifolds. For attractors and repellors, the eigenvalues and eigenvectors of $\boldsymbol{J}$ can be complex-valued. In this case, trajectories will spiral inwards/outwards the solution. We have also sketched with dashed lines possible heteroclinic orbits. A heteroclinic orbit is a path that connects an unstable solution to a stable one. Note that some solutions may be missing from our maps, because they can lie in a region we have not investigated (large amplitudes or amplitudes smaller than 0.01), or they can be strange attractors that we cannot locate.

Although we have only partial information about phase-planes, they help to identify possible routes that thermoacoustic oscillations undertake before converging to an attractor. For example, let us consider Figure 4.13a, which corresponds to the x_f location just before the Neimark–Sacker bifurcation marked in Figure 4.9. Starting from the quiescent state $A_1 = A_2 = 0$, the oscillations will be attracted towards the stable limit cycle solution along $A_2 = 0$. However, starting from an excited state with $A_2 \neq 0$ or by triggering the system, the oscillations may converge to a different attractor. Here, the other possible attractors are quasiperiodic. We have added a non-calculated solution (marked with a question mark) in order to sketch some heteroclinic paths. The position of this solution however is not entirely arbitrary; by slowly varying the bifurcation parameter, the limit cycle solution at $A_2 = 0$ loses its stability. A possible scenario is that, at the bifurcation point, a quasiperiodic repellor (or another type of oscillation) collapses onto the stable limit cycle solution. After the bifurcation (Figure 4.13b), the limit cycle on A_1 turns into a saddle-node, changing the topology of the phase-plane. Now, starting from a quiescent state thermoacoustic oscillations are first attracted towards the limit cycle solution along the $A_2 = 0$ axis (which is the limit cycle

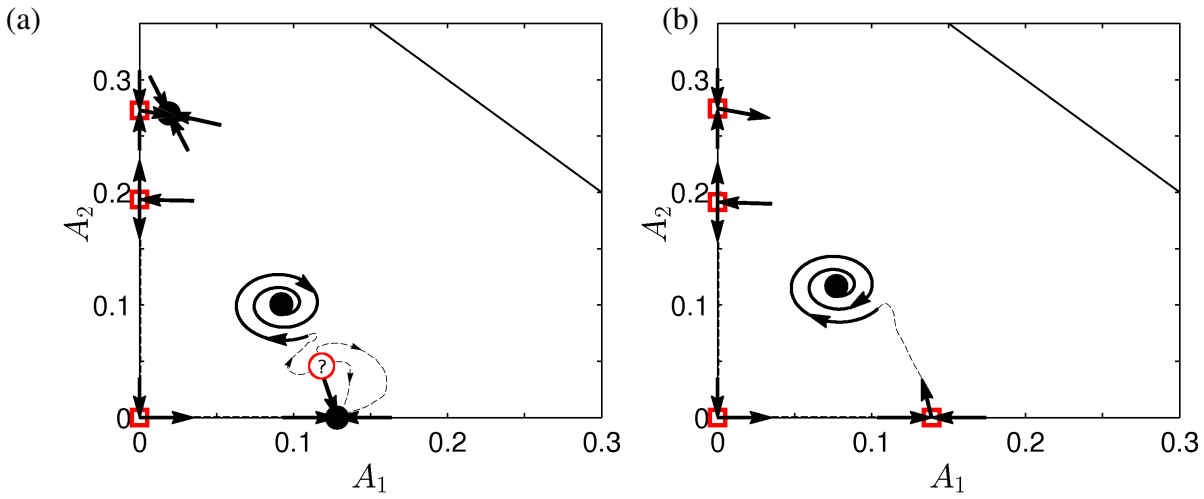

Fig. 4.13 Sketch of phase-planes before (a) and after (b) the Neimark–Sacker bifurcation at $x_f = 0.53$. The arrows pointing inwards and outwards the solutions indicate the directions of the Jacobian eigenvectors with a negative and positive growth rate, respectively. Some hypothetical heteroclinic orbits are sketched with dashed lines. Across the bifurcation, the amplitude A_1 (A_2) of the attractor reached starting from a quiescent state suddenly decreases (increases).

stable manifold), and only later are repelled from it along the unstable manifold towards the stable quasiperiodic oscillation. This is exactly what is observed in time domain simulations, although not shown here. Analogous time domain results can be find in Kashinath *et al.* (2014).

Lastly, Figure 4.13 also shows that the amplitudes A_1 and A_2 suddenly vary across the bifurcation. This is possible across a Neimark–Sacker bifurcation, as solutions are suddenly attracted towards a different attractor. Time domain results of the same bifurcation shown in Figure 4.10 are in line with this FDIDF prediction. Indeed, The FFT of the time signal before and after the bifurcation shows that the amplitudes A_1 (A_2) suddenly decreases (increases) across the bifurcation. This feature of Neimark–Sacker bifurcations is also seen in the time domain results shown in Figure 4.9. At $x_f = 0.50$ the maximum amplitude of the oscillations suddenly deviates from the limit cycle amplitude before the bifurcation. A fair comparison between the oscillation amplitudes predicted by the FDIDF and time marching is seen by looking at the position of the stable quasiperiodic attractor in Figure 4.13 and the intensity of the peaks in Figure 4.10. Note that, however, these figures contain information at slightly different values of x_f, because the location of the Neimark–Sacker bifurcation predicted by the two methods is slightly different, due to the FDIDF approximations.

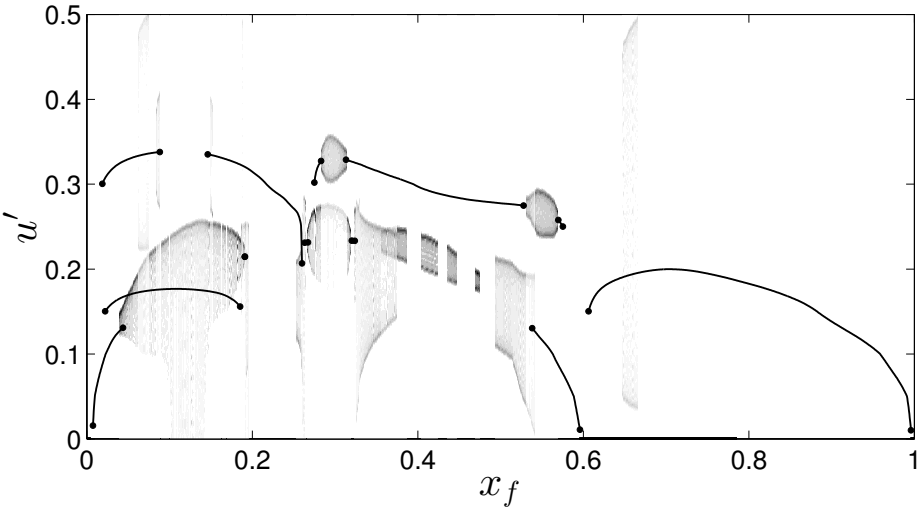

Fig. 4.14 Overview of the FDIDF bifurcation diagram. PDF of stable quasiperiodic solutions' peaks (shaded regions) are plotted on top of stable limit cycle amplitudes (lines). The PDF intensity is higher in darker regions. The location of Neimark–Sacker bifurcations is highlighted with dots.

We conclude the chapter by showing in Figure 4.14 the bifurcation diagram calculated with the FDIDF in the entire range $0 \leq x_f \leq 1$. We have plotted only the peaks of stable oscillations, which are those observable in self-excited experiments or time domain simulations. For limit cycle solutions, these peaks are shown as lines corresponding at the oscillations' amplitude. For quasiperiodic solutions, we calculate the Probability Density Functions (PDF) of their peaks. These are shown as shaded regions in Figure 4.14. The locations of Neimark–Sacker bifurcations have been highlighted with black dots. One can see that there is a nice match between their location and the onset of stable quasiperiodic solutions. This does not happen if we apply the stability criterion for quasiperiodic solutions contained in Moeck & Paschereit (2012). In the region $0.60 \leq x_f \leq 1$, quasiperiodic oscillations tend to have a large amplitude, which exceeds the $A = 0.5$ threshold we have set when calculating the FDIDF. This is partly consistent with time domain results, in which very large oscillations, e.g. at $x_f = 0.83$, are occasionally observed. In some regions, multiple stable solutions are found. With time marching methods, a thorough investigation of the initial condition is required to find these solutions.

4.5 Summary and conclusions

We have presented a numerical approach for the investigation of non-periodic thermoacoustic oscillations. A Flame Double Input Describing Function (FDIDF) of a non-static nonlin-

ear flame model based on the *G*-equation has been calculated by forcing the flame with a quasiperiodic signal composed of two harmonic components with independent amplitudes and incommensurate frequencies. The FDIDF assumptions and limitations have been outlined, and the FDIDF has been tested against the Flame Describing Function (FDF) in the limit in which the amplitude of a mode is small. The FDIDF has been embedded into a thermoacoustic network and, through the harmonic balance method, stable and unstable thermoacoustic oscillations have been calculated. Furthermore, a criterion to assess their stability has been derived.

The FDIDF contains a far more accurate approximation of the nonlinear flame response than the FDF. Exploiting all its information, one can predict the amplitude and stability of quasiperiodic solutions. Also, via the Centre Manifold Theorem, it can be used to sketch phase-planes to understand the path that thermoacoustic oscillations trajectories will take. Quantitative comparisons between the FDIDF and time marching results have been presented. We have shown that the FDIDF is capable of predicting the location of Neimark–Sacker bifurcations, the frequency of the unstable modes and the amplitude of the final quasiperiodic oscillations. We have discussed in detail the change in behaviour of a system at a Neimark–Sacker bifurcation, across which a new mode becomes unstable and the amplitude of the oscillations varies abruptly. This can lead to quasiperiodic oscillations or mode-switching to another stable periodic oscillation at a different frequency. Neither type of behaviour can be predicted by linear stability analysis nor by the FDF framework.

Although the FDIDF is an expensive object to calculate, for simple dynamical flame models, such as the *G*-equation, this is affordable. Also, we have shown how its cost can be greatly reduced if one is interested in calculating only the stability of limit cycles. This accounts for the nonlinear interaction between modes, which the FDF ignores, and provides the location of Neimark–Sacker bifurcations. Only the information at which one of the amplitudes is fixed at a very small value is needed for this, and the cost of the FDIDF reduces to the cost of a second FDF, making it affordable for experimental purposes too. We find that, for our system, most of the limit cycles that are predicted to be stable by the FDF method, are predicted to be unstable by the FDIDF method. This is consistent with self-excited time marching results of the same thermoacoustic system. Within this framework, the FDIDF is capable of predicting the frequency of oscillations that will grow in time around limit cycles. Knowing these frequencies, Helmholtz resonators can be tuned and retro-fitted to the thermoacoustic system in order to make it less prone to oscillations.

Chapter 5

Weakly nonlinear analysis of thermoacoustic bifurcations

In this chapter, a weakly nonlinear formulation of the equations governing thermoacoustic oscillations in the Rijke tube is presented. In contrast to previous expansions available in the literature, which approximate the acoustic response with a single Fourier mode, here the contribution of multiple modes is retained. Because of this, adjoint methods are required to derive the Stuart–Landau equations, which govern the oscillations' saturation mechanism. Although the weakly nonlinear expansion is strictly valid only close to the expansion point, it is shown how it provides an accurate and inexpensive method for the investigation of nonlinear effects.

This work was the result of a collaboration with Dr. Georgios Rigas. Part of the content of this chapter is under consideration for publication in Orchini *et al.* (2016).

5.1 Introduction

Weakly nonlinear analysis is a nonlinear method capable of tracking the evolution of the oscillations' amplitude. It is based on an asymptotic expansion of the governing equations in the vicinity of a bifurcation point. This approach provides an analytical description of the perturbation dynamics, which is exact up to the order of the truncated expansion. In general, a weakly nonlinear solution is calculated as a superposition of one or more spatial modes with a time dependent amplitude. The temporal evolution of the amplitude is reduced to an ordinary differential equation (ODE) - appearing as a Stuart–Landau equation - for every linearly unstable mode. Solving the latter equation is much faster than time marching the full

nonlinear system, and also provides physical insight into the nonlinear interactions between the modes.

Weakly nonlinear analysis has been widely used in hydrodynamics to study the transition of globally unstable flows and derive low-order models of the Navier–Stokes equations around bifurcation points (Chomaz, 2005). In the simple case of the cylinder flow, which undergoes a supercritical Hopf bifurcation at a diameter-based Reynolds number $\mathrm{Re} \approx 46$, the Stuart–Landau equation accurately captures the amplitude of the most unstable global shedding mode close to the threshold of bifurcation (Landau, 1944*b*; Provansal *et al.*, 1987). Sipp & Lebedev (2007) showed how the Stuart–Landau equation can be derived from the Navier–Stokes equations using global stability analysis and a multiple timescale expansion. As a consequence of the global character of the analysis, adjoint methods were required to identify the Landau coefficients of the model.

Weakly nonlinear tools have been applied also to thermoacoustic systems. Culick (2006) used the method of averaging to derive the amplitude evolution for thermoacoustic models with one or two oscillating modes. In the same framework, Juniper (2012) described how the averaged quantities can be connected to the Flame Describing Function methodology. Ghirardo *et al.* (2015) applied the method of averaging to azimuthal thermoacoustic instabilities, in which two counter-rotating azimuthal modes with the same frequency are simultaneously unstable. Subramanian *et al.* (2013) used the method of multiple scales to derive a Stuart–Landau equation at third order describing the evolution of the oscillation amplitude in a Rijke tube. The Landau coefficients showed that the Hopf bifurcation was subcritical, and the low-amplitude limit cycles arising close to the Hopf point were unstable, in agreement with experimental studies.

The unstable limit cycles arising from subcritical bifurcations in a Rijke tube may undergo a fold bifurcation to become stable, and create a region of bi-stability (Ananthkrishnan *et al.*, 2005; Juniper, 2011; Jegadeesan & Sujith, 2013). In the weakly nonlinear analysis performed by Subramanian *et al.* (2013), however, the expansion was truncated at third order. Therefore, the fold point, the amplitude of stable limit cycles, and the bistable region could not be predicted by their weakly nonlinear methods, because this would require expansion to at least fifth order. In their case, however, even an expansion at higher order would not have captured the fold point for reasons explained in section §5.2.2. It is also worth noting that in the weakly nonlinear studies on the Rijke tube (Juniper, 2012; Subramanian *et al.*, 2013) only one Galerkin mode was used to describe the dynamics. This can be a rough approximation for some thermoacoustic networks, because considering only one acoustic mode may alter the nature and amplitude of the oscillations, as was discussed by Jahnke & Culick (1994); Ananthkrishnan *et al.* (2005).

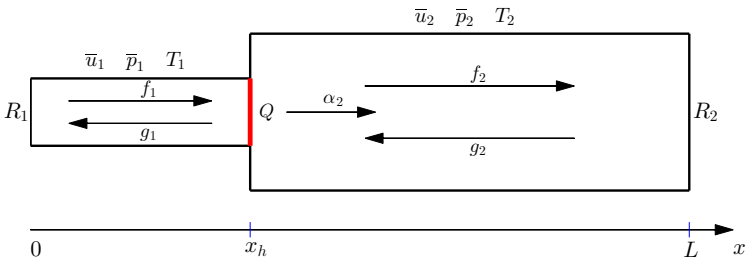

Fig. 5.1 Horizontal Rijke tube model. Subscripts $_1$ and $_2$ indicate flow and wave properties in the upstream and downstream ducts respectively. The intensity of the heat release fluctuations will be used as a control parameter.

In this chapter, we perform a high order weakly nonlinear analysis of thermoacoustic oscillations in a Rijke tube close to a subcritical Hopf bifurcation. The high order expansion allows us to obtain analytical expressions for the location of the bistable region and the amplitude of both unstable and stable limit cycles. In our analysis, this is achieved by using a wave-based approach when solving the linear acoustic equations. It provides a more general description of a thermoacoustic network, and enables us to include temperature and area variations in the analysis. We also retain the contribution of multiple acoustic modes to the dynamics of the thermoacoustic system. This corresponds to approaching the problem in a global framework, and adjoint methods are required to calculate the Landau coefficients through solvability conditions (Sipp & Lebedev, 2007).

The chapter is organised as follows. In §5.2 we present the Rijke tube thermoacoustic set-up and the wave-based governing equations; the nonlinear heat release model adopted for this study is discussed; the damping mechanisms adopted to stabilise high-frequency modes are presented. In §5.3 we perform a linear stability analysis of the system and we identify the location of Hopf bifurcations, when the heat release power is used as a control parameter. In §5.4 we present the theoretical framework for the weakly nonlinear analysis, deriving in detail the equations for the amplitude evolution of the dominant mode up to fifth order. In §5.5 we validate our weakly nonlinear results against the exact solutions of the fully-nonlinear equations, obtained with a continuation algorithm method and time domain simulations. For our system, we find that, depending on the width of the subcritical region, an expansion up to seventh order is needed to obtain a good agreement with the exact solutions. In §5.6 we discuss how the method could be applied to more complex systems. Finally, in §5.7 we summarise our findings and discuss possible future applications.

5.2 Thermoacoustic modelling

The configuration considered in this chapter is a horizontal Rijke tube, as shown in Figure 5.1. It has been extensively considered by many authors (Matveev, 2003; Juniper, 2011; Subramanian *et al.*, 2013; Magri & Juniper, 2013*b*; Mariappan *et al.*, 2015) for the analysis of thermoacoustic phenomena. However, weakly nonlinear analyses of thermoacoustic oscillations presented in these studies have been approximated by considering a single pair of Galerkin modes for the acoustic response. It was shown by Jahnke & Culick (1994); Ananthkrishnan *et al.* (2005); Kashinath *et al.* (2014) that considering only one acoustic mode may alter the amplitude and type of thermoacoustic oscillations. Also, mean flow and temperature jump effects are often neglected, although their presence affects the thermoacoustic eigenmodes and the stability of the system. Although our model remains low-order, we consider a wave-based approach which naturally yields a more realistic description of the acoustic response of the system (Dowling, 1995; Orchini *et al.*, 2015), and is easily scalable to more complex acoustic networks, which is important when considering, say, gas turbines.

5.2.1 Acoustic model

The acoustic network we consider is a duct of length L with an inlet of area A_1. We prescribe mean flow $\overline{u}_1$, mean pressure $\overline{p}_1$, and inlet temperature T_1. The heater is located at a distance x_h downstream. Across the heater we impose a temperature jump $\Delta \equiv (T_2/T_1)^{1/2} = c_2/c_1$, determined by the heater mean heat release, and an area change $\Theta \equiv A_2/A_1$. We decompose the acoustic velocity, pressure and density fluctuations into downstream (f) and upstream (g) travelling acoustic waves and an entropy (α) wave. Entropy waves play a minor role in this study, but their contribution would be more relevant if the system were to have a choked exit. Mass, momentum and energy fluxes are conserved through the heater via the Rankine-Hugoniot jump conditions (Dowling, 1995; Stow & Dowling, 2001).

The reflection coefficients provide the relations $f_1 = R_1 g_1 e^{-s\tau_1}$ and $g_2 = R_2 f_2 e^{-s\tau_2}$, where $\tau_1 \equiv 2x_h c_1/(c_1^2 - \overline{u}_1^2)$ and $\tau_2 \equiv 2(L-x_h)c_2/(c_2^2 - \overline{u}_2^2)$. The inlet reflection coefficient is chosen to be $R_1 = -0.9$. For the outlet, we use either $R_2 = -0.9$ or a frequency dependent reflection coefficient, depending on the damping model adopted, as discussed in §5.2.3.

By following a procedure analogous to that described in Dowling (1995); Orchini *et al.* (2015), we calculate the linear acoustic response to heat release fluctuations q', which is

given by the equations:

$$M \begin{bmatrix} g_1 \\ f_2 \\ \alpha_2 \end{bmatrix} = \begin{bmatrix} M_{11} & M_{12} & M_{13} \\ M_{21} & M_{22} & M_{23} \\ M_{31} & M_{32} & M_{33} \end{bmatrix} \begin{bmatrix} g_1 \\ f_2 \\ \alpha_2 \end{bmatrix} = \begin{bmatrix} 0 \\ 0 \\ q'/(A_1 c_1) \end{bmatrix}, \tag{5.1}$$

which represent mass, momentum and energy conservation across the heater element.

The coefficients in the matrix M are reported in Appendix D. By setting the determinant of M equal to zero (i.e., by solving a nonlinear eigenvalue problem) we find the acoustic eigenfrequencies. Solving for the wave amplitudes as a function of q' provides the acoustic transfer functions of pressure, velocity and density fluctuations with respect to heat release oscillations at any point in the duct. We are interested in the velocity response u' just upstream the flame for the coupling with the heater. We cast this response in state-space form:

$$\frac{\mathrm{d}\boldsymbol{x}}{\mathrm{d}t} = A\boldsymbol{x} + \boldsymbol{B}q' \tag{5.2a}$$

$$u' = \boldsymbol{C}\boldsymbol{x}, \tag{5.2b}$$

by following the procedure described in Chapter 2. If an expression for the heat release is provided, the above equation describes the dynamics of thermoacoustic oscillations.

5.2.2 Heat release model

King's law (King, 1914) expresses the heat transferred from a hot-wire to the flow under steady flow conditions. With a quasi-steady argument, (i.e., assuming that the instantaneous heat transfer is determined by the instantaneous velocity), an unsteady, nonlinear model for the heat release fluctuations is obtained:

$$Q = k(T_w - T_1)L_w \left(1 + \sqrt{\frac{2\pi c_p d_w}{k}|\bar{u} + u'(t-\tau)|}\right), \tag{5.3}$$

where k, T_w and L_w are the air thermal conductivity, wire temperature and total length respectively, c_p the specific heat per unit volume, d_w the wire diameter, and τ a time delay. The heat release time delayed response with respect to acoustic velocity fluctuations models the low-frequency response of the heater, as found by Lighthill (1954). The non-dimensional fluctuations are given by:

$$q' = K\left(\sqrt{|1 + u'(t-\tau)|} - 1\right), \tag{5.4}$$

with $K \equiv \sqrt{2\pi c_p d_w \bar{u}/k}$. Note that the gain of (5.4) does not decrease at high frequencies, because it is a static heat release model (i.e., q' does not depend on $\mathrm{d}u'/\mathrm{d}t$). This is problematic because, if not damped, high-frequency modes are as likely to be unstable as low-frequency modes, which is unphysical. To overcome this issue, two damping mechanism are used, to highlight some features of the weakly nonlinear expansions, and are discussed in §5.2.3.

In Subramanian *et al.* (2013) a Taylor expansion of the heat release fluctuations (5.4) around $u' = 0$ was considered for a weakly nonlinear analysis. However, due to the presence of an absolute value in equation (5.4), such a Taylor series converges to the original heat release expression only for $u' > -1$, as shown in Figure 5.2a. This is problematic because the fact that q' increases when $u' < -1$ decreases is the only saturation mechanism, which we want to model in this analysis. The weakness of the Taylor expansion for this model can be quantitatively shown by calculating the Describing Function (DF) of King's model. Imposing harmonic velocity oscillations $u' = A\cos(\omega t)$, the DF is defined as (Gelb & Velde, 1968):

$$\mathrm{DF}(q') \equiv \frac{K}{A\pi}\int_0^{2\pi}\left(\sqrt{|1+A\cos(\theta-\omega\tau)|}-1\right)e^{\mathrm{i}\theta}\,\mathrm{d}\theta. \tag{5.5}$$

Its gain is shown in Figure 5.2b together with the DF gain of the Taylor expansion, which does not saturate when the amplitude increases. Note that the unsteady King's law DF gain first increases up to an amplitude of $A = 1$ and then decreases. The initial increase in gain is probably a non-physical feature of the model. It arises upon the introduction of a time-delayed unsteady velocity dependence in King's law, which was originally derived under steady-flow assumptions. Although time-delayed unsteady flow effects provide the correct connection between King's law at small amplitudes with the linear dynamical theory of Lighthill (1954) at low-frequencies, it is questionable if these effects correctly capture the nonlinear dynamics of the heater at high amplitudes. Indeed, CFD simulations performed by Selimefendigil *et al.* (2012) on the fully nonlinear unsteady equations of a pulsating flow around a hot-wire have shown that the gain of heat release describing function monotonically decreases when the forcing amplitude increases. Furthermore, Witte & Polifke (2015) reported that the Reynolds number Re based on the wire diameter has a great influence on the linear response of the heater, which, for low values of Re, is very different from the one predicted by Lighthill (1954).

Because a smooth, nonlinear, dynamical model for a heater response is not available in the literature, we perform a least square fit of equation (5.4) onto a fifth order polynomial of the form:

$$q'(t) = K\sum_{n=1}^{5}\alpha_n u'^n(t-\tau). \tag{5.6}$$

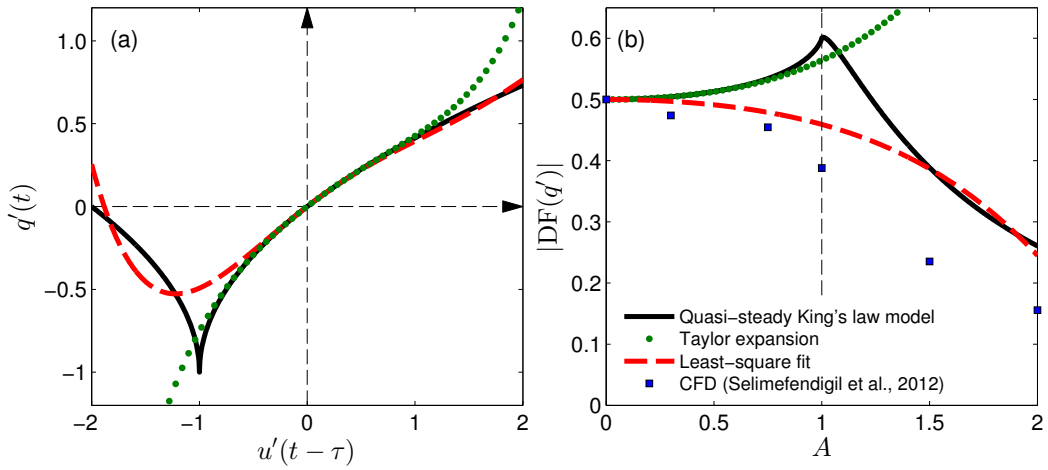

Fig. 5.2 Nonlinear heat release models. (a): comparison between unsteady King's law, fifth order Taylor expansion and polynomial fit approximations. K is fixed to 1. (b): the DF's gain of King's model and its approximations. The saturation mechanism starts at $A = 1$ and is due to the abrupt change of sign of the heat release derivative. The Taylor expansion around $u' = 0$ cannot capture this mechanism. CFD results from Selimefendigil *et al.* (2012) (scaled to match the linear gain) are in qualitative agreement with the least-square fit model that we use in this chapter.

In order to ensure that the linear stability of the thermoacoustic problem is not affected by the fitting, we constrain the linear coefficient to be $\alpha_1 = 1/2$, which is the first order Taylor coefficient of King's law (5.4). The α coefficients depend on the range chosen for the fit. We choose the range $u' \in [-2,2]$, which is wide enough to capture the saturation mechanism up to amplitudes which are much larger than those we will consider in this study. The coefficients obtained with the fit are $\alpha_2 = -0.108$, $\alpha_3 = -0.044$, $\alpha_4 = +0.059$, $\alpha_5 = -0.012$. From Figure 5.2, one can see that the least square fit model has the same linear behaviour as the unsteady King's law and a qualitatively similar nonlinear behaviour, but with a smooth saturation mechanism. The saturation starts at values smaller than $u' = 1$, which is consistent with the experimental observations of Heckl (1990). Also, the gain decreases monotonically with the amplitude forcing, which is consistent with the nonlinear unsteady calculations of Selimefendigil *et al.* (2012). Note that a monotonic decrease in the gain does not preclude the possibility of having a subcritical bifurcation, as this can be caused by the variations of the phase response with the amplitude, as is the case for our system. In the following, we will find that oscillations saturate with amplitudes $|u'| < 1$, for which our fit is in good agreement with CFD results. If an appropriate model for the nonlinear dynamic response of the heater is provided, the α coefficients can be obtained via a Taylor expansion up to the desired order.

In the following, variables are presented in a non-dimensional form. We scale lengths with the duct length L, velocities with the mean flow velocity $\overline{u}_1$ and time with the characteristic timescale L/c_1.

5.2.3 Damping models

Two damping models that reduce the gain of the system at high frequency are discussed next. They rely on different physical damping mechanisms, and, although lead to analogous results, exhibit quantitative differences in the weakly nonlinear analysis, as will be discussed in §5.5.

Model I: boundary and viscous-thermal losses

As a first damping model, we model acoustic losses at the boundaries via a frequency dependent reflection coefficient for the outlet, of the form (Cargill, 1982; Hughes & Dowling, 1990):

$$R_2 = -(1+0.9M_2)\left(1-\frac{1}{2}\zeta\left(\frac{\omega r_d}{c_2}\right)^2\right), \tag{5.7}$$

where M_2 is the Mach number after the heater, r_d is the duct radius, and ζ is a constant ($\zeta \approx 3$) that accounts for the fact that hot air meets ambient temperature at the outlet. As a drawback, equation (5.7) determines a threshold frequency at which the reflection coefficient changes sign. This is non-physical, so we cannot investigate modes above this threshold frequency. This can be problematic because, for the weakly nonlinear expansion to converge, a large number of acoustic modes need to be included in the state-space model. However, the number of modes that we can consider is limited by the threshold frequency at which the reflection coefficient changes sign with this model.

Additional damping due to viscous-thermal boundary layer losses is accounted for via a wavenumber correction (Peters *et al.*, 1993):

$$k_\pm = \frac{\omega}{c \pm \overline{u}}\left(1+\frac{a}{\sqrt{\omega}}+\frac{b}{\omega}\right) \tag{5.8a}$$

$$a \equiv \frac{(1-\mathrm{i})\sqrt{\nu}}{\sqrt{2}r_d}\left(1+\frac{\gamma-1}{\sqrt{\mathrm{Pr}}}\right) \qquad b \equiv -\frac{\mathrm{i}\nu}{r_d^2}\left(1+\frac{\gamma-1}{\sqrt{\mathrm{Pr}}}-\frac{\gamma(\gamma-1)}{2\mathrm{Pr}}\right), \tag{5.8b}$$

where c is the speed of sound, Pr is the Prandtl number, ν the kinematic viscosity and γ the specific heat ratio.

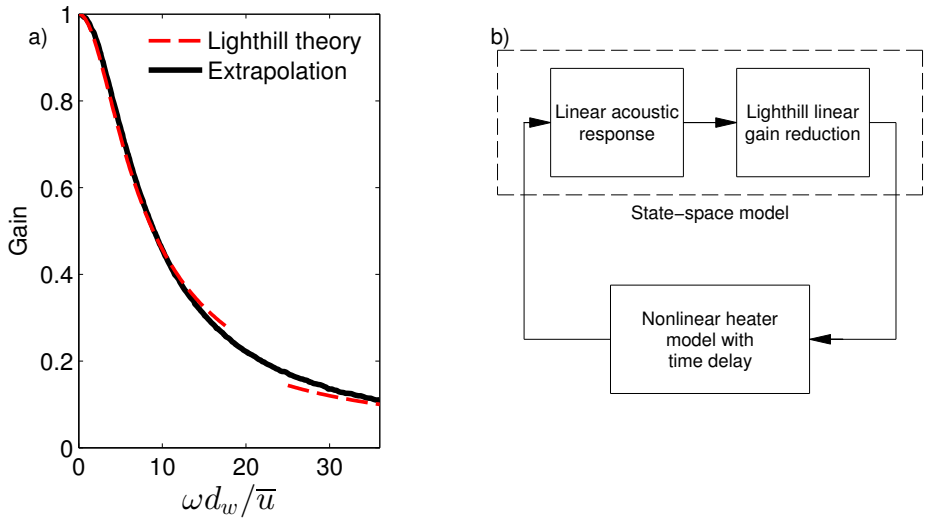

Fig. 5.3 *a*): Lighthill (1954) gain saturation with frequency of the linear hot-wire response. The theoretical predictions (dashed lines) are extrapolated at all frequencies (solid line). *b*): schematic of the feedback mechanism with damping model II. High frequencies are saturated with Lighthill's theory that, being linear, can be combined with the acoustic response to construct a single state-space approximation.

Model II: Lighthill's dynamic response

In Lighthill (1954), the linear dynamic response of a hot-wire was derived analytically, showing that its behaviour is analogous to that of a low-pass filter. Lighthill's results for the gain saturation with the frequency are reported in Figure 5.3a. The low-pass filter cutoff frequency is a function of the wire diameter d_w and mean flow intensity $\overline{u}$. A gain reduction with the frequency stabilises the high-frequency modes, which is what we are seeking.

The total response of the heater is therefore given by the product between a linear dynamic response and a nonlinear amplitude saturation, which is a Wiener-Hammerstein model. Note that here we are retaining the heater phase response due to the time delay in the nonlinear element. Furthermore, because Lighthill's theory is linear, it can be combined with the linear acoustic response, as shown in Figure 5.3b.

In this way, their combined linear response can be approximated with a single state-space model. Thus, the thermoacoustic system is modelled as a Lur'e system (a linear component in feedback loop with a nonlinear component), as was the case for damping model I, and the theory developed in the next can be applied using both models with no changes.

5.3 Linear stability analysis

By coupling the acoustic response (5.2) with the heat release model (5.6), we obtain a nonlinear, delayed dynamical system that describes the evolution of thermoacoustic oscillations. The dynamics of the state variables $\boldsymbol{x}$ is coupled upon the introduction of the heat element through the acoustic velocity $u' = \boldsymbol{C}\boldsymbol{x}$:

$$\dot{\boldsymbol{x}}(t) = A\boldsymbol{x}(t) + K\boldsymbol{B}\sum_{n=1}^{5}\alpha_n(\boldsymbol{C}\boldsymbol{x}(t-\tau))^n, \tag{5.9}$$

where K is the control parameter, which determines the intensity of the heat release fluctuations. The matrix A and the column and row vectors $\boldsymbol{B}$ and $\boldsymbol{C}$ are functions of the state-space model order of approximation and of the flame location x_h. The latter is fixed to $x_h = 0.17$ and 0.13 for damping mechanisms I and II respectively, which is the location at which the thermoacoustic network is most prone to thermoacoustic oscillations at its lowest eigenfrequency. This was obtained by looking for the maximum value of the Rayleigh index $\mathrm{Ry} \equiv \int_0^T p'_{x_h}(t)q'(t)\,\mathrm{d}t$, assuming harmonic oscillations and using equation (5.6) to relate heat release to velocity fluctuations.

Fixing all the other parameters, there are specific values of K, called critical points, at which the system is marginally stable, meaning that all the eigenvalues of the linearised spectrum have a negative growth rate except for a complex conjugate pair, which has a zero growth rate. At these critical points, Hopf bifurcations occur, and the linear stability of the system changes across them. In order to perform a weakly nonlinear analysis, we need to first locate critical points and then expand the governing equations around them. This yields the amplitude and frequency of limit cycle oscillations that occur after the bifurcation.

The fixed point $\boldsymbol{x} = \boldsymbol{0}$ is a solution of the dynamical system (5.9) for any value of K. Its stability is determined by the eigenvalues of the linearised system:

$$\dot{\boldsymbol{x}}(t) = A\boldsymbol{x}(t) + \alpha_1 K\boldsymbol{B}\boldsymbol{C}\boldsymbol{x}(t-\tau). \tag{5.10}$$

Taking the Laplace transform we have:

$$\left(sI - A - \alpha_1 K\boldsymbol{B}\boldsymbol{C}e^{-s\tau}\right)\hat{\boldsymbol{x}} = \boldsymbol{0}, \tag{5.11}$$

where $s \equiv \sigma + \mathrm{i}\omega$ is the non-dimensional Laplace variable, and I the identity matrix. Note that, because $\boldsymbol{B}$ and $\boldsymbol{C}$ are column and row vectors respectively, their (outer) product results in a matrix. The values of s for which the determinant of the linear operator vanishes are the

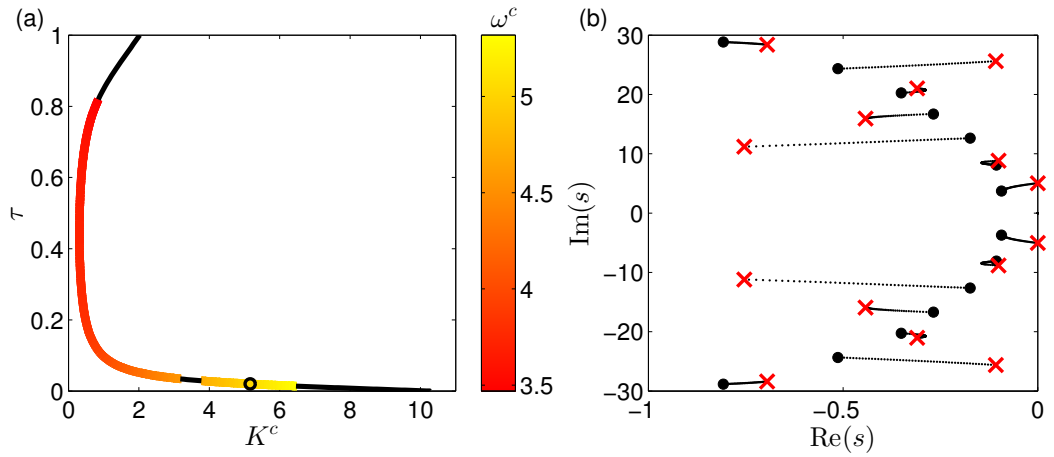

Fig. 5.4 (a): Neutral line in the $K-\tau$ plane. Along it, the eigenmode with the smallest eigenfrequency has zero growth rate. Colours refer to the frequency of the marginally stable mode. Black lines indicate that mode(s) with a higher frequency have a positive growth rate. (b): Spectrum of the acoustic (circles) and thermoacoustic (crosses) system for the set of parameters chosen for the weakly nonlinear analysis, marked with a circle in the left plot. The paths of the eigenvalues from their acoustic values ($K=0$, dots) to their thermoacoustic values ($K=K^c$, crosses) are shown as dotted lines. These graphs have been calculated using damping model I; analogous results are obtained with model II.

thermoacoustic eigenvalues. The nonlinear eigenvalue problem (5.11) is solved iteratively while varying K until a marginally stable solution is found.

We first perform a parametric study in the $K-\tau$ plane to identify a set of Hopf bifurcations of the thermoacoustic mode with the smallest eigenfrequency (see Figure 5.4a). This is achieved using the open-source package DDE-BIFTOOL (Engelborghs *et al.*, 2002; Sieber *et al.*, 2015), tracking the critical values of the heater power K^c at which the growth rate associated with the smallest eigenfrequency is zero. However, we find that, for some of these solutions, mode(s) with a higher frequency have a positive growth rate along the neutral lines of the first mode. This is physically possible when the values of K^c or τ are large. We show these solutions with black lines in Figure 5.4a. At these locations the system is not marginally stable, and the theory presented in the following cannot be applied. A typical value for the time delay can be estimated from Lighthill (1954)'s theory, $\tau = 0.2\,d_w/\overline{u}$. In the following, two values of τ are chosen depending on the damping model: for model I, we will fix $\tau = 0.02$, for which the critical power is $K^c = 5.04$; for model II, we will fix $\tau = 0.04$, for which the critical power is $K^c = 1.422$. Figure 5.4b shows the spectrum of the acoustic and thermoacoustic systems at this Hopf bifurcation for damping model I.

Because, for damping model I, the value of K^c is fairly large, the thermoacoustic eigenmodes are significantly shifted from the pure acoustic ones. The order of approximation of

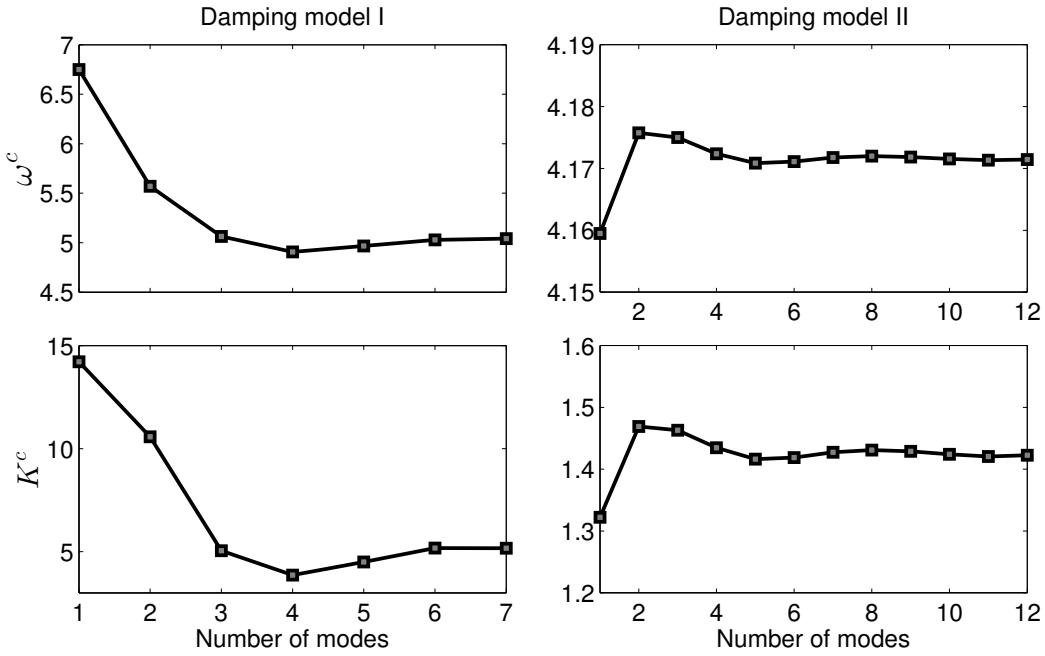

Fig. 5.5 Convergence of the marginally stable angular frequency ω^c (top) and critical power K^c (bottom) with respect to the number of modes considered in the state-space approximation. A single-mode approximation does not accurately capture the correct response of the system. For damping model I, we cannot consider modes above the seventh, because their frequency exceeds the threshold frequency imposed by the choice of the reflection coefficient.

the state-space - which is twice the number of modes considered - has to be large enough in order to capture the thermoacoustic response correctly, as was shown by Ananthkrishnan *et al.* (2005); Kashinath *et al.* (2014). A single-mode approximation of the acoustic response (as was considered by Juniper (2011); Subramanian *et al.* (2013) for weakly nonlinear expansions) is not able to capture the system response accurately in this case. Figure 5.5 shows that the marginally stable eigenfrequency and heat power obtained with a single-mode approximation are significantly different from the saturated ones obtained with more modes. For damping model I, modes above the seventh have a frequency which is above the threshold frequency of the reflection coefficient (5.7). They give rise to non-physical high-frequency oscillations that are not damped, and are not included in the analysis. In this case, we will retain all 7 modes (N_{modes}) when performing the weakly nonlinear analysis. For damping model II we can account for more modes, and we will retain 12 modes to analyse this case.

Our thermoacoustic system is composed of $2 \times N_{modes}$ coupled differential equations. As a consequence, the use of adjoint methods is required to obtain solvability conditions of the weakly nonlinear equations, as discussed in §5.4.3.

5.4 Weakly nonlinear analysis

We now perturb the bifurcation parameter from the critical point, $K = K^c + \Delta K$, with $|\Delta K| \ll 1$. After the Hopf bifurcation, the system is linearly unstable and oscillations will grow and can saturate to limit cycle oscillations due to nonlinear effects. In the case in which the Hopf bifurcation is subcritical, a bistable region exists before the Hopf point in which, by triggering the system, stable solutions with a finite amplitude can be found (Ananthkrishnan *et al.*, 2005; Juniper, 2011). To calculate the amplitudes and frequencies of these oscillations, nonlinear methods are required. We accomplish this with a weakly nonlinear analysis, by expanding the evolution of the dynamical system (5.9) around the Hopf location. We denote with $0 < \varepsilon \ll 1$ a small quantity that quantifies the amplitude of the oscillations close to the Hopf point. We then seek for solutions $\boldsymbol{x}$ expressed as power series of ε:

$$\boldsymbol{x} = \varepsilon \boldsymbol{x}_1 + \varepsilon^2 \boldsymbol{x}_2 + \varepsilon^3 \boldsymbol{x}_3 + \varepsilon^4 \boldsymbol{x}_4 + \varepsilon^5 \boldsymbol{x}_5 + \mathcal{O}(\varepsilon^6). \tag{5.12}$$

For a subcritical bifurcation, an expansion at third order yields unstable limit cycle solutions. However, such oscillations are typically not observable in self-excited experiments, although they can be studied experimentally by forcing the system close to the unstable solutions (Jegadeesan & Sujith, 2013). For subcritical phenomena, however, one is also interested in calculating the amplitude of stable solutions, and in identifying the width of the bistable region. This requires terms of at least order 5 in a weakly nonlinear expansion.

We choose to work with the method of multiple scales. With this method, one assumes that several, independent timescales act on the system. One is the fast timescale t_0, at which the oscillations of the marginally stable frequency respond. The slow timescales $\tilde{t}_2$ and $\tilde{t}_4$ are associated with long time saturation or growth processes. The total time derivative therefore reads:

$$\frac{\mathrm{d}}{\mathrm{d}t} = \frac{\partial}{\partial t_0} + \frac{\partial}{\partial \tilde{t}_2} + \frac{\partial}{\partial \tilde{t}_4} + \dots. \tag{5.13}$$

By Taylor expanding the dynamical system (5.9) around the fixed point solution $\boldsymbol{x} = \boldsymbol{0}$ at the critical point $K = K^c$ we obtain:

$$\begin{aligned} \frac{\partial \boldsymbol{x}}{\partial t_0} + \frac{\partial \boldsymbol{x}}{\partial \tilde{t}_2} + \frac{\partial \boldsymbol{x}}{\partial \tilde{t}_4} = A\boldsymbol{x} + \sum_{n=1}^{5} \alpha_n K^c \boldsymbol{B}(\boldsymbol{C}\boldsymbol{x}(t-\tau))^n \dots \\ + \sum_{n=1}^{5} \alpha_n \Delta K \boldsymbol{B}(\boldsymbol{C}\boldsymbol{x}(t-\tau))^n. \end{aligned} \tag{5.14}$$

It is important to note that the orders of magnitude of $\mathcal{O}(\boldsymbol{x}) = \varepsilon$ and those of $\mathcal{O}(\Delta K)$, $\mathcal{O}(\tilde{t}_2)$, and $\mathcal{O}(\tilde{t}_4)$ are not independent. Upon the expansion of the equations, one can show

that, at odd orders larger than 1, secular terms (i.e., forcings at resonant frequencies) arise due to nonlinear interactions. Solvability conditions need to be imposed on these forcings, which have to be balanced by contributions arising from slow timescales and control parameter terms (Rosales, 2004; Strogatz, 2015). This reasoning leads to balances between the order of magnitudes of the various terms, which read:

$$\mathcal{O}(\boldsymbol{x}\Delta K) = \varepsilon^3, \qquad \mathcal{O}\left(\frac{\partial \boldsymbol{x}}{\partial \tilde{t}_2}\right) = \varepsilon^3, \qquad \mathcal{O}\left(\frac{\partial \boldsymbol{x}}{\partial \tilde{t}_4}\right) = \varepsilon^5. \tag{5.15}$$

We shall then rewrite all the quantities in terms of ε by defining $\Delta K \equiv \varepsilon^2 \delta_2$, $t_2 \equiv \varepsilon^2 \tilde{t}_2$ and $t_4 \equiv \varepsilon^4 \tilde{t}_4$. The parameter δ_2 can take the values ± 1 depending on the side of the Hopf point we are investigating. From the definition of ΔK, we also obtain a measure of the expansion parameter in terms of the distance from the Hopf location:

$$\varepsilon = \sqrt{|K - K^c|}. \tag{5.16}$$

Lastly, the time delay contained in our system acts at all the timescales we are considering (Das & Chatterjee, 2002). Considering the ε scalings just discussed for the slow timescales, delayed variables are therefore functions of $t_0 - \tau$, $t_2 - \varepsilon^2\tau$, and $t_4 - \varepsilon^4\tau$. These terms are then expanded in series of ε. For ease of notation, in the following we will adopt the short notation $\boldsymbol{x}(t)$ for $\boldsymbol{x}(t_0, t_2, t_4)$, and $\boldsymbol{x}(t-\tau)$ for $\boldsymbol{x}(t_0 - \tau, t_2, t_4)$.

We now substitute the relations (5.12), (5.15) into equation (5.14). The complete list of terms we obtain is given in Appendix E. By matching these terms by their ε order, we obtain a set of linear, inhomogeneous differential equations which have to be solved in ascending order. Although we perform the weakly nonlinear expansion up to $\mathcal{O}(\varepsilon^7)$ for the case with damping model I, in the following subsections we will solve and discuss the equations in detail up to order ε^5 for brevity, and will justify the need of the seventh order expansion in §5.5.

5.4.1 $\mathcal{O}(\varepsilon)$: eigenvalue problem

At order ε we retrieve the homogeneous linear equations (5.17) for the evolution of $\boldsymbol{x}_1$:

$$\frac{\partial \boldsymbol{x}_1}{\partial t_0} - A\boldsymbol{x}_1 - \alpha_1 K^c \boldsymbol{B}(\boldsymbol{C}\boldsymbol{x}_1(t-\tau)) = \boldsymbol{0}. \tag{5.17}$$

Because the left hand structure of the equations will be the same at all ε orders, it is convenient to define the spectral operator:

$$M_s \equiv \left(sI - A - \alpha_1 K^c \boldsymbol{B}\boldsymbol{C} e^{-s\tau}\right), \tag{5.18}$$

where $s \equiv \sigma + \mathrm{i}\omega$ denotes the Laplace variable, so that the nonlinear eigenvalue problem in the frequency domain can be rewritten as $M_s \boldsymbol{x}_1 = \boldsymbol{0}$. This is the same eigenvalue problem of equation (5.11). Also, because here we have fixed $K = K^c$, we know that the system is marginally stable (its spectrum is shown in Figure 5.4b with crosses).

We can simplify the evolution of the dynamical system to the evolution of only the marginally stable thermoacoustic eigenmode, i.e., we ignore the contribution of the eigenmodes with a negative growth rate, because they will quickly be damped (Sipp & Lebedev, 2007). Close to the Hopf bifurcation, we expect the dynamical system to saturate to limit cycle oscillations at the slow timescales, therefore we can write:

$$\boldsymbol{x}_1 \approx W(t_2, t_4) \boldsymbol{x}_1^W e^{\mathrm{i}\omega^c t_0} + \text{c.c.}, \tag{5.19}$$

where ω^c is the angular frequency of the marginally stable eigenmode, $\boldsymbol{x}_1^W$ the corresponding right eigenvector and $W(t_2, t_4)$ a complex valued variable which depends on the slow timescales only. W contains information on the amplitude saturation and frequency shift effects caused by nonlinear effects. At the next odd orders, we will explicitly find the dependence of W with respect to the slow timescales.

5.4.2 $\mathcal{O}(\varepsilon^2)$: mean shift and second harmonic

At this order we obtain the equations for the evolution of $\boldsymbol{x}_2$. From this order on, forcing terms will appear in the r.h.s. of the equations. In general, the forcing terms at order ε^N are due to the nonlinear interactions between the solutions $\boldsymbol{x}_k$ at orders $k < N$, which are known. The only forcing term at this order is $\alpha_2 K^c \boldsymbol{B}(\boldsymbol{C}\boldsymbol{x}_1(t-\tau))^2$, which is due to the interaction of $\boldsymbol{x}_1$ with itself. By using the expression (5.19) for $\boldsymbol{x}_1$, we obtain the inhomogeneous linear equations:

$$\frac{\partial \boldsymbol{x}_2}{\partial t_0} - A\boldsymbol{x}_2 - \alpha_1 K^c \boldsymbol{B}(\boldsymbol{C}\boldsymbol{x}_2(t-\tau)) = |W|^2 \boldsymbol{F}_2^{|W|^2} + \left(W^2 \boldsymbol{F}_2^{W^2} e^{2\mathrm{i}\omega^c t_0} + \text{c.c.}\right), \tag{5.20}$$

where

$$\begin{aligned} \boldsymbol{F}_2^{W^2} &\equiv \alpha_2 K^c \boldsymbol{B}(\boldsymbol{C}\boldsymbol{x}_1^W)^2 e^{-2\mathrm{i}\omega^c\tau} \\ \boldsymbol{F}_2^{|W|^2} &\equiv 2\alpha_2 K^c \boldsymbol{B}|\boldsymbol{C}\boldsymbol{x}_1^W|^2. \end{aligned} \tag{5.21}$$

The superscripts are used to classify the forcing terms by their dependence on the complex amplitudes W. This forcing is composed of two components: a steady forcing with zero frequency (due to the interaction between the eigenmode $\boldsymbol{x}_1^W$ and its complex conjugate), and second harmonic contributions at frequency $2\omega^c$ (due to the interaction between the eigenmode $\boldsymbol{x}_1^W$ and itself). These are not resonant terms, because the spectrum of the linear operator does not contain $2\omega^c$ or 0 as eigenvalues (see Figure 5.4b), and equations (5.20) can be readily solved.

We look for a steady-state solution $\boldsymbol{x}_2$ which has the same shape as the forcing, by using the ansatz

$$\boldsymbol{x}_2 = |W|^2 \boldsymbol{x}_2^{|W|^2} + \left(W^2 \boldsymbol{x}_2^{W^2} e^{2\mathrm{i}\omega^c t_0} + \text{c.c.} \right). \tag{5.22}$$

By substituting the latter into equation (5.20), taking the Laplace transform (with respect to the fast timescale t_0), and matching the terms according to their amplitude dependence, we obtain the sets of linear equations:

$$M_{2\mathrm{i}\omega^c} \boldsymbol{x}_2^{W^2} = \boldsymbol{F}_2^{W^2} \tag{5.23a}$$

$$M_0 \boldsymbol{x}_2^{|W|^2} = \boldsymbol{F}_2^{|W|^2}. \tag{5.23b}$$

The matrices $M_{2\mathrm{i}\omega^c}$ and M_0 are non-singular and can be inverted, yielding the solutions at the various amplitude levels of $\boldsymbol{x}_2$.

In particular, $\boldsymbol{x}_2^{W^2}$ (and its c.c.) describes second harmonic oscillations, whereas $\boldsymbol{x}_2^{|W|^2}$, having zero frequency, will cause a shift in the mean acoustic level. This is a well-known effect in hydrodynamics, where zero frequency corrections are due to quadratic terms arising from the nonlinear convective term of the Navier–Stokes equations. A weakly nonlinear expansion allows distinction between the base flow (solution of the steady Navier–Stokes equations) and the mean flow (time averaged solution of the unsteady Navier–Stokes equations) (Sipp & Lebedev, 2007; Meliga *et al.*, 2009). These effects are not found if the nonlinearity expansion contains only odd terms. This is often the case for low-order thermoacoustic modelling (Noiray *et al.*, 2011; Noiray & Schuermans, 2013*b*; Ghirardo *et al.*, 2015), although some experimental evidence of acoustic level mean shifts can be found in the literature (Flandro *et al.*, 2007).

5.4.3 $\mathcal{O}(\varepsilon^3)$: third harmonic and saturation

At this order we obtain the equations for the evolution of $\boldsymbol{x}_3$:

$$\begin{aligned}\frac{\partial \boldsymbol{x}_3}{\partial t_0} - A\boldsymbol{x}_3 - \alpha_1 K^c \boldsymbol{B}(\boldsymbol{C}\boldsymbol{x}_3(t-\tau)) = -\frac{\partial \boldsymbol{x}_1}{\partial t_2} - \tau \boldsymbol{B}\alpha_1 K^c \boldsymbol{C}\frac{\partial \boldsymbol{x}_1}{\partial t_2}(t-\tau)\dots \\ + \left(W\boldsymbol{F}_3^W e^{\mathrm{i}\omega^c t_0} + |W|^2 W \boldsymbol{F}_3^{|W|^2 W} e^{\mathrm{i}\omega^c t_0} + W^3 \boldsymbol{F}_3^{W^3} e^{3\mathrm{i}\omega^c t_0} + \text{c.c.}\right).\end{aligned} \tag{5.24}$$

The explicit expressions of the forcing terms are reported in Appendix F.1. The slow timescale derivative may be rewritten as:

$$\frac{\partial \boldsymbol{x}_1}{\partial t_2}(t) = \frac{\partial W}{\partial t_2}\boldsymbol{x}_1^W e^{\mathrm{i}\omega^c t} + \text{c.c.}. \tag{5.25}$$

Resonant forcings with angular frequency ω^c arise at this order, which act on two different amplitude levels, W and $|W|^2 W$. A solvability condition, known as the Fredholm alternative (Oden & Demkowicz, 2010), needs to be satisfied for a solution to exist. This condition requires the sum of the resonant forcing terms to be orthogonal to the kernel (nullspace) of the (singular) adjoint operator $M^\dagger_{\mathrm{i}\omega^c}$ (Sipp & Lebedev, 2007; Meliga *et al.*, 2009). This generalises the idea of cancelling the secular terms used for weakly nonlinear analysis of scalar problems.

The adjoint matrix $M_{\mathrm{i}\omega^c}$ is defined through the scalar product:

$$\left\langle \boldsymbol{y}, M_{\mathrm{i}\omega^c}\boldsymbol{x}\right\rangle = \left\langle M^\dagger_{\mathrm{i}\omega^c}\boldsymbol{y}, \boldsymbol{x}\right\rangle, \tag{5.26}$$

and corresponds to the Hermitian of the direct matrix $M_{\mathrm{i}\omega^c}$. The latter is singular, because $s = \mathrm{i}\omega^c$ is an eigenvalue of (5.11). Thus, $M_{\mathrm{i}\omega^c}$ is also singular, and its kernel is spanned by the adjoint eigenvector $\boldsymbol{x}_1^\dagger$ only. This can be calculated as the Hermitian of the left nullspace of the operator $M_{\mathrm{i}\omega^c}$. The solvability condition therefore requires:

$$\left\langle \boldsymbol{x}_1^\dagger, -\frac{\partial W}{\partial t_2}P\boldsymbol{x}_1^W + W\boldsymbol{F}_3^W + |W|^2 W \boldsymbol{F}_3^{|W|^2 W}\right\rangle = 0, \tag{5.27}$$

where the right terms in the bracket are all the resonant forcings, and we have defined the matrix $P \equiv \left(I + \tau\alpha_1 K^c \boldsymbol{B}\boldsymbol{C}e^{-\mathrm{i}\omega^c\tau}\right)$. By rearranging equation (5.27), we obtain:

$$\frac{\partial W}{\partial t_2} = \lambda_3 W + \nu_3 |W|^2 W, \tag{5.28}$$

where the complex values λ_3, ν_3, known as the Landau coefficients, are defined by:

$$\lambda_3 \equiv \frac{\left\langle \boldsymbol{x}_1^\dagger, \boldsymbol{F}_3^W \right\rangle}{\left\langle \boldsymbol{x}_1^\dagger, P\boldsymbol{x}_1^W \right\rangle}, \qquad \nu_3 \equiv \frac{\left\langle \boldsymbol{x}_1^\dagger, \boldsymbol{F}_3^{|W|^2W} \right\rangle}{\left\langle \boldsymbol{x}_1^\dagger, P\boldsymbol{x}_1^W \right\rangle}. \tag{5.29}$$

For damping model I, the values we found for the Landau coefficients when $K < K^c$ are $\lambda_3 = -0.0291 - 0.2181\mathrm{i}$ and $\nu_3 = 0.0157 - 0.0203\mathrm{i}$. For damping model II, the dependence of the Landau coefficients on the number of modes retained in the acoustic state-space model is shown in Figure 5.6a. Note that, in this case, we find that the sign of $\mathrm{Re}(\nu_3)$ with one mode is different from the sign of the saturated value, containing multiple modes, whereas the sign of $\mathrm{Re}(\lambda_3)$ does not change. This shows that the nature of the bifurcation predicted with a single mode approximation may be different from the actual response of the system. For the case shown in Figure 5.6a, the single mode approximation predicts a supercritical bifurcation, whereas the saturated values show that the bifurcation is actually subcritical.

We then seek a solution $\boldsymbol{x}_3$ via the ansatz:

$$\boldsymbol{x}_3 = W\boldsymbol{x}_3^W e^{\mathrm{i}\omega^c t_0} + |W|^2 W \boldsymbol{x}_3^{|W|^2W} e^{\mathrm{i}\omega^c t_0} + W^3 \boldsymbol{x}_3^{W^3} e^{3\mathrm{i}\omega^c t_0} + \text{c.c.}. \tag{5.30}$$

By using the relation (5.28), we match the solution and forcing terms of (5.24) by their dependence on the amplitude W, and obtain the sets of linear equations:

$$M_{\mathrm{i}\omega^c}\boldsymbol{x}_3^W = \boldsymbol{F}_3^W - \lambda_3 P\boldsymbol{x}_1^W \tag{5.31a}$$

$$M_{\mathrm{i}\omega^c}\boldsymbol{x}_3^{|W|^2W} = \boldsymbol{F}_3^{|W|^2W} - \nu_3 P\boldsymbol{x}_1^W \tag{5.31b}$$

$$M_{3\mathrm{i}\omega^c}\boldsymbol{x}_3^{W^3} = \boldsymbol{F}_3^{W^3}. \tag{5.31c}$$

Although the matrix $M_{\mathrm{i}\omega^c}$ is singular, the values of the Landau coefficients guarantee that solutions for $\boldsymbol{x}_3^W$ and $\boldsymbol{x}_3^{|W|^2W}$ exist. They can be calculated, e.g., by using the pseudo-inverse matrix of $M_{\mathrm{i}\omega^c}$. These solutions provide a nonlinear correction to the shape of the linearly unstable mode. Equation (5.31c), instead, can be readily solved by inverting the matrix $M_{3\mathrm{i}\omega^c}$, which is non-singular. $\boldsymbol{x}_3^{W^3}$ accounts for third harmonic contributions to the oscillatory solution.

Stuart–Landau equation: $\mathcal{O}(\varepsilon^3)$

Equation (5.28) is known as the Stuart–Landau equation. Its roots yield the amplitude of limit cycle solutions and the frequency shift of the nonlinear oscillation with respect to the marginally stable eigenfrequency. By using the polar representation $W = re^{\mathrm{i}\theta}$, and by

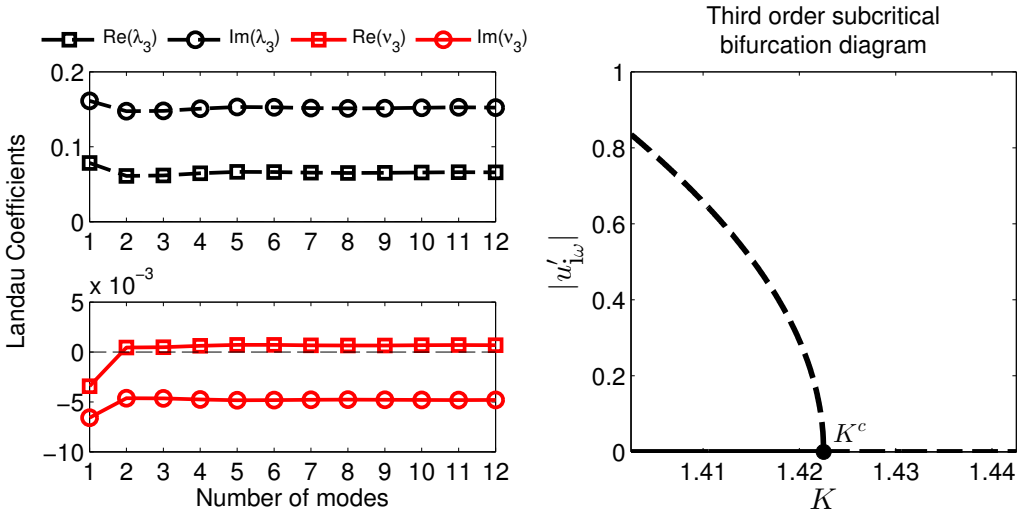

Fig. 5.6 (a): Dependence of the Landau coefficients λ_3, ν_3 with respect to the number of modes. (b): Subcritical Hopf bifurcation diagram. Solid and dashed lines represent stable and unstable solutions, respectively. The oscillation amplitude at the fundamental frequency with corrections up to ε^3 is shown. Results are shown for damping model II; analogous graphs are found for damping model I.

splitting the real and the imaginary parts, we have:

$$\frac{\partial r}{\partial t_2} = \mathrm{Re}(\lambda_3) r + \mathrm{Re}(\nu_3) r^3 \tag{5.32a}$$

$$\frac{\partial \theta}{\partial t_2} = \mathrm{Im}(\lambda_3) + \mathrm{Im}(\nu_3) r^2. \tag{5.32b}$$

The equation for the phase θ is valid only for solutions with non-zero amplitude. Steady-state solutions are reached when the amplitude r does not vary in time. The amplitude levels at which this happens are:

$$r_1 = 0, \qquad r_2 = \sqrt{-\frac{\mathrm{Re}(\lambda_3)}{\mathrm{Re}(\nu_3)}}. \tag{5.33}$$

From the definitions (5.29), (F.2a), one can see that λ_3, being proportional to $\delta_2 = \pm 1$, changes sign across the critical point K^c, whereas ν_3 does not vary when we change the bifurcation parameter. Therefore, the solution r_2 is real only on one side of the Hopf location. The stability of the solutions is connected to the sign of the eigenvalue of the Jacobian $J \equiv \mathrm{Re}(\lambda_3) + 3\mathrm{Re}(\nu_3) r^2$ evaluated at the two solutions:

$$J(r_1) = \mathrm{Re}(\lambda_3), \qquad J(r_2) = -2\mathrm{Re}(\lambda_3). \tag{5.34}$$

Note that, in the region where two solutions coexist, their stability is different. This distinguishes between super- and subcritical Hopf bifurcations. For the set of parameters we have chosen, we find that the bifurcation is subcritical: before the Hopf bifurcation, stable fixed points and unstable limit cycle solutions exist, and after it only unstable fixed point solutions are found, as shown in Figure 5.6b. The present analysis could be also applied to configurations in which the bifurcation is supercritical.

The solution of the phase equation (5.32b) on the unstable limit cycle solution reads:

$$\theta = \varepsilon^2 \left(\mathrm{Im}(\lambda_3) - \mathrm{Im}(\nu_3) \frac{\mathrm{Re}(\lambda_3)}{\mathrm{Re}(\nu_3)} \right) t_0 \equiv \Delta\omega t_0, \tag{5.35}$$

where we have used the scaling $t_2 = \varepsilon^2 t_0$ between the fast and slow timescales. $\Delta\omega$ represents the frequency shift between the fundamental oscillation frequency of limit cycles and the marginally stable frequency ω^c.

Combining the power expansion (5.12), the weakly nonlinear solutions (5.19), (5.22), (5.30) and the solution of the Stuart–Landau equation, we obtain an analytical expression for the time evolution of the thermoacoustic states up to third order, which reads:

$$\begin{aligned} \boldsymbol{x} = \varepsilon^2 r^2 \boldsymbol{x}_2^{|W|^2} + \left[\varepsilon r \boldsymbol{x}_1^W + \varepsilon^3 r \boldsymbol{x}_3^W + \varepsilon^3 r^3 \boldsymbol{x}_3^{|W|^2 W} \right] e^{\mathrm{i}(\omega^c + \Delta\omega)t_0} \dots \\ + \varepsilon^2 r^2 \boldsymbol{x}_2^{W^2} e^{2\mathrm{i}(\omega^c + \Delta\omega)t_0} + \varepsilon^3 r^3 \boldsymbol{x}_3^{W^3} e^{3\mathrm{i}(\omega^c + \Delta\omega)t_0} + \mathrm{c.c.} + \mathcal{O}(\varepsilon^4). \end{aligned} \tag{5.36}$$

Figure 5.6b shows the subcritical bifurcation diagram we obtain at this order. It contains the amplitude level of the velocity fluctuations $u' = \boldsymbol{C}\boldsymbol{x}$ calculated from equation (5.36) at the fundamental frequency. We shall postpone the discussion of the response at other frequencies to section §5.5. Because these limit cycle oscillations are unstable, the amplitudes that the Stuart–Landau equation predicts at this order correspond approximately to the level of triggering which is required to excite finite amplitude oscillations. In order to predict the amplitude of stable limit cycles, we need to extend the weakly nonlinear expansion to higher orders.

5.4.4 $\mathcal{O}(\varepsilon^4)$: mean shift and fourth harmonic

At this order we obtain the equations for the evolution of $\boldsymbol{x}_4$:

$$\begin{aligned} \frac{\partial \boldsymbol{x}_4}{\partial t_0} - A\boldsymbol{x}_4 - \alpha_1 K \boldsymbol{B}(\boldsymbol{C}\boldsymbol{x}_4(t-\tau)) = |W|^4 \boldsymbol{F}_4^{|W|^4} + |W|^2 \boldsymbol{F}_4^{|W|^2} \dots \\ + \left(W^2 \boldsymbol{F}_4^{W^2} e^{2\mathrm{i}\omega^c t_0} + |W|^2 W^2 \boldsymbol{F}_4^{|W|^2 W^2} e^{2\mathrm{i}\omega^c t_0} + W^4 \boldsymbol{F}_4^{W^4} e^{4\mathrm{i}\omega^c t_0} + \mathrm{c.c} \right). \end{aligned} \tag{5.37}$$

None of the forcing terms resonates. Their expressions are provided in Appendix F.2. Using the ansatz:

$$\begin{aligned} \boldsymbol{x}_4 = |W|^2 \boldsymbol{x}_4^{|W|^2} + |W|^4 \boldsymbol{x}_4^{|W|^4} \dots \\ + \left(W^2 \boldsymbol{x}_4^{W^2} e^{2\mathrm{i}\omega^c t_0} + |W|^2 W^2 \boldsymbol{x}_4^{|W|^2 W^2} e^{2\mathrm{i}\omega^c t_0} + W^4 \boldsymbol{x}_4^{W^4} e^{4\mathrm{i}\omega^c t_0} + \text{c.c.} \right), \end{aligned} \tag{5.38}$$

we can readily calculate the solutions

$$\boldsymbol{x}_4^{|W|^2} = M_0^{-1} \boldsymbol{F}_4^{|W|^2} \tag{5.39a}$$

$$\boldsymbol{x}_4^{|W|^4} = M_0^{-1} \boldsymbol{F}_4^{|W|^4} \tag{5.39b}$$

$$\boldsymbol{x}_4^{W^2} = M_{2\mathrm{i}\omega^c}^{-1} \boldsymbol{F}_4^{W^2} \tag{5.39c}$$

$$\boldsymbol{x}_4^{|W|^2 W^2} = M_{2\mathrm{i}\omega^c}^{-1} \boldsymbol{F}_4^{|W|^2 W^2} \tag{5.39d}$$

$$\boldsymbol{x}_4^{W^4} = M_{4\mathrm{i}\omega^c}^{-1} \boldsymbol{F}_4^{W^4}, \tag{5.39e}$$

which provide contributions to the mean acoustic level shift, and second and fourth harmonic oscillations.

5.4.5 $\mathcal{O}(\varepsilon^5)$: fifth harmonic and saturation

At this order we obtain the equations for the evolution of $\boldsymbol{x}_5$:

$$\begin{aligned} \frac{\partial \boldsymbol{x}_5}{\partial t_0} - A\boldsymbol{x}_5 - \alpha_1 K^c \boldsymbol{B}(\boldsymbol{C}\boldsymbol{x}_5) = -P\frac{\partial \boldsymbol{x}_1}{\partial t_4} \dots \\ + \left(W \boldsymbol{F}_5^W + |W|^2 W \boldsymbol{F}_5^{|W|^2 W} + |W|^4 W \boldsymbol{F}_5^{|W|^4 W} \right) e^{\mathrm{i}\omega^c (t_0 - \tau)} \dots \\ + \left(|W|^2 W^3 \boldsymbol{F}_5^{|W|^2 W^3} + W^3 \boldsymbol{F}_5^{W^3} \right) e^{3\mathrm{i}\omega^c (t_0 - \tau)} + W^5 \boldsymbol{F}_5^{W^5} e^{5\mathrm{i}\omega^c (t_0 - \tau)} + \text{c.c.}. \end{aligned} \tag{5.40}$$

In this section, we will not explicitly calculate the solution $\boldsymbol{x}_5$, but we will only derive the dependence of the amplitude W with respect to the slow timescale t_4. This is achieved by applying the Fredholm alternative solvability condition on the resonant forcings at frequency ω^c which appear on the r.h.s. of equation (5.40).

By imposing that the resonant terms are orthogonal to the kernel of the adjoint operator $M_{\mathrm{i}\omega^c}^{\dagger}$, we obtain:

$$\left\langle \boldsymbol{x}_1^{\dagger}, -\frac{\partial W}{\partial t_4} P \boldsymbol{x}_1^W + W \boldsymbol{F}_5^W + |W|^2 W \boldsymbol{F}_5^{|W|^2 W} + |W|^4 W \boldsymbol{F}_5^{|W|^4 W} \right\rangle = 0. \tag{5.41}$$

The resonant forcing expressions can be found in Appendix F.3. Equation (5.41) can be simplified into the Stuart–Landau equation:

$$\frac{\partial W}{\partial t_4} = \lambda_5 W + \nu_5 |W|^2 W + \mu_5 |W|^4 W, \tag{5.42}$$

where the Landau coefficients are defined by:

$$\lambda_5 \equiv \frac{\left\langle \boldsymbol{x}_1^\dagger, \boldsymbol{F}_5^W \right\rangle}{\left\langle \boldsymbol{x}_1^\dagger, P\boldsymbol{x}_1^W \right\rangle}, \qquad \nu_5 \equiv \frac{\left\langle \boldsymbol{x}_1^\dagger, \boldsymbol{F}_5^{|W|^2 W} \right\rangle}{\left\langle \boldsymbol{x}_1^\dagger, P\boldsymbol{x}_1^W \right\rangle}, \qquad \mu_5 \equiv \frac{\left\langle \boldsymbol{x}_1^\dagger, \boldsymbol{F}_5^{|W|^4 W} \right\rangle}{\left\langle \boldsymbol{x}_1^\dagger, P\boldsymbol{x}_1^W \right\rangle}. \tag{5.43}$$

For damping model I, the values we obtain for these coefficients when $K < K^c$ are $\lambda_5 = 0.0019 - 0.0077\mathrm{i}$, $\nu_5 = -0.0235 + 0.004\mathrm{i}$, $\mu_5 = -0.0147 - 0.0136\mathrm{i}$. The coefficient ν_5 changes sign across the Hopf location.

Stuart–Landau equation: $\mathcal{O}(\varepsilon^5)$

The overall slow timescale evolution of the amplitude W is obtained by combining the results at the two timescales t_2 and t_4 (Fujimura, 1991; Gambino *et al.*, 2012). By using the scaling $t_4 = t_2\varepsilon^2$, we obtain:

$$\frac{\mathrm{d}W}{\mathrm{d}t_2} = \frac{\partial W}{\partial t_2} + \frac{\partial W}{\partial t_4}\frac{\partial t_4}{\partial t_2} = \left(\lambda_3 + \varepsilon^2\lambda_5\right) W + \left(\nu_3 + \varepsilon^2\nu_5\right)|W|^2 W + \varepsilon^2\mu_5|W|^4 W. \tag{5.44}$$

By using the polar representation $W = re^{\mathrm{i}\theta}$, this decouples into:

$$\frac{\mathrm{d}r}{\mathrm{d}t_2} = \mathrm{Re}(\lambda)r + \mathrm{Re}(\nu)r^3 + \mathrm{Re}(\mu)r^5 \tag{5.45a}$$

$$\frac{\mathrm{d}\theta}{\mathrm{d}t_2} = \mathrm{Im}(\lambda) + \mathrm{Im}(\nu)r^2 + \mathrm{Im}(\mu)r^4, \tag{5.45b}$$

where $\lambda = \lambda_3 + \varepsilon^2\lambda_5$, and similarly for ν and μ. The fixed points of the amplitude equation are:

$$r_1 = 0, \qquad r_{2,3} = \sqrt{\frac{-\mathrm{Re}(\nu) \pm \sqrt{(\mathrm{Re}(\nu))^2 - 4\mathrm{Re}(\lambda)\mathrm{Re}(\mu)}}{2\mathrm{Re}(\mu)}}. \tag{5.46}$$

The existence of real solutions for $r_{2,3}$ depends only on the sign of the terms under the square roots. Because the bifurcation is subcritical, we have two solutions after the Hopf location (an unstable fixed point and a stable limit cycle), a bistable region between the Hopf and the fold points with three solutions (a stable fixed point and two limit cycles, one unstable and one stable), and a region with only one stable fixed point before the fold. This is shown

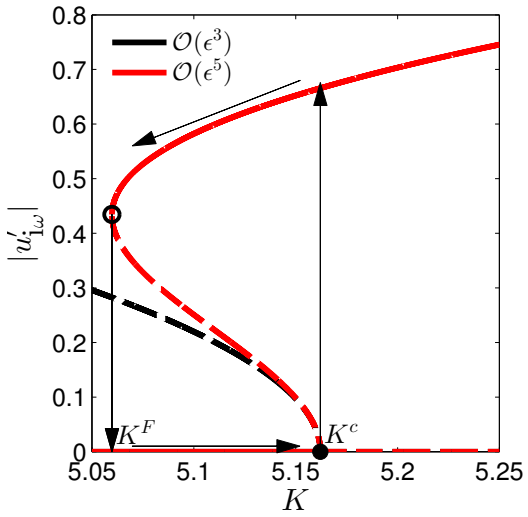

Fig. 5.7 Comparison between third order (black) and fifth order (red) bifurcation with damping model I. Analogous results are found with damping model II. The analytically calculated amplitude of the acoustic velocity at the fundamental frequency is shown, according to (5.36). At fifth order the limit cycle saturates, so the limit cycle amplitude and the location of the fold point K^F can be calculated.

in Figure 5.7, where the path followed by the oscillations when the bifurcation parameter is varied across the bistable region is shown with arrows. As expected, close to the Hopf point the fifth order expansion correctly matches the third order one.

The stability of the solutions is determined by the sign of the Jacobian $J = \mathrm{Re}(\lambda) + 3\mathrm{Re}(\nu)r^2 + 5\mathrm{Re}(\mu)r^4$ evaluated at the solutions. These values are:

$$J(r_1) = \mathrm{Re}(\lambda) \tag{5.47a}$$

$$J(r_{2,3}) = -4\mathrm{Re}(\lambda) + \frac{(\mathrm{Re}(\nu))^2}{\mathrm{Re}(\mu)} \mp \mathrm{Re}(\nu)\sqrt{(\mathrm{Re}(\nu))^2 - 4\mathrm{Re}(\lambda)\mathrm{Re}(\mu)}. \tag{5.47b}$$

The frequency shift $\Delta\omega$ on the limit cycles can be readily calculated from equation (5.45b) by using the scaling $t_2 = \varepsilon^2 t_0$:

$$\Delta\omega_{2,3} \equiv \varepsilon^2 \left(\mathrm{Im}(\lambda) + \mathrm{Im}(\nu)r_{2,3}^2 + \mathrm{Im}(\mu)r_{2,3}^4\right). \tag{5.48}$$

5.5 Results validation

We now compare the weakly nonlinear analysis discussed in §5.4 with the fully-nonlinear results obtained by solving the nonlinear dynamical system (5.9) with no approximations. This is achieved with two methods: time marching the governing equations, and numerical

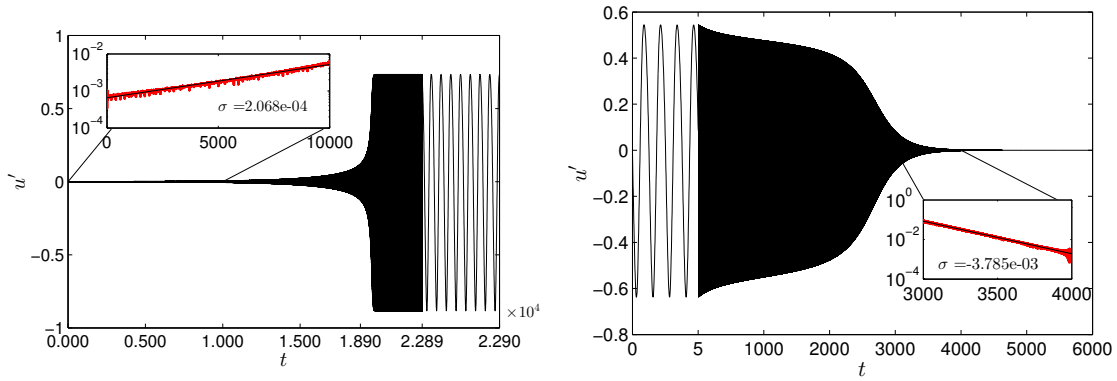

Fig. 5.8 Time marching simulations with damping model I. a): at $K = K^c + \Delta K$ the fixed point solution becomes unstable and oscillations grow to a limit cycle. b): at $K = 5.03$ no limit cycle solutions exist, and the system converges to fixed point solutions even when initialised to a highly perturbed state. The insets show the exponential growth/decay rates of the oscillations in log-scale.

continuation of limit cycles. Time domain simulations are performed using a delay differential equations solver, and the numerical continuation algorithm is based on the DDE-BIFTOOL package (Engelborghs *et al.*, 2002). Although the latter can only predict periodic oscillations and their stability, we find that, for the set of parameters we have investigated, the system always converges towards fixed points or periodic oscillations. Therefore, the two methods yield the same results, as was verified.

For time domain simulations we proceed as follows: we initialise the integration to a state which is slightly perturbed from the fixed point solution. Because the equations are time delayed, the initial state covers the history of the system for a time $-\tau \leq t \leq 0$. We start from a value of $K < K^c$, and then increase it in steps of ΔK. Until $K \leq K^c$, the initial perturbations are damped and the system converges to fixed points solutions. Focusing on the numerical results of model I, at $K^c = 5.17$, the oscillations start growing and converge towards a limit cycle attractor with a large amplitude (see Figure 5.8a). This solution is used to initialise the subsequent integrations, for which the control parameter K is varied in both directions in steps of $\pm\Delta K = \pm 0.01$. The amplitude of the oscillations gets larger as K increases. The largest value of the control parameter that we consider is $K_{\max} = 5.25$, for which the parameter expansion of the weakly nonlinear analysis is $\varepsilon_{\max} = \sqrt{K_{\max} - K_c} = 0.29$. On the other hand, the amplitude of the velocity fluctuations decreases smoothly for $K < K^c$, until we reach the fold location at $K^F = 5.03$. At this location, the highly perturbed initial state decays to the fixed point solution, as shown in Figure 5.8b.

To validate the linear analysis, the growth/decay rates close to the Hopf/fold locations are extracted from the time series by using a linear regression on the logarithm of the

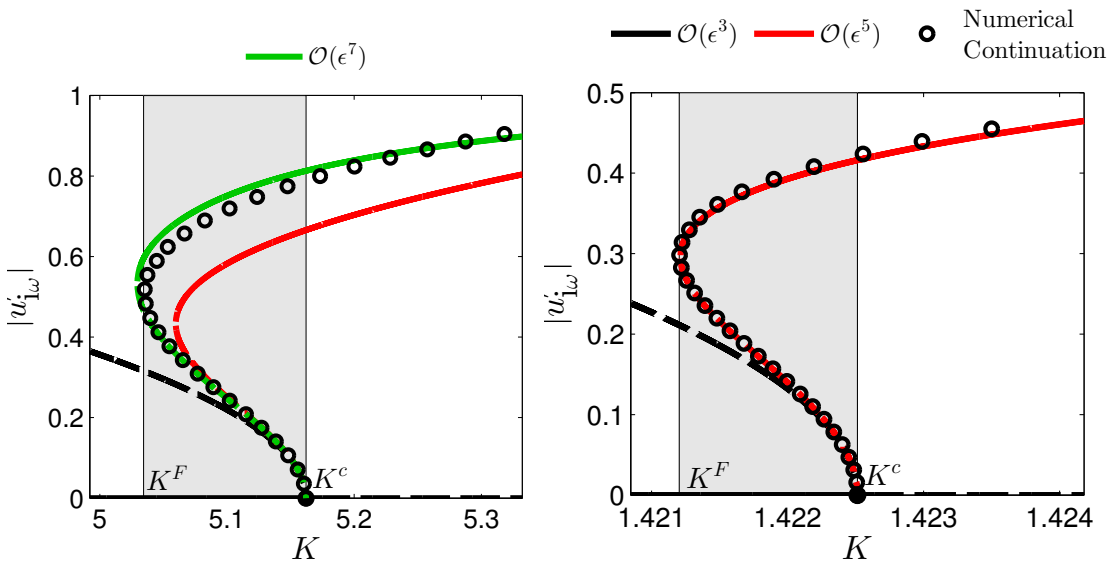

Fig. 5.9 Comparison between the weakly nonlinear analysis at various orders (lines) and numerical continuation results (circles). The bistable region is highlighted in grey. Solid and dashed lines indicate stable and unstable solutions, respectively. Left and right panels contain the results obtained with damping models I and II respectively.

fluctuations amplitude. The latter is obtained using the Hilbert transform on portions of the time series. The growth and decay rates, reported in Figure 5.8, can be compared with those we obtain when solving the eigenvalue problem (5.11) at the same locations. These values are $\sigma = 2.097 \times 10^{-4}$ and $\sigma = -3.82 \times 10^{-3}$ respectively, and are in good agreement with the time marching results. To validate the weakly nonlinear analysis, we compare the oscillation amplitudes at the various frequency components with those predicted by numerical continuation of limit cycles. This is because the latter also yields information about the unstable limit cycles, which are more difficult to investigate with time marching simulations.

The bifurcation diagram in Figure 5.9 shows the amplitude of the oscillations at the fundamental frequency as predicted from the weakly nonlinear analysis at fifth order (red line) and limit cycle continuation (black circles). For damping model II (right inset), the prediction between the amplitude of the limit cycles calculated with numerical continuation compares well with the fifth order weakly nonlinear expansion, in red. However, this is not true for damping model I. In this case, although the fifth order analysis improves the predictions of the third order one (it predicts the existence of stable limit cycles of the bistable region), these results do not compare well with the exact solutions. This is because, in this case, the width of the bistable region is much larger than in the other case. The value of the expansion parameter ε at the fold point for the two damping models is $\varepsilon_{\mathrm{I}} = 0.35$ and $\varepsilon_{\mathrm{II}} = 0.045$, where $\varepsilon_{\mathrm{I}} \equiv \sqrt{K_{\mathrm{I}}^c - K_{\mathrm{I}}^F}$. The weakly nonlinear expansion is strictly valid only

for $\varepsilon \ll 1$. This condition is well satisfied at the fold point for model II, i.e., $\varepsilon_{\mathrm{II}} \ll 1$, but it is not for model I. Thus, to improve the quality of the weakly nonlinear analysis, expansion to a higher order is required in the latter case.

This is achieved by introducing a third slow timescale $t_6 = \varepsilon^6 t_0$ and expanding equations (5.14) up to order ε^7. The expansion terms at these orders are lengthy and are not reported here. We can solve straightforwardly the equations at $\mathcal{O}(\varepsilon^6)$, which yields even harmonic contributions, because they contain no resonant terms. At order ε^7 we look only at the response at the fundamental frequency, which contains resonant terms. By imposing the solvability condition we obtain the Stuart–Landau equation:

$$\frac{\partial W}{\partial t_6} = \lambda_7 W + \nu_7 |W|^2 W + \mu_7 |W|^4 W + \xi_7 |W|^6 W. \tag{5.49}$$

The Landau coefficient definitions are analogous to those in equation (5.43). The values we obtain for these coefficients when $K < K^c$ are $\lambda_7 = (9.63 + 5.59\mathrm{i}) \times 10^{-5}$, $\nu_7 = 0.012 - 0.013\mathrm{i}$, $\mu_7 = 0.0168 + 0.003\mathrm{i}$, and $\xi_7 = 0.003 + 0.002\mathrm{i}$. λ_7 and μ_7 change sign across the bifurcation. The overall evolution of the complex-valued amplitude W is obtained by summing the contributions at all orders:

$$\frac{\mathrm{d}W}{\mathrm{d}t_2} = \sum_{n=1}^{3} \varepsilon^{2n-2} \frac{\partial W}{\partial t_{2n}} = \lambda W + \nu |W|^2 W + \mu |W|^4 W + \xi |W|^6 W, \tag{5.50}$$

with $\lambda = \lambda_3 + \varepsilon^2 \lambda_5 + \varepsilon^4 \lambda_7$ and similarly for the other coefficients. Amplitude roots and the corresponding stability and phase shifts are then calculated numerically.

The seventh order weakly nonlinear bifurcation diagram is shown in Figure 5.9a (green line). No significant changes are observed for the unstable solutions close to the Hopf location, but the fold location and the amplitude of oscillation predicted greatly improves at this order.

Further information can be extracted from the weakly nonlinear analysis, which is shown in Figure 5.10 for damping model I only, at the seventh order expansion. This is the difference between the frequency of limit cycle oscillations compared with that of the marginally stable eigenvalue, and the amplitude of the harmonics in the spectrum of the oscillatory solution. The zeroth harmonic corresponds to the mean shift in the acoustic level previously discussed, which is indeed observed in time domain simulations, due to the fact that the nonlinearity is not odd. All these results show a good agreement with those obtained from the exact solution.

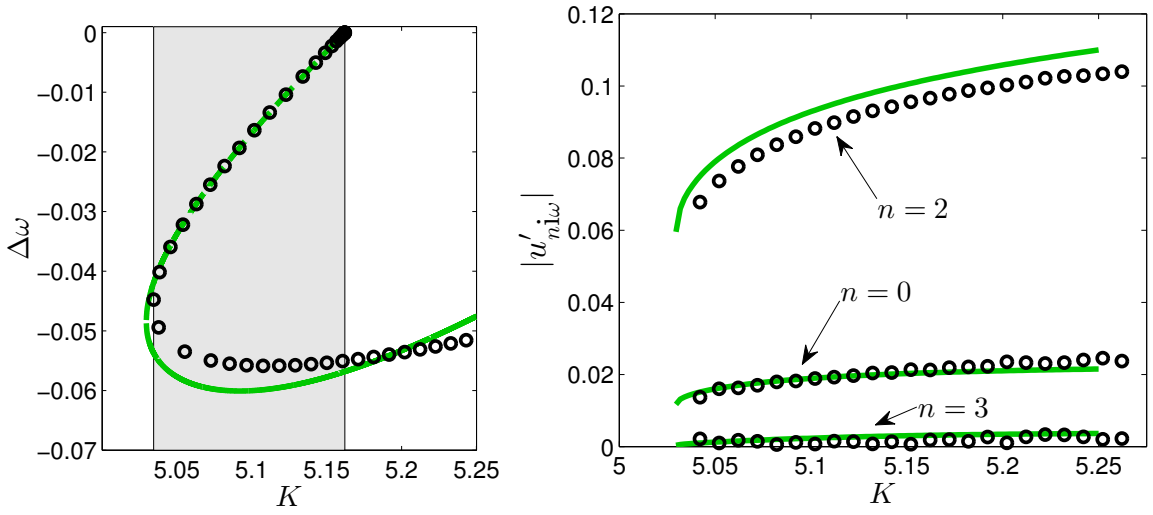

Fig. 5.10 Left: frequency shift $\Delta\omega$ of the oscillations with respect to the marginally stable frequency at the Hopf bifurcation. Right: magnitude of the harmonic contributions in the spectrum of the stable oscillatory solutions. Results from weakly nonlinear analysis (lines) and amplitude of FFT of time domain simulations (circles) are compared.

5.6 Practical implementation

One of the attractive characteristics of the weakly nonlinear analysis is that it is computationally very cheap. The expansion of the equations can be tedious at high orders, but the process can be automatised with symbolic solvers. The information needed for the analysis is (i) a marginally stable solution, (ii) the direct and adjoint eigenvectors corresponding to the marginally stable solution, and (iii) the Taylor expansion of the nonlinear heat release fluctuations. Once these components have been found, the calculation of a bifurcation diagram reduces to a series of matrix inversions and multiplications. This is affordable even for systems with a large number of degrees of freedom, as was shown by Sipp & Lebedev (2007); Meliga *et al.* (2009) for the analysis of flow bifurcations. An alternative technique, numerical continuation (Waugh *et al.*, 2014), requires time-marching for several cycles in order to converge to a limit cycle. Another technique, time marching, requires even more cycles and can converge only to stable oscillations. For our low-order model, we find that the weakly nonlinear analysis is 20 times faster than numerical continuation, and three orders of magnitude faster than time marching.

It can be challenging, however, to obtain an analytical model for the nonlinear heat release when the combustion system is complex, e.g. turbulent. A possible solution is to measure the Flame Transfer Function (FTF) for small amplitude oscillations and to combine this with an acoustic network to obtain a marginally stable solution, which will be at a

given frequency. The direct and adjoint eigenvectors of this solution can be calculated easily. The Taylor expansion coefficients α for the nonlinear heat release dynamics can be obtained through experiments or DNS, by forcing the system at various amplitudes at the marginally stable frequency. One can then calculate the Taylor coefficients by finite difference methods, although this may be prone to inaccuracies at large amplitudes due to error propagation. Alternatively, as in this study, the nonlinear response can be fitted, in a least squared sense, onto a polynomial over the amplitude range of interest. This expansion can also be generalised to non-static nonlinearities, meaning that the heat release fluctuation q' is a function of the velocity fluctuation u' and its time derivative $\dot{u}'$.

With this procedure, all the information required for the weakly nonlinear analysis is known and the theory can be applied. Assuming that the measured nonlinear behaviour changes slowly with frequency, the entire bifurcation diagram can be constructed, which would require many more measurements if determined experimentally or numerically. Moreover, the dynamic evolution of the oscillations associated with the global mode can be obtained for various values of the bifurcation parameter, by direct integration of the Stuart–Landau equation.

5.7 Conclusions

In this chapter we have investigated nonlinear thermoacoustic oscillations in a Rijke tube using a high order weakly nonlinear expansion of the governing equations. The framework we analysed, composed of a wave-based approach for the linear acoustic equations and a nonlinear model for the heat release response, is general and can be extended to more complex networks easily. We have shown how a high order expansion close to the Hopf bifurcations can be used to predict the amplitude of stable and unstable limit cycles, the frequency shift with respect to the marginally stable solution, and the region of bistability for subcritical bifurcations. We have compared our results with the exact solutions of the fully-nonlinear equations and shown that the method yields accurate results when the expansion is truncated at fifth/seventh order. Using this type of analysis, the numerical/experimental effort needed to construct a bifurcation diagram can be significantly reduced.

The weakly nonlinear analysis we have performed is valid for a deterministic system, close to a Hopf bifurcation, and assumes that only one mode is marginally stable and all the other thermoacoustic modes are damped. The influence of turbulence and combustion noise can be modelled phenomenologically as random forcing (Noiray & Schuermans, 2013*b*; Rigas *et al.*, 2015); their effects can be captured by including stochastic terms in the Stuart–Landau equation. Other possible extensions of the theory are the following: varying the

bifurcation parameter, a second mode may become marginally stable in the vicinity of the first Hopf location, resulting in a sudden change in the system dynamics, as discussed by (Sipp, 2012). In this case, the theory could be extended by considering a codimension two bifurcation, as described in Meliga *et al.* (2009). It can also be extended to investigate the response of the system to external forcing. In this case, the forcing terms appear explicitly in the amplitude equations, as shown by Sipp (2012), and the weakly nonlinear interaction between the global mode and the forcing is taken explicitly into account. Moreover, the unknown Landau coefficients of the model can be identified from self-excited limit cycles oscillations of the system, as described in Noiray & Schuermans (2013*a*), or from transient and steady-state measurements when the system is subjected to external forcing (Rigas *et al.*, 2016). This method could provide a systematic way for devising open-loop control strategies for the regulation of thermoacoustic oscillations (Paschereit & Gutmark, 2008; Ćosić *et al.*, 2012).

Chapter 6

Heat release response to forced flow oscillations of a low-order modelled laboratory scale dump combustor

In this chapter, a low-order model for the dynamics of a bluff-body stabilised flame is developed. The model, based on the kinematic G-equation, aims to obtain a numerically cheap but qualitatively reasonable approximation for the heat release dynamics. This could be coupled in an acoustic network to estimate the frequencies at which thermoacoustic oscillations can occur. The low-order model developed mimics the flame dynamics over forced cycles reasonably well. This is because a rather accurate description of the flame-flow interaction is considered here, using an Unsteady Reynolds Averaged Navier–Stokes (URANS) meanflow, provided by Dr. Carol Armitage. However, it is found that the heat release response tends to be overestimated by the model, which is also very sensitive to parameters such as the convection speed.

The content of this chapter was published in Orchini & Juniper (2015).

6.1 Introduction

Low-order modelling in thermoacoustics relies on radical (but physically-based) approximations in the flame-flow-acoustic coupling, and allows for a great reduction of the number of degrees of freedom needed to describe the thermoacoustic interaction. As the computational cost required to integrate the system is highly reduced, low-order models can be used to investigate a large variety of parameters and gain insight into the physical mechanisms that cause thermoacoustic oscillations to arise. For premixed flames, the kinematic G-equation

is a common model used to determine the position and evolution of a thin flame front, as well as the amount of heat released by the flame. In the linear limit, transfer functions of conical and V shaped flames to harmonic velocity and heat release fluctuations have been evaluated analytically for a variety of underlying flow fields (Schuller *et al.*, 2003; Preetham *et al.*, 2008). In particular, a travelling wave model for flow perturbations has been shown to accurately reproduce the flow-flame interaction. Also, transfer functions of heat release fluctuations to harmonic velocity disturbances for these flame shapes have been proven to match experimental results (Durox *et al.*, 2009; Karimi *et al.*, 2009). In the nonlinear regime, 2-dimensional tent and axisymmetric conical flames have been investigated with a variety of tools both in the frequency and time domain. Frequency domain analyses are based on the Flame Describing Function (Dowling, 1999; Noiray *et al.*, 2008), and allow for the prediction of frequencies and amplitudes of oscillations when the oscillations are associated with a single thermoacoustic mode. Time domain analyses allow for a more extensive investigation of thermoacoustic systems, and phenomena linked to the nonlinear dynamical nature of the system, such as period-doubling, secondary Hopf bifurcations, and routes to chaos, can be observed (Kashinath *et al.*, 2014; Waugh *et al.*, 2014; Orchini *et al.*, 2015), as was shown in Chapter 3.

In this chapter, we extend the models derived for conical flames to a more realistic combustor configuration. The combustor we investigate is a dump combustor which has been developed by Balachandran *et al.* (2005), and is shown in Figure 6.1. As the experiments performed on this setup represent one of the first set of measurements of forced turbulent flames in the nonlinear regime, low-order and CFD simulations of this rig have already been performed. In Graham (2012) a G-equation based low-order model has been developed. However, in that study the flow field was treated as a potential flow generated by a pulsating spherical source upstream of the bluff-body. This does not include the characteristic formation of vortices at the slot and their roll up. Also, each side of the flame was treated explicitly as a single-valued function in one of the coordinates; this condition is not necessarily satisfied if the flame shape becomes very wrinkled. More accurate numerical simulations based on unsteady Reynolds-averaged Navier–Stokes (URANS) models were performed by Armitage *et al.* (2006); Ruan *et al.* (2013).

Our goal is to develop a low-order model based on the fully implicit G-equation that describes the flame-flow interaction in this configuration. The implicit formulation naturally includes the possibility for the flame to assume configurations that are not necessarily single-valued in any simple coordinate system. The flame is stabilised by a bluff-body, and, although it resembles the structure of a V-flame, it differs from it in the fact that the reactants are enclosed between inner and outer flame surfaces, which are assumed to be axisymmetric.

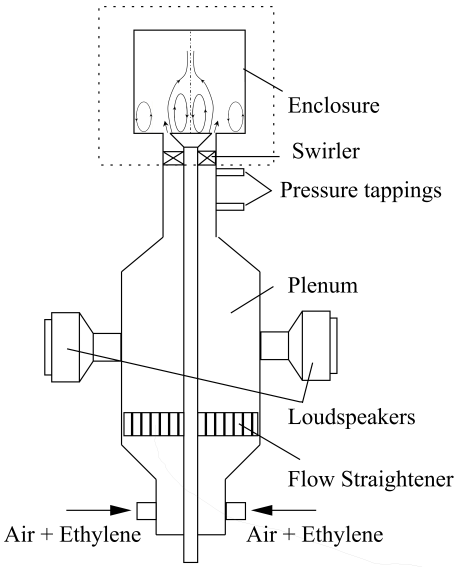

Fig. 6.1 Schematic of the bluff-body combustor rig developed by Balachandran *et al.* (2005). Air and fuel are premixed far upstream of the dump plane. A schematic of the flow field in the combustion zone is shown.

The flame mean shape and evolution are strongly affected by the interaction of the flow with the walls and the presence of recirculation zones in the combustion chamber (see Figure 6.1). Here, we propose a flow model which is based on experimental and numerical observations of the acoustically forced flow field. Then, we perform a qualitative comparison between the forced response of flame and heat release dynamics of our model and results obtained in previous studies. Although qualitatively the flame shape mimics the experimental flame dynamics, major quantitative differences are observed in the heat release response. This is because the model is low-order, and we are neglecting, e.g., turbulence effects and heat losses in the outer recirculation zone. We conclude discussing our results and commenting on how our low-order model could be improved in a future study. Once a satisfactory agreement with the realistic forced response is achieved, the flame-flow model can be coupled with a linear acoustic network as in Orchini *et al.* (2015), to obtain a flame-acoustic feedback loop and have a complete low-order thermoacoustic model able to predict frequencies and amplitudes of oscillations both in the frequency and time domain with a small computational cost.

The chapter is structured as follows: in §6.2 the flame and flow field modelling for the configuration under consideration are developed, considering experimental results and extending models available in the literature. In §6.3 the model FDF is evaluated, by forcing the flame acoustically at various frequencies and amplitudes. Results are compared against

experiments and URANS simulations. In §6.4 the role of the convection speed on the system response is discussed. Finally, in §6.5 the analysis results are summarised.

6.2 Modelling

In this section we describe in detail the low-order model and our assumptions. The main concept is to first obtain a mean flow representative of the geometry under consideration and freeze it, thus solving only for the linearised acoustic equations which induce fluctuations in the mean flow. As a consequence, the full Navier–Stokes equations need to be solved only once, for the mean flow, greatly reducing the computational cost needed. The geometry we consider is axisymmetric, and we will therefore use cylindrical polar coordinates.

6.2.1 Flow field

We decompose the flow field $\boldsymbol{u}$ into a mean component $\overline{\boldsymbol{u}}$ and a fluctuation $\boldsymbol{u}'$. The latter is not necessarily small, and we will perform a fully nonlinear analysis. In the literature, most low-order analyses involving a kinematic description of the flame assume the mean flow to be uniform in the axial direction, and zero in the radial and azimuthal components. However, for the combustor we are modelling, we cannot make this assumption: the presence of a conical bluff-body just upstream the combustion zone introduces a strong radial component of the flow at the inlet, creating a side recirculation zone at the dump plane. Also, the wake induced by the bluff-body forms a large central recirculation zone. These recirculation zones guarantee the flame stabilization, as they promote flame anchoring at the dump plane, and also greatly affect the flame's shape and dynamics.

On account of this, we want to use a realistic mean flow, i.e., a mean flow that accurately describes the location of the recirculation zones. This can be obtained solving the Reynolds-averaged Navier–Stokes (RANS) equations in the enclosed domain of Figure 6.1. The mean flow we use in the following analysis has been obtained by time-averaging unsteady RANS simulations performed by Armitage *et al.* (2006). The radial ($\overline{u}_r$) and axial ($\overline{u}_z$) components of the averaged velocity field are shown in Figure 6.2, and the azimuthal component is zero, because we are considering a perfectly axisymmetric configuration.

On top of the mean flow, fluctuations develop when the system is acoustically forced by a loudspeaker, or when a thermoacoustic oscillation arises. Experimental cold flow smoke visualizations have shown that acoustic fluctuations cause the formation of a pair of counter rotating vortices in the inner and outer sides of the flame (one in each recirculation zone) (Balachandran *et al.*, 2005). The vortices are transported downstream with a

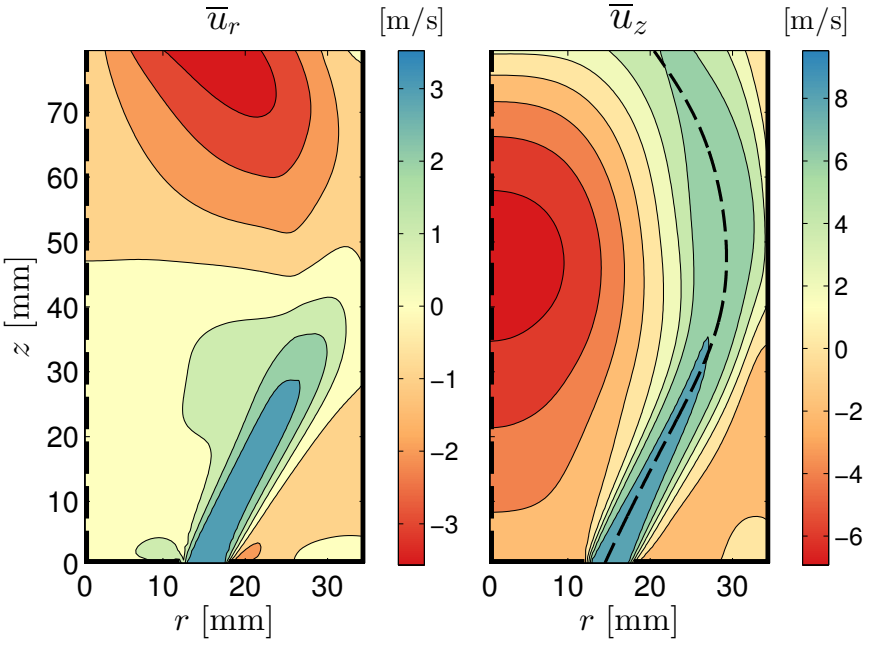

Fig. 6.2 Averaged URANS flow field components in the combustion zone. Solid thick lines indicate walls. The dashed lines indicate the centerline (left boundaries) and the streamline $r = \rho_s(z)$ that passes through the slot midpoint (only in the right frame).

characteristic velocity, the convection speed, causing flame wrinkling and consequent heat release fluctuations. The scenario is similar to the one observed for conical flames. In that case, oscillations are axisymmetric with respect to the centerline, and it has been shown that an axial developing travelling wave velocity model, with radial fluctuations computed by means of mass conservation, allows for a realistic description of the flame-flow coupling mechanism (Schuller *et al.*, 2003; Preetham *et al.*, 2008; Durox *et al.*, 2009).

Mimicking this description, we want to generate a fluctuating flow field which is convected axially with a certain convection speed and generates vorticity in the inner and outer sides of the flame. For the axial component, we impose acoustic velocity fluctuations at the inlet, and we convect them downstream. For the convection, we use as a reference velocity the axial velocity of the streamline $r = \rho_s(z)$ that passes through the centre of the slot (see Figure 6.2). This assumes that axial fluctuations do not vary in the radial direction. Finally, we solve for mass conservation to obtain radial fluctuations. We want these oscillations to have opposite sign on the two sides of the flame, in order to emulate the formation of counter rotating vortices. This is achieved by imposing radial fluctuations to be zero along the streamline $r = \rho_s(z)$. Summarising, we solve

$$\frac{\partial u'_z}{\partial t} + \overline{u}_z\left(\rho_s\left(z\right), z\right)\frac{1}{K}\frac{\partial u'_z}{\partial z} = 0, \qquad u'_z\left(z,t\right)|_{z=0} = u'_{ac}(t) \tag{6.1}$$

for the convection, and

$$\frac{1}{r}\frac{\partial\left(r\,u_r'\right)}{\partial r}+\frac{\partial u_z'}{\partial z}=0, \qquad u_r'\left(r,z,t\right)|_{r=\rho_s(z)}=0 \tag{6.2}$$

for mass conservation. The parameter K introduced in equation (6.1) is the ratio between the mean and convection speeds, which in general may not be equal to 1 (Preetham *et al.*, 2008; Kashinath *et al.*, 2013*b*). In the following, we fix $K=1.5$; this particular choice for K is discussed in §6.4.

As we have assumed that axial fluctuations are not a function of the radial direction, equation (6.2) can be solved yielding an expression for radial fluctuations, which reads:

$$u_r'(r,z,t)=-\frac{1}{2}\frac{\partial u_z'}{\partial z}r\left(1-\frac{\rho_s^2\left(z\right)}{r^2}\right). \tag{6.3}$$

Note that, with this model, radial fluctuations diverge when approaching the centerline $r=0$. However, because we use a kinematic equation for the dynamics of the flame (see next section), we need to evaluate the velocity field only around the flame front, which is always distant from the centerline, and the use of equation (6.3) is justified.

Flame model

We use the kinematic G-equation to describe the flame and heat release dynamics. We define a field G whose level set $G=0$ identifies the flame surface, which separates reactants ($G<0$) from products ($G>0$). The flame front evolves according to the transport equation (Markstein, 1964):

$$\frac{\partial G}{\partial t}+\boldsymbol{u}\cdot\nabla G=s_L\left|\nabla G\right|. \tag{6.4}$$

Aside for its sign, the G-field away from the zero contour line has no physical meaning, and we define it as a signed distance function. We define the zero level set line implicitly, i.e., as $G(r,z,t)=0$, without assuming that the flame is single-valued in one of the two coordinates as is done in Preetham *et al.* (2008); Graham (2012). This allows us to naturally describe topological changes in the solution, which occur when pocket of fuels detach from the flame's main body, and to be able to describe very wrinkled flame shapes, which in general cannot be found with an explicit treatment of the flame front. Topological changes and highly wrinkled structure are the main features of this flame, as can be observed in Figures 6.5 and 6.6, and need to be accounted for. In equation (6.4) $\boldsymbol{u}=\overline{\boldsymbol{u}}+\boldsymbol{u}'$ is the underlying flow field and s_L the flame speed. The flame speed is in general a function of the equivalence ratio, turbulence intensity, and local stretch effects. In this analysis, we consider fully premixed, laminar

flames. The equivalence ratio ϕ is used to define the flame speed of the laminar flat flame sheet, which is given by the empirical relation:

$$s_L^0(\phi) = k_1 \phi_2^k e^{-k_3(\phi - k_4)^2}. \tag{6.5}$$

The fuel we consider is an air-ethylene gaseous mixture, for which the coefficients in equation (6.5) are given by $k_1 = 1.32176$, $k_2 = 3.11023$, $k_3 = 1.72307$, $k_4 = 0.36196$ (Armitage *et al.*, 2006). We consider a uniform equivalence ratio $\phi = 0.65$, yielding $s_L^0 = 0.3$ m/s. Corrections to the unstretched flame speed are due to curvature effects (Markstein, 1964; Tien & Matalon, 1991), and are typically accounted for by:

$$s_L = s_L^0 (1 - \mathcal{L}\kappa), \tag{6.6}$$

where $\mathcal{L}$ is the Markstein length and $\kappa = \nabla \cdot \hat{\boldsymbol{n}} = -\nabla \cdot \frac{\nabla G}{|\nabla G|}$ the flame curvature. We fix $\mathcal{L} = 1.2 \times 10^{-3}$ m; this value is consistent with the Markstein numbers which have been used in similar studies on the conical flame modelled with the G-equation (Waugh *et al.*, 2014; Orchini *et al.*, 2015). However, equation (6.6) is a linear correction to the flame speed with respect to the local curvature. Looking at the flame shapes that were observed experimentally and numerically, we expect to find very wrinkled flame structures and the formation of pinch-offs. When a pinch-off forms, the flame becomes cuspy and the local curvature can be very high: higher-order stretch corrections are needed. Other studies (Ronney & Sivashinsky, 1989; Kelley & Law, 2009) have addressed the question of developing nonlinear models for the influence of highly stretched flame sheets on the flame speed. We shall adopt one of the nonlinear models they have proposed, which reads:

$$s_L(\kappa) : \begin{cases} \left(\frac{s_L}{s_L^0}\right)^2 \log \frac{s_L}{s_L^0} = -\mathcal{L}\kappa & \kappa \leq \frac{1}{2\mathcal{L}e} \\ \\ s_L = s_L^0 e^{-\frac{1}{2}} & \kappa > \frac{1}{2\mathcal{L}e} \end{cases}, \tag{6.7}$$

and is plotted in Figure 6.3. In equation 6.7 the flame speed s_L is defined implicitly as a function of the curvature κ.

Expanding equation (6.7) around $s_L = s_L^0$ (i.e., small curvature) yields:

$$\begin{aligned} \kappa(s_L) \approx -\frac{1}{\mathcal{L}} \left[\kappa|_{s_L = s_L^0} + \left.\frac{\mathrm{d}\kappa}{\mathrm{d}s_L}\right|_{s_L = s_L^0} \left(s_L - s_L^0\right) \right] = \\ = -\frac{1}{\mathcal{L}} \frac{s_L - s_L^0}{s_L^0}, \end{aligned} \tag{6.8}$$

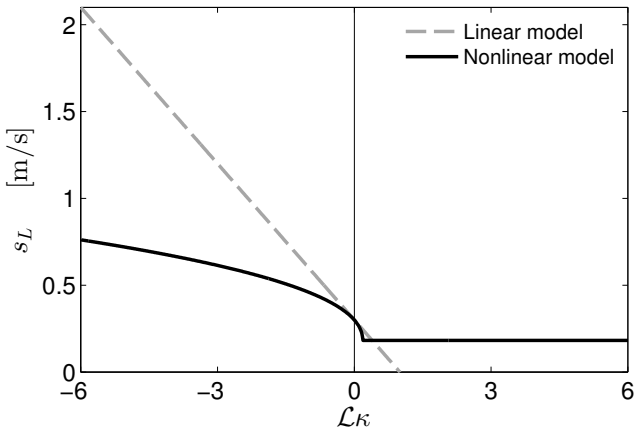

Fig. 6.3 Nonlinear model adopted for the flame speed curvature dependence for $s_L^0 = 0.3$. High-order terms decrease the curvature's influence on the flame speed.

showing that in this limit we recover the linear model (6.6). The saturation in equation (6.7) for $\kappa > 1/(2\mathcal{L}e)$ is necessary to keep the flame speed single-valued with respect to the curvature. Nevertheless, it is unlikely that curvature values will lie within this range because premixed flames propagate normal to themselves and cusps form pointing towards the products (Lieuwen, 2012). Large positive curvature values would indicate that a cusp has formed pointing towards the reactants, which is unlikely to arise and can be checked afterwards. Adopting the nonlinear model (6.7), the influence that the curvature has on the flame speed is reduced for very wrinkled flame sheets.

6.2.2 Numerical implementation and mean flame shape

To numerically integrate equation (6.4) we define the following set of non-dimensional variables:

$$t^* = t\frac{u_{ref}}{H} \qquad \boldsymbol{u}^* = \frac{\boldsymbol{u}}{u_{ref}} \qquad s_L^* = \frac{s_L}{u_{ref}}$$
$$z^* = \frac{z}{H} \qquad r^* = \beta\frac{r}{H} \qquad \mathcal{M} = \frac{\mathcal{L}}{H} \tag{6.9}$$

where $\beta \equiv H/D$, H and D are the enclosure height and the diameter of the bluff-body respectively (see Figure 6.1), and u_{ref} is a reference speed chosen to be the one at the slot midpoint. In contrast to the G-equation notation widespread in the literature, in which the stretch parameter β represents the flame's aspect ratio (Preetham *et al.*, 2008; Kashinath *et al.*, 2014), here β does not have a particular physical meaning and is just a geometrical parameter. This is because the mean flow is non-uniform and therefore we cannot derive an analytical expression that relates the flame's aspect ratio to the flame speed.

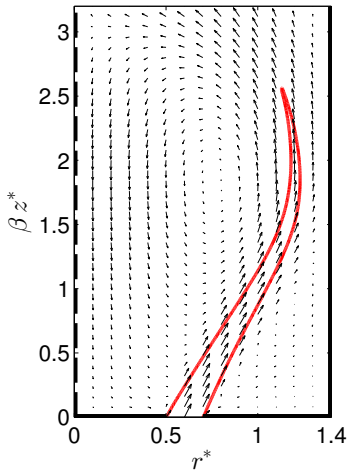

Fig. 6.4 Mean flame shape contour $G = 0$ (red line) and mean flow vector plot for $\phi = 0.65$, $\mathcal{M} = 0.015$.

Setting $H = 80$ mm, $D = 25$ mm, and $u_{ref} = 10$ m/s, we fully determine the non-dimensional variables in (6.9). The numerical method we use to integrate equation (6.4) was discussed in §1.3.

Figure 6.4 shows the G-field zero level set obtained by setting the acoustic fluctuations $u'_{ac} = 0$ in equation (6.1), thus solving the stationary problem:

$$\beta \overline{u}_r{}^* \frac{\partial G}{\partial r^*} + \overline{u}_z{}^* \frac{\partial G}{\partial z^*} = s_L^*(\kappa) \sqrt{\left(\beta \frac{\partial G}{\partial r^*}\right)^2 + \left(\frac{\partial G}{\partial z^*}\right)^2}. \tag{6.10}$$

The steady flame shape compares favourably with the shapes that have been computed numerically by URANS simulations (Armitage *et al.*, 2006; Ruan *et al.*, 2013). This steady solution is used as an initial condition in the following analysis.

6.3 Forced acoustic response

For the enclosure length we have considered ($H = 80$ mm), the system is thermoacoustically stable. Consequently we investigate the forced (rather than self-excited) response of the system to axial flow oscillations. This will allow us to compare the unsteady flame structures and heat release response predicted by the low-order model with the ones observed experiments and URANS simulations.

We force the system by imposing velocity fluctuations with amplitudes in the range $|u'| \in [0.1\,,\,3.0]$ m/s and frequencies in the range $f \in [40\,,\,500]$ Hz at the inlet of the domain,

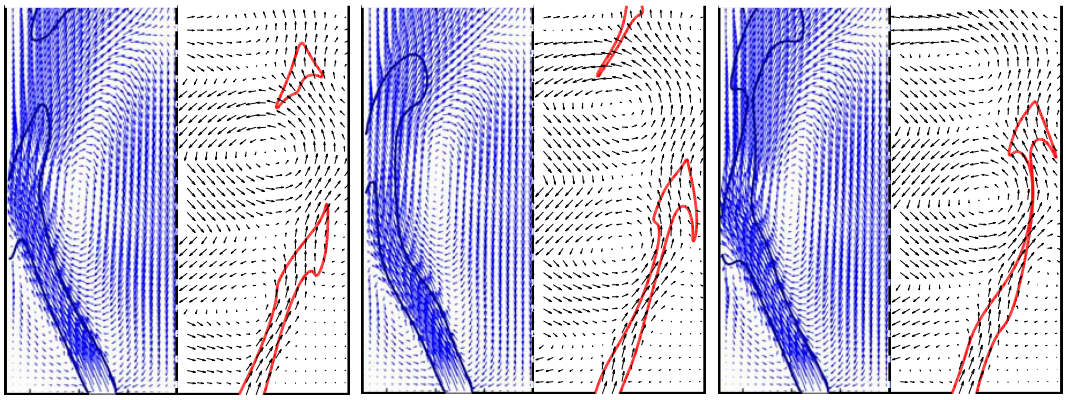

(a) $\varphi_{\text{cycle}} = \pi/6$ (b) $\varphi_{\text{cycle}} = 3\pi/6$ (c) $\varphi_{\text{cycle}} = 5\pi/6$

Fig. 6.5 Comparison between (left) URANS and (right) low-order model flame shapes and flow fields over a forcing cycle with $\text{St} = 1.28$, $A = 0.1$.

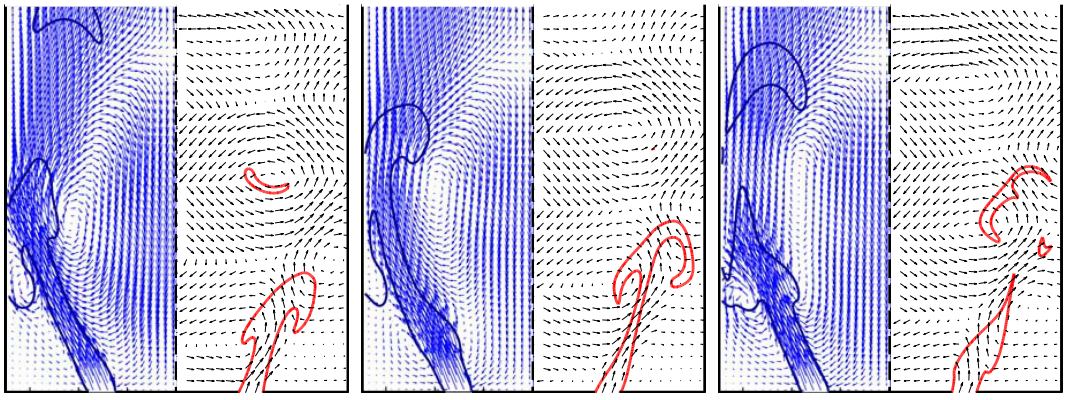

(a) $\varphi_{\text{cycle}} = \pi/6$ (b) $\varphi_{\text{cycle}} = 3\pi/6$ (c) $\varphi_{\text{cycle}} = 5\pi/6$

Fig. 6.6 Comparison between (left) URANS and (right) low-order model flame shapes and flow fields over a forcing cycle with $\text{St} = 1.28$, $A = 0.25$.

i.e., by setting the boundary condition of equation (6.1) to

$$u'_{ac}{}^{*}(t^*) = A \sin\left(2\pi \,\text{St}\, t^*\right), \tag{6.11}$$

where we have defined the non-dimensional amplitude of forcing $A = u'/u_{ref}$, and the Strouhal number $\text{St} = fH/u_{ref}$.

We numerically integrate the system forward in time for a time sufficient to reach the steady-state response and compute a few limit cycles on it.

6.3.1 Qualitative comparison

As our model is low-order, we do not expect a quantitative agreement with the experimental results. We are nevertheless interested in a qualitative comparison, in order to understand whether the model is capturing the main physical features of the system.

We focus the discussion on the two cases forced at a frequency $\mathrm{St} = 1.28$ ($f = 160$ Hz) and amplitudes $A = 0.1, 0.25$. In Figures 6.5 and 6.6, we compare our instantaneous flame fronts and velocity vector fields with those of Armitage *et al.* (2006)'s URANS simulations[1] at three phase angles over a forced cycle. A comparison with the simulations is easier, because we can compare the flame front $G = 0$ from our simulations with the contour lines of URANS snapshots corresponding to the $c = 0.5$ isocontour of the progress variable c, which is a good indicator of the flame front position. Experimental results only provide OH chemiluminescence fields, which are difficult to compare with the G-field, because the latter has no physical meaning away from the flame surface. An indirect comparison with the experiments can be found in Armitage *et al.* (2006).

At small forcing amplitudes (Figure 6.5), the intensity of the vortices is fairly small, and the flame tends to be long, undergoing a severe stretching. This eventually creates a large pinch-off which detaches from the flame far downstream and is then advected while burning; this large pocket of reactants does not burn completely before exiting the computational domain, meaning that part of the heat release is not accounted for. However, the latter problem is found also in DNS simulations and in the experiments, where the domain of computation of heat release is limited by the camera window for the OH chemiluminescence measurements.

At higher amplitudes (Figure 6.6), the flame structure over a cycle is very different. As the strength of the vortices is higher, the flame pinches off at a shorter axial distance, and as a consequence the flame is shorter on average. Also, the roll up of the vortices causes the formation of a characteristic mushroom-shape at the top of the flame, which we capture well. On the other hand, there are a few features that we cannot describe, such as the flame's impingement at the wall, which is responsible for some differences in the flame front shapes. Also, we note that the flames evaluated with the low-order model tend to be shorter than URANS flames. This is a common feature of all our simulations, and is probably due to the fact that we are not modelling gas expansion across the flame. The flame average length could be adjusted by varying the unstretched flame speed s_L^0 or the equivalence ratio as in equation (6.5). Also, we recall that the flow field model has to be valid only close to the flame surface, and no comparison should be sought far away from the $G = 0$ lines.

[1] Reprinted from Armitage *et al.* (2006), with permission from Elsevier.

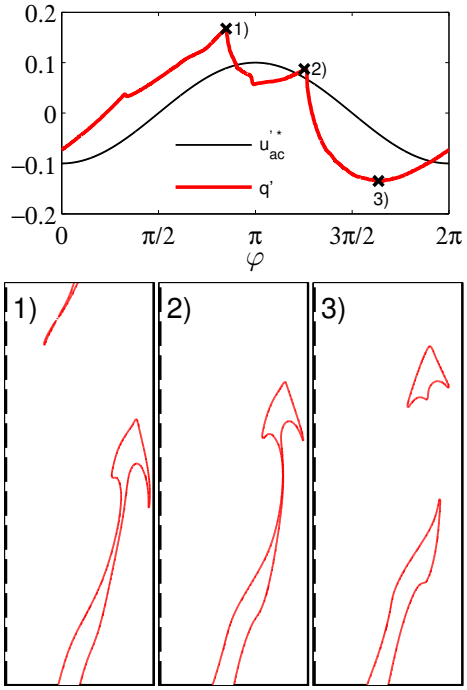

Fig. 6.7 Heat release response over a forced cycle with St = 1.28 and $A = 0.1$. Flame front snapshots corresponding to key moments in the heat release response.

Although improvements are possible, we find that the low-order flame-flow interaction model gives a reasonable description of the main kinematic features of the flame front, and it represents a significant improvement in the description of this type of flames respect to previous models involving the G-equations, such as the one presented in Graham (2012).

6.3.2 Heat release response

The heat release response is computed by calculating the amount of fuel burned at every instant in the domain, by

$$Q = 2\pi h_r \int_0^R \int_0^H \rho(r,z) s_L(\kappa) \sqrt{\left(\frac{\partial G}{\partial r}\right)^2 + \left(\frac{\partial G}{\partial z}\right)^2}\, \delta(G)\, r\, \mathrm{d}r\, \mathrm{d}z, \tag{6.12}$$

where δ is the Dirac delta function. The non-dimensional heat release fluctuations are defined by $q' = (Q - \overline{Q})/\overline{Q}$, where $\overline{Q}$ is the heat release averaged over a forcing cycle.

The integrated heat release over a forced cycle with St = 1.28 and $A = 0.1$ is shown in Figure 6.7. The heat release signal is strongly non-harmonic, meaning that it is a strongly nonlinear function of the imposed velocity. The amplitude of heat release oscillations is

greater than the amplitude of the forcing, meaning that the gain of the system exceeds 1, and the two oscillations are about $\pi/2$ out of phase.

A few key points of the heat release response have been highlighted in Figure 6.7. Point 1) corresponds to the absolute maximum of the heat release response, and is one of the cusps in the signal. To gain insight into the physical causes of the appearance of sharp peaks, we have plotted in the corresponding bottom panel of Figure 6.7 the flame front at the same instant. The main body of the flame is quite stretched, and there is a pocket of fuel, which had been released during the previous cycle, that is exiting the domain. On closer inspection, one can see that, at the instant under consideration, this pocket of fuel is breaking into two parts, i.e., the flame has just pinched off. A pinch-off creates a discontinuity in the flame shape, and the local flame curvature close to the pinch-off location suddenly becomes highly negative. Thus, according to equation (6.7), the local flame speed becomes higher. This has two effects:

(i) from equation (6.12) we see that the flame speed directly enters into the evaluation of heat release fluctuations. Therefore, it is expected that the moment at which the flame pinches off corresponds to an instantaneously high heat release response;

(ii) at the same time, a higher flame speed increases the rate of kinematic restoration (kinematic restoration is the process that smooths out the flame's wrinkles, and it is due to the fact that the flame propagates normal to itself (Lieuwen, 2012)). As a consequence, the cusps formed on the flame front are smoothed out quickly, decreasing the magnitude of curvature corrections and destroying flame surface area. Because both these effects have a negative impact on the total heat released by the flame, a rapid decrease of q' is expected after a pinch-off.

This is consistent with our observations. The same features just discussed are observed also in the second peak of the heat release time series, at point 2), where the main body of the flame undergoes a pinch-off. Finally, point 3) is the absolute minimum of q', as it corresponds to a moment in which the flame is short, and cusps on the flame surface have been smoothed out by kinematic restoration. From this instant on, the flame will elongate, increasing flame surface and thus heat release, until point 1) is reached again and the cycle restarts.

These arguments suggest that, for this particular flame structure, the formation of pinch-offs has an important role in the heat release response, because it induces high-amplitude fluctuations and the formation of cusps in the time-signal, which enhance nonlinear effects. Note that this effect cannot be observed in the simpler configuration of a conical flame (Waugh *et al.*, 2014; Orchini *et al.*, 2015). For conical flames, pinch-offs occur at the centerline

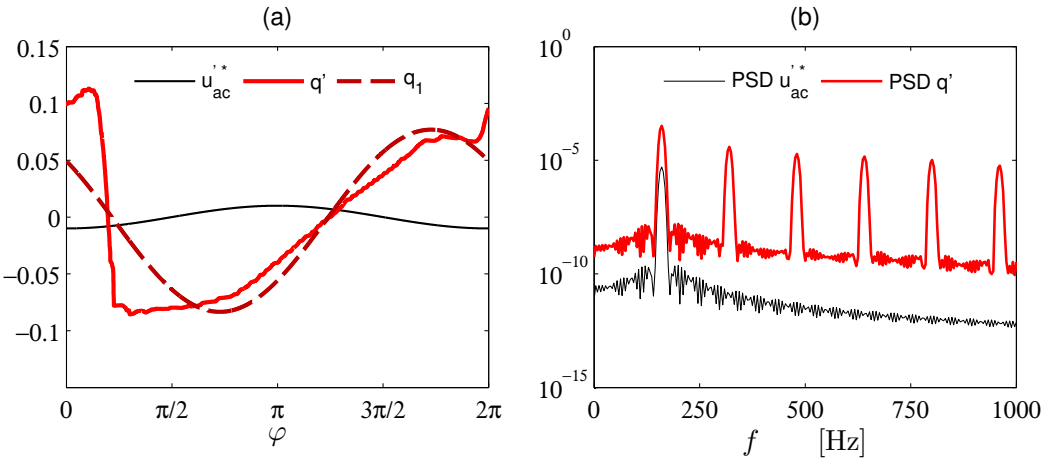

Fig. 6.8 (a): heat release response over a forced cycle with $\mathrm{St} = 1.28$ and $A = 0.01$. The contribution of the first harmonic is highlighted. (b): PSD of velocity and heat release fluctuations.

$r = 0$: because the flame is axisymmetric, the contribution of a flame element to the heat release is proportional to the radial distance (see equation (6.12)), and even if the local flame structure is highly wrinkled on the pinch-offs, its weight on the evaluation of the heat release is negligible. On the other hand, for the flame under consideration in this chapter, pinch-offs occur at a large radial distances, and provide large contributions to the integration of total heat release.

Flame Describing Function

Having integrated the forced response of heat release to velocity fluctuations, we can evaluate the Flame Describing Function (FDF) for this flame-flow configuration. The FDF is evaluated by extracting the heat released at the forcing frequency q_1, neglecting higher harmonics, and is calculated by:

$$\mathrm{FDF}(\mathrm{St},A) = F_1(\mathrm{St},A)\, e^{\mathrm{i}\phi_1(\mathrm{St},A)}, \tag{6.13}$$

where i is the imaginary unit, $F_1(\mathrm{St},A) \equiv \left|\frac{\hat{q}_1(\mathrm{St},A)}{A}\right|$ and $\phi_1(\mathrm{St},A)$ are respectively the gain and phase of the heat release first harmonic component to inlet velocity fluctuations.

Figure 6.8 (a) shows the heat release signal (and its first harmonic component) when the system is forced at 160 Hz with the smallest amplitude we have considered, $A = 0.01$: although the forcing amplitude is small, it is sufficient to induce the formation of pinch-offs, which is a nonlinear effect. This causes heat release fluctuations to have a very large amplitude, and the system's gain exceeds 1 by a large amount. Note that, in experiments and URANS simulations, the system response is linear for this forcing amplitude; this suggests

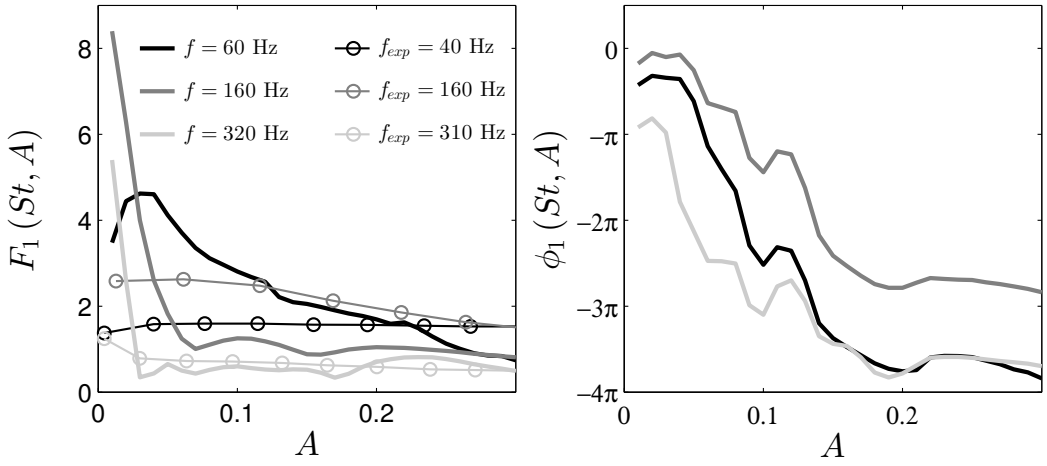

Fig. 6.9 FDF gain and phase as a function of the forcing amplitude at the frequencies $\mathrm{St} = 0.48, 1.28, 2.56$. Thick lines correspond to the low-order model results, circles to experimental measurements.

that the low-order model is too nonlinear, and corrections should be made to prevent the formation of pinch-offs at small forcing amplitudes. The presence of cusps in the heat release signals causes higher harmonics to have large contributions. The PSD plot of heat release fluctuations in Figure 6.8 (b) shows how strong the contribution of higher harmonics is even at this small forcing amplitude. Thus, if we want to use this FDF in a thermoacoustic feedback loop, we must assume that higher harmonics in the heat release are filtered out by the acoustic transfer function, which has to act as a strong low-pass filter for the feedback loop analysis to work (this assumption is not required if one uses time-domain techniques such as continuation analysis (Waugh *et al.*, 2014; Orchini *et al.*, 2015)).

Figure 6.9 shows the FDF amplitude dependence for three forcing frequencies. For all the frequencies we have considered, the gain shows an overall monotonical decay with the amplitude. At small amplitudes the gain exceeds the unitary value for all the frequencies shown. This is expected (to some extent) because of the similarity between this flame shape and V shaped flames (Schuller *et al.*, 2003; Durox *et al.*, 2009). In the linear limit, we find that the gain increases with the forcing frequency, reaches a maximum value at a forcing of 160 Hz, and then decreases for higher frequencies; the same feature was observed in experimental and URANS investigations (Balachandran, 2005; Balachandran *et al.*, 2005; Armitage *et al.*, 2006; Ruan *et al.*, 2013). By linear limit we mean the smallest forcing amplitude we have considered, $A = 0.01$. Nevertheless, as we have shown that pinch-offs can form at this amplitude, inducing nonlinear effects, the behaviour of the system in the linear limit is not properly characterised, and simulations with even smaller forcing amplitudes need to be performed, or the contribution of pinch-offs on the heat release has to be reduced.

We note that the gain values we find are much higher than those of the real system, especially in the low-amplitude limit. The gain reaches a maximum value of about 8, against the maximum value of 3 found in experiments at the same frequency. Excluding the influence of pinch-offs on the heat release that we have already discussed, a second possible explanation for such a strong overestimation of the gain can be found in the lack of a turbulence model in the underlying flow field in our equations. Indeed, in Hemchandra *et al.* (2011); Shin & Lieuwen (2013) it has been shown that, because of nonlinearities in the governing equations, turbulent fluctuations modelled as stochastic fluctuations couple with the forced oscillations and flame dynamics, affecting the kinematic restoration process, hence the formation of cusps, the rate at which flames wrinkles are smoothed out, and the evolution of the heat release. Lastly, we are also neglecting heat losses through the combustor wall in the outer recirculation zone. Because the temperature here is lower, the combustion process is less efficient, as was observed experimentally by Balachandran *et al.* (2005), via OH Planar Laser Induced Fluorescence (PLIF) (see Figure fig:Comparebalach).

6.4 Convection speed

In order to have a qualitatively reasonable comparison between URANS and low-order simulations in Figures 6.5 and 6.6, we have only looked at the flame's structures. As it turns out, this results in a disagreement between the velocity phases of the images we have compared. For the URANS simulations, the starting point of the limit cycle corresponds to a minimum in the velocity fluctuations at the slot; we denote this condition as φ^0_{min}. For the low-order simulations, we find that the phase that allows for a good comparison of flame fronts does not correspond to φ^0_{min}, but it has a shift $\Delta\varphi \approx \pi/4$ rad.

This shift is likely to be caused by our choice for the convection speed of velocity fluctuations. Indeed, several studies have shown that this parameter plays a key role in the correct description of the dynamics (Preetham *et al.*, 2008; Kashinath *et al.*, 2013*b*). In the advection equation (6.1) we have chosen the ratio between the mean and convection velocities to be $K = 1.5$. This was based on DNS simulations performed by Kashinath *et al.* (2013*b*), which predicted a value of K in the range $[1.1\,,\,2.0]$; values in this range have already been used in other studies (Waugh *et al.*, 2014; Kashinath *et al.*, 2014; Orchini *et al.*, 2015). However, the latter results were obtained for a laminar, conical flame configuration, and it is not surprising that the value of the convection speed may significantly vary for a bluff-body stabilised, turbulent flame. We nevertheless used laminar flame results because of the lack of information on the convection speed for the dump combustor under investigation when we started this analysis. More recently, new experiments have been performed on the

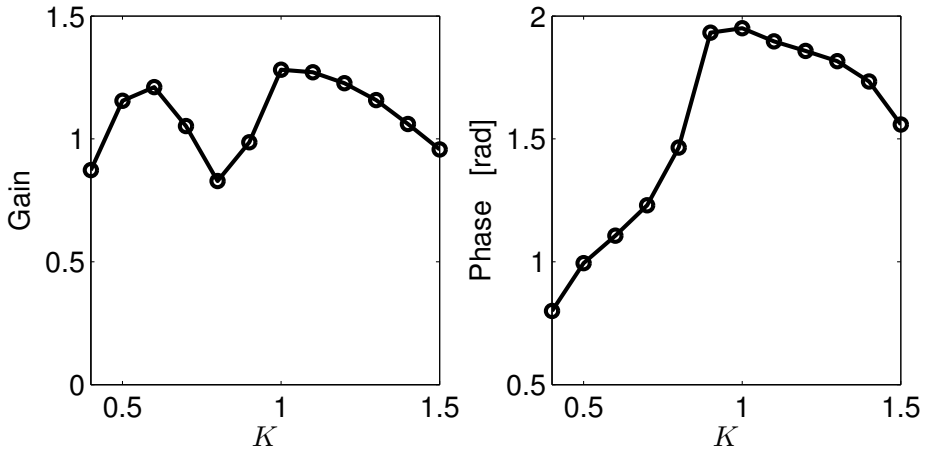

Fig. 6.10 Effect of the convection speed on the heat release gain and phase response. Forcing amplitude and frequency have been fixed to $A = 0.25$ and $\mathrm{St} = 1.28$ respectively.

same combustor by Kypraiou *et al.* (2015). Applying Proper Orthogonal Decomposition (POD) analysis on phase-averaged OH^* chemiluminescence images and computing the Power Spectral Density (PSD) of the POD time coefficients on self-excited thermoacoustic cycles, they have estimated the ratio between the mean flow and the convection speeds to be in the range $K = [0.59\,, 0.72]$. Unfortunately this information was not available to us when we performed the numerical simulations for the calculation of the FDF. A lower value of K means that fluctuations are advected downstream with a velocity that on average is higher than that of the mean flow, whereas in our calculations we have assumed them to move more slowly. A smaller convection speed corresponds to a larger wavelength between two vortices on the same side of the flame. This has a direct impact on the phase between the shedding of the vortices and the flame structure over time, and thus on the formation of pinch-offs and the heat release phase with respect to velocity fluctuations. It is worth mentioning that the convection speed is in general a function of the frequency (as found by Kashinath *et al.* (2013*b*)), and the analysis performed by Kypraiou *et al.* (2015) is not exhaustive, as it is performed on self-excited oscillations, which tend to have a frequency of about 350 Hz, close to the first resonant frequency of the burner.

Having gained knowledge of experimentally determined values for the convection speed, we have performed some numerical simulations fixing the amplitude and frequency of inlet oscillations, and varying the parameter K in the range $[0.4, 1.5]$ in steps of $\Delta K = 0.1$. To quantify the impact of K on the dynamics of the flame, we show in Figure 6.10 the gain and phase dependence on K of the FDF (defined as in equation (6.13)) evaluated at $A = 0.25$ and $f = 160$ Hz. The phase follows a clear path: it reaches a maximum when the convection speed is $K = 1$ and monotonically decreases for other values of K. Looking at the phase

values for $K = 1.5$ (our simulations), and $K = 0.6$ (experimentally determined), we observe that we can correct the phase of heat release fluctuations of about $\pi/6$ rad. On the other hand, the gain has an oscillatory dependence with respect to the convection speed, and the system's amplitude response is not so sensitive to variations in K. This means that convection speed variations are not enough to explain the strong gain overestimation we have observed.

6.5 Conclusions

In this chapter we have developed a low-order model to investigate the forced response of a bluff-body stabilised dump combustor, with a view to perform low-order analysis on self-excited oscillations in this combustor in the future. The flame front has been described by the kinematic G-equation evolving in a non-uniform flow field, which has been computed with URANS simulations. We have attempted to extend the classical travelling wave model that describes the interaction between conical flames and flows to this configuration. The model has been developed by analysing experimentally determined cold flow smoke visualizations of the forced system.

The resulting forced dynamics has been investigated by examining the system's response over a cycle: although a quantitative comparison cannot be performed because of fundamental differences between the systems, an acceptable qualitative agreement between URANS and low-order flame shapes is found, meaning that our model captures the main kinematic features of the flame surface dynamics, such as the formation of distorted mushroom-shaped fronts and pinch-offs. We have evaluated the Flame Describing Function (FDF) to inlet velocity fluctuations, and shown its amplitude dependence for three forcing frequencies. The dependence of the gain on the amplitude and frequency qualitatively compares favourably with experimental results, but we overestimate the system's gain by a large amount. This can have two causes. First, we find that pinch-offs form even at fairly small forcing amplitudes for this flame's structure, and they have a major role in the description of the flame and heat release dynamics. In particular, because they create cuspy flame fronts, they lead to large maximum values in the heat release, followed by a rapid destruction of flame surface. This occurs even if we have adopted a nonlinear model for the flame speed dependence on the curvature, which reduces the importance of very wrinkled flame front portions on the flame dynamics and heat release evaluation. As a consequence, the amplitude of heat release fluctuations is enhanced, and peaks in its signal are created, which in turn augments the heat release nonlinear response. This is a characteristic of this flame shape, and cannot be observed on conical flames, where pinch-offs occur at the centerline and have a very small influence on the heat release evaluation. The second cause of the gain overestimate is

probably due to the lack of a turbulent model for the flow field, which has a non-negligible impact on the flame and heat release dynamics.

The level of reliability of the low-order model can be improved. The convection speed of velocity perturbations can be varied according to the latest experimental results on the experimental apparatus. It was shown that adjusting the convection speed to experimentally determined values has a strong effect on the system response. In particular, it improves the agreement between the phases of heat release and velocity fluctuations, but cannot address the overestimation of the gain. The impact of pinch-offs on the heat release response can be reduced by varying the value of the Markstein length. Heat losses in the outer recirculation zone can be included using temperature profiles. Finally, a stochastic component can be added to the flow field to emulate turbulence effects. The latter two changes should reduce the heat release gain response to velocity fluctuations. The qualitative agreement obtained so far is encouraging for further research on this model. If further modifications prove satisfactory, the flame-flow model could then be used as a reliable, low-cost tool that can be coupled with an acoustic solver in order to obtain a complete low-order thermoacoustic network.

Chapter 7

Modelling of equivalence ratio fluctuations

In this chapter, an alternative model for the response of bluff-body stabilised flames is considered. An imperfectly premixed flame is considered here. Rather than focusing on the flame-flow interaction, we accurately model the convection of equivalence ratio fluctuations, which dominate the heat release response. An FDF is evaluated and compared with experiments, showing a reasonable quantitative agreement. The FDF calculated is approximated with a sum of time delays. It is shown that the sum of time delays provides an alternative point of view to the FDF results, which can help to understand the physical mechanisms dominating the heat release response. The FDF is embedded in an acoustic network and the harmonic balance method is applied to the system.

Part of the content of this chapter has been published in Semlitsch *et al.* (2016).

7.1 Introduction

In the previous chapter, we have seen how a realistic flow field model could be included in the *G*-equation framework, as an attempt to describe the flame and heat release dynamics in a bluff-body stabilised flame combustor with low-order models. Although it was found that considering a realistic flow field yields reasonable results for the flame structure, the heat release response largely overestimates the experimental one, because of the crude assumption that the heat release is proportional to the flame surface area. Although this could be improved, for example by considering turbulent flame speeds and shear layer effects on the combustion processes, the model would become computationally more expensive, in

contrast with the idea lying behind the G-equation as a quick tool to estimate the heat release response.

The latter is of interest to industry, as it would provide a tool able to quickly assess the stability of a given combustor, and estimate the potentially dangerous frequencies and the amplitude of the oscillations. This was one of the goals of Rolls-Royce's AMEL (Advanced Methods for prediction of Lean burn combustor unsteady phenomena) project, which is part of European research Clean Sky. This motivates the modelling and analysis of this chapter. Although I was not directly part of this project, I have developed the G-equation numerical framework that was used into it, and have actively collaborated with Prof. Ann Dowling, Prof. Matthew Juniper, and Dr. Bernhard Semlitsch (who ran some of the numerical simulations presented here) to improve the model and couple it with LOTAN. I also acknowledge discussions with Dr. Simon Stow, particularly for the suggestion of approximating an FDF with a sum of time delays.

To obtain a low-order model that can predict thermoacoustic instabilities with bluff-body stabilised flames, a simpler flame model than the one of the previous chapter is considered. The main idea, which consists in modelling the flow field with a potential flow, is based on the analysis performed by Dr. Owen Graham during his PhD (Graham, 2012). This model was shown to predict heat release dynamics comparable with that measured in the experiments. However, here we treat the G-equation in its fully nonlinear implicit form, whereas Graham tracked the two sides of the flame separately as single-valued functions, which were merged as a post-processing step. With such an approach, it is not straightforward to detect and track pinch-offs, and curvature effects cannot be applied at the flame tip, where they have the largest contribution. These issues are naturally solved by adopting an implicit formulation.

In this analysis, we will consider the effect of equivalence ratio fluctuations caused by velocity fluctuations at the injection location. The stiff injector model discussed by Polifke & Lawn (2007) is adopted. We perform calculations with and without curvature corrections, and compare the resulting FDFs. A sum of time delays model is used to fit the measured FDFs onto analytic functions. Insight into the physics captured by the model can be gained from the intensity of the response at the various time delays. We show, using the harmonic balance, how the resulting frequency associated with the most unstable mode matches the one observed in the experiments.

7.1.1 Mean flow model

Following the modelling approach proposed by Graham (2012), we adopt a potential flow field generated by a spherical source to model the mean flow around the bluff-body. This is a crude model, as it does not account for the presence of recirculation zones or the interaction

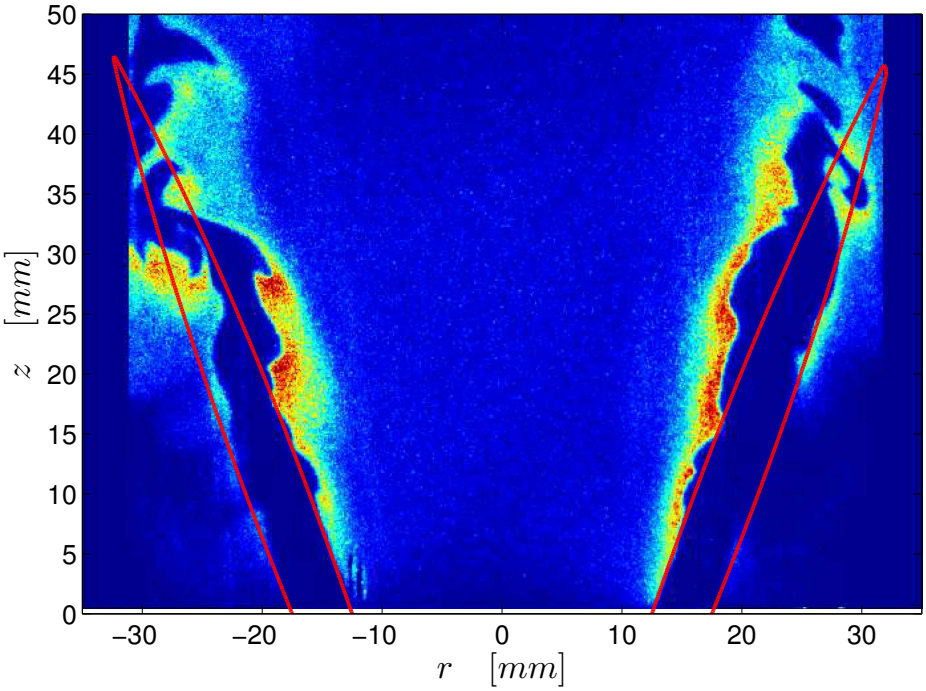

Fig. 7.1 Comparison between the instantaneous OH Planar Laser Induced Fluorescence (PLIF) of an unforced flame with $\overline{\phi} = 0.55$ from Balachandran (2005) and the steady G-equation model (red line). The parameters L and k_0 are tuned to match the experimental results at the flame base.

between the flame and the walls. However, the results obtained by Graham (2012) with this flow field model showed a qualitative good comparison with the experimental results. The velocity potential P for a spherical source in cylindrical coordinates $(\hat{r}, \hat{\theta}, \hat{z})$ is:

$$P = \frac{-\dot{M}}{\sqrt{r^2 + (z+L)^2}}, \tag{7.1}$$

where $\dot{M}$ is the source flow rate, and L is the axial distance between the source and the origin. The mean velocity field is:

$$\overline{\boldsymbol{u}} = \nabla P = (\overline{u}_r, \overline{u}_\theta, \overline{u}_z) = \left(\frac{\dot{M} r}{[r^2 + (z+L)^2]^{3/2}}, 0, \frac{\dot{M}(L+z)}{[r^2 + (z+L)^2]^{3/2}} \right). \tag{7.2}$$

The coefficient $\dot{M}$ is chosen so that the absolute value of the velocity measured at a reference point matches the experiments. The reference velocity ($u_{ref} = 10\,\text{m/s}$) is measured at the centre of the burner slit, located at $r = \frac{(r_{in}+r_{out})}{2}$, $z = z_b = 0$, where $r_{in} = 12.5\,\text{mm}$, $r_{out} = 17.5\,\text{mm}$ are the inner and outer radial distances of the burner slit, and z_b is the burner axial

location (see Figure 7.1). Thus we have:

$$\dot{M} = u_{ref}\left[\left(\frac{r_{in}+r_{out}}{2}\right)^2 + L^2\right]. \tag{7.3}$$

The value of L is adjusted so that the angle that the steady flame forms with the inlet plane matches the one observed experimentally (see Figure 7.1). A good comparison is observed when $L = 40\,\text{mm}$, in agreement with with the analysis of Graham (2012).

7.1.2 Velocity and equivalence ratio perturbations

If the thermoacoustic system is unstable or acoustically forced, acoustic velocity and pressure fluctuations will arise in the combustor. These oscillations will directly influence the flame response, but will also cause modulation of the velocity at the fuel injection location. We model the acoustic velocity perturbations as a pulsation of the spherical source, so that the total velocity can be written as:

$$\boldsymbol{u} \equiv \overline{\boldsymbol{u}}\left(1 + u'_{ac}(t)\right), \tag{7.4}$$

where $u'_{ac}(t)$ is the instantaneous, non-dimensional acoustic velocity. Given the naïve modelling of the flow field for this analysis, no further modelling of the unsteady flow field (e.g., travelling waves) is introduced. This is also because we will consider fluctuations in the equivalence ratio field, which have a stronger influence on the flame dynamics than the direct velocity perturbations (Lieuwen, 2003; Cho & Lieuwen, 2005).

For the combustor geometry we are considering here, the fuel injection location is close to the combustion chamber inlet, $z_{inj} = -55\,\text{mm}$. Thus, fuel and air cannot mix uniformly before reaching the flame. To model the equivalence ratio fluctuations, we adopt the stiff-injector model proposed by Polifke & Lawn (2007). Here, one assumes that acoustic oscillations affect only the air mass flow rate, and not the fuel one. Therefore the instantaneous equivalence ratio at the injection point is given by:

$$\phi(z_{inj},t) \equiv \frac{\dot{m}^{st}_{air}}{\dot{m}^{st}_{fuel}}\frac{\dot{m}_{fuel}}{\dot{m}_{air}} = \frac{\frac{\dot{m}^{st}_{air}}{\dot{m}^{st}_{fuel}}\dot{\overline{m}}_{fuel}}{\dot{\overline{m}}_{air}+\dot{m}'_{air}} = \frac{\frac{\dot{m}^{st}_{air}}{\dot{m}^{st}_{fuel}}\frac{\dot{\overline{m}}_{fuel}}{\dot{\overline{m}}_{air}}}{1+\frac{\dot{m}'_{air}}{\dot{\overline{m}}_{air}}} = \frac{\overline{\phi}}{1+u'_{ac}(t)}, \tag{7.5}$$

where overlines and primes denotes mean and fluctuating quantities, and the superscript st indicates stoichiometric conditions. In the last equality, we have exploited the fact that the distance between the injection point and the flame (the speakers, if the system is forced) is

acoustically compact, so that the acoustic fluctuations generated by the flame (by the speakers) directly influence the equivalence ratio fluctuations at the injector. These fluctuations are then convected in the upstream duct, from the injection point to the flame inlet. We shall assume that, in this region, a uniform flow advects the equivalence ratio fluctuations. Imposing mass flux conservation in the sections upstream of the combustor inlet, one can calculate the time needed for the equivalence ratio perturbations to travel from the injector to the flame inlet (Graham, 2012). The total time is $\tau_c = \tau_1 + \tau_2$, where $\tau_1 = 9 \times 10^{-3}$ s and $\tau_2 = 1.6 \times 10^{-3}$ s are the times needed for the equivalence ratio perturbations to be transported from the injection point to the base of the bluff-body, and from the latter to the combustion chamber inlet, respectively.

For forced simulations, where $u'_{ac}(t) = A\sin(\omega t)$, the convection process can be treated as a time delay, so that the equivalence ratio at the combustion chamber inlet can be explicitly written as:

$$\phi(z_b,t) = \frac{\overline{\phi}}{1 + A\sin(\omega(t-\tau_c))}. \tag{7.6}$$

In self excited cases instead, the history of the acoustic velocity perturbations from time $t - \tau_c$ is stored, so that the nonlinear equivalence ratio perturbations at the burner can be calculated as:

$$\phi(z_b,t) = \frac{\overline{\phi}}{1 + u'_{ac}(t-\tau_c)}. \tag{7.7}$$

7.1.3 Flame dynamics

We assume that the flame is anchored to the bluff-body, and its dynamics is modelled through the kinematic G-equation:

$$\frac{\partial G}{\partial t} + \boldsymbol{u}\cdot G = s_T|\nabla G|, \tag{7.8}$$

where the turbulent flame velocity is given by:

$$s_T = s_T^0(\phi)(1 - \mathcal{L}\kappa). \tag{7.9}$$

Here s_T^0 contains the turbulent flame speed dependence on the local equivalence ratio, and curvature corrections on the flame speed are proportional to the Markstein length $\mathcal{L}$. An analytical model for a laminar flame speed that fits experimental data was provided by Abu-Orf (1996); Cho & Lieuwen (2005), and reads:

$$s_L^0 = k_1 \phi^{k_2} e^{-k_3(\phi - k_4)^2}, \tag{7.10}$$

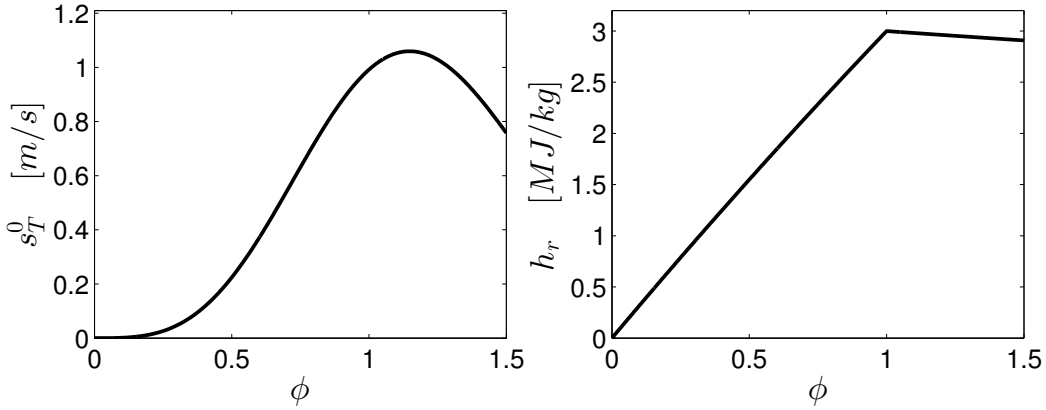

Fig. 7.2 Equivalence ratio dependence of the flame properties. Left: turbulent flame speed s_T^0. Right: enthalpy of reaction h_r.

with $k_1 = 1.322\,\text{m/s}$, $k_2 = 3.110$, $k_3 = 1.723$ and $k_4 = 0.362$. As in Graham (2012), we then model the (higher) turbulent flame speed as $s_T^0 = k_0 s_L^0$ (see Figure 7.2), i.e., we assume that it has the same equivalence ratio dependence as in the laminar case. The scaling factor $k_0 = 1.513$ is obtained by matching the length of the experimental steady flame shape with the numerical one (see Figure 7.1).

Lastly, the total heat release rate in the domain $\mathcal{D}$ is then given by:

$$Q = 2\pi\rho \int_{\mathcal{D}} h_r(\phi) s_T(\phi) |\nabla G| \delta(G) r \,\mathrm{d}r \,\mathrm{d}z. \tag{7.11}$$

This expression accounts for the fact that the flame speed and enthalpy of reaction are functions of the local equivalence ratio, which is not uniformly distributed in space. The enthalpy of reaction, shown in Figure 7.2, is assumed to increase with the intensity of the equivalence ratio and saturate at stoichiometric conditions, $\phi = 1$, according to the expression:

$$h_r = \frac{3.2 \times 10^6 \min(\phi, 1)}{1 + 0.067\phi} \,\text{J/kg}. \tag{7.12}$$

7.2 FDF calculation and comparison with the experiments

In this section, the bluff-body stabilised flame model is forced harmonically over a wide range of amplitudes and frequencies, and an FDF is extracted from the simulations results. We perform the calculations for a flame with no curvature correction on the flame speed (Markstein number $\mathcal{M} \equiv \mathcal{L}/H = 0$, where $H = 80\,\text{mm}$ is a geometrical characteristic length), and for a configuration with $\mathcal{M} = 0.005$. Although the steady flame shape is not affected

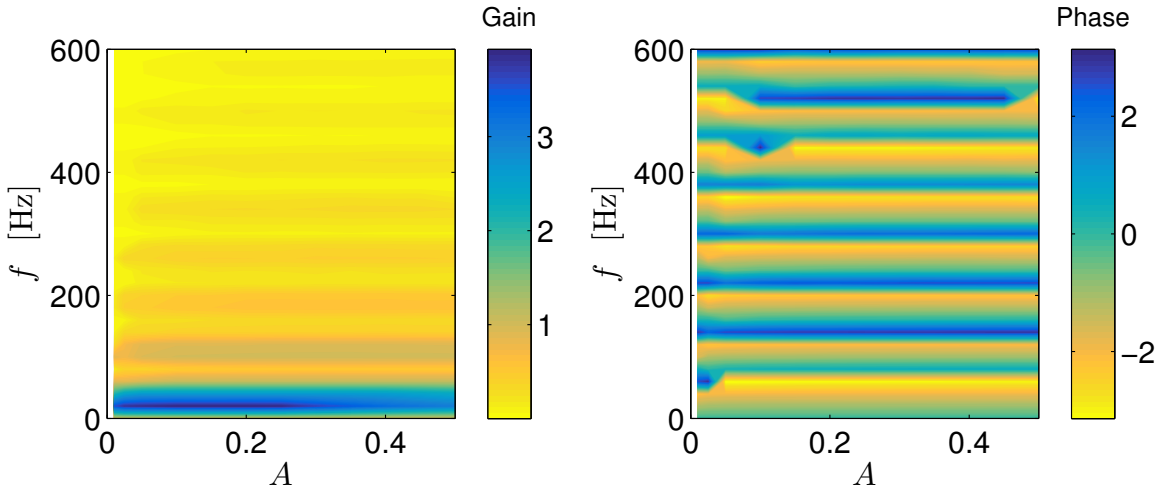

Fig. 7.3 Perfectly premixed FDF. The velocity model here is very simplistic and no relevant saturation effects are observed even at high forcing amplitudes.

much by curvature corrections, the heat release response varies greatly at high frequencies. This is because, as discussed in Chapter 6, curvature corrections on the flame speed enhance the effect of kinematic restoration, whose contribution to the heat release dynamics is large when the flame exhibits a pinch-off.

7.2.1 Perfectly premixed response

In the perfectly premixed case, no equivalence ratio fluctuations are considered, and the flame oscillates only due to acoustically induced velocity perturbations according to equation (7.4), where $u'_{ac} = A\sin(\omega t)$. The effect of the local flame's curvature on the flame speed is neglected here, by setting $\mathcal{M} = 0$. Because of the simplistic velocity field model, the FDF calculated here is not expected to compare well with the experimental results. However, the perfectly premixed FDF is calculated in order to have a reference case against which the imperfectly premixed case can be compared. This will help in understanding the role of equivalence ratio fluctuations and flame speed curvature corrections on the FDF.

The perfectly premixed FDF is shown in Figure 7.3. One can see that the flame acts as a low-pass filter as the gain tends to decrease with the frequency. The large gain at low-frequencies is typical of V- and M-shaped flames (Durox *et al.*, 2009). However, no saturation mechanism is observed as the forcing amplitude is increased. This is because the simplistic velocity field model adopted (a pulsating spherical source) causes the flame to stretch and compress along the radial direction, without causing wrinkles on the flame surface. Therefore, the relevant saturation mechanisms of the G-equation model, such as kinematic

restoration of flame front corrugations and pinch-offs, are not triggered, and the response is quasi-linear even at large amplitudes. Lastly, one can observe that regions with high and low gain (and similarly for the phase) alternate when the frequency is varied. The distance between two peaks or troughs is about 80 Hz. This is due to constructive or destructive interference between acoustic perturbations on the flame front and perturbations caused by the anchoring boundary condition (Preetham *et al.*, 2008). For simple flame configurations, such as conical or V flames in uniform flow fields, the frequency gap between two consecutive gain peak/troughs can be predicted with analytical results in the linear limit. This frequency gap is related to the characteristic time that perturbations need to travel from the flame base to the tip (Preetham *et al.*, 2008; Blumenthal *et al.*, 2013). However, the radial dependence of the flow field makes it harder to find such a scaling analytically for the current model. In the next subsection a method is discussed through which a physical understanding of the frequency gap between peaks in the gain peaks can be obtained.

7.2.2 Sum of time delays approximation

As is common practice, the FDF was measured only for purely harmonic excitations, i.e., for values of the Laplace variable $s \equiv \sigma + \mathrm{i}\omega$ having zero growth rate σ. The FDF is then extended in the entire Laplace space via the analytic continuation technique[1].

In Chapter 3, analytic continuation was achieved by fitting the measured FDF data onto state-space models. This was used to estimate the growth rate of thermoacoustic oscillations far from limit cycle or fixed point solutions, and build stability maps. Although this method is correct, it provides little insight into the heat release dynamics mechanisms, which are hidden in the values of the fitted parameters. An alternative approach that provides more physical understanding of the flame dynamics is provided by approximating the FDF with a sum of time delays (Macquisten *et al.*, 2014; Subramanian *et al.*, 2015).

A transfer function (here a slice of the FDF at a given amplitude level A), can be calculated as the Laplace transform of the impulse response of the system, $h_A(t)$:

$$\mathrm{FDF}(A,s) = \int_{-\infty}^{+\infty} h_A(t) e^{-st}\,\mathrm{d}t \approx \sum_{n=0}^{N-1} h_A(n\Delta\tau) e^{-sn\Delta\tau}\Delta\tau, \tag{7.13}$$

where the integral has been approximated with a Riemann sum, and we have exploited the fact that the system does not respond at times $t < 0$. $\Delta\tau$ needs to be sufficiently small for the approximation to work well, and the largest time considered in the sum, $t_{max} = (N-1)\Delta\tau$,

[1] This assumes that the FDF is an analytic function, i.e., that it is differentiable with respect to the complex variable s at all points of interest.

has to be large enough for the impulse response to have decayed. By defining the coefficients

$$k(n\Delta\tau, A) \equiv h_A(n\Delta\tau)\Delta\tau, \tag{7.14}$$

one can see that the FDF can be approximated as a superposition of time delay responses, each with a different time delay, $\tau = n\Delta\tau$, and a specific coefficient, k:

$$\mathrm{FDF}(A, s) \approx \sum_{n=0}^{N-1} k(n\Delta\tau, A) e^{-sn\Delta\tau}. \tag{7.15}$$

In order to obtain the coefficients k, we can make use of the information collected when measuring the FDF at the purely imaginary values of the Laplace variable $s = \mathrm{i}\omega$. Indeed, the inverse Fourier transform of $\mathrm{FDF}(\mathrm{i}\omega, A)$ yields the impulse response $h_A(t)$, so we have:

$$h_A(n\Delta\tau) = \frac{1}{2\pi} \int_{-\infty}^{\infty} \mathrm{FDF}(\mathrm{i}\omega, A)\, e^{\mathrm{i}\omega n\Delta\tau}\, \mathrm{d}\omega = \frac{1}{\pi} \int_{0}^{\infty} \mathrm{Re}[\mathrm{FDF}(\mathrm{i}\omega, A)\, e^{\mathrm{i}\omega n\Delta\tau}]\, \mathrm{d}\omega. \tag{7.16}$$

In the latter equality we have exploited the fact that, because the impulse response is a real valued object, the FDF satisfies the property $\mathrm{FDF}(-\mathrm{i}\omega, A) = \mathrm{FDF}^*(\mathrm{i}\omega, A)$, where * denotes complex conjugation.

Combining equations (7.15), (7.14) and (7.16), an analytic continuation of the FDF is obtained, which can be exploited when its coupling with a linear acoustic network response is considered.

Because (7.15) is a sum of time delayed responses, the amplitudes of the coefficients k are determined by the influence of a perturbation on the heat release response after a time τ. The intensity of the coefficients $k(\tau, A)$ is shown in Figure 7.4 as a function of the forcing amplitude and the time delay. The values of the coefficients k are approximately independent of the amplitude level, because no saturation mechanism is captured by this model, as discussed earlier. The dependence of k upon the time delay, however, has a clear physical explanation. Acoustic perturbations directly influence the flame dynamics at time $t = 0$, therefore we have $k(0, A) \geq 0$. These perturbation propagate along the flame front from the base to the tip. Because the geometry we are considering is axisymmetric and the flame has an M-shape, the effect of downstream perturbations on the heat release is larger, as more flame surface area is present. This explains why the value of k increases with τ, until a critical time delay is reached. After that, the coefficients at larger times drop to zero. This is because the flame tip has been reached, and after this critical time delay perturbations generated at time $t = 0$ can no longer affect the heat release dynamics.

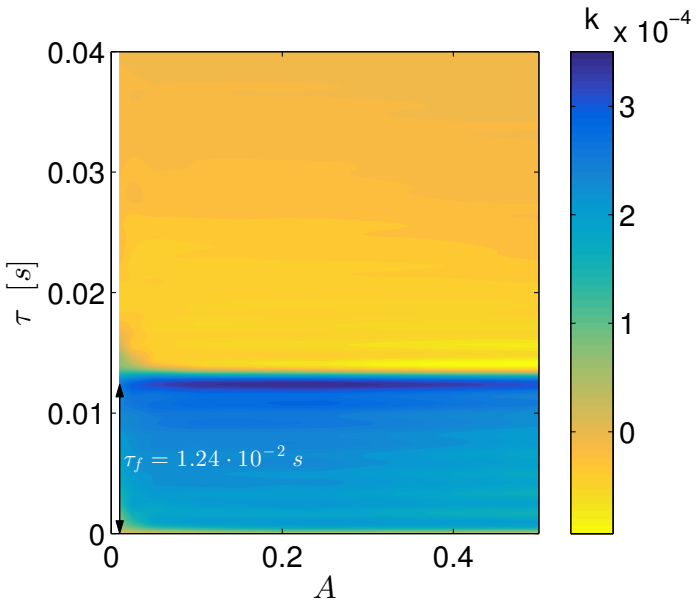

Fig. 7.4 Weights of the sum of time delays approximation for the perfectly premixed flame. The time delay at which the coefficients k have the largest magnitude corresponds to the time τ_f that an acoustically induced perturbation needs to travel from the flame base to the tip.

The time needed for an acoustic perturbation to travel along the flame front can be roughly estimated as the convective time needed for a perturbation to be transported by the mean flow from the centre of the burner slit (at a distance $\rho_1 = 42.72$ mm, where ρ is a the radial distance in spherical coordinates centred in the source) to the steady flame tip (at a distance $\rho_2 \approx 90.14$ mm, from Figure 7.1). This is an approximation because it ignores the flame speed contribution to the total speed at which perturbations are convected along the flame front. However, for the configuration we are considering, the mean flame speed is $s_T^0(\overline{\phi} = 0.55) = 0.29$ m/s, which is much smaller than the smallest value that the radial mean velocity assumes, $\overline{u}(\rho_2) = \dot{M}/\rho_2^2 = 2.25$ m/s, and this approximation should yield a reasonable result. The convective time along the flame is:

$$\tau_f \approx \int_{\rho_1}^{\rho_2} \frac{1}{\overline{u}(\rho)} \mathrm{d}\rho = \int_{\rho_1}^{\rho_2} \frac{\rho^2}{\dot{M}} \mathrm{d}\rho = \frac{1}{3\dot{M}} \left(\rho_2^3 - \rho_1^3\right) = 0.0120 \tag{7.17}$$

which compares well with the time delay at which the largest k coefficient is observed in the sum of time delays approximation ($\tau_f = \tau(k_{max}) = 0.0124$, see Figure 7.5).

Furthermore, perturbations proportional to $\sin(\omega t)$ and to $\sin[(\omega + \Delta\omega)t]$, will generate the same type of constructive/destructive interference if the perturbations at the flame base

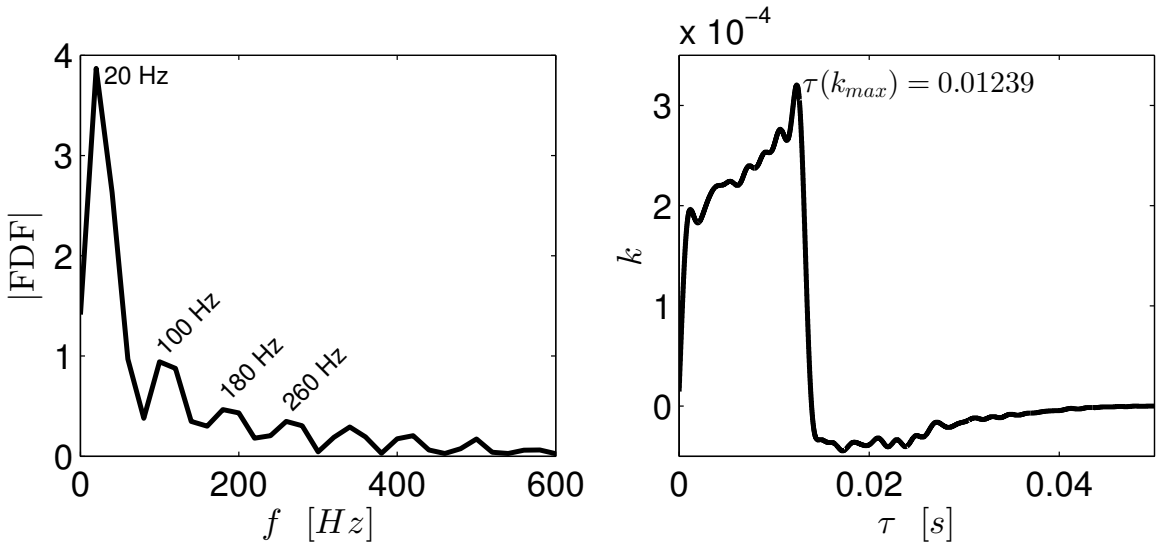

Fig. 7.5 Slice of the FDF gain (left) and of the sum of time delays coefficients (right) at $A = 0.05$. The frequency gap between the FDF peaks is about 80 Hz, which is consistent with the reciprocal of the characteristic time $\tau(k_{max})$ that acoustically induced perturbations take to travel along the flame front.

and tip are the same at every instant t, and in phase. This is achieved when:

$$\Delta\omega\tau_f = 2\pi n \quad \Longrightarrow \quad \Delta f = \frac{n}{\tau_f}, \quad n \in \mathbb{N}^+. \tag{7.18}$$

Therefore we can expect the frequency gap between gain peaks to be $\Delta f = 1/\tau_f = 80.7$ Hz, which compares well with the results from the measured FDF. Note that, when multiple sources of heat release disturbances are included, multiple waves, which in general propagate at different speeds, affect the heat release dynamics. Although the various contributions may be separated linearly (Lieuwen, 2003), nonlinear terms may trigger non-trivial interactions between the waves, and a simple scaling as the one discussed above cannot expected to be found in general (Ćosić *et al.*, 2014).

The discussion in this section shows how an analytic continuation of the FDF based on a sum of time delays yields physical understanding into the heat release dynamics, which a brute force fit onto a state-space model fails to capture. In the following sections, equivalence ratio perturbations and curvature corrections are included, and their effect on the FDF and on the coefficients of the sum of time delays approximation is discussed.

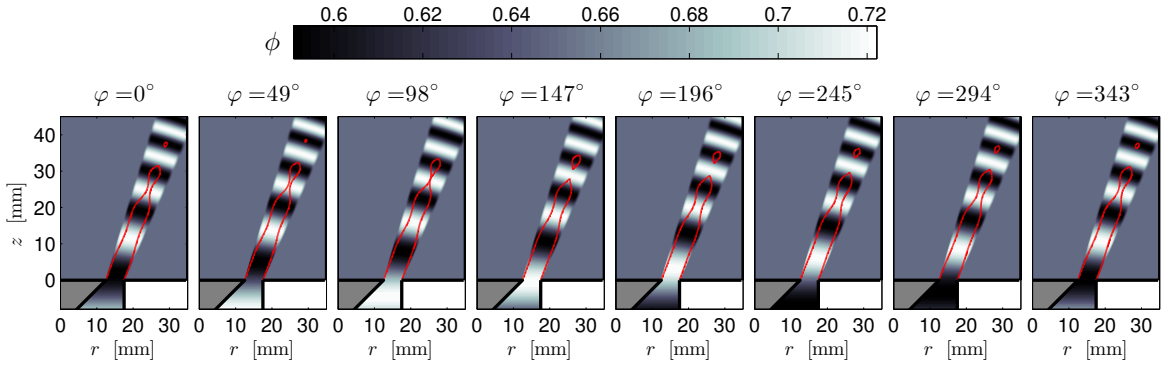

Fig. 7.6 Imperfectly premixed flame shape (red line) on top of the equivalence ratio field over a forced cycle $u'_{ac}(t) = A\sin(\mathrm{St}t)$ with $\overline{\phi} = 0.65$, $A = 0.1$, $\mathrm{St} = 17.093$. Snapshots at eight instants over a cycle are plotted as a function of the angle $\varphi = 360(t - t_0)/T$, where T is the oscillation period. Where the equivalence ratio is higher, the flame burns faster and eventually forms a pinch-off.

7.2.3 Imperfectly premixed response

We now consider the case in which fuel is injected close to the combustion chamber, so that air and fuel have no time to mix perfectly together. The equivalence ratio field is transported in the flame domain as a passive scalar, and obeys the advection equation:

$$\frac{\partial \phi}{\partial t} + \boldsymbol{u} \cdot \nabla \phi = 0, \tag{7.19}$$

where $\boldsymbol{u}$ is the pulsating flow field (7.4), and the equivalence ratio at the burner inlet is given by the stiff-injector model (7.6). Curvature corrections to the flame speed are neglected for now, and the system is forced harmonically at various amplitudes and frequencies.

The FDF extracted from the imperfectly premixed heat release rate response is shown in Figure 7.7. Equivalence ratio fluctuations strongly vary the flame dynamics: where the equivalence ratio fluctuations are higher, the flame burns faster and tends to close, as shown in Figure 7.6. When the amplitude of the perturbations is high enough, this causes the flame to pinch off. The formation of pinch-offs has a strong influence on the heat release time series analysis, as discussed in Chapter 6. However, because here pinch-offs are always found in regions in which the equivalence ratio has low values, and therefore the flame speed is smaller, the influence of pinch-offs on the total heat release here is less relevant than in the previous chapter. The saturation mechanism induced by the equivalence ratio fluctuations are seen in Figure 7.7 as a reduction in the FDF's gain with respect to the forcing amplitude.

A pattern can be observed in the location of the FDF's gain minima (and maxima) as the amplitude increases. The gap between the gain's minima can be predicted with an

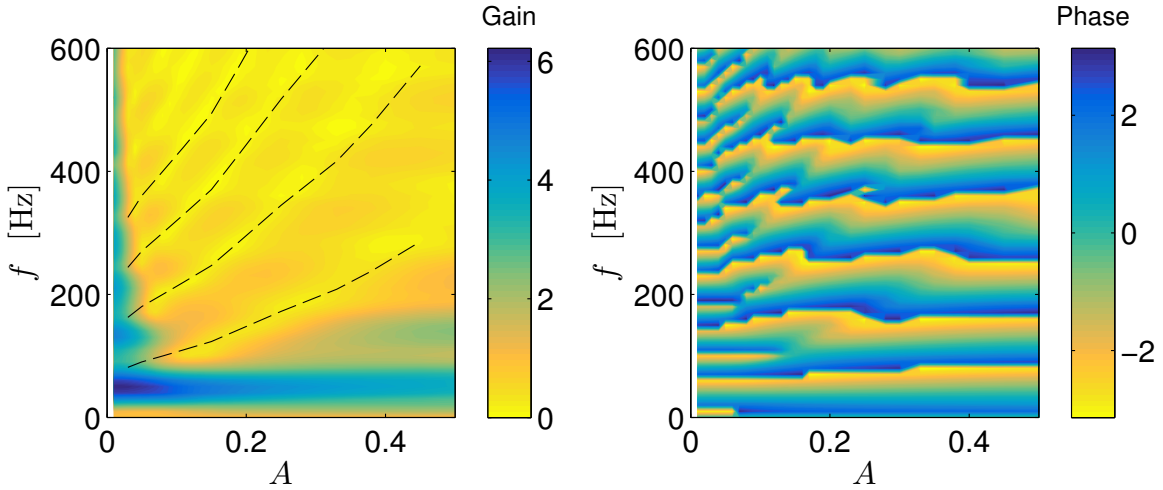

Fig. 7.7 Imperfectly premixed FDF with $\mathcal{M} = 0$. Equivalence ratio fluctuations cause the flame to pinch off at large amplitudes, and the gain to saturate with the amplitude. However, at low amplitudes the gain remains very high at all frequencies. The location of the FDF gain minima calculated using the sum of time delay approximation is shown with dashed lines.

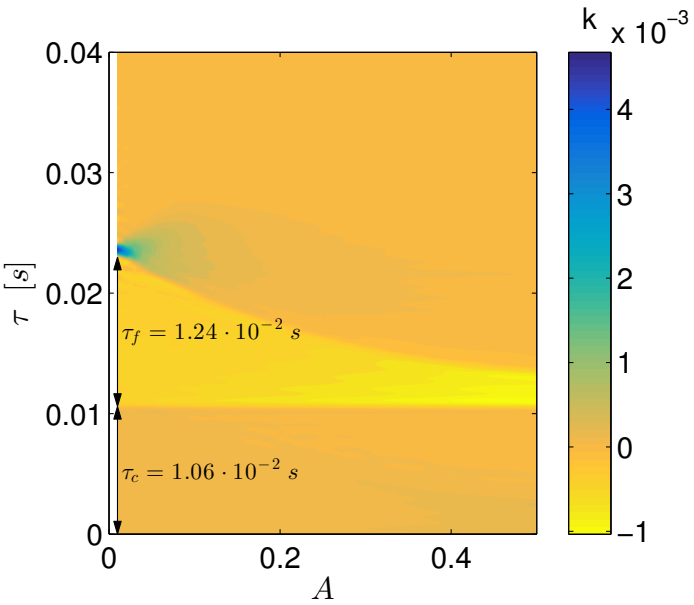

Fig. 7.8 Weights of the sum of time delays approximation for the imperfectly premixed flame with no curvature corrections. Equivalence ratio perturbations generated at the injection location need to travel for a time $\tau_c = 1.06 \cdot 10^{-2}$ before influencing the flame dynamics.

argument similar to that discussed in the previous section. The map of the sum of time delays coefficients for the imperfectly premixed flame is shown in Figure 7.8. Its structure is very different from the perfectly premixed one. Two characteristic time scales can be distinguished: τ_c, the time that equivalence ratio perturbations need to be convected from the injection location to the flame base, which does not vary with the forcing amplitude level, and τ_f, the time the perturbations need to travel along the flame surface to to tip, which varies with the amplitude level. At times $0 < \tau < \tau_c$, only acoustic perturbations influence the flame dynamics, as in the perfectly premixed scenario. However, at time τ_c equivalence ratio perturbations reach the flame and start contributing to the heat release response, until time $\tau_c + \tau_f$, when they reach the flame tip. Their contribution to the flame dynamics is stronger than the acoustic perturbations (the magnitude of the coefficients is larger), because they significantly alter the flame speed, and hence the flame shape and rate of heat release. Also note, in Figure 7.8, that the sign of the coefficients k suddenly changes across τ_c. This is because the effect of equivalence ratio perturbations at first order is given by:

$$\phi(z_b,t) = \frac{\overline{\phi}}{1+u'_{ac}(t-\tau_c)} \approx -\overline{\phi}\,u'_{ac}(t-\tau_c), \tag{7.20}$$

i.e., equivalence ratio perturbations are linearly proportional to (delayed) velocity fluctuations perturbations, but have opposite sign.

Lastly, we also observe that the time τ_f that perturbations need to travel along the flame decays with the amplitude. This is because equivalence ratio fluctuations cause the flame to pinch off (see Figure 7.6). The larger is the perturbation amplitude, the lower is the axial location at which the flame pinches off, thus reducing the effective mean length of the flame over a cycle. In the small amplitude limit, we recover the value of τ_f calculated in the previous section, because the flame does not pinch off in this limit, and the mean flame length corresponds to the steady flame length. From equation (7.17), the mean flame length can be estimated as:

$$L_f(A) \approx \rho_2(A) - \rho_1 = \sqrt[3]{3\dot{M}\tau_f(A) - \rho_1^3} - \rho_1 \tag{7.21}$$

This provides a physically relevant length scale for the flame dynamics (as a function of the forcing amplitude), which could be used in a non-dimensional scheme to scale the data. We can also make use of the characteristic time responses of this flame to predict the frequency gaps between two peaks/troughs in the FDF gain. Because equivalence ratio fluctuations largely dominate the dynamics, it is reasonable to assume that the most important time scale is $\tau_f(A)$. With the same argument provided in the previous section, we can predict that the frequency gap between gain's minima or maxima is given by $\Delta f(A) = \frac{1}{\tau_f(A)}$. The dashed

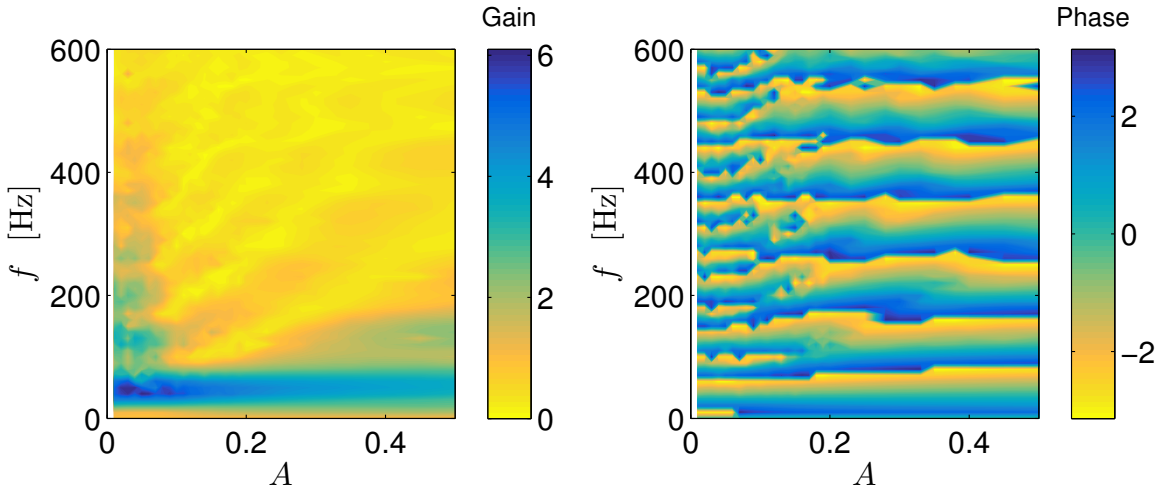

Fig. 7.9 Imperfectly premixed FDF with $\mathcal{M} = 0.005$. The gain at low forcing amplitudes and large frequencies is greatly reduced because of kinematic restoration effects.

lines in Figure 7.7 have been plotted using this equation, and match well the FDF regions in which the gain reaches minimum values.

Curvature effects

One of the weaknesses of the model presented so far is that the flame response at low amplitudes has a large gain at all frequencies. Indeed, from Figure 7.7 one can see that the gain in the $A \to 0$ limit is almost always larger than one.

This is not consistent with the experimental results, in which a gain larger than one is measured at low-frequencies, but quickly drops at values less than unity as the frequency is increased. In order to account for frequency dissipation effects, we include curvature corrections to the flame speed. These corrections are known to damp high-frequency oscillations in flames modelled with the G-equation, because they enhance the effect of kinematic restoration, which quickly smooths highly wrinkled flame sheets, thus reducing the flame surface area (Lieuwen, 2003). It was also shown by Shin & Lieuwen (2013) that their effect is analogous to that of turbulent flow effects (modelled with white noise) on the flame dynamics.

The FDF of the imperfectly premixed flame with curvature corrections on the flame speed is shown in Figure 7.9. The structure of the FDF with respect to the case with no curvature corrections (Figure 7.7) is mostly unchanged, but the gain at high frequencies in the low-amplitude limit has greatly decreased. Also the structure of the sum of time delays' coefficients, shown in Figure 7.10, is mostly unchanged, and the physics underlying the response at the various time delays is the same as in the case with no curvature. The

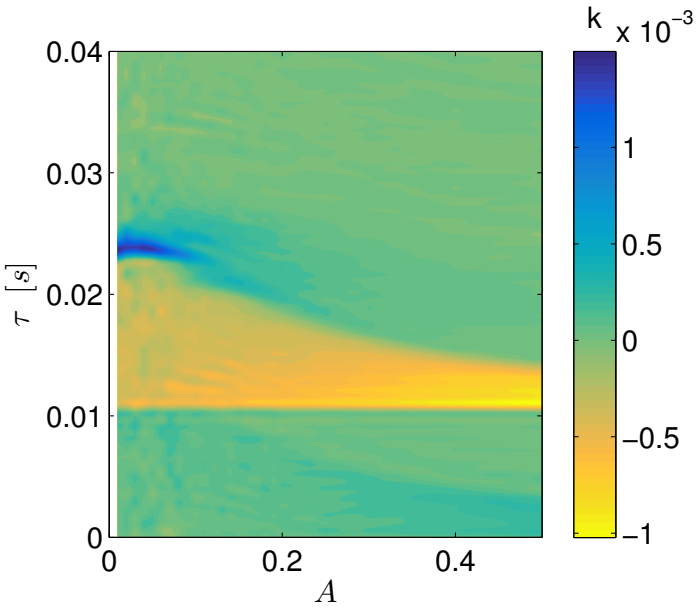

Fig. 7.10 Weights of the sum of time delays approximation for the imperfectly premixed flame with curvature corrections. The structure of the coefficients is very similar to the case with no curvature corrections on the flame speed (see Figure 7.8), but the intensity of the coefficients is decreased, because the FDF gain is now lower.

reduction in gain can be seen here as a reduction of the intensity of the coefficients k at small amplitudes.

This FDF contains all the physical features we are aiming to model here, and will be the one used in the next section for the modelling of thermoacoustic oscillations. A comparison between the FDF evaluated with the current model, the model of Graham (2012), and the experimental results of Balachandran (2005) is shown in Figure 7.11. A qualitatively good agreement between the model and the experiments is observed at all frequencies and amplitudes. Our model improves the results of Graham (2012) in that it is able to capture better the increase in gain at low-frequencies. The differences between our results and those of Graham (2012) can be justified by recalling that we are solving the G-equation in its fully implicit form, whereas Graham (2012) tracked independently the two sides of the flame front and merged them. This causes curvature effects to be stronger in our model (particularly at the flame tip), and therefore the flame and heat release dynamics to vary.

7.3 Harmonic balance analysis

Having obtained a reasonable model for the heat release rate response of the imperfectly premixed flame, we need to develop an acoustic model of the combustor geometry for

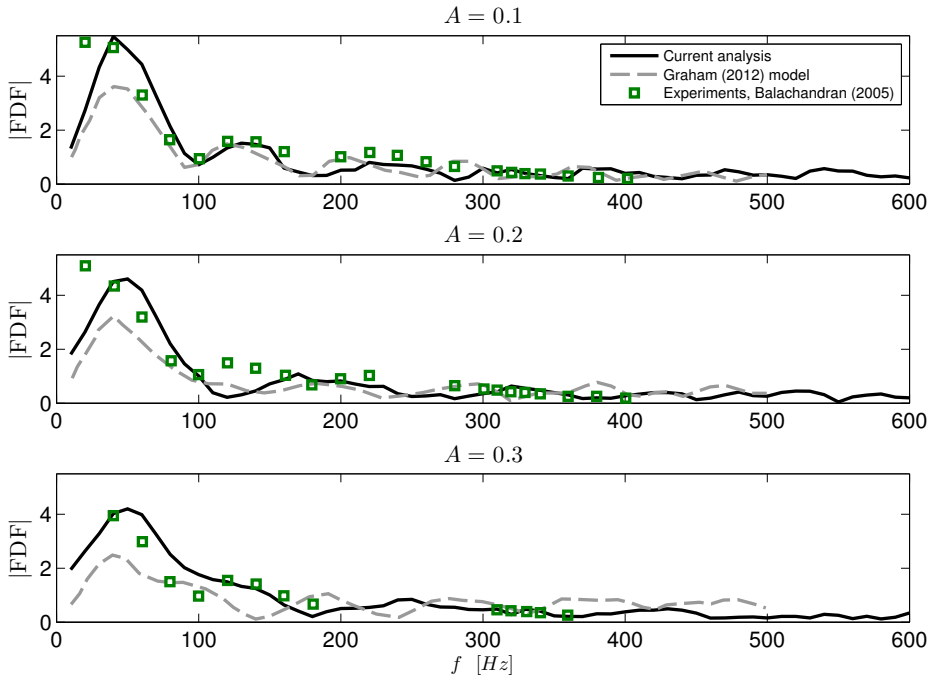

Fig. 7.11 Comparison between the FDF gains extracted from the current analysis (solid line), Graham (2012) model (dashed line), and experimental results Balachandran (2005) at three forcing amplitudes. The model captures the increase in gain at low-frequencies and shown a qualitative good agreement for all frequencies and amplitudes. The phase behaviour is reported and commented in Semlitsch *et al.* (2016).

investigating thermoacoustic oscillations. A detailed sketch of the acoustic network under consideration is shown in Figure 7.12. The geometry is axisymmetric, but we consider only acoustic waves propagating in the axial direction z. The inlet mean flow is chosen so that the velocity at the burner slit corresponds to the experimental reference velocity, $u_{ref} = 10\,\text{m/s}$. A temperature jump $T_2/T_1 = 4$ is imposed at the inlet of the combustion chamber. The outlet is modelled as acoustically open, whereas the reflection coefficient of the inlet is chosen to be $R_1 = 0.8$.

In the experiments performed by Balachandran (2005), the setup in which the FDF was measured had an enclosure duct of length $L_{duct} = 80\,\text{mm}$. This length was chosen to minimise the acoustic interference between the acoustically forced waves used to calculate the FDF, and the natural acoustic response of the combustor. In this non-resonant configuration, the combustor did not show self-sustained thermoacoustic oscillations. However, by increasing the length of the enclosure duct to $L_{duct} = 350\,\text{mm}$, the resonance of the combustor was exploited to investigate self-excited oscillations. The latter is the scenario we will start considering here.

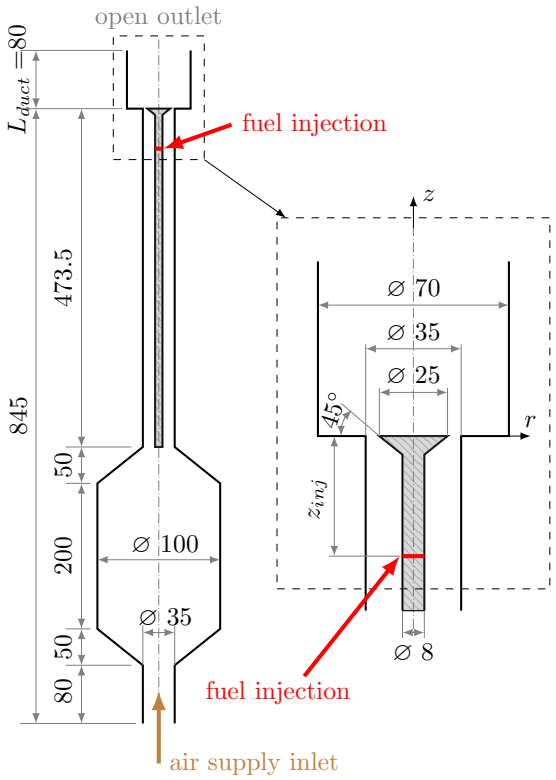

Fig. 7.12 Schematic of the acoustic network modelled with LOTAN. Dimensions are in mm. The burner and and plenum dimensions are based on the experimental setup of Balachandran (2005). The fuel injection location for the imperfectly premixed case is highlighted. The length of the enclosure duct, L_{duct}, is varied. Image credit to Dr. B. Semlitsch.

The acoustic geometry of Figure 7.12 is implemented in LOTAN, and the transfer function H – the response of velocity fluctuations just upstream of the flame with respect to heat release excitations – is calculated and fitted onto a state-space model:

$$u'_{ac} = H(s)\,q' = \boldsymbol{C}(sI - A)^{-1}\boldsymbol{B}\,q'. \tag{7.22}$$

The harmonic balance is then used to couple the FDF (expressed in terms of the sum of time delays) and acoustic response. The harmonic balance dispersion relation $\mathrm{FDF}(A,s)H(s) = 1$ is solved. Poles with a non-negative growth rate are shown in Figure 7.13. Five thermoacoustic modes are found to be linearly unstable: a low-frequency mode, with a frequency of 65 Hz, 3 modes with frequencies between 290 and 360 Hz, and a mode at 480 Hz. This is roughly consistent with the acoustic characterisation of the experimental setup carried out by Balachandran (2005), in which acoustic peaks in the velocity response (in cold flow conditions) were measured at about 30, 290 and 390 Hz.

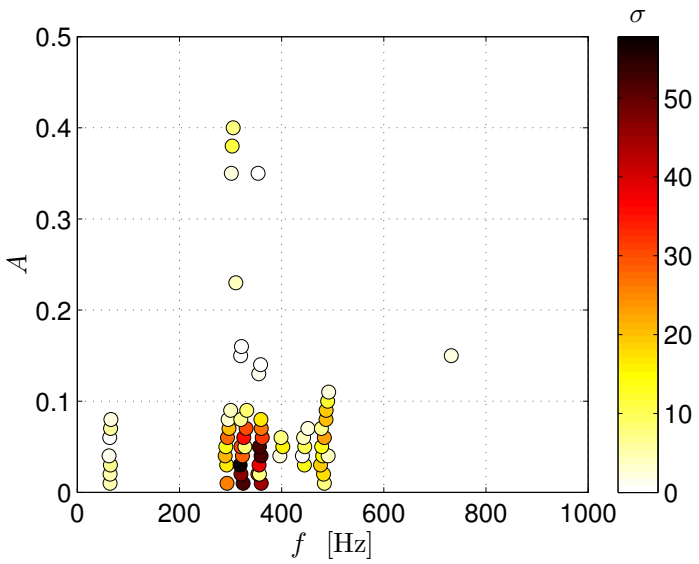

Fig. 7.13 Stability map of thermoacoustic oscillations in the configuration in which $L_{duct} = 350\,\text{mm}$. Only solutions of the harmonic balance dispersion relation with non-negative growth rates σ (grey scale) are shown. The mode with the linearly largest growth rate has a frequency of 323 Hz.

Because multiple modes are found to be linearly unstable, in the fully nonlinear regime it is possible that one mode dominates over the others – resulting in periodic oscillations with a frequency close to one of the modes detected here – or that multiple modes contribute to the oscillations – resulting in non-periodic oscillations (Moeck & Paschereit, 2012; Orchini & Juniper, 2016*a*). In the experiments, it was found that the spectrum of self-excited oscillations in this configuration contained only a dominant peak, with frequency 348 Hz. To interpret the FDF analysis results, we may argue that the nonlinear interaction between the modes suppresses the oscillations at all frequencies but one. If this frequency is chosen to be the one with the largest growth rate in the linear regime, we should expect oscillations at 325 Hz. This is, however, just a speculation, as the transient data from the experiments are not available in the literature. Also, we do not have information about the nonlinear coupling between the modes, such as an FDIDF, as discussed in Chapter 4.

To test the accuracy of the model, we verify that, by decreasing the length of the enclosure duct, the system becomes more stable. The growth rate maps for different values of the enclosure duct length are shown in Figure 7.14. At $L_{duct} = 300\,\text{mm}$ no significant differences are observed with respect to the $L_{duct} = 350\,\text{mm}$ case. At $L_{duct} = 250\,\text{mm}$ the modes at 60 and 480 Hz stabilise, but new unstable modes are observed at frequency 580 and 780 Hz. Because these modes have high frequencies, it is possible that the acoustic model under consideration does not damp high-frequency oscillations enough. Nonetheless, the mode at

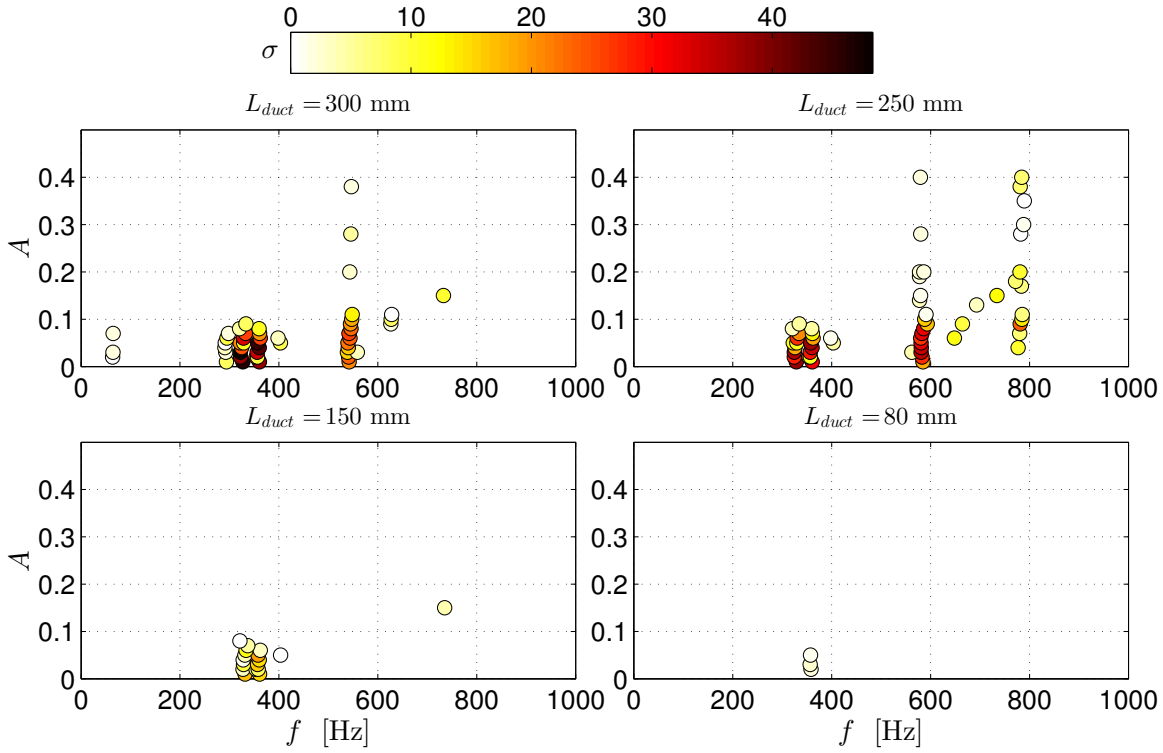

Fig. 7.14 Stability map of thermoacoustic oscillations for various values of the enclosure duct length L_{duct}. Consistently with the experiments, the system becomes more stable when L_{duct} is decreased.

325 Hz still has the largest growth rate. At $L_{duct} = 150$ mm most of the modes have stabilised. The mode at 325 Hz remains the most unstable mode, but its growth rate has largely decreased. Lastly, all the thermoacoustic modes are stabilised when $L_{duct} = 80$ mm (the growth rate of the only unstable mode is only marginally positive). Thus, the thermoacoustic characteristics of the modelled network are consistent with the experimental results.

An interesting result of this analysis is that it predicts a low-frequency mode to be thermoacoustically unstable when the length of the enclosure duct is long enough. This low-frequency thermoacoustic mode originates from the fact that the configuration under investigation has a low-frequency acoustic resonant mode, $f \approx 50$ Hz. This was reported in the experimental characterisation of the rig conducted by Balachandran (2005), and is captured by our acoustic network model. The amplitude of the pressure modeshape at this frequency as calculated by LOTAN is shown in Figure 7.15. Furthermore, the imperfectly premixed FDF gain at low-frequencies is high (see Figs. 7.9 and 7.11). This makes it likely that the thermoacoustic modes close to this frequency will satisfy the harmonic balance criterion and be unstable.

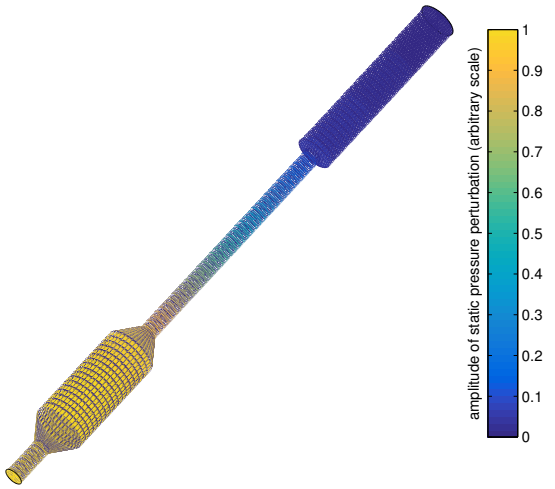

Fig. 7.15 Amplitude of pressure modeshape for the acoustic eigenmode at frequency 49 Hz and growth rate $\sigma = -28.83\,\mathrm{s}^{-1}$. Configuration with $L_{duct} = 80\,\mathrm{mm}$. The mode has a maximum at the inlet (approximately a closed boundary), and a zero at the outlet (open boundary).

Because this mode has such a low-frequency, its wavelength is therefore high, with an order of magnitude of 5 m. For this reason, it is likely that such waves also interact with the environment surrounding the combustor in the real configuration. The reflection of acoustic waves on the walls surrounding the combustor may play a crucial role in determining the stability of this mode. This could be modelled with complex-valued reflection coefficients, whose imaginary part (which supposedly quickly decays with the frequency) represents the time needed for waves to be reflected from the room's walls and travel back to the combustor inlet/outlet.

We also note that, in the analogous low-order modelling of this thermoacoustic network performed by Graham (2012), no unstable thermoacoustic modes were found at low-frequencies. This was surprising to us because, by coupling the FDF contained in Graham (2012) in our acoustic network, modes with a positive growth rate and a frequency of about 50 Hz were still observed. A good agreement was instead observed between modes with $f \approx 340\,\mathrm{Hz}$. We realised that, in the work of Graham (2012), the diameter of the combustion chamber (70 mm), was mistakenly doubled (a radius of 70 mm was used, see for example Figure 6.6 in Graham (2012)). This appears to be the only difference in the acoustic modelling between the two analysis. This shows how the system stability, particularly at low frequencies where the FDF gain is very high, is very sensitive to the acoustic network geometry and, probably, reflection coefficients.

7.4 Conclusions

In this chapter, a potential flow field generated by a pulsating spherical source was considered in order to develop a low-order model for a bluff-body stabilised flame combustor. Equivalence ratio fluctuations have been included in the flame model, by assuming that acoustic velocity fluctuations modulate the inlet air mass flow rate, whereas the fuel mass flow rate remains constant. Including curvature effects on the flame speed, a kinematic model based on the *G*-equations was shown to reproduce reasonably well the flame heat release response measured in experiments. The agreement is due to the fact that equivalence ratio perturbations, which are convected by the flow along the flame, dominate the heat release response. Thus, a detailed modelling of the coupling between the flame and the acoustic field is not required.

It was shown how the measured FDF can be approximated as a sum of time delays. The latter provides an alternative point of view on the flame response, which can be useful to understand what mechanisms dominate the heat release response. In particular, it was shown how the coefficients of the sum of time delays approximation can be used to separate acoustic and equivalence ratio fluctuations effects, confirming that the latter have a stronger impact on the flame dynamics. Also, they provide estimates for the relevant time and length scales of the system. This information gives a better understanding on the FDF results, and could be used to develop strategies to change the system in order to make it less susceptible to thermoacoustic oscillations.

Lastly, by coupling the calculated FDF with an accurate linear acoustic model, multiple thermoacoustic modes are found to have a positive growth rate. Consistently with the experiments, we verified that the system becomes more stable when the length of the enclosure duct is reduced, and that the mode with the largest growth rate has a frequency of about 350 Hz.

This model provides a tool that can be used to quickly estimate the frequencies at which a thermoacoustic system may be prone to instabilities. It improves the work of Graham (2012) because it relies an a fully implicit *G*-equation formulation, which avoids problems in tracking pinch-offs or including curvature effects on the flame speed. It has been used in the context of Rolls-Royce AMEL project to investigate the susceptibility of the thermoacoustic system with respect to geometrical (e.g., fuel injection location) and operating condition (e.g., mean equivalence ratio value) parameters. These results have been partly published in Semlitsch *et al.* (2016).

Chapter 8

Conclusions and future work

In this thesis, methods for the analysis of thermoacoustic systems have been developed.

In Chapter 2, linear stability and adjoint methods on a thermoacoustic system with a premixed flame have been demonstrated for the first time. In particular, adjoint methods were shown to be a quick and reliable tool to understand what physical mechanisms drive the instabilities, and what parameters in the system can be changed to make it less susceptible to thermoacoustic oscillations. The analysis, however, was applied to a simplistic system. Even if a more complex network were to be considered, approximations would be introduced in the thermoacoustic model in order to make it analytically treatable. The effect of such approximations on the eigenvalues' sensitivity is non-trivial, and needs to be assessed. A series of experiments was recently performed in Cambridge by Dr. George Rigas and Nicholas Jamieson to compare the actual shifts of a thermoacoustic system's eigenvalues (a Rijke tube) with those obtained with adjoint methods on a low-order model. They showed that a good comparison is generally observed for the growth/decay rate shifts, but the frequency shift was not predicted so well. The sensitivity information gathered with the experiments can be used to improve the accuracy of the model, which can then be reused in different thermoacoustic configurations to assess their stability/eigenvalues sensitivity. Future analysis can extend the adjoint analysis to systems with premixed flames using more elaborate models for the flame and heat release dynamics and to the more sophisticated question of optimizing the shape of a burner or combustion chamber. Note that, however, when addressing this question for a real application, one has to consider many factors that the manufacturer faces in the design process, such as the system efficiency, structural stability, and boundary conditions due to the connection between the combustion chamber and the compressor/turbine stages. It is a big challenge to accurately formulate an optimization problem that accounts for all these constraints. This research subject is currently being considered by José Aguilar.

In Chapter 3, nonlinear methods were introduced to investigate the amplitude and nature of saturated thermoacoustic oscillations. Time marching, Flame Describing Function (FDF) and numerical continuation methods have been used. This analysis improved previous nonlinear analysis on similar networks in that it considered more realistic acoustic configurations. The results obtained with the various methods have been compared, highlighting their strengths and weaknesses. This information was crucial for understanding what novel methods had to be developed to improve nonlinear modelling of thermoacoustic systems.

In Chapter 4, the FDF method, which can predict only harmonic oscillations, was extended to consider cases in which two frequencies simultaneously excite the flame. A similar analysis was performed by Prof. Jonas Moeck in Berlin, but only static (frequency independent) nonlinearities were considered there, which makes the analysis simpler. Real flames have a dynamic (frequency dependent) nonlinear response, and the theory developed here for this case is one of the main novelties of this thesis. The approximation of the nonlinearity calculated, called the Flame Double Input Describing Function (FDIDF), can be embedded in an acoustic network in a similar manner to an FDF. The dispersion relations that determine the thermoacoustic system behaviour were derived, together with conditions to assess the stability of saturated states. These saturated states can be either fixed points, limit cycles or quasiperiodic oscillations. It was shown how, for limit cycles, the FDIDF corrects the predictions on the system stability obtained with the FDF in some cases, because it accounts for the nonlinear interaction between the modes, which is neglected by the FDF. Although more expensive to obtain from experiments or numerical simulations, the FDIDF contains more accurate information about the flame nonlinear response. A natural follow-up for this analysis would be to measure an FDIDF from experiments, and verify its accuracy. To overcome the cost issue, a low-cost procedure to only assess the stability of limit cycle solutions using the FDIDF was proposed in this thesis. It could be exploited in experiments at a cost roughly equal to that of two FDFs. This information can be used to predict more accurately the stability of limit cycle solutions, the frequency of modes that are linearly unstable around limit cycles, and can explain phenomena like mode switching. The latter can be important information when designing feedback loop controllers/tuning Helmholtz resonators to stabilise thermoacoustic oscillations, which need to be tuned at specific frequencies.

In Chapter 5, a rigorous weakly nonlinear expansion of the equations governing thermoacoustic oscillations in a Rijke tube around a Hopf point was performed. This extended previous weakly nonlinear analysis formulations of thermoacoustic oscillations, as it considered wave-based acoustics, which can be easily scaled to larger systems, and was not limited to a single Galerkin-mode approximation. The latter was the state-of-the-art for

weakly nonlinear expansions of thermoacoustic systems, and it was shown here how a single mode approximation can lead to inaccurate results. The formulation was general in that the acoustic response was embedded in a state-space model, thus not relying on a particular configuration. The nonlinear element considered here was an electrical heater, for which a Wiener-Hammerstein model based on King's law and Lighthill's theory was considered. As a side result, it was discussed how the nonlinear, unsteady King's law model, typically adopted in thermoacoustics to describe the nonlinear dynamics of the heat released by a hot-wire, appears to be non-physical and does not agree with fully nonlinear CFD calculations performed in TU Munich. This calls for research in this area, as a reliable nonlinear dynamical model for the unsteady heat released by a wire is needed if quantitative comparisons with experiments are sought. Although the weakly nonlinear analysis is strictly valid only close to the bifurcation point, it was shown how performing a high-order expansion of the governing equations, one can obtain accurate results on the amplitude, stability and frequency of limit cycle solutions around the Hopf points. This framework could be extended in multiple ways in future analyses. For example, one can consider a realistic model for a premixed flame as a nonlinear element rather than a model for a heater, or can use the weakly nonlinear framework to investigate the nonlinear interaction between multiple unstable modes. Deriving the weakly nonlinear equations can be tedious at high-orders or for complex nonlinearities, but the process can be easily automatised with symbolic solvers. The main advantage of the method is its numerical cost: only matrix multiplications and inversions need to be performed to calculate the amplitude and stability of thermoacoustic oscillations, making it much cheaper than any nonlinear numerical method currently available in thermoacoustics.

Finally, in Chapters 6 and 7 nonlinear low-order models based on the *G*-equation for turbulent bluff-body stabilised flames were developed. The goal was to obtain a cheap but qualitatively accurate estimate of the nonlinear response of non-conical flame shapes, which can be used in industry as a tool to quickly assess the stability of a thermoacoustic network. The idea underlying the first model was to describe the flame-flow interaction mechanism, and the consequent formation of vortices on the flame structure and their roll-up. Although the dynamic response of the flame front was shown to compare well against experimental results, the heat release response overestimated the actual response of the system. This model can be improved by taking into account more physical mechanisms in the heat release dynamics, such as turbulent flame speeds and the role of shear layers in the combustion process. However, this would make the model more expensive, in contrast with the original low-order modelling requirement. The second model was based on the interaction between the flame and equivalence ratio fluctuations in imperfectly premixed flames. Equivalence ratio fluctuations largely dominate the heat release dynamics, and an accurate description of

the flame-flow interaction was not needed here. Results showed that the low-order modelled heat release response compares well with that measured from experiments. An FDF was evaluated and approximated with a sum of time delays. The latter yields an alternative point of view to the heat release response. It can be used to separate the roles of acoustic and equivalence ratio fluctuations, and to estimate the relevant time and length scales of the system. The FDF was embedded in an acoustic network and was able to predict the frequency at which thermoacoustic oscillations grow in experiments. This model was used in the context of Rolls-Royce's AMEL project to investigate the sensitivity of a thermoacoustic system's stability to parameters like the mean equivalence ratio and fuel injection location.

Appendix A

Non-dimensional variables

The complete set of non-dimensional variables and parameters we define is:

$$
\begin{array}{lll}
x = \dfrac{\tilde{x}}{L_f} & \beta = \dfrac{L_f}{R} & r = \dfrac{\tilde{r}}{R} = \beta \dfrac{\tilde{r}}{L_f} \\
\overline{F} = \dfrac{\tilde{\overline{F}}}{L_f} & f = \dfrac{\tilde{f}}{L_f} & \nabla = L_f \tilde{\nabla} = \left(\dfrac{\partial}{\partial x}, \beta \dfrac{\partial}{\partial r} \right) \\
t = \tilde{t} \dfrac{\overline{U}}{L_f} & \mathrm{St} = \dfrac{\omega L_f}{\overline{U}} & K = \dfrac{\overline{U}}{\overline{U}_c} = \dfrac{k L_f}{\mathrm{St}} \\
u_x = \dfrac{\tilde{u}_x}{\overline{U}} & u_r = \dfrac{\tilde{u}_r}{\overline{U}} & \dfrac{\tilde{s}_L^0}{\overline{U}} = \dfrac{1}{\sqrt{1+\beta^2}} \\
\kappa = \tilde{\kappa} L_f & \mathcal{M} = \dfrac{\mathcal{L}}{L_f} & \sin\alpha(r) = \left[1 + \beta^2 \left(\dfrac{d\overline{F}}{dr} \right)^2 \right]^{-1/2}.
\end{array}
\tag{A.1}
$$

Appendix B

Eigenvalue problem

The eigenvalue problem we want to solve reads:

$$-\frac{\beta^2}{\sqrt{1+\beta^2}}\left(h_1(r)\frac{\mathrm{d}\hat{f}}{\mathrm{d}r}+h_2(r)\frac{\mathrm{d}^2\hat{f}}{\mathrm{d}r^2}\right)+\left(\hat{u}'_x+\frac{r}{2}\frac{\mathrm{d}\overline{F}}{\mathrm{d}r}\frac{\mathrm{d}\hat{u}'_x}{\mathrm{d}x}\right)_{x=\overline{F}}=\lambda\hat{f} \tag{B.1a}$$

$$A\hat{\boldsymbol{s}}+\boldsymbol{B}\frac{\beta^2}{2\sqrt{1+\beta^2}}\int_0^1\left(h_1(r)\frac{\mathrm{d}\hat{f}}{\mathrm{d}r}+h_2(r)\frac{\mathrm{d}^2\hat{f}}{\mathrm{d}r^2}r\right)\mathrm{d}r=\lambda\hat{\boldsymbol{s}} \tag{B.1b}$$

$$-\frac{1}{K}\frac{\mathrm{d}\hat{u}'_x}{dx}=\lambda\hat{u}'_x, \tag{B.1c}$$

where h_1 and h_2 are functions of the mean flame shape only, obtained by inspection from the relation:

$$h_1(r)\frac{\mathrm{d}\hat{f}}{\mathrm{d}r}+h_2(r)\frac{\mathrm{d}^2\hat{f}}{\mathrm{d}r^2}=\left(\sin\alpha\frac{\mathrm{d}\overline{F}}{\mathrm{d}r}+2\mathcal{M}\beta^2\sin^4\alpha\frac{\mathrm{d}\overline{F}}{\mathrm{d}r}\frac{\mathrm{d}^2\overline{F}}{\mathrm{d}r^2}-\mathcal{M}\frac{1}{r}\right)\frac{\mathrm{d}\hat{f}}{\mathrm{d}r}-\mathcal{M}\sin^2\alpha\frac{\mathrm{d}^2\hat{f}}{\mathrm{d}r^2}.$$

We discretize the radial and axial components into:

$$\begin{aligned} r\to\boldsymbol{r}&=\left[r_0=1,r_1,\ldots,r_j,\ldots,r_{N_r+1}=0\right]\\ \hat{f}(r)\to\hat{f}(\boldsymbol{r})=\hat{\boldsymbol{f}}&=\left[\hat{f}^0,\hat{f}^1,\ldots,\hat{f}^j,\ldots,\hat{f}^{N_r+1}\right], \end{aligned} \tag{B.2}$$

and

$$\begin{aligned} x\to\boldsymbol{x}&=\left[x_0=0,x_1,\ldots,x_j,\ldots,x_{N_x+1}\right]\\ \hat{u}'_x(x)\to\hat{u}'_x(\boldsymbol{x})=\hat{\boldsymbol{u}}'_x&=\left[\hat{u}'^0_x,\hat{u}'^1_x,\ldots,\hat{u}'^j_x,\ldots,\hat{u}'^{N_x+1}_x\right], \end{aligned} \tag{B.3}$$

where N_r+2 is the number of discretization points for the flame, and N_x+2 the number of discretization points for the velocity field, which has to be sufficiently high to store the value

of the axial velocity inside the flame. Also, the velocity has to be evaluated at the mean flame positions: it is therefore natural to discretize the radial and axial directions with the same number of points, i.e., $N_r = N_x$ with $\boldsymbol{x} = \overline{F}(\boldsymbol{r})$. The boundary conditions (2.21) determine the flame position at $r = 0$ and $r = 1$, so we are left with N_r degrees of freedom. We indicate with D_x, D_r and $D_{r,r}$ the $(N_r+2)\times(N_r+2)$ first and second differentiation matrices in the axial and radial directions respectively; D_x and D_r differ because, if $\mathcal{M} \neq 0$, the steady solution is not a straight line, and the discretization in the axial direction is non-uniform. Finally, the heat release integration is discretized as:

$$\begin{aligned}\int_0^1 \left(h_1(r)\frac{\mathrm{d}\hat{f}}{\mathrm{d}r} + h_2(r)\frac{\mathrm{d}^2\hat{f}}{\mathrm{d}r^2}\right) r\mathrm{d}r &\approx \sum_{k=0}^{N_r+1} \Delta r\,\mu_k\, r_k \left(h_1(r_k)\left.\frac{\mathrm{d}\hat{f}}{\mathrm{d}r}\right|_k + h_2(r_k)\left.\frac{\mathrm{d}^2\hat{f}}{\mathrm{d}r^2}\right|_k\right) = \\ &= \sum_{k=0}^{N_r+1}\sum_{j=1}^{N_r} \Delta r\,\mu_k\, r_k \left(h_1^k D_r^{k,j}\hat{f}^j + h_2^k D_{r,r}^{k,j}\hat{f}^j\right) = \\ &= \sum_{j=1}^{N_r}\left[\sum_{k=0}^{N_r+1} \Delta r\,\mu_k\, r_k \left(h_1^k D_r^{k,j} + h_2^k D_{r,r}^{k,j}\right)\right]\hat{f}^j \equiv \sum_{j=1}^{N_r} \Delta q^j \hat{f}^j,\end{aligned} \tag{B.4}$$

where μ_k are the weights of the integral discretization chosen.

We can finally express the submatrices of the eigenvalue problem as (2.37), defining:

$$M_{ff}^{i,j} = -\frac{\beta^2}{\sqrt{1+\beta^2}}\left(h_1^i D_r^{i,j} + h_2^i D_{r,r}^{i,j}\right) \qquad i = 1,\dots,N_r \qquad j = 1,\dots,N_r \tag{B.5a}$$

$$M_{fs}^{i,j} = \frac{1}{2} r_i \left.\frac{\mathrm{d}\overline{F}}{\mathrm{d}r}\right|_i \xi_i\left(\delta_{1,i} + \delta_{2,i}\right) C_u^j \qquad i = 1,\dots,N_r \qquad j = 1,\dots,N_s \tag{B.5b}$$

$$M_{fu}^{i,j} = \delta_{i,j} + \frac{1}{2} r_i \left.\frac{\mathrm{d}\overline{F}}{\mathrm{d}r}\right|_i D_x^{i,j} \qquad i = 1,\dots,N_r \qquad j = 1,\dots,N_x \tag{B.5c}$$

$$M_{sf}^{i,j} = \frac{\beta^2}{2\sqrt{1+\beta^2}} B^i \Delta q^j \qquad i = 1,\dots,N_s \qquad j = 1,\dots,N_r \tag{B.5d}$$

$$M_{ss}^{i,j} = A^{i,j} \qquad i = 1,\dots,N_s \qquad j = 1,\dots,N_s \tag{B.5e}$$

$$M_{su}^{i,j} = 0 \qquad i = 1,\dots,N_s \qquad j = 1,\dots,N_x \tag{B.5f}$$

$$M_{uf}^{i,j} = 0 \qquad i = 1,\dots,N_x \qquad j = 1,\dots,N_r \tag{B.5g}$$

$$M_{us}^{i,j} = -\frac{1}{K}\xi_i\left(\delta_{1,i} + \delta_{2,i}\right) C_u^j \qquad i = 1,\dots,N_x \qquad j = 1,\dots,N_s \tag{B.5h}$$

$$M_{uu}^{i,j} = -\frac{1}{K} D_x^{i,j} \qquad i = 1,\dots,N_x \qquad j = 1,\dots,N_x, \tag{B.5i}$$

where $\delta_{i,j}$ is the Kronecker delta, and ξ_i are finite difference coefficients which apply the boundary condition (2.36) for the velocity at the flame base; because we use a second order scheme, only two of them are non-zero.

Appendix C

Growth rate variations by implicit function theorem

For convenience, let us rewrite the dispersion relations (4.11) in a compact form by splitting them into real and imaginary part as $\boldsymbol{N}(\boldsymbol{A},\boldsymbol{y}) \equiv (N_{10}^{\mathrm{Re}}, N_{10}^{\mathrm{Im}}, N_{01}^{\mathrm{Re}}, N_{01}^{\mathrm{Im}}) = \boldsymbol{0}$, where we have defined

$$\begin{aligned} N_{10}^{\mathrm{Re}} &\equiv \mathrm{Re}\left[\mathcal{F}_{10}(A_1,\omega_1,A_2,\omega_2,)H(\sigma_1+\mathrm{i}\omega_1)-1\right] \\ N_{10}^{\mathrm{Im}} &\equiv \mathrm{Im}\left[\mathcal{F}_{10}(A_1,\omega_1,A_2,\omega_2,)H(\sigma_1+\mathrm{i}\omega_1)-1\right] \\ N_{01}^{\mathrm{Re}} &\equiv \mathrm{Re}\left[\mathcal{F}_{01}(A_1,\omega_1,A_2,\omega_2,)H(\sigma_2+\mathrm{i}\omega_2)-1\right] \\ N_{01}^{\mathrm{Im}} &\equiv \mathrm{Im}\left[\mathcal{F}_{01}(A_1,\omega_1,A_2,\omega_2,)H(\sigma_2+\mathrm{i}\omega_2)-1\right], \end{aligned} \tag{C.1}$$

where $\boldsymbol{A} \equiv (A_1, A_2)$ is the vector of amplitudes, and $\boldsymbol{y} \equiv (\sigma_1, \omega_1, \sigma_2, \omega_2)$ is the vector of growth rates and frequencies. This is a system of four equations through which the four dependent variables (frequencies and growth rates) are implicit functions of the amplitude levels, i.e., $\boldsymbol{y} = \boldsymbol{y}(\boldsymbol{A})$. By implicit differentiation of the dispersion relations, one obtains

$$\mathrm{d}\boldsymbol{N} = \frac{\partial \boldsymbol{N}}{\partial \boldsymbol{y}}\mathrm{d}\boldsymbol{y} + \frac{\partial \boldsymbol{N}}{\partial \boldsymbol{A}}\mathrm{d}\boldsymbol{A} = \boldsymbol{0}, \tag{C.2}$$

or, by rearranging

$$\frac{\mathrm{d}\boldsymbol{y}}{\mathrm{d}\boldsymbol{A}} = \begin{bmatrix} \frac{\partial \sigma_1}{\partial A_1} & \frac{\partial \sigma_1}{\partial A_2} \\ \frac{\partial \omega_1}{\partial A_1} & \frac{\partial \omega_1}{\partial A_2} \\ \frac{\partial \sigma_2}{\partial A_1} & \frac{\partial \sigma_2}{\partial A_2} \\ \frac{\partial \omega_2}{\partial A_1} & \frac{\partial \omega_2}{\partial A_2} \end{bmatrix} = -\left(\frac{\partial \boldsymbol{N}}{\partial \boldsymbol{y}}\right)^{-1}\frac{\partial \boldsymbol{N}}{\partial \boldsymbol{A}}. \tag{C.3}$$

The latter expression yields the growth rates and frequencies sensitivities with respect to amplitudes variations. The right hand side terms can be evaluated by finite difference by

imposing small perturbations (one by one) in the dispersion relations (C.1). No iterative methods are required when using the implicit function theorem, which makes the method more reliable because it is not susceptible to convergence problems.

Appendix D

Acoustic matrix coefficients

The coefficients of the matrix in equation (5.1) are given by:

$$M_{11} = (1-M_1) - (1+M_1)R_1 e^{-s\tau_1} \tag{D.1}$$

$$M_{12} = \left((1+M_2) + (M_2-1)R_2 e^{-s\tau_2}\right)\frac{\Theta}{\Delta} \tag{D.2}$$

$$M_{13} = M_2\frac{\Theta}{\Delta} \tag{D.3}$$

$$M_{21} = (2-M_1)M_1 - \Theta - \left((2+M_1)M_1 + \Theta\right)R_1 e^{-s\tau_1} \tag{D.4}$$

$$M_{22} = \left((1+M_2)^2 + (M_2-1)^2 R_2 e^{-s\tau_2}\right)\Theta \tag{D.5}$$

$$M_{23} = M_2^2\Theta \tag{D.6}$$

$$M_{31} = \frac{(1-M_1)(2+(M_1-2)M_1(\gamma-1)) - (1+M_1)(2+M_1(2+M_1)(\gamma-1))R_1 e^{-s\tau_1}}{2(\gamma-1)} \tag{D.7}$$

$$M_{32} = \frac{(M_2-1)(2+(M_2-2)M_2(\gamma-1))R_2 e^{-s\tau_2} + (1+M_2)(2+M_2(2+M_2)(\gamma-1))}{2(\gamma-1)}\Delta\Theta \tag{D.8}$$

$$M_{33} = \frac{1}{2}M_2^3\Delta\Theta. \tag{D.9}$$

When damping model I is adopted (see §5.2.3), the Laplace variable s implicitly accounts for the wavenumber correction defined in equation (5.8). In case of damping model II, no further correction to s is introduced.

Appendix E

Nonlinear expansion terms

In the following all the terms obtained by expanding equation (5.9) to fifth order in ε are listed and classified by their physical origin.

1. **Fast timescale** ($\frac{\partial \boldsymbol{x}}{\partial t_0}$):

$$\varepsilon \frac{\partial \boldsymbol{x}_1}{\partial t_0} + \varepsilon^2 \frac{\partial \boldsymbol{x}_2}{\partial t_0} + \varepsilon^3 \frac{\partial \boldsymbol{x}_3}{\partial t_0} + \varepsilon^4 \frac{\partial \boldsymbol{x}_4}{\partial t_0} + \varepsilon^5 \frac{\partial \boldsymbol{x}_5}{\partial t_0}. \tag{E.1}$$

2. **First slow timescale** ($\frac{\partial \boldsymbol{x}}{\partial t_2}$):

$$\varepsilon^3 \frac{\partial \boldsymbol{x}_1}{\partial t_2} + \varepsilon^4 \frac{\partial \boldsymbol{x}_2}{\partial t_2} + \varepsilon^5 \frac{\partial \boldsymbol{x}_3}{\partial t_2}. \tag{E.2}$$

3. **Second slow timescale** ($\frac{\partial \boldsymbol{x}}{\partial t_4}$):

$$\varepsilon^5 \frac{\partial \boldsymbol{x}_1}{\partial t_4}. \tag{E.3}$$

4. **Linear acoustics** ($A\boldsymbol{x}$):

$$\varepsilon A\boldsymbol{x}_1 + \varepsilon^2 A\boldsymbol{x}_2 + \varepsilon^3 A\boldsymbol{x}_3 + \varepsilon^4 A\boldsymbol{x}_4 + \varepsilon^5 A\boldsymbol{x}_5. \tag{E.4}$$

5. **Linear heat release** ($\alpha_1 K^c \boldsymbol{B}(\boldsymbol{C}\boldsymbol{x}(t-\tau))$):

$$\begin{aligned} \varepsilon \alpha_1 K^c \boldsymbol{B}(\boldsymbol{C}\boldsymbol{x}_1(t-\tau)) + \varepsilon^2 \alpha_1 K^c \boldsymbol{B}(\boldsymbol{C}\boldsymbol{x}_2(t-\tau)) + \varepsilon^3 \alpha_1 K^c \boldsymbol{B}(\boldsymbol{C}\boldsymbol{x}_3(t-\tau)) \dots \\ + \varepsilon^4 \alpha_1 K^c \boldsymbol{B}(\boldsymbol{C}\boldsymbol{x}_4(t-\tau)) + \varepsilon^5 \alpha_1 K^c \boldsymbol{B}(\boldsymbol{C}\boldsymbol{x}_5(t-\tau)). \end{aligned} \tag{E.5}$$

6. **Quadratic heat release** $(\alpha_2 K^c \boldsymbol{B}(\boldsymbol{C}\boldsymbol{x}(t-\tau))^2)$:

$$\begin{aligned}\varepsilon^2\alpha_2 K^c \boldsymbol{B}(\boldsymbol{C}\boldsymbol{x}_1(t-\tau))^2 + \varepsilon^3 2\alpha_2 K^c \boldsymbol{B}(\boldsymbol{C}\boldsymbol{x}_1(t-\tau))(\boldsymbol{C}\boldsymbol{x}_2(t-\tau))\dots\\ +\varepsilon^4 2\alpha_2 K^c \boldsymbol{B}(\boldsymbol{C}\boldsymbol{x}_1(t-\tau))(\boldsymbol{C}\boldsymbol{x}_3(t-\tau)) + \varepsilon^5 2\alpha_2 K^c \boldsymbol{B}(\boldsymbol{C}\boldsymbol{x}_1(t-\tau))(\boldsymbol{C}\boldsymbol{x}_4(t-\tau))\dots\\ +\varepsilon^4\alpha_2 K^c \boldsymbol{B}(\boldsymbol{C}\boldsymbol{x}_2(t-\tau))^2 + \varepsilon^5 2\alpha_2 K^c \boldsymbol{B}(\boldsymbol{C}\boldsymbol{x}_2(t-\tau))(\boldsymbol{C}\boldsymbol{x}_3(t-\tau)).\end{aligned} \tag{E.6}$$

7. **Linear heat release and** ΔK **coupling** $(\alpha_1\delta_2 \boldsymbol{B}(\boldsymbol{C}\boldsymbol{x}(t-\tau)))$:

$$\varepsilon^3\alpha_1\delta_2 \boldsymbol{B}(\boldsymbol{C}\boldsymbol{x}_1(t-\tau)) + \varepsilon^4\alpha_1\delta_2 \boldsymbol{B}(\boldsymbol{C}\boldsymbol{x}_2(t-\tau)) + \varepsilon^5\alpha_1\delta_2 \boldsymbol{B}(\boldsymbol{C}\boldsymbol{x}_3(t-\tau)). \tag{E.7}$$

8. **Cubic heat release** $(\alpha_3 K^c \boldsymbol{B}(\boldsymbol{C}\boldsymbol{x}(t-\tau))^3)$:

$$\begin{aligned}\varepsilon^3\alpha_3 K^c \boldsymbol{B}(\boldsymbol{C}\boldsymbol{x}_1(t-\tau))^3 + \varepsilon^4 3\alpha_3 K^c \boldsymbol{B}(\boldsymbol{C}\boldsymbol{x}_1(t-\tau))^2(\boldsymbol{C}\boldsymbol{x}_2(t-\tau))\dots\\ +\varepsilon^5 3\alpha_3 K^c \boldsymbol{B}(\boldsymbol{C}\boldsymbol{x}_1(t-\tau))^2(\boldsymbol{C}\boldsymbol{x}_3(t-\tau)) + \varepsilon^5 3\alpha_3 K^c \boldsymbol{B}(\boldsymbol{C}\boldsymbol{x}_1(t-\tau))(\boldsymbol{C}\boldsymbol{x}_2(t-\tau))^2.\end{aligned} \tag{E.8}$$

9. **Quadratic heat release and** ΔK **coupling** $(\alpha_2\delta_2 \boldsymbol{B}(\boldsymbol{C}\boldsymbol{x}(t-\tau))^2)$:

$$\varepsilon^4\alpha_2\delta_2 \boldsymbol{B}(\boldsymbol{C}\boldsymbol{x}_1(t-\tau))^2 + \varepsilon^5 2\alpha_2\delta_2 \boldsymbol{B}(\boldsymbol{C}\boldsymbol{x}_1(t-\tau))(\boldsymbol{C}\boldsymbol{x}_2(t-\tau)). \tag{E.9}$$

10. **Quartic heat release** $(\alpha_4 K^c \boldsymbol{B}(\boldsymbol{C}\boldsymbol{x}(t-\tau))^4)$:

$$\varepsilon^4\alpha_4 K^c \boldsymbol{B}(\boldsymbol{C}\boldsymbol{x}_1(t-\tau))^4 + \varepsilon^5 4\alpha_4 K^c \boldsymbol{B}(\boldsymbol{C}\boldsymbol{x}_1(t-\tau))^3(\boldsymbol{C}\boldsymbol{x}_2(t-\tau)). \tag{E.10}$$

11. **Cubic heat release and** ΔK **coupling** $(\alpha_3\delta_2 \boldsymbol{B}(\boldsymbol{C}\boldsymbol{x}(t-\tau))^3)$:

$$\varepsilon^5\alpha_3\delta_2 \boldsymbol{B}(\boldsymbol{C}\boldsymbol{x}_1(t-\tau))^3. \tag{E.11}$$

12. **Quintic heat release** $(\alpha_5 K^c \boldsymbol{B}(\boldsymbol{C}\boldsymbol{x}(t-\tau))^5)$:

$$\varepsilon^5\alpha_5 K^c \boldsymbol{B}(\boldsymbol{C}\boldsymbol{x}_1(t-\tau))^5. \tag{E.12}$$

13. **Time delay** (proportional to τ, τ^2)

$$
\begin{aligned}
&-\tau \boldsymbol{B}\alpha_1 K^c \boldsymbol{C}\frac{\partial \boldsymbol{x}_1}{\partial t_2}(t-\tau)\varepsilon^3 \ldots \\
&+\tau \boldsymbol{B}\left(-2\alpha_2 K^c \boldsymbol{C}\boldsymbol{x}_1(t-\tau)\boldsymbol{C}\frac{\partial \boldsymbol{x}_1}{\partial t_2}(t-\tau) - \alpha_1 K^c \boldsymbol{C}\frac{\partial \boldsymbol{x}_2}{\partial t_2}(t-\tau)\right)\varepsilon^4 \ldots \\
&+\tau \boldsymbol{B}\left[-\alpha_1 K^c \boldsymbol{C}\frac{\partial \boldsymbol{x}_1}{\partial t_4}(t-\tau) - \alpha_1 \delta_2 \boldsymbol{C}\frac{\partial \boldsymbol{x}_1}{\partial t_2}(t-\tau) \ldots\right. \\
&-3\alpha_3 K^c (\boldsymbol{C}\boldsymbol{x}_1(t-\tau))^2 \boldsymbol{C}\frac{\partial \boldsymbol{x}_1}{\partial t_2}(t-\tau) - 2\alpha_2 K^c \boldsymbol{C}\boldsymbol{x}_2(t-\tau)\boldsymbol{C}\frac{\partial \boldsymbol{x}_1}{\partial t_2}(t-\tau) \ldots \\
&-2\alpha_2 K^c \boldsymbol{C}\boldsymbol{x}_1(t-\tau)\boldsymbol{C}\frac{\partial \boldsymbol{x}_2}{\partial t_2}(t-\tau) - \alpha_1 K^c \boldsymbol{C}\frac{\partial \boldsymbol{x}_3}{\partial t_2}(t-\tau) \ldots \\
&\left.+\frac{1}{2}\tau\alpha_1 K^c \boldsymbol{C}\frac{\partial^2 \boldsymbol{x}_1}{\partial t_2^2}(t-\tau)\right]\varepsilon^5.
\end{aligned}
\tag{E.13}
$$

Appendix F

Forcing terms

F.1 $\mathcal{O}(\varepsilon^3)$

The list of forcing terms is:

$$2\alpha_2 K^c \boldsymbol{B}(\boldsymbol{C}\boldsymbol{x}_1(t-\tau))(\boldsymbol{C}\boldsymbol{x}_2(t-\tau)) + \alpha_3 K^c \boldsymbol{B}(\boldsymbol{C}\boldsymbol{x}_1(t-\tau))^3 + \alpha_1 \delta_2 \boldsymbol{B}(\boldsymbol{C}\boldsymbol{x}_1(t-\tau)). \tag{F.1}$$

Using the solutions (5.19),(5.22), we can expand these terms and classify them by their amplitude dependence as:

$$\boldsymbol{F}_3^W \equiv \alpha_1 \boldsymbol{B}\delta_2(\boldsymbol{C}\boldsymbol{x}_1^W)e^{-\mathrm{i}\omega^c\tau}, \tag{F.2a}$$

$$\begin{aligned}\boldsymbol{F}_3^{|W|^2W} \equiv \boldsymbol{B}K^c \Big[3\alpha_3(\boldsymbol{C}\boldsymbol{x}_1^W)|(\boldsymbol{C}\boldsymbol{x}_1^W)|^2 \ldots \\ +2\alpha_2\left((\boldsymbol{C}\boldsymbol{x}_2^{W^2})(\boldsymbol{C}\boldsymbol{x}_1^W)^* + (\boldsymbol{C}\boldsymbol{x}_1^W)(\boldsymbol{C}\boldsymbol{x}_2^{|W|^2})\right)\Big] e^{-\mathrm{i}\omega^c\tau},\end{aligned} \tag{F.2b}$$

$$\boldsymbol{F}_3^{W^3} \equiv \boldsymbol{B}K^c(\boldsymbol{C}\boldsymbol{x}_1^W)\left(\alpha_3(\boldsymbol{C}\boldsymbol{x}_1^W)^2 + 2\alpha_2(\boldsymbol{C}\boldsymbol{x}_2^{W^2})\right)e^{-3\mathrm{i}\omega^c\tau}. \tag{F.2c}$$

F.2 $\mathcal{O}(\varepsilon^4)$

The list of forcing terms is:

$$\begin{aligned}-\frac{\partial \boldsymbol{x}_2}{\partial t_2}+\tau\boldsymbol{B}\left(-2\alpha_2 K^c \boldsymbol{C}\boldsymbol{x}_1(t-\tau)\boldsymbol{C}\frac{\partial \boldsymbol{x}_1}{\partial t_2}(t-\tau)-\alpha_1 K^c \boldsymbol{C}\frac{\partial \boldsymbol{x}_2}{\partial t_2}(t-\tau)\right)\dots\\ +2\alpha_2 K\boldsymbol{B}(\boldsymbol{C}\boldsymbol{x}_1(t-\tau))(\boldsymbol{C}\boldsymbol{x}_3(t-\tau))+\alpha_2 K\boldsymbol{B}(\boldsymbol{C}\boldsymbol{x}_2(t-\tau))^2\dots\\ +\alpha_1\delta_2\boldsymbol{B}(\boldsymbol{C}\boldsymbol{x}_2(t-\tau))+3\alpha_3 K\boldsymbol{B}(\boldsymbol{C}\boldsymbol{x}_1(t-\tau))^2(\boldsymbol{C}\boldsymbol{x}_2(t-\tau))\dots\\ +\alpha_2\delta_2\boldsymbol{B}(\boldsymbol{C}\boldsymbol{x}_1(t-\tau))^2+\alpha_4 K\boldsymbol{B}(\boldsymbol{C}\boldsymbol{x}_1(t-\tau))^4.\end{aligned} \tag{F.3}$$

The definitions of the forcings in eq (5.37) read:

$$\boldsymbol{F}_4^{W^4}\equiv\boldsymbol{B}K\left(\alpha_4(\boldsymbol{C}\boldsymbol{x}_1^W)^4+3\alpha_3(\boldsymbol{C}\boldsymbol{x}_1^W)^2(\boldsymbol{C}\boldsymbol{x}_2^{W^2})+2\alpha_2(\boldsymbol{C}\boldsymbol{x}_1^W)(\boldsymbol{C}\boldsymbol{x}_3^{W^3})+\alpha_2(\boldsymbol{C}\boldsymbol{x}_2^{W^2})^2\right), \tag{F.4a}$$

$$\begin{aligned}\boldsymbol{F}_4^{|W|^4}\equiv\boldsymbol{B}K^c\left(6\alpha_4|\boldsymbol{C}\boldsymbol{x}_1^W|^4+(\boldsymbol{C}\boldsymbol{x}_2^{W^2})^*\left(3\alpha_3(\boldsymbol{C}\boldsymbol{x}_1^W)^2+2\alpha_2(\boldsymbol{C}\boldsymbol{x}_2^{W^2})\right)\dots\right.\\ +3\alpha_3(\boldsymbol{C}\boldsymbol{x}_2^{W^2})\left((\boldsymbol{C}\boldsymbol{x}_1^W)^*\right)^2+2(\boldsymbol{C}\boldsymbol{x}_1^W)^*(3\alpha_3(\boldsymbol{C}\boldsymbol{x}_1^W)(\boldsymbol{C}\boldsymbol{x}_2^{|W|^2})+\alpha_2(\boldsymbol{C}\boldsymbol{x}_3^{|W|^2W}))\dots\\ \left.+\alpha_2\left(2(\boldsymbol{C}\boldsymbol{x}_1^W)(\boldsymbol{C}\boldsymbol{x}_3^{|W|^2W})^*+(\boldsymbol{C}\boldsymbol{x}_2^{|W|^2})^2\right)\right)-2\boldsymbol{B}K^c\tau\mathrm{Re}(\nu_3)\left(\alpha_1(\boldsymbol{C}\boldsymbol{x}_2^{|W|^2})\dots\right.\\ \left.+2\alpha_2(\boldsymbol{C}\boldsymbol{x}_1^W)(\boldsymbol{C}\boldsymbol{x}_1^W)^*\right)-2\boldsymbol{x}_2^{|W|^2}\mathrm{Re}(\nu_3),\end{aligned} \tag{F.4b}$$

$$\begin{aligned}\boldsymbol{F}_4^{|W|^2W^2}\equiv\boldsymbol{B}K^c\left(2(\boldsymbol{C}\boldsymbol{x}_1^W)^*\left((\boldsymbol{C}\boldsymbol{x}_1^W)\left(2\alpha_4(\boldsymbol{C}\boldsymbol{x}_1^W)^2+3\alpha_3(\boldsymbol{C}\boldsymbol{x}_2^{W^2})\right)+\alpha_2(\boldsymbol{C}\boldsymbol{x}_3^{W^3})\right)\dots\right.\\ \left.+(\boldsymbol{C}\boldsymbol{x}_1^W)(3\alpha_3(\boldsymbol{C}\boldsymbol{x}_1^W)(\boldsymbol{C}\boldsymbol{x}_2^{|W|^2})+2\alpha_2(\boldsymbol{C}\boldsymbol{x}_3^{|W|^2W}))+2\alpha_2(\boldsymbol{C}\boldsymbol{x}_2^{W^2})(\boldsymbol{C}\boldsymbol{x}_2^{|W|^2})\right)e^{-2\mathrm{i}\omega^c\tau}\dots\\ -2\boldsymbol{B}K^c\nu_3\tau\left(\alpha_1(\boldsymbol{C}\boldsymbol{x}_2^{W^2})+\alpha_2(\boldsymbol{C}\boldsymbol{x}_1^W)^2\right)e^{-2\mathrm{i}\omega^c\tau}-2\nu_3\boldsymbol{x}_2^{W^2},\end{aligned} \tag{F.4c}$$

$$\begin{aligned}\boldsymbol{F}_4^{|W|^2}\equiv\boldsymbol{B}\left(2\alpha_2\left((\boldsymbol{C}\boldsymbol{x}_1^W)^*(K^c(\boldsymbol{C}\boldsymbol{x}_3^W)+\delta_2(\boldsymbol{C}\boldsymbol{x}_1^W))+K^c(\boldsymbol{C}\boldsymbol{x}_1^W)(\boldsymbol{C}\boldsymbol{x}_3^W)^*\right)\dots\right.\\ \left.+\alpha_1\delta_2(\boldsymbol{C}\boldsymbol{x}_2^{|W|^2})\right)-2\boldsymbol{B}K^c\tau\mathrm{Re}(\lambda_3)\left(\alpha_1(\boldsymbol{C}\boldsymbol{x}_2^{|W|^2})+2\alpha_2(\boldsymbol{C}\boldsymbol{x}_1^W)(\boldsymbol{C}\boldsymbol{x}_1^W)^*\right)\dots\\ -2\boldsymbol{x}_2^{|W|^2}\mathrm{Re}(\lambda_3),\end{aligned} \tag{F.4d}$$

$$\begin{aligned}\boldsymbol{F}_4^{W^2}\equiv\boldsymbol{B}\left(\alpha_2(\boldsymbol{C}\boldsymbol{x}_1^W)(2K(\boldsymbol{C}\boldsymbol{x}_3^W)+\delta_2(\boldsymbol{C}\boldsymbol{x}_1^W))+\alpha_1\delta_2(\boldsymbol{C}\boldsymbol{x}_2^{W^2})\right)e^{-2\mathrm{i}\omega^c\tau}\dots\\ -2\boldsymbol{B}K^c\lambda_3\tau\left(\alpha_1(\boldsymbol{C}\boldsymbol{x}_2^{W^2})+\alpha_2(\boldsymbol{C}\boldsymbol{x}_1^W)^2\right)e^{-2\mathrm{i}\omega^c\tau}-2\lambda_3\boldsymbol{x}_2^{W^2}.\end{aligned} \tag{F.4e}$$

F.3 $\mathcal{O}(\varepsilon^5)$

The list of forcing terms is:

$$\begin{aligned}
&-\frac{\partial \boldsymbol{x}_3}{\partial t_2}+\tau\boldsymbol{B}\Big[-\alpha_1\delta_2\boldsymbol{C}\frac{\partial \boldsymbol{x}_1}{\partial t_2}(t-\tau)-3\alpha_3K^c(\boldsymbol{C}\boldsymbol{x}_1(t-\tau))^2\boldsymbol{C}\frac{\partial \boldsymbol{x}_1}{\partial t_2}(t-\tau)\dots\\
&-2\alpha_2K^c\boldsymbol{C}\boldsymbol{x}_2(t-\tau)\boldsymbol{C}\frac{\partial \boldsymbol{x}_1}{\partial t_2}(t-\tau)-2\alpha_2K^c\boldsymbol{C}\boldsymbol{x}_1(t-\tau)\boldsymbol{C}\frac{\partial \boldsymbol{x}_2}{\partial t_2}(t-\tau)\dots\\
&-\alpha_1K^c\boldsymbol{C}\frac{\partial \boldsymbol{x}_3}{\partial t_2}(t-\tau)+\frac{1}{2}\tau\alpha_1K^c\boldsymbol{C}\frac{\partial^2 \boldsymbol{x}_1}{\partial t_2^2}(t-\tau)\Big]\dots\\
&+2\alpha_2K^c\boldsymbol{B}(\boldsymbol{C}\boldsymbol{x}_1(t-\tau))(\boldsymbol{C}\boldsymbol{x}_4(t-\tau))+2\alpha_2K^c\boldsymbol{B}(\boldsymbol{C}\boldsymbol{x}_2(t-\tau))(\boldsymbol{C}\boldsymbol{x}_3(t-\tau))\dots\\
&+\alpha_1\delta_2\boldsymbol{B}(\boldsymbol{C}\boldsymbol{x}_3(t-\tau))+3\alpha_3K^c\boldsymbol{B}(\boldsymbol{C}\boldsymbol{x}_1(t-\tau))^2(\boldsymbol{C}\boldsymbol{x}_3(t-\tau))\dots\\
&+3\alpha_3K^c\boldsymbol{B}(\boldsymbol{C}\boldsymbol{x}_1(t-\tau))(\boldsymbol{C}\boldsymbol{x}_2(t-\tau))^2+2\alpha_2\delta_2\boldsymbol{B}(\boldsymbol{C}\boldsymbol{x}_1(t-\tau))(\boldsymbol{C}\boldsymbol{x}_2(t-\tau))\dots\\
&+4\alpha_4K^c\boldsymbol{B}(\boldsymbol{C}\boldsymbol{x}_1(t-\tau))^3(\boldsymbol{C}\boldsymbol{x}_2(t-\tau))+\alpha_3\delta_2\boldsymbol{B}(\boldsymbol{C}\boldsymbol{x}_1(t-\tau))^3+\alpha_5K^c\boldsymbol{B}(\boldsymbol{C}\boldsymbol{x}_1(t-\tau))^5.
\end{aligned}\tag{F.5}$$

For the purpose of this study, we are interested only in the explicit expressions of the resonant forcing terms in equation (5.40), which read:

$$\begin{aligned}
\boldsymbol{F}_5^W\equiv\alpha_1\delta_2\boldsymbol{B}(\boldsymbol{C}\boldsymbol{x}_3^W)e^{-\mathrm{i}\omega^c\tau}-\boldsymbol{B}\alpha_1\lambda_3\tau\Big(&(\delta_2(\boldsymbol{C}\boldsymbol{x}_1^W)+K^c(\boldsymbol{C}\boldsymbol{x}_3^W)\dots\\
&-\frac{1}{2}K^c\lambda_3\tau(\boldsymbol{C}\boldsymbol{x}_1^W)\Big)e^{-\mathrm{i}\omega^c\tau}-\lambda_3\boldsymbol{x}_3^W,
\end{aligned}\tag{F.6a}$$

$$\begin{aligned}
\boldsymbol{F}_5^{|W|^2W}\equiv\boldsymbol{B}\big(&3\alpha_3\delta_2(\boldsymbol{C}\boldsymbol{x}_1^W)|\boldsymbol{C}\boldsymbol{x}_1^W|^2+2(\boldsymbol{C}\boldsymbol{x}_1^W)^*(3\alpha_3K^c(\boldsymbol{C}\boldsymbol{x}_1^W)(\boldsymbol{C}\boldsymbol{x}_3^W)\dots\\
&+\alpha_2K^c(\boldsymbol{C}\boldsymbol{x}_4^{W^2})+\alpha_2\delta_2(\boldsymbol{C}\boldsymbol{x}_2^{W^2}))+K^c(\boldsymbol{C}\boldsymbol{x}_3^W)^*\Big(3\alpha_3(\boldsymbol{C}\boldsymbol{x}_1^W)^2+2\alpha_2(\boldsymbol{C}\boldsymbol{x}_2^{W^2})\Big)\dots\\
&+2\alpha_2(K^c(\boldsymbol{C}\boldsymbol{x}_1^W)(\boldsymbol{C}\boldsymbol{x}_4^{|W|^2})+K^c(\boldsymbol{C}\boldsymbol{x}_2^{|W|^2})(\boldsymbol{C}\boldsymbol{x}_3^W)+\delta_2(\boldsymbol{C}\boldsymbol{x}_1^W)(\boldsymbol{C}\boldsymbol{x}_2^{|W|^2}))\dots\\
&+\alpha_1\delta_2(\boldsymbol{C}\boldsymbol{x}_3^{|W|^2W})\Big)e^{-\mathrm{i}\omega^c\tau}-\boldsymbol{B}\tau\Big(\delta_2(\boldsymbol{C}\boldsymbol{x}_1^W)\alpha_1\nu_3+K^c((\boldsymbol{C}\boldsymbol{x}_3^{|W|^2W})\alpha_1\lambda_3\dots\\
&+2(\boldsymbol{C}\boldsymbol{x}_1^W)(\boldsymbol{C}\boldsymbol{x}_2^{|W|^2})\alpha_2\lambda_3+\alpha_1\nu_3((\boldsymbol{C}\boldsymbol{x}_3^W)-(\boldsymbol{C}\boldsymbol{x}_1^W)\lambda_3\tau))+K^c(2(\boldsymbol{C}\boldsymbol{x}_3^{|W|^2W})\alpha_1\dots\\
&+4(\boldsymbol{C}\boldsymbol{x}_1^W)(\boldsymbol{C}\boldsymbol{x}_2^{|W|^2}\alpha_2-(\boldsymbol{C}\boldsymbol{x}_1^W)\alpha_1\nu_3\tau)\mathrm{Re}(\lambda_3)3K^c(\boldsymbol{C}\boldsymbol{x}_1^W)\alpha_3|\boldsymbol{C}\boldsymbol{x}_1^W|^2(\lambda_3+2\mathrm{Re}(\lambda_3))\dots\\
&+2K^c(\boldsymbol{C}\boldsymbol{x}_2^{W^2})\alpha_2(\boldsymbol{C}\boldsymbol{x}_1^W)^*(\lambda_3+2\mathrm{Re}(\lambda_3))\Big)e^{-\mathrm{i}\omega^c\tau}\dots\\
&-2\boldsymbol{x}_3^{|W|^2W}\mathrm{Re}(\lambda_3)-\nu_3\boldsymbol{x}_3^W-\lambda_3\boldsymbol{x}_3^{|W|^2W},
\end{aligned}\tag{F.6b}$$

$$
\begin{aligned}
\boldsymbol{F}_5^{|W|^4W} \equiv \boldsymbol{B}K^c \Big(& 12\alpha_4(\boldsymbol{C}\boldsymbol{x}_1^W)(\boldsymbol{C}\boldsymbol{x}_2^{|W|^2})|\boldsymbol{C}\boldsymbol{x}_1^W|^2 + 2(\boldsymbol{C}\boldsymbol{x}_2^{W^2})^* \big(2\alpha_4 C^2(\boldsymbol{C}\boldsymbol{x}_1^W)^3 \ldots \\
& + 3\alpha_3(\boldsymbol{C}\boldsymbol{x}_1^W)(\boldsymbol{C}\boldsymbol{x}_2^{W^2}) + \alpha_2(\boldsymbol{C}\boldsymbol{x}_3^{W^3})\big) + (\boldsymbol{C}\boldsymbol{x}_3^{|W|^2W})^* \Big(3\alpha_3(\boldsymbol{C}\boldsymbol{x}_1^W)^{+}2\alpha_2(\boldsymbol{C}\boldsymbol{x}_2^{W^2})\Big) \ldots \\
& + 2(\boldsymbol{C}\boldsymbol{x}_1^W)^*(3\alpha_3((\boldsymbol{C}\boldsymbol{x}_1^W)(\boldsymbol{C}\boldsymbol{x}_3^{|W|^2W}) + (\boldsymbol{C}\boldsymbol{x}_2^{W^2})(\boldsymbol{C}\boldsymbol{x}_2^{|W|^2})) + \alpha_2(\boldsymbol{C}\boldsymbol{x}_4^{|W|^2W^2})) \ldots \\
& + 3\left((\boldsymbol{C}\boldsymbol{x}_1^W)^*\right)^2(4\alpha_4(\boldsymbol{C}\boldsymbol{x}_1^W)(\boldsymbol{C}\boldsymbol{x}_2^{W^2}) + \alpha_3(\boldsymbol{C}\boldsymbol{x}_3^{W^3}))\Big) + \boldsymbol{B}K^c \Big(3\alpha_3(\boldsymbol{C}\boldsymbol{x}_1^W)(\boldsymbol{C}\boldsymbol{x}_2^{|W|^2})^2 \ldots \\
& + 2\alpha_2(\boldsymbol{C}\boldsymbol{x}_1^W)(\boldsymbol{C}\boldsymbol{x}_4^{|W|^4}) + 2\alpha_2(\boldsymbol{C}\boldsymbol{x}_2^{|W|^2})(\boldsymbol{C}\boldsymbol{x}_3^{|W|^2W})\Big) e^{-\mathrm{i}\omega^c\tau} \\
& - \frac{1}{2}\boldsymbol{B}K^c\tau(\nu_3 + 2\mathrm{Re}(\nu_3)) \Big(2\alpha_1(\boldsymbol{C}\boldsymbol{x}_3^{|W|^2W}) + 4\alpha_2(\boldsymbol{C}\boldsymbol{x}_1^W)(\boldsymbol{C}\boldsymbol{x}_2^{|W|^2}) \ldots \\
& - \alpha_1\nu_3\tau(\boldsymbol{C}\boldsymbol{x}_1^W) + 4\alpha_2(\boldsymbol{C}\boldsymbol{x}_2^{W^2})(\boldsymbol{C}(\boldsymbol{x}_1^W)^*) + 6\alpha_3(\boldsymbol{C}\boldsymbol{x}_1^W)(\boldsymbol{C}\boldsymbol{x}_1^W)(\boldsymbol{C}(\boldsymbol{x}_1^W)^*)\Big) e^{-\mathrm{i}\omega^c\tau} \\
& - 2\boldsymbol{x}_3^{|W|^2W}\mathrm{Re}(\nu_3) - \nu_3\boldsymbol{x}_3^{|W|^2W}.
\end{aligned}
\tag{F.6c}
$$

References

ABU-ORF, G. M. 1996 Laminar flamelet reaction rate modelling for spark-ignition engines. PhD thesis, University of Manchester. (Cited on page 159.)

ANANTHKRISHNAN, N., DEO, S. & CULICK, F. E. C. 2005 Reduced-order modeling and dynamics of nonlinear acoustic waves in a combustion chamber. *Combustion Science and Technology* **177**, 221–248. (Cited on pages 106, 108, 116, and 117.)

ANISIMOV, V. V., CHIARIONI, A., ROFI, L., OZZANO, C., HERMETH, S., HANNEBIQUE, G., STAFFELBACH, G. & POINSOT, T. 2015 Bi-stable flame behaviour of heavy duty gas turbine burner. RANS, LES and experiment comparison. In *Proceedings of ASME Turbo Expo*, pp. GT2015–42536. (Cited on page 80.)

ARMITAGE, C.A., BALACHANDRAN, R., MASTORAKOS, E. & CANT, R.S. 2006 Investigation of the nonlinear response of turbulent premixed flames to imposed inlet velocity oscillations. *Combustion and Flame* **146** (3), 419–436. (Cited on pages 136, 138, 141, 143, 145, and 149.)

BAILLOT, F., DUROX, D. & PRUD'HOMME, R. 1992 Experimental and theoretical study of a premixed vibrating flame. *Combustion and Flame* **88**, 149–168. (Cited on page 18.)

BALACHANDRAN, R. 2005 Experimental investigation of the response of turbulent premixed flames to acoustic oscillations. PhD thesis, University of Cambridge. (Cited on pages 149, 157, 170, 171, 172, and 174.)

BALACHANDRAN, R., AYOOLA, B.O., KAMINSKI, C.F., DOWLING, A.P. & E., MASTORAKOS 2005 Experimental investigation of the nonlinear response of turbulent premixed flames to imposed inlet velocity oscillations. *Combustion and Flame* **143**, 37–55. (Cited on pages 136, 137, 138, 149, and 150.)

BALACHANDRAN, R., DOWLING, A.P. & E., MASTORAKOS 2008 Non-linear response of turbulent premixed flames to imposed inlet velocity oscillations of two frequencies. *Flow, Turbulence and Combustion* **80**, 455–487. (Cited on page 80.)

BALASUBRAMANIAN, K. & SUJITH, R. I. 2008 Non-normality and nonlinearity in combustion-acoustic interaction in diffusion flames. *Journal of Fluid Mechanics* **594**, 29–57. (Cited on page 2.)

BASSO, M., GENESIO, R. & TESI, A. 1997 A frequency method for predicting limit cycle bifurcations. *Nonlinear Dynamics* **13** (4), 339–360. (Cited on page 74.)

BELLUCCI, V., SCHUERMANS, B., NOWAK, D., FLOHR, P. & PASCHEREIT, C. O. 2005 Thermoacoustic modeling of a gas turbine combustor equipped with acoustic dampers. *Journal of Turbomachinery* **127**, 372. (Cited on page 8.)

BIRBAUD, A. L., DUROX, D. & CANDEL, S. 2006 Upstream flow dynamics of a laminar premixed conical flame submitted to acoustic modulations. *Combustion and Flame* **146**, 541–552. (Cited on pages 18, 29, 30, 36, 40, and 55.)

BLANCHARD, M., SCHULLER, T., SIPP, D. & SCHMID, P. J. 2015 Response analysis of a laminar premixed M-flame to flow perturbations using a linearized compressible Navier–Stokes solver. *Physics of Fluids* **27** (4), 043602. (Cited on page 36.)

BLOXSIDGE, G. J., DOWLING, A. P. & LANGHORNE, P. J. 1988 Reheat buzz: an acoustically coupled combustion instability. Part 2. Theory. *Journal of Fluid Mechanics* **193**, 445–473. (Cited on page 19.)

BLUMENTHAL, R. S., SUBRAMANIAN, P., SUJITH, R. I. & POLIFKE, W. 2013 Novel perspectives on the dynamics of premixed flames. *Combustion and Flame* **160** (7), 1215–1224. (Cited on page 162.)

BOTHIEN, M. R., MOECK, J. P., LACARELLE, A. & PASCHEREIT, C. O. 2007 Time domain modelling and stability analysis of complex thermoacoustic systems. *Journal of Power and Energy* **221** (5), 657–668. (Cited on pages 18, 24, and 37.)

BOUDY, F., DUROX, D., SCHULLER, T., JOMAAS, G. & CANDEL, S. 2011 Describing Function analysis of limit cycles in a multiple flame combustor. *Journal of Engineering for Gas Turbines and Power* **133**, 061502. (Cited on pages 3 and 6.)

CAMPA, G., CAMPOREALE, S. M., A., GUAUS., FAVIER, J., BARGIACCHI, M., BOTTARO, A., COSATTO, E. & MORI, G. 2011 A quantitative comparison between a low order model and a 3D FEM code for the study of thermoacoustic combustion instabilities. In *Proceedings of ASME Turbo Expo*, pp. GT2011–45969. (Cited on page 8.)

CANDEL, S. M. 1992 Combustion instabilities coupled by pressure waves and their active control. In *24th Symposium on Combustion*, pp. 1277–1296. (Cited on page 2.)

CARGILL, A. M. 1982 Low frequency acoustic radiation from a jet pipe - a second order theory. *Journal of Sound and Vibration* **83**, 339–354. (Cited on pages 40 and 112.)

CAZALENS, M., ROUX, S., SENSIAU, C. & POINSOT, T. 2008 Combustion instability problems analysis for high-pressure jet engine cores. *Journal of Propulsion and Power* **24**, 770–778. (Cited on page 80.)

CHANDLER, G. J., JUNIPER, M. P., NICHOLS, J. W. & SCHMID, P. J. 2012 Adjoint algorithms for the Navier–Stokes equations in the low Mach number limit. *Journal of Computational Physics* **231**, 1900–1916. (Cited on pages 47 and 48.)

CHO, J. H. & LIEUWEN, C. 2005 Laminar premixed flame response to equivalence ratio oscillations. *Combustion and Flame* **140**, 116–129. (Cited on pages 158 and 159.)

CHOMAZ, J.-M. 2005 Global instabilities in spatially developing flows: non-normality and nonlinearity. *Annual Review of Fluid Mechanics* **37**, 357–392. (Cited on page 106.)

CHU, B.-T. 1963 Analysis of a self-sustained thermally driven nonlinear vibration. *Physics of Fluids (1958-1988)* **6** (11), 1638–1644. (Cited on pages 40 and 58.)

CHU, B.-T. & KOVÁSZNAY, L. S. G. 1958 Non-linear interactions in a viscous heat-conducting compressible gas. *Journal of Fluid Mechanics* **3**, 494–514. (Cited on page 6.)

ĆOSIĆ, B., BOBUSCH, B. C., MOECK, J. P. & PASCHEREIT, C. O. 2012 Open-loop control of combustion instabilities and the role of the flame response to two-frequency forcing. *Journal of Engineering for Gas Turbines and Power* **134**, 061502. (Cited on page 133.)

ĆOSIĆ, B., TERHAAR, S., MOECK, J. P. & PASCHEREIT, C. O. 2014 Response of a swirl-stabilized flame to simultaneous perturbations in equivalence ratio and velocity at high oscillation amplitudes. *Combustion and Flame* **162**, 1046–1062. (Cited on page 165.)

COURTINE, E., SELLE, L. & POINSOT, T. 2015 DNS of intrinsic thermoacoustic modes in laminar premixed flames. *Combustion and Flame* **162**, 4331–4341. (Cited on page 83.)

CRETA, F. & MATALON, M. 2011 Strain rate effects on the nonlinear development of hydrodynamically unstable flames. *Proceedings of the Combustion Institute* **33** (1), 1087–1094. (Cited on pages 19, 25, 32, and 55.)

CULICK, F. E. C. 1971 Non-linear growth and limiting amplitude of acoustic oscillations in combustion chambers. *Combustion Science and Technology* **3** (1), 1–16. (Cited on pages 40 and 58.)

CULICK, F. E. C. 1976*a* Nonlinear behavior of acoustic waves in combustion chambers-i. *Acta Astronautica* **3** (9-10), 715–734. (Cited on page 17.)

CULICK, F. E. C. 1976*b* Nonlinear behavior of acoustic waves in combustion chambers-ii. *Acta Astronautica* **3** (9-10), 735–757. (Cited on page 17.)

CULICK, F. E. C. 2006 *Unsteady motions in combustion chambers for propulsion systems*. AGARDograph, RTO AG-AVT-039. (Cited on pages 1, 6, 37, 53, and 106.)

CUQUEL, A., DUROX, D. & SCHULLER, T. 2011 Theoretical and experimental determination of the Flame Transfer Function of confined premixed conical flames. In *7th Mediterranean Combustion Symposium*. (Cited on pages 19, 26, 30, 31, 35, and 83.)

CUQUEL, A., DUROX, D. & SCHULLER, T. 2013*a* Impact of flame base dynamics on the non-linear frequency response of conical flames. *Comptes Rendus Mecanique* **341**, 171–180. (Cited on page 19.)

CUQUEL, A., DUROX, D. & SCHULLER, T. 2013*b* Scaling the Flame Transfer Function of confined premixed conical flames. *Proceeding of the Combustion Institute* **34**, 1007–1014. (Cited on page 19.)

DARRIEUS, G. 1938 Propagation d'un front de flamme. Essai de théorie des vitesses anomales de déflagration par développemcnt spontané de la turbulence. In *6th International Congress of Applied Mechanics*. Paris, unpublished work. (Cited on pages 25 and 32.)

DAS, S. L. & CHATTERJEE, A. 2002 Multiple scales without Center Manifold reductions for delay differential equations near Hopf bifurcations. *Nonlinear Dynamics* **30**, 323–335. (Cited on page 118.)

DOWLING, A. P. 1995 The calculation of thermoacoustic oscillations. *Journal of Sound and Vibration* **180** (4), 557–581. (Cited on pages 5, 8, 22, and 108.)

DOWLING, A. P. 1997 Nonlinear self-excited oscillations of a ducted flame. *Journal of Fluid Mechanics* **346**, 271–290. (Cited on pages 5, 23, 53, and 54.)

DOWLING, A. P. 1999 A kinematic model of a ducted flame. *Journal of Fluid Mechanics* **394**, 51–72. (Cited on pages 36, 53, and 136.)

DOWLING, A. P. & STOW, S. R. 2003 Acoustic analysis of gas turbine combustors. *Journal of Propulsion and Power* **19** (5), 751–764. (Cited on pages 6, 8, 40, and 58.)

DUCRUIX, S., DUROX, D. & CANDEL, S. 2000 Theoretical and experimental determinations of the Transfer Function of a laminar premixed flame. *Proceedings of the Combustion Institute* **28** (1), 765–773. (Cited on page 82.)

DUNSTAN, W. J., BITMEAD, R. R. & SAVARESI, S. M. 2001 Fitting nonlinear low-order models for combustion instability control. *Control Engineering Practice* **9**, 1301–1317. (Cited on page 80.)

DURAN, I. & MOREAU, S. 2013 Solution of the quasi-one-dimensional linearized Euler equations using flow invariants and the Magnus expansion. *Journal of Fluid Mechanics* **723**, 190–231. (Cited on page 22.)

DUROX, D., SCHULLER, T., NOIRAY, N. & CANDEL, S. 2009 Experimental analysis of nonlinear flame transfer functions for different flame geometries. *Proceedings of the Combustion Institute* **32**, 1391–1398. (Cited on pages 12, 82, 136, 139, 149, and 161.)

ELDREDGE, J. D. & DOWLING, A. P. 2003 The absorption of axial acoustic waves by a perforated liner with bias flow. *Journal of Fluid Mechanics* **485**, 307–335. (Cited on page 40.)

EMMERT, T., BOMBERG, S. & POLIFKE, W. 2014 Intrinsic thermoacoustic instability of premixed flames. *Combustion and Flame* (162), 75–85. (Cited on page 83.)

EMMERT, T., LEANDRO, R., HUBER, A. & POLIFKE, W. 2013 TaX manual documentation. *Tech. Rep.*. Technische Universität München. (Cited on page 8.)

EMMONS, H. W. 1958 Flow discontinuities associated with combustion. *High Speed Aerodynamics and Jet Propulsion* **3**, 584. (Cited on page 8.)

ENGELBORGHS, K., LUZYANINA, T. & ROOSE, D. 2002 Numerical bifurcation analysis of delay differential equations using DDE-BIFTOOL. *ACM Transactions on Mathematical Software* **28**, 1–21. (Cited on pages 115 and 128.)

EVESQUE, S., DOWLING, A. P. & ANNASWAMY, A. M. 2003 Self-tuning regulators for combustion oscillations. *Proceedings of the Royal Society of London A* **459** (2035), 1709–1749. (Cited on page 21.)

FERREIRA, M. A. & CARVALHO JR., J. A. 1997 A simple derivation of the Rayleigh criterion in integral form. *Journal of Sounds and Vibrations* **203** (5), 889–893. (Cited on page 46.)

FLANDRO, G. A., FISCHBACH, S. R. & MAJDALANI, J. 2007 Nonlinear rocket motor stability prediction: limit amplitude, triggering, and mean pressure shift. *Physics of Fluids* **19**, 094101. (Cited on page 120.)

FUJIMURA, K. 1991 Methods of Centre Manifold and multiple scales in the theory of weakly nonlinear stability for fluid motions. *Proceedings of the Royal Society of London A* **434**, 719–733. (Cited on page 126.)

GAMBINO, G., LOMBARDO, M. C. & SAMMARTINO, M. 2012 Turing instability and traveling fronts for a nonlinear reaction-diffusion system with cross-diffusion. *Mathematics and Computers in Simulations* **82**, 1112–1132. (Cited on page 126.)

GELB, A. & VELDE, W. E. C. 1968 *Multiple-Input Describing Functions and nonlinear system design*. McGraw-Hill. (Cited on pages 80, 82, 87, and 110.)

GHIRARDO, G. & JUNIPER, M. P. 2013 Azimuthal instabilities in annular combustors: standing and spinning modes. *Proceedings of the Royal Society of London A* **469**, 2157. (Cited on page 8.)

GHIRARDO, G., JUNIPER, M. P. & MOECK, J. P. 2015 Stability criteria for standing and spinning waves in annular combustors. In *Proceedings of ASME Turbo Expo*, pp. GT2015–43127. (Cited on pages 106 and 120.)

GIANNETTI, F. & LUCHINI, P. 2007 Structural sensitivity of the first instability of the cylinder wake. *Journal of Fluid Mechanics* **581**, 167–197. (Cited on page 46.)

GOTODA, H., NIKIMOTO, H., MIYANO, T. & TACHIBANA, S. 2011 Dynamic properties of combustion instability in a lean premixed gas-turbine combustor. *Chaos* **21** (1), 013124. (Cited on pages 2, 54, 64, and 65.)

GOTODA, H., SHINODA, Y., KOBAYASHI, M., OKUNO, Y. & TACHIBANA, S. 2014 Detection and control of combustion instability based on the concept of dynamical system theory. *Physical Review E* **89**, 022910. (Cited on page 54.)

GOTTLIEB, S. & SHU, C. W. 1998 Total variation diminishing Runge-Kutta schemes. *Mathematics of Computation of the American Mathematical Society* **67** (221), 73–85. (Cited on page 33.)

GRAHAM, OWEN STEWART 2012 Modelling the thermoacoustic response of premixed flames. PhD thesis, University of Cambridge. (Cited on pages 136, 140, 146, 156, 157, 158, 159, 160, 170, 171, 175, and 176.)

GUCKENHEIMER, J. & HOLMES, P. 1983 *Nonlinear oscillations, dynamical systems, and bifurcations of vector fields*. Springer. (Cited on pages 67, 68, and 101.)

GUTMARK, E., WILSON, K., PARR, T. & K., SCHADOW 1992 Feedback control of multi-mode combustion instability. In *30th AIAA Meeting*. (Cited on page 80.)

HAN, X., LI, J. & MORGANS, A. S. 2015 Prediction of combustion instability limit cycle oscillations by combining Flame Describing Function simulations with a thermoacoustic network model. *Combustion and Flame* **162**, 3632–3647. (Cited on page 96.)

HARTMANN, D., MEINKE, M. & SCHRÖDER, W. 2010 The constrained reinitialization equation for Level Set methods. *Journal of Computational Physics* **229** (5), 1514–1535. (Cited on page 10.)

HARTMANN, R. 2007 Adjoint consistency analysis of discontinuous Galerkin discretizations. *SIAM Journal on Numerical Analysis* **45** (6), 2671–2696. (Cited on page 48.)

HECKL, M. A. 1988 Active control of the noise from a Rijke tube. *Journal of Sound and Vibration* **124** (1), 117–133. (Cited on pages 5 and 17.)

HECKL, M. A. 1990 Non-linear acoustic effects in the Rijke tube. *Acustica* **72**, 63–71. (Cited on page 111.)

HECKL, M. A. & HOWE, M. S. 2007 Stability analysis of the Rijke tube with a Green's function approach. *Journal of Sound and Vibration* **305**, 672–688. (Cited on page 17.)

HEMCHANDRA, S. 2009 Dynamics of turbulent premixed flames in acoustic fields. PhD thesis, Georgia Institute of Technology. (Cited on page 11.)

HEMCHANDRA, S. 2012 Premixed flame response to equivalence ratio fluctuations: Comparison between reduced order modeling and detailed computations. *Combustion and Flame* **159**, 3530–3543. (Cited on page 36.)

HEMCHANDRA, S., PETERS, N. & LIEUWEN, T. 2011 Heat release response of acoustically forced turbulent premixed flames - role of kinematic restoration. *Proceedings of the Combustion Institute* **33** (1), 1609–1617. (Cited on page 150.)

HIGGINS, B. 1802 On the sound produced by a current of hydrogen gas passing through a tube. *Journal of Natural Philosophy, Chemistry and the Arts* **1**, 129–131. (Cited on page 1.)

HOEIJMAKERS, M., KORNILOV, V., ARTEAGA, I. L., DE GOEY, P. & NIJMEIJER, H. 2014*a* Flames in context of thermo-acoustic stability bounds. *Proceedings of the Combustion Institute* **35** (1), 1073–1078. (Cited on page 83.)

HOEIJMAKERS, M., KORNILOV, V., ARTEAGA, I. L., DE GOEY, P. & NIJMEIJER, H. 2014*b* Intrinsic instability of flame-acoustic coupling. *Combustion and Flame* **161**, 2860–2867. (Cited on page 83.)

HUGHES, I. J. & DOWLING, A. P. 1990 The absorption of sound by perforated linings. *Journal of Fluid Mechanics* **218**, 299–335. (Cited on page 112.)

HUMPHREY, L., ACHARYA, V., SHIN, D. H. & LIEUWEN, T. 2014 Techinical note - Coordinate systems and integration limits for global Flame Transfer Function calculations. *International Journal of Spray and Combustion Dynamics* **6** (4), 411–416. (Cited on page 27.)

ILLINGWORTH, S. J. & JUNIPER, M. P. 2014 Acoustic state-space model using a wave-based approach. In *21st ICSV*. (Cited on page 25.)

ILLINGWORTH, S. J., WAUGH, I. C. & JUNIPER, M. P. 2013 Finding thermoacoustic limit cycles for a ducted Burke-Schumann flame. *Proceedings of the Combustion Institute* **34** (1), 911–920. (Cited on page 3.)

JAHNKE, C. C. & CULICK, F. E. C. 1994 Application of dynamical systems theory to nonlinear combustion instabilities. *Journal of Propulsion and Power* **10** (4), 508–517. (Cited on pages 106 and 108.)

JEGADEESAN, V. & SUJITH, R. I. 2013 Experimental investigation of noise induced triggering in thermoacoustic systems. *Proceedings of the Combustion Institute* **34**, 3175–3183. (Cited on pages 2, 106, and 117.)

JUNIPER, M. P. 2011 Triggering in the horizontal Rijke tube: non-normality, transient growth and bypass transition. *Journal of Fluid Mechanics* **667**, 272–308. (Cited on pages 2, 106, 108, 116, and 117.)

JUNIPER, M. P. 2012 Weakly nonlinear analysis of thermoacoustic oscillations. In *19th ICSV*, pp. 1–5. (Cited on page 106.)

JUNIPER, M. P., LI, L. & NICHOLS, J. 2008 Forcing of self-excited round jet diffusion flames. *Proceedings of the Combustion Institute* **32**, 1191–1198. (Cited on page 82.)

KABIRAJ, L., SAURABH, A., WAHI, P. & SUJITH, R. I. 2012*a* Route to chaos for combustion instability in ducted laminar premixed flames. *Chaos* **22**, 023129. (Cited on pages 3, 54, and 80.)

KABIRAJ, L., SAURABH, A., WAHI, P. & SUJITH, R. I. 2012*b* Route to chaos for combustion instability in ducted laminar premixed flames. *Chaos* **22** (2), 023129. (Cited on page 74.)

KABIRAJ, L. & SUJITH, R. I. 2012 Nonlinear self-excited thermoacoustic oscillations: intermittency and flame blowout. *Journal of Fluid Mechanics* **713**, 376–397. (Cited on pages 2, 19, 39, 54, 64, 65, 74, and 75.)

KANTZ, H. & SCHREIBER, T. 2004 *Nonlinear time series analysis*. Cambridge University Press. (Cited on page 67.)

KARIMI, N., BREAR, M. J., JIN, S.-H. & MONTY, J. P. 2009 Linear and non-linear forced response of a conical, ducted, laminar premixed flame. *Combustion and Flame* **156** (11), 2201–2212. (Cited on pages 12, 19, 35, 59, 61, 82, 83, and 136.)

KASHINATH, K., HEMCHANDRA, S. & JUNIPER, M. P. 2013*a* Nonlinear phenomena in thermoacoustic systems with premixed flames. *Journal of Engineering for Gas Turbines and Power* **135** (6), 061502. (Cited on pages 36, 37, 40, and 83.)

KASHINATH, K., HEMCHANDRA, S. & JUNIPER, M. P. 2013*b* Nonlinear thermoacoustics of ducted premixed flames: the influence of perturbation convection speed. *Combustion and Flame* **160**, 2856–2865. (Cited on pages 19, 26, 29, 30, 35, 40, 48, 55, 57, 59, 140, 150, and 151.)

KASHINATH, K., WAUGH, I. C. & JUNIPER, M. P. 2014 Nonlinear self-excited thermoacoustic oscillations of a ducted premixed flame: bifurcations and routes to chaos. *Journal of Fluid Mechanics* (761), 399 – 430. (Cited on pages 2, 11, 12, 54, 56, 64, 67, 76, 81, 97, 100, 102, 108, 116, 136, 142, and 150.)

KELLEY, A. P. & LAW, C. K. 2009 Nonlinear effects in the extraction of laminar flame speeds from expanding spherical flames. *Combustion and Flame* **156**, 1844–1851. (Cited on page 141.)

KHALIL, H. K. 2001 *Nonlinear systems*, 3rd edn. Prentice Hall. (Cited on page 58.)

KHALIL, H. K. 2002 *Nonlinear systems*, 3rd edn. Prentice Hall. (Cited on page 4.)

KING, L. V. 1914 On the convection of heat from small cylinders in a stream of fluid: determination of the convection constants of small platinum wires, with application to hot-wire anemometry. *Philosophical Transactions of the Royal Society A* **214**, 373–432. (Cited on page 109.)

KYPRAIOU, A. M., DOWLING, A. P., MASTORAKOS, E. & KARIMI, N. 2015 Proper Orthogonal Decomposition analysis of a turbulent swirling self-excited premixed flame. In *53rd AIAA Aerospace Sciences Meeting*, pp. doi:10.2514/6.2015–0425. (Cited on page 151.)

LAMAROUI, A., RICHECOEUR, F., DUCRUIX, S. & SCHULLER, T. 2011 Experimental analysis of simultaneous non-harmonic related unstable modes in a swirled combustor. In *Proceedings of ASME Turbo Expo*, pp. GT2011–46701. (Cited on page 80.)

LANDAU, L. 1944*a* On the theory of slow combustion. *Acta physicochimica* **19**, 77–85. (Cited on pages 25 and 32.)

LANDAU, L. D. 1944*b* On the problem of turbulence. *C.R. Acad. Sci. URSS* **44** (31), 1–314. (Cited on page 106.)

LANG, W., POINSOT, T. & CANDEL, S. 1987 Active control of combustion instability. *Combustion and Flame* **70**, 281–289. (Cited on page 17.)

LI, J., YANG, D., LUZZATO, C. & MORGANS, A. S. 2014 Open Source Combustion Instability Low Order Simulator (OSCILOS-Long). *Tech. Rep.*. Imperial College London. (Cited on page 8.)

LIEUWEN, T. 2003 Modeling premixed combustion-acoustic wave interactions: a review. *Journal of Propulsion and Power* **19** (5), 765–781. (Cited on pages 19, 158, 165, and 169.)

LIEUWEN, T., YANG, V. & YETTER, R. 2010 *Synthesis gas combustion*. CRC Press. (Cited on page 1.)

LIEUWEN, T. C. 2012 *Unsteady combustor physics*. Cambridge University Press. (Cited on pages 1, 28, 53, 142, and 147.)

LIGHTHILL, M. J. 1954 The response of laminar skin friction and heat transfer to fluctuations in the stream velocity. *Proceedings of the Royal Society of London A* **224**, 1–23. (Cited on pages 109, 110, 113, and 115.)

LUCHINI, P. & BOTTARO, A. 2014 Adjoint equations in stability analysis. *Annual Review of Fluid Mechanics* **46**, 493–517. (Cited on pages 20, 46, and 47.)

MACQUISTEN, M. A., WHITEMAN, M., STOW, S. R. & MORAN, A. J. 2014 Exploitation of measured Flame Transfer Functions for a two-phase lean fuel injector to predict thermoacoustic modes in full annular combustors. In *Proceedings of ASME Turbo Expo*, pp. GT2014–25036. (Cited on page 162.)

MAGRI, L. & JUNIPER, M. P. 2013*a* A theoretical approach for passive control of thermoacoustic oscillations: application to ducted flames. *Journal of Engineering for Gas Turbines and Power* **135**, 091604. (Cited on page 2.)

MAGRI, L. & JUNIPER, M. P. 2013*b* Sensitivity analysis of a time-delayed thermo-acoustic system via an adjoint-based approach. *Journal of Fluid Mechanics* **719**, 183–202. (Cited on pages 2, 20, 46, 47, 58, and 108.)

MAGRI, L. & JUNIPER, M. P. 2014 Global modes, receptivity, and sensitivity analysis of diffusion flames coupled with duct acoustics. *Journal of Fluid Mechanics* **752**, 237–265. (Cited on page 47.)

MANGESIUS, H. & POLIFKE, W. 2011 A discrete-time, state-space approach for the investigation of non-normal effects in thermoacoustic systems. *International Journal of Spray and Combustion Dynamics* **3** (4), 331–350. (Cited on pages 18, 24, and 37.)

MARBLE, F. E. & CANDEL, S. M. 1977 Acoustic disturbance from gas non-uniformities convected through a nozzle. *Journal of Sound and Vibrations* **55** (2), 225–243. (Cited on page 22.)

MARIAPPAN, S., SUJITH, R. I. & SCHMID, P. J. 2015 Experimental investigation of non-normality of thermoacoustic interaction in an electrically heated Rijke tube. *International Journal of Spray and Combustion Dynamics* **7** (4), 315–352. (Cited on page 108.)

MARKSTEIN, G. H. 1964 *Non-steady flame propagation*. Pergamon Press. (Cited on pages 8, 31, 55, 140, and 141.)

MATVEEV, K. 2003 Thermoacoustic instabilities in the Rijke tube: experiments and modeling. PhD thesis, California Institute of Technology. (Cited on page 108.)

MELIGA, P., CHOMAZ, J.-M. & SIPP, D. 2009 Global mode interaction and pattern selection in the wake of a disk: a weakly nonlinear expansion. *Journal of Fluid Mechanics* **633**, 159. (Cited on pages 120, 121, 131, and 133.)

MOECK, J. P. & PASCHEREIT, C. O. 2012 Nonlinear interactions of multiple linearly unstable thermoacoustic modes. *International Journal of Spray and Combustion Dynamics* **4** (1), 1–28. (Cited on pages 3, 73, 80, 81, 89, 92, 98, 99, 101, 103, and 173.)

MOIN, P. & APTE, V. 2006 Large-Eddy Simulation of realistic gas turbine combustors. *AIAA Journal* **44** (4), 698–708. (Cited on page 1.)

MOUREAU, V., FIORINA, B. & PITSCH, H. 2009 A level set formulation for premixed combustion LES considering the turbulent flame structure. *Combustion and Flame* **156**, 801–812. (Cited on pages 1 and 26.)

MUNT, R. M. 1977 The interaction of sound with a subsonic jet issuing from a semi-infinite cylindrical pipe. *Journal of Fluid Mechanics* **83** (4), 609–640. (Cited on page 40.)

NICOUD, F., BENOIT, L., SENSIAU, C. & POINSOT, T. 2007 Acoustic modes in combustors with complex impedances and multidimensional active flames. *AIAA Journal* **45** (2), 426–441. (Cited on page 58.)

NICOUD, F & POINSOT, T 2005 Thermoacoustic instabilities: should the Rayleigh criterion be extended to include entropy changes? *Combustion and Flame* **142**, 153–159. (Cited on page 46.)

NOIRAY, N., BOTHIEN, M. & SCHUERMANS, B. 2011 Investigation of azimuthal staging concepts in annular gas turbines. *Combustion Theory and Modelling* **15** (5), 585–606. (Cited on pages 7, 8, and 120.)

NOIRAY, N., DUROX, D., SCHULLER, T. & CANDEL, S. 2008 A unified framework for nonlinear combustion instability analysis based on the Flame Describing Function. *Journal of Fluid Mechanics* **615**, 139–167. (Cited on pages 2, 3, 6, 19, 53, 54, 58, 80, and 136.)

NOIRAY, N. & SCHUERMANS, B. 2013*a* Deterministic quantities characterizing noise driven Hopf bifurcations in gas turbine combustors. *International Journal of Non-Linear Mechanics* **50**, 152–163. (Cited on page 133.)

NOIRAY, N. & SCHUERMANS, B. 2013*b* On the dynamic nature of azimuthal thermoacoustic modes in annular gas turbine combustion chambers. *Proceedings of the Royal Society of London A* **469**, 20120535. (Cited on pages 4, 120, and 132.)

ODEN, J. T. & DEMKOWICZ, L. F. 2010 *Applied functional analysis*, 2nd edn. CRC Press. (Cited on page 121.)

ORCHINI, A., ILLINGWORTH, S. J. & JUNIPER, M. P. 2015 Frequency domain and time domain analysis of thermoacoustic oscillations with wave-based acoustics. *Journal of Fluid Mechanics* **775**, 387–414. (Cited on pages 8, 17, 37, 40, 43, 53, 81, 83, 86, 89, 97, 108, 136, 137, 141, 147, 149, and 150.)

ORCHINI, A. & JUNIPER, M. P. 2015 Heat release response to forced flow oscillations of a low-order modelled laboratory scale dump combustor. *Proceedings of ASME Turbo Expo* pp. GT2015–43219. (Cited on pages 48, 83, and 135.)

ORCHINI, A. & JUNIPER, M. P. 2016*a* Flame Double Input Describing Function analysis. *Combustion and Flame* **171**, 87–=102. (Cited on pages 79 and 173.)

ORCHINI, A. & JUNIPER, M. P. 2016*b* Linear stability and adjoint sensitivity analysis of thermoacoustic networks with premixed flames. *Combustion and Flame* **165**, 97–108. (Cited on page 17.)

ORCHINI, A., RIGAS, G. & JUNIPER, M. P. 2016 Weakly nonlinear analysis of thermoacoustic bifurcations in the Rijke tube. *Journal of Fluid Mechanics* . (Cited on page 105.)

PASCHEREIT, C. O. & GUTMARK, E. 2008 Combustion instability and emission control by pulsating fuel injection. *Journal of Turbomachinery* **130**, 011012. (Cited on page 133.)

PENG, D., MERRIMAN, B., OSHER, S., ZHAO, H. & KANG, M. 1999 A PDE-based fast local Level Set method. *Journal of Computational Physics* **155** (2), 410–438. (Cited on page 10.)

PETERS, M. C. A., HIRSCHBERG, A., REIJNEN, A. J. & WIJNANDS, A. P. J. 1993 Damping and reflection coefficient measurements for an open pipe at low Mach and low Helmholtz numbers. *Journal of Fluid Mechanics* **256**, 499–534. (Cited on pages 40 and 112.)

PITSCH, H. 2002 A G-equation formulation for large-eddy simulation of premixed turbulent combustion. In *Center for Turbulence Research Annual Research Briefs*, pp. 3–14. (Cited on page 1.)

POINSOT, T. 2013 Simulation methodologies and open questions for acoustic combustion instability studies. In *Center for Turbulence Research Annual Research Briefs*, pp. 179–188. (Cited on page 1.)

POLIFKE, W. & LAWN, C. 2007 On the low-frequency limit of Flame Transfer Functions. *Combustion and Flame* **151**, 437–451. (Cited on pages 156 and 158.)

PREETHAM, HEMCHANDRA, S. & LIEUWEN, T. 2008 Dynamics of laminar premixed flames forced by harmonic velocity disturbances. *Journal of Propulsion and Power* **24** (6), 1390–1402. (Cited on pages 12, 18, 19, 20, 29, 30, 31, 36, 48, 54, 59, 83, 85, 136, 139, 140, 142, 150, and 162.)

PREETHAM, THUMULURU, S. K., LIEUWEN, T. & HEMCHANDRA, S. 2010 Linear response of laminar premixed flames to flow oscillations: unsteady stretch effects. *Journal of Propulsion and Power* **26** (3), 524–532. (Cited on page 19.)

PROVANSAL, M., MATHIS, C. & BOYER, L. 1987 Bénard-von Kármán instability: transient and forced regimes. *Journal of Fluid Mechanics* **182**, 1–22. (Cited on page 106.)

RAYLEIGH, LORD 1878 The explanation of certain acoustical phenomena. *Nature* **18**, 319–321. (Cited on pages 1 and 46.)

RIGAS, G., MORGANS, A. S., BRACKSTON, R. D. & MORRISON, J. F. 2015 Diffusive dynamics and stochastic models of turbulent axisymmetric wakes. *Journal of Fluid Mechanics* **778**, R2. (Cited on page 132.)

RIGAS, G., MORGANS, A. S. & MORRISON, J. F. 2016 Weakly nonlinear modelling of a forced turbulent wake. *In preparation, Journal of Fluid Mechanics* . (Cited on page 133.)

RONNEY, P. D. & SIVASHINSKY, G. I. 1989 A theoretical study of propagation and extinction of nonsteady spherical flame fronts. *SIAM Journal of Applied Mathematics* **49** (4), 1029–1046. (Cited on page 141.)

ROSALES, R. 2004 Hopf bifurcations. MIT OpenCourseWare 18.385J/2.036J, lecture notes on nonlinear dynamics and chaos. (Cited on page 118.)

RUAN, S., DUNSTAN, T. D., SWAMINATHAN, N. & BALACHANDRAN, R. 2013 Computation of turbulent premixed flames response to inlet velocity oscillation. In *24th International Colloquium on the Dynamics of Explosions and Reactive Systems*. (Cited on pages 136, 143, and 149.)

SAAD, Y. & SCHULTZ, M. H. 1986 GMRES: a Generalized Minimal RESidual algorithm for solving nonsymmetric linear systems. *SIAM Journal on Scientific and Statistical Computing* **7** (3), 856–869. (Cited on page 68.)

SCHMID, M., BLUMENTHAL, R. S., SCHULZE, M., POLIFKE, W. & SATTELMAYER, T. 2013 Quantitative stability analysis using real-valued frequency response data. *Journal of Engineering for Gas Turbines and Power* **135**, 121601. (Cited on pages 62, 86, and 92.)

SCHUERMANS, B. 2003 Modeling and control of thermoacoustic instabilities. PhD thesis, Ecole Polytechnique Fédérale de Lausanne. (Cited on pages 6, 8, 17, and 18.)

SCHULLER, T., DUCRUIX, S., DUROX, D. & CANDEL, S. 2002 Modeling tools for the prediction of premixed Flame Transfer Functions. *Proceedings of the Combustion Institute* **29**, 107–113. (Cited on pages 19, 26, 35, 82, and 85.)

SCHULLER, T., DUROX, D. & CANDEL, S. 2003 A unified model for the prediction of laminar Flame Transfer Functions: comparisons between conical and V-flames dynamics. *Combustion and Flame* **134** (1-2), 21–34. (Cited on pages 12, 19, 31, 35, 54, 61, 83, 85, 136, 139, and 149.)

SELIMEFENDIGIL, F., FÖELLER, S. & POLIFKE, W. 2012 Nonlinear identification of unsteady heat transfer of a cylinder in pulsating cross flow. *Computers and Fluids* **53**, 1–14. (Cited on pages 81, 110, and 111.)

SELIMEFENDIGIL, F. & POLIFKE, W. 2011 A nonlinear frequency domain model for limit cycles in thermoacoustic systems with modal coupling. *International Journal of Spray and Combustion Dynamics* **3**, 303–330. (Cited on page 81.)

SEMLITSCH, B., ORCHINI, A., DOWLING, A. P. & JUNIPER, M. P. 2016 *G*-equation modelling of thermoacoustic oscillations of partially premixed flames. In *International Symposium: Thermoacoustics Instabilities in Gas Turbines and Rocket Engines*, pp. GTRE–009. (Cited on pages 155, 171, and 176.)

SETHIAN, J. A. 1999 *Level Set methods and Fast Marching methods*, 2nd edn. Cambridge University Press. (Cited on page 10.)

SHIN, D.-H. & LIEUWEN, T. 2013 Flame wrinkle destruction processes in harmonically forced, turbulent premixed flames. *Journal of Fluid Mechanics* **721**, 484–513. (Cited on pages 36, 150, and 169.)

SHREEKRISHNA, HEMCHANDRA, S. & LIEUWEN, T. 2010 Laminar premixed flame response to equivalence ratio oscillations. *Combustion Theory and Modelling* **14** (5), 681–714. (Cited on page 54.)

SIEBER, J., ENGELBORGHS, K., LUZYANINA, T., SAMAEY, G. & ROOSE, D. 2015 Bifurcation analysis of delay differential equations. DDE-BIFTOOL v. 3.1. Manual. (Cited on page 115.)

SIPP, D. 2012 Open-loop control of cavity oscillations with harmonic forcings. *Journal of Fluid Mechanics* **1** (1), 1–30. (Cited on page 133.)

SIPP, D. & LEBEDEV, A. 2007 Global stability of base and mean flows: a general approach and its applications to cylinder and open cavity flows. *Journal of Fluid Mechanics* **593**, 333–358. (Cited on pages 106, 107, 119, 120, 121, and 131.)

SIPP, D., MARQUET, O., MELIGA, P. & BARBAGALLO, A. 2010 Dynamics and control of global instabilities in open-flows: a linearized approach. *Applied Mechanics Reviews* **63**, 030801. (Cited on pages 20, 46, and 47.)

STOW, S. R. & DOWLING, A. P. 2001 Thermoacoustic oscillations in an annular combustor. In *Proceedings of ASME Turbo Expo*, pp. GT2001–0037. (Cited on pages 7, 8, 39, 40, and 108.)

STOW, S. R. & DOWLING, A. P. 2004 Low-order modelling of thermoacoustic limit cycles (GT2004-54245). (Cited on page 40.)

STROGATZ, S. H. 2015 *Nonlinear dynamics and chaos*, 2nd edn. Westview Press. (Cited on page 118.)

SUBRAMANIAN, P., BLUMENTHAL, R. S., POLIFKE, W. & SUJITH, R. I. 2015 Distributed time lag response functions for the modeling of combustion dynamics. *Combustion Theory and Modelling* **19** (2), 223–237. (Cited on page 162.)

SUBRAMANIAN, P., MARIAPPAN, S., SUJITH, R. I. & WAHI, P. 2010 Bifurcation analysis of thermoacoustic instability in a horizontal Rijke tube. *International Journal of Spray and Combustion Dynamics* **2** (4), 325–356. (Cited on page 54.)

SUBRAMANIAN, P., SUJITH, R. I. & WAHI, P. 2013 Subcritical bifurcation and bistability in thermoacoustic systems. *Journal of Fluid Mechanics* **715**, 210–238. (Cited on pages 106, 108, 110, and 116.)

TAY-WO-CHONG, L., BOMBERG, S., ULHAQ, A., KOMAREK, T. & POLIFKE, W. 2012 Comparative validation study on identification of premixed Flame Transfer Function. *Journal of Engineering for Gas Turbines and Power* **134** (021502). (Cited on page 83.)

THOMPSON, J. M. T. & STEWART, H. B. 2001 *Nonlinear dynamics and chaos*, second edition edn. Wiley. (Cited on page 67.)

TIEN, J. H. & MATALON, M. 1991 On the burning velocity of stretched flames. *Combustion and Flame* **8**, 238–248. (Cited on page 141.)

WANG, H. Y., LAW, C. K. & LIEUWEN, T. 2009 Linear response of stretch-affected premixed flames to flow oscillations. *Combustion and Flame* **156**, 889–895. (Cited on page 19.)

WAUGH, I., ILLINGWORTH, S. & JUNIPER, M. 2013 Matrix-free continuation of limit cycles for bifurcation analysis of large thermoacoustic systems. *Journal of Computational Physics* **240**, 225–247. (Cited on pages 67 and 68.)

WAUGH, I. C. 2013 Methods for analysis of nonlinear thermoacoustic systems. PhD thesis, University of Cambridge. (Cited on page 12.)

WAUGH, I. C. & JUNIPER, M. P. 2011 Triggering in a thermoacoustic system with stochastic noise. *International Journal of Spray and Combustion Dynamics* **3** (3), 225–242. (Cited on page 2.)

WAUGH, I. C., KASHINATH, K. & JUNIPER, M. P. 2014 Matrix-free continuation of limit cycles and their bifurcations for a ducted premixed flame. *Journal of Fluid Mechanics* **759**, 1–27. (Cited on pages 12, 40, 54, 56, 58, 67, 76, 81, 95, 96, 131, 136, 141, 147, 149, and 150.)

WILLIAMS, A. FOREMAN 1985 *Combustion theory*. Benjamin Cummings. (Cited on pages 8 and 55.)

WITTE, A. & POLIFKE, W. 2015 Heat transfer frequency response of a cylinder in pulsating laminar cross flow. In *17th STAB-Workshop, Göttingen*. (Cited on page 110.)

ZINN, B. T. & LORES, M. E. 1971 Application of the galerkin method in the solution of non-linear axial combustion instability problems in liquid rockets. *Combustion Science and Technology* **4** (1), 269–278. (Cited on page 17.)